# Parametric polarization pulse shaping methods and control of excitation dynamics in ultracold rubidium


**im**
**Fachbereich Physik**
**der**
**Freien Universität Berlin**
**eingereichte Dissertation**

**vorgelegt von**
**Fabian Weise**

**Mai 2010**

Die Arbeit wurde in der Arbeitsgruppe von Herrn Prof. Dr. Ludger Wöste im Zeitraum von Mai 2006 bis Mai 2010 am Fachbereich Physik der Freien Universität Berlin durchgeführt.

| | |
|---|---|
| Erstgutachter: | Prof. Dr. Ludger Wöste<br>Freie Universität Berlin |
| Zweitgutachter: | Prof. Dr. Gerard Meijer<br>Fritz-Haber-Institut der Max-Planck-Gesellschaft<br>Freie Universität Berlin |

Tag der Disputation: 30. Juni 2010

## Kurzfassung

Kern dieser Arbeit ist die Manipulation von ultrakurzen Laserpulsen und deren Anwendung auf molekulare Quantensysteme.

Zwecks uneingeschränkter Formung der Phase, Amplitude und Polarisation von Laserpulsen wurde ein neuer Pulsformer entwickelt. In diesem nicht-interferometrischen Aufbau werden vier aufeinander folgende Flüssigkristallarrays für die Modulation des Lichtfeldes verwendet. Für die gezielte Kontrolle des geformten elektrischen Feldes wurde ein Verfahren zur Erstellung von Pulssequenzen entwickelt. Die Unterpulse dieser Sequenzen können in ihren physikalisch intuitiven Parametern Energie, zeitliche Position, Phase, Chirps und der Polarisation, die durch die Orientierung, die Elliptizität und die Helizität gegeben ist, individuell kontrolliert werden. Die Funktionsweise des Pulsformers und der Parametrisierung wird anhand von experimentell erstellten und charakterisierten Pulsen veranschaulicht. Pulsformen von höherer Komplexität bieten Einblicke in die Möglichkeiten und die Präzision der vorgestellten Methoden.

Für einige Anwendungsgebiete ist es wünschenswert, die geformten Laserpulse durch optische Fasern zu transportieren. Insbesondere würde im Bereich Biowissenschaften und Medizin von endoskopisch verfügbaren Femtosekunden-Laserpulsen profitiert werden. In dieser Arbeit wird die Erstellung von ultrakurzen Laserpulsen vorgestellt, die nach der Transmission durch optische Fasern gezielt in Phase, Amplitude und Polarisation geformt werden. Hierbei müssen die speziellen Eigenschaften der Faser berücksichtigt werden. Dies wird exemplarisch für eine konventionelle Step-Index-Glasfaser sowie für eine photonische Hohlkern-Kristall-Faser gezeigt. Aufgrund der unterschiedlichen Eigenschaften dieser Fasern ist zur Erstellung parametrisch geformter Pulse ein jeweils eigenständiges Verfahren notwendig. Ähnlich wie bei der Vorstellung des Pulsformers werden die Möglichkeiten der Kontrolle der Pulssequenzen mit Beispielpulsen belegt. Die durch die Faser transmittierten und in Phase, Amplitude und Polarisation parametrisch geformten Pulse werden zur Untersuchung der Moleküldynamik genutzt. Zu diesem Zweck wird die Mehrphotonen-Ionisation des Kalium-Dimers in einem Molekularstrahl in einer Rückkopplungsschleife unter Verwendung evolutionärer Algorithmen optimiert. Ferner wird eine durch den Pulsformer erstellte Doppelpulssequenz für zeitaufgelöste Pump-Probe-Messungen genutzt. Beide Experimente geben Aufschluss über die Vibrationsdynamik und den Anregungsweg der Moleküle. Dabei wird die Relevanz der Polarisationsänderung für den Prozess der Mehrphotonen-Ionisation deutlich.

In einem weiteren Experiment werden Methoden der kohärenten Kontrolle angewendet, um die Wechselwirkung zwischen geformten ultrakurzen Laserpulsen und ultrakalten Atomen und Molekülen zu untersuchen. Die Kontrolle und Untersuchung der Photoassoziation eines ultrakalten atomaren Stoßpaares zu einem gebundenen Molekül war hier von besonderem Interesse. Dieser Prozess wurde mittels Zweifarben-Pump-Probe-Spektroskopie untersucht. Die experimentell erhaltenen Transienten wurden mit theoretischen Berechnungen verglichen. Deren Analyse gab Aufschluss über die Wechselwirkung, die in der Zeit- und Frequenzdomäne diskutiert wird. Des Weiteren wird die Mehrphotonen-Ionisation des ultrakalten Rubidium-Dimers in einer Rückkopplungsschleife optimiert. Hierfür wurde zur Identifikation der für die Anregung relevanten Frequenzen eine Parametrisierung des Pulses in der Frequenzdomäne genutzt. In Verbindung mit den Ergebnissen eines komplementären Experiments konnte der Anregungsprozess erfolgreich entschlüsselt werden.

## Abstract

This work focuses on the developments of ultrafast laser pulse shaping techniques and their application to diatomic molecular systems in order to reveal fundamental effects in light matter interaction.

It describes the development of a new pulse shaper consisting of a sequence of four liquid crystal arrays and a polarizer. This pulse shaper is the first non-interferometric setup for unrestricted phase, amplitude, and polarization shaping. Moreover, a parametric encoding of the electric field was developed which allowed for generating pulse sequences consisting of several sub-pulses. Each sub-pulse can be controlled in its physically apparent parameters: energy, position in time, phase, and chirps as well as state of polarization with ellipticity, orientation, and helicity. The feasibility of the setup is illustrated by systematic variations of single and double pulses, which are experimentally generated and measured. In these series of pulses, one of the pulses parameters is varied while the other parameters are kept constant. This proves the precise control of the pulse shape. Further, more complex pulses are shown to give an impression of the capabilities of this setup in combination with the parameterization.

For some fields of application, it could be desirable to guide the phase, amplitude and polarization shaped pulses through an optical fiber. For example, life science could benefit from shaped pulses in the area of imaging and photodynamic therapy. In order to make the shaped pulses available at the distal end of an optical fiber, the effects of the fiber have to be compensated. In this work, the generation of phase, amplitude, and polarization shaped pulses after transmission trough an optical fiber is presented. This is demonstrated for two types of optical fibers – a standard single-mode fiber and a microstructured hollow core photonic crystal fiber. The procedure for the determined generation of parametrically shaped pulses differs for both types of optical fibers. The capabilities of parametrically shaped pulse sequences are – again – illustrated by a series of example pulses.

The parametrically shaped pulses transmitted through the hollow core fiber are implemented in a coherent control experiment. For this purpose, the potassium dimer produced in a molecular beam serves as a test system. The multi-photon ionization is studied by a closed feedback loop optimization and shaper-assisted pump-probe spectroscopy. These experiments revealed the excitation path including the vibrational dynamics in the first and second excited state. Further, the relevance of the polarization control in the excitation process is highlighted.

Moreover, coherent control techniques are applied to investigate the interaction of shaped femtosecond laser pulses with ultracold atoms and molecules. The focus of these experiments is the control of the photoassociation of a colliding atom pair to a bound molecule. This process is investigated using two-color pump-probe spectroscopy. The molecular transients are compared to theoretical calculations. The analysis of this data reveals the interaction process which is discussed in the time and frequency domain. In a second experiment, the multi-photon ionization of ultracold rubidium dimers is optimized in a closed feedback loop. In this optimization, a parameterization in the frequency domain is employed which extracts the relevant transition frequencies. In combination with a complementary experiment the excitation pathway was revealed.

# Contents

# Chapter 1

# Introduction

The investigation of nature and the desire to manipulate and even intervene in the processes of nature are driven by the curiosity of mankind. Using light for this purpose is one of the most obvious approaches. In the beginning, the sun was the only source of light. Today, there is a large variety of light sources available. An important milestone to modern science was the development of the laser by T. H. Maiman in the 1960s [1]. The coherence and high intensity of laser light makes it an ideal tool for atomic and molecular physics. Continuous wave lasers, which have a narrow frequency band, facilitated spectroscopy of molecules. The invention of pulsed lasers allowed for time-resolved measurements. Due to the Heisenberg uncertainty principle, these laser pulses cover a broad frequency spectrum whose width is inversely proportional to the pulse duration. When a femtosecond laser pulse excites a molecule, several vibrational states are coherently addressed. The superposition of the vibrational states forms a wavepacket. The evolution of the wavepacket is described by quantum mechanics and can be related to the motion of the atoms in the chemical bond.

In this excitation process, the dynamics of the wavepacket are directly connected to the shape of the exciting laser pulse. The development of pulse shapers allowed for controlling the electric field of the laser pulses. The laser pulses could be tailored to be optimally suited for a specific excitation in a specific molecule in order to control the outcome of the excitation process. This new technique was denoted as coherent control. To circumvent the solution of the often very complex Hamiltonian, the optimal pulse shape can be found in feedback loop optimizations. In this approach, the pulse shaper is controlled by a computer on the basis of a measured signal that is characteristic for the desired final state. In an optimization employing an evolutionary algorithm, the pulse adapts iteratively to the particular quantum system facilitating the improvement of the excitation efficiency. The analysis of the optimal pulses provides insight into the underlying excitation process.

This procedure has been successfully applied to a number of experiments in different fields of physics. In the majority of these experiments, the pulses have been modulated in the scalar parameters phase and amplitude. However, since the majority of quantum objects are three-dimensional, the extension of the modulation to polarization is a logical consequence. Several experiments have revealed the relevance of the vectorial character of the light field in the excitation process. They range from the control of ionization efficiency in potassium and iodine dimers [2], control of the angular momentum distribution [3],

modulation of the optical near field [4], and control in non-linear spectroscopy [5]. Possibly they would increase the efficiency in high-harmonic generation [6, 7], would allow for fabrication of enantiomers [8, 9], and could induce ring-currents in molecules [10].

New pulse shapers have been developed for polarization shaping of ultrafast pulses. These setups utilize liquid crystal arrays for the modulation of the pulse. However, all these pulse shapers are either restricted in the modulation of the polarization or they rely on interferometric pulse construction, which, in turn, requires very stable setups.

In chapter 4 of this work, the history of polarization pulse shaping is presented and a new pulse shaper setup is introduced. This setup is stable and is not restricted in polarization control. It is capable of simultaneous phase, amplitude, and polarization shaping. The modulation is achieved using four liquid crystal arrays that are placed in the Fourier plane of a 4-f line. Moreover, a parametric sub-pulse encoding is developed, which allows for the generation of pulse sequences that consist of a number of sub-pulses. Each sub-pulse can be individually controlled by the physically intuitive parameters energy, position in time, phase, and chirps as well in the polarization including orientation, ellipticity, and helicity.

The functionality of the setup and the parameterization is systematically demonstrated with series of double pulses as well as more complex pulses, as presented in section 4.7 and 4.9. Further, it is implemented in a feedback loop optimization in order to prove the application to coherent control experiments. For this purpose, the second-harmonic generation was chosen as a test system. The results are presented in section 4.11.1 and show the advantages of the parametric encoding.

For many applications it could be desirable to guide the shaped pulses through optical fibers. This would allow for an application, for example, via endoscopes for non-linear imaging or photo-dynamic therapy; an aspect of particular interest for life sciences [11, 12]. To date, pulse shapers have only been utilized for compensation of dispersion and polarization mode dispersion. This only allowed for the generation of simple, short single pulses after propagation through the fiber. In chapter 5, the developments for the generation of more complex, arbitrary shaped pulses after transmission through optical fibers are presented. In order to provide phase, amplitude, and polarization shaped pulses at the distal end of the optical fiber, the effects induced by the propagation through the fiber have to be considered. Two different types of optical fibers are employed for guiding the laser pulses: a standard step-index fiber and a microstructured hollow core photonic crystal fiber. The generation of polarization shaped pulses after transmission through optical fibers requires a different method for each type of fiber. The procedure for the step-index fiber is described in section 5.5. In the case of the hollow core photonic crystal fiber, pulses of larger energy can be transmitted through the fiber. The scheme for generating arbitrarily shaped pulses after transmission through this fiber is presented in section 5.6. The generation of parametrically shaped pulse sequences is implemented for both optical fibers. The feasibility of this approach is demonstrated using example pulses of different complexity, which are available after propagation through the optical fiber.

In a feedback loop experiment, which is presented in chapter 6, these methods are applied to a molecular system. The multi-photon ionization of the potassium dimer is optimized using the parametric sub-pulse encoding in combination with the hollow core photonic crystal fiber. Three sub-pulses are optimized to match the number of photons required for

the ionization process. Each sub-pulse of the optimized pulse sequence can be associated intuitively to the respective excitation steps. Further, a shaped double pulse with variable time delay is utilized to perform shaper-assisted pump-probe spectroscopy through the optical fiber. The analyses of both experiments reveal the excitation dynamics and highlight the relevance of polarization control.

This feedback loop optimization of the ionization is a representative example for many coherent control experiments. Another two basic processes in chemistry are bond breaking and bond formation. The fragmentation of specific molecular bonds has already been investigated in many experiments using shaped femtosecond laser pulses. The bond formation by laser pulses, however, has not yet been investigated. The process in which a free atom pair is assembled to a molecule with the help of light, is denoted as photoassociation. In ultracold physics, the photoassociation was first demonstrated by P. D. Lett *et al.* in 1993 [13]. A colliding ultracold atom pair is excited by a continuous wave laser of narrow bandwidth to a bound molecular state. Since direct methods for obtaining ultracold molecules are not available, photoassociation is an indirect way to produce ultracold molecules. The interest in ultracold molecules is increasing, due to their extreme potential in the realm of fundamental research, ranging from high precision spectroscopy to the investigation of new quantum effects.

A new approach, which is complementary to the high precision spectroscopy with narrow band laser, is the use of pulsed lasers for the investigation of ultracold atoms and molecules. Theory proposes that higher efficiencies for photoassociation are possible by utilizing wavepacket dynamics [14, 15, 16]. In addition, the broadband pulses could be used for stabilization of the weakly bound molecules in the trap [17, 18].

In chapter 7, some of the first experiments combining the world of ultrafast lasers and ultracold atoms are presented. In these experiments, the ultracold rubidium atoms and molecules in a magneto-optical trap are investigated using femtosecond laser pulses. The molecular formation is studied using time-resolved pump-probe spectroscopy. Pulse shaping is applied to the pump pulse in order to explore the interaction process. The resulting transients are reproduced by quantum dynamical calculations. The analysis of the transient molecular signal reveals the dynamics of the interaction of ultrashort laser pulses and the ultracold matter.

In the second part of chapter 7.6, the multi-photon ionization of ultracold rubidium dimers is investigated. For this purpose, a feedback loop optimization is performed, using parametric amplitude shaping to extract the relevant transitions. The results are presented along with data of a second experiment in which the transition bands are localized by frequency filtering. These experiments reveal the ionization pathway including the participating electronic states. Moreover, the effect of photoassociation and the binding length of the molecules are also discussed.

Each chapter starts with a short statement about the motivation behind the experiment and provides an introduction to the physical background. At the end of each chapter, the results are summarized and an outlook is provided.

# Chapter 2

# Fundamental physics

This chapter describes the basic principles of physics that are essential for this work. Beginning with the classical electrodynamics and the description of light waves in section 2.1 the properties of the electric field are reconsidered in section 2.2 focussing on the state of polarization. The Jones formalism will be introduced in section 2.3 for the characterization and manipulation of the polarization state. In section 2.4, the description of the light field will be extended to pulses which are composed of a broad band of phase-locked frequencies. These pulses will be described in the time and frequency domain. The representation of the electric field in the frequency domain provides access to manipulation and control of the electric field. This is described in section 2.4.2. This manipulation of ultrafast laser pulses is the central point in this work. The theoretical frame for the description of the interaction of a laser pulse with a quantum system is laid out in section 2.5. Finally, different approaches of coherent control are introduced in section 2.6. The technique of closed feedback loop optimizations and suitable optimization algorithms are discussed in section 2.7.

## 2.1 Solution of Maxwell's equations

The classical electro-magnetic phenomena are described by Maxwell's equations [19]. This set of four coupled differential equations relates the electric and magnetic field to their sources. An electric field which varies in time causes a magnetic field, and vice versa. These fields are inseparably associated. In vacuum, the combination of them yields the wave equation for the electric field $\tilde{\mathbf{E}}(\mathbf{r},t)$.

$$\frac{\partial^2}{\partial t^2}\mathbf{E}(\mathbf{r},t) - c_0^2 \cdot \nabla^2 \mathbf{E}(\mathbf{r},t) = 0 \tag{2.1}$$

Solutions of this equation are sinusoidal waves which are traveling at the speed of light $c_0$. A commonly used solution is the complex electric field:

$$\tilde{\mathbf{E}}(\mathbf{r},t) = \tilde{\mathbf{E}}_0 e^{i(\omega t - \mathbf{k}\cdot\mathbf{r} + \phi)} \tag{2.2}$$

This describes a wave traveling in space $\mathbf{r}$ and time $t$ at the speed of light. Here $\tilde{\mathbf{E}}_0$ is the amplitude, $\omega$ the frequency and $\phi$ the phase of the wave. Further, Maxwell's equations

imply that the electric vector, the magnetic vector, and the direction of propagation **k** are all pairwise perpendicular. In the following, the description of light is reduced to the electric field. Without loss of generality, the direction of the propagation is defined as **z**. The vector of the electric field in free space is composed of its x and y component.

$$\begin{aligned} \tilde{\mathbf{E}}(\mathbf{z},t) &= \tilde{E}_x(\mathbf{z},t)\hat{\mathbf{x}} + \tilde{E}_y(\mathbf{z},t)\hat{\mathbf{y}} && (2.3)\\ &= E_{0x}e^{i(\omega t - \mathbf{k}\cdot\mathbf{z}+\phi_x)}\hat{\mathbf{x}} + E_{0y}e^{i(\omega t-\mathbf{k}\cdot\mathbf{z}+\phi_y)}\hat{\mathbf{y}} && (2.4)\end{aligned}$$

Then, equation 2.4 can be separated in a propagator and a vector.

$$\tilde{\mathbf{E}}(\mathbf{z},t) = \begin{bmatrix} E_{0x}e^{i\phi_x} \\ E_{0y}e^{i\phi_y} \end{bmatrix} e^{i(\omega t-\mathbf{k}\cdot\mathbf{z})} \tag{2.5}$$

Since the spatial propagation is not relevant in this work, it is neglected by setting the observer to $\mathbf{z} = 0$. The electric field simplifies to

$$\tilde{\mathbf{E}}(t) = \begin{bmatrix} E_{0x}e^{i\phi_x} \\ E_{0y}e^{i\phi_y} \end{bmatrix} e^{i\omega t}. \tag{2.6}$$

This vector is called Jones vector and is described in detail in section 2.3. It describes the polarization state of the electric field which is completely determined by the relative phase $\epsilon = \phi_x - \phi_y$ and the ratio of the amplitudes $E_{0x}$ and $E_{0y}$.

## 2.2 Instantaneous electric field: the polarization ellipse

The curve generated by this vector will be derived here. Since the polarization state is determined by the relative phase $\epsilon$, the following substitution can be made: $\phi_x = \phi_0$ and $\phi_y = \phi_0 + \epsilon$. When only considering the real part of equation 2.6, the transverse components of the electric field can be written as a parameterized curve.

$$\begin{aligned} E_x(\omega t) &= E_{0x}cos(\omega t) && (2.7)\\ E_y(\omega t) &= E_{0y}cos(\omega t + \epsilon) && (2.8)\end{aligned}$$

These two equations have the form of restricted Lissajous figures. The shape of the curve generated by these equations describes the polarization state. It can be classified in three types: in case of $\epsilon = 0 \pm n \times \pi$ it describes linear polarization wherein the orientation is set by the ratio of the amplitudes ($n \in \mathbb{Z}$). If $n$ is odd-numbered, the direction of the vector of the electric field is mirrored on the y axis. If the amplitudes $E_{0x}$ and $E_{0y}$ are equal and the relative phase is set to $\epsilon = \pi/2 + n \times \pi$, the polarization is circular . Any other combinations result in elliptical polarization. The sign of $\epsilon$ determines the direction of rotation, which is termed helicity. If $\epsilon \geq 0$, the x component of the electric field is faster than the y component, the field $E_x$ leads $E_y$ and the vector of the electric field rotates counter-clockwise seen in direction of propagation. This is denoted left-handed polarization[1].

[1]Some references define the helicity of the polarization ellipse as observed from the receiver.

The equations of the Lissajous figures 2.7 and 2.8 can be transformed to

$$\frac{E_x(\omega t)}{E_{0x}} = cos(\omega t) \tag{2.9}$$

$$\frac{E_y(\omega t)}{E_{0y}} = cos(\omega t + \epsilon) \tag{2.10}$$

$$= cos(\omega t)cos(\epsilon) - sin(\omega t)sin(\epsilon) \tag{2.11}$$

By combining equation 2.9 and 2.11 one can obtain

$$\frac{E_y(\omega t)}{E_{0y}} - \frac{E_x(\omega t)}{E_{0x}}cos(\epsilon) = sin(\omega t)sin(\epsilon). \tag{2.12}$$

Using the identity $sin(\omega t) = \sqrt{1 - \frac{E_x(\omega t)^2}{E_{x0}}}$ obtained from equation 2.9, $\omega t$ can be eliminated and equation 2.12 can be reformed to the parametric ellipse expression based on the Lissajous description

$$(E_x(\omega t))^2 \frac{1}{E_{0x}^2 sin^2(\epsilon)} - (E_y(\omega t))^2 \frac{1}{E_{0y}^2 sin^2(\epsilon)} - 2E_x(\omega t)E_y(\omega t)\frac{cos(\epsilon)}{E_{0x}E_{0y}sin^2(\epsilon)} = 1 \tag{2.13}$$

### 2.2.1 Parameterization of the polarization ellipse

The ellipse of the electric field can be described by two sets of parameters. One set comprises the parameters of the Lissajous representation: amplitudes in x and y direction and the relative phase shift $\epsilon$ as presented before. An alternative way to describe the ellipse of the electric field uses the parameters intensity $I$, ellipticity $r$, orientation of the major axis $\gamma$, and helicity. The intensity $I$ and ellipticity $r$ can be expressed by expressed by the principal axes of the polarization ellipse: $A_{major}$ and $A_{minor}$.

$$I = A_{major}^2 + A_{major}^2 \tag{2.14}$$

$$r = \frac{A_{minor}}{A_{major}} \tag{2.15}$$

The orientation of the ellipse is determined by the angle of the major axis, which is measured counter-clockwise starting from the horizontal x axis. The ellipse with its parameters is depicted in figure 2.1. The equation of a rotated ellipse in Cartesian coordinates is given by

$$\left(\frac{E_x(\omega t)cos(\gamma) + E_y(\omega t)sin(\gamma)}{A_{major}}\right)^2 + \left(\frac{-E_x(\omega t)sin(\gamma) + E_y(\omega t)cos(\gamma)}{A_{minor}}\right)^2 = 1 \tag{2.16}$$

which can be sorted by its coefficients:

$$\begin{aligned} &E_x(\omega t)^2 \left(\frac{cos^2(\gamma)}{A_{major}^2} + \frac{sin^2(\gamma)}{A_{minor}^2}\right) \\ &+E_y(\omega t)^2 \left(\frac{cos^2(\gamma)}{A_{minor}^2} + \frac{sin^2(\gamma)}{A_{major}^2}\right) \\ &+2E_x(\omega t)E_y(\omega t) \left(\frac{cos(\gamma)sin(\gamma)}{A_{minor}^2} - \frac{cos(\gamma)sin(\gamma)}{A_{major}^2}\right) = 1 \end{aligned} \tag{2.17}$$

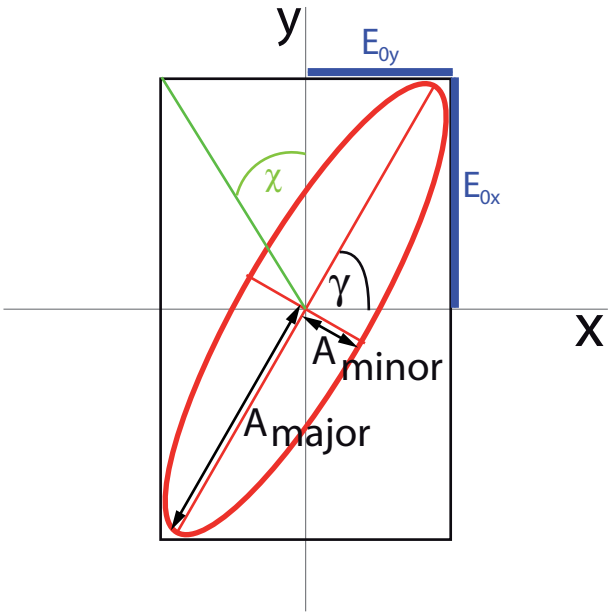


Figure 2.1: The ellipse characterizing the instantaneous electric field. It is described by either the parameter set intensity $I = A_{minor}^2 + A_{major}^2$, ellipticity $r = \frac{A_{minor}}{A_{major}}$ and orientation $\gamma$ or by the components of the electric field in horizontal and vertical direction $E_{0x}$ and $E_{0y}$ and their relative phase.

The equations 2.13 and 2.17 describe the same electric field. Therefore, it is possible to transfer the set of parameters from the Lissajous description $\{E_{0x}, E_{0y}, \epsilon\}$ to the Cartesian description $\{I, r, \gamma\}$. A transformation from one set of parameters to the other is achieved by comparing the coefficients of equation 2.13 and 2.17.

$$\frac{1}{E_{0x}^2 sin^2(\epsilon)} = \frac{cos^2(\gamma)}{A_{major}^2} + \frac{sin^2(\gamma)}{A_{minor}^2} \tag{2.18}$$

$$\frac{1}{E_{0y}^2 sin^2(\epsilon)} = \frac{cos^2(\gamma)}{A_{minor}^2} + \frac{sin^2(\gamma)}{A_{major}^2} \tag{2.19}$$

$$\frac{cos(\epsilon)}{E_{0x}E_{0y} sin^2(\epsilon)} = \frac{cos(\gamma)sin(\gamma)}{A_{minor}^2} - \frac{cos(\gamma)sin(\gamma)}{A_{major}^2} \tag{2.20}$$

### 2.2.2 Transformation $\{E_{0x}, E_{0y}, \epsilon\} \Rightarrow \{I, r, \gamma\}$

Equation 2.20 can be transformed to

$$\frac{cos(\epsilon)}{sin^2(\epsilon)} \frac{2}{E_{0x}E_{0y}} = sin(2\gamma) \left( \frac{1}{A_{minor}^2} - \frac{1}{A_{major}^2} \right). \tag{2.21}$$

The sum of the equations 2.18 and 2.19 gives:

$$\frac{1}{sin^2(\epsilon)} \left( \frac{1}{E_{0x}^2} + \frac{1}{E_{0y}^2} \right) = \frac{1}{A_{major}^2} + \frac{1}{A_{minor}^2} \tag{2.22}$$

The differences of the equations 2.18 and 2.19 gives:

$$\frac{1}{sin^2(\epsilon)} \left( \frac{1}{E_{0x}^2} - \frac{1}{E_{0y}^2} \right) = \left( \frac{1}{A_{major}^2} - \frac{1}{A_{minor}^2} \right) cos(2\gamma) \tag{2.23}$$

Dividing equation 2.21 by 2.23 eliminates $A_{major}$ and $A_{minor}$ and gives:

$$2E_{0x}E_{0y}cos(\epsilon) = \left(E_{0x}^2 - E_{0y}^2\right) tan(2\gamma) \tag{2.24}$$

This can be transformed to an expression for the orientation $\gamma$:

$$\gamma = \frac{1}{2} arctan\left(\frac{2E_{0x}E_{0y}cos(\epsilon)}{E_{0x}^2 - E_{0y}^2}\right) \tag{2.25}$$

By using the equations 2.22 and 2.23 a formula for the major and minor axis of the ellipse is obtained:

$$A_{major/minor}^2 = \frac{2E_{0x}^2E_{0y}^2sin^2(\epsilon)}{E_{0x}^2 + E_{0y}^2 \pm \frac{E_{0y}^2 - E_{0x}^2}{cos(2\gamma)}} \tag{2.26}$$

The positive sign corresponds to the major axis $A_{major}$ and the negative sign to the minor axis $A_{minor}$. The parameter $\gamma$ is eliminated by using equation 2.25 and the relation $cos(arctan(\zeta)) = 1/\sqrt{1+\zeta^2}$. This leads to:

$$A_{major/minor} = \sqrt{\frac{2E_{0x}^2E_{0y}^2sin^2(\epsilon)}{E_{0x}^2 + E_{0y}^2 \pm \left(E_{0y}^2 - E_{0x}^2\right)\sqrt{1 + \frac{4E_{0x}^2E_{0y}^2cos^2(\epsilon)}{\left(E_{0x}^2 - E_{0y}^2\right)}}}} \tag{2.27}$$

The ellipticity $r$ is calculated as the ratio of the minor to the major axis of the ellipse:

$$r = \frac{A_{minor}}{A_{major}} = \pm\sqrt{\frac{E_{0x}^2 + E_{0y}^2 - \left(E_{0y}^2 - E_{0x}^2\right)\sqrt{1 + \frac{4E_{0x}^2E_{0y}^2cos^2(\epsilon)}{\left(E_{0x}^2 - E_{0y}^2\right)}}}{E_{0x}^2 + E_{0y}^2 + \left(E_{0y}^2 - E_{0x}^2\right)\sqrt{1 + \frac{4E_{0x}^2E_{0y}^2cos^2(\epsilon)}{\left(E_{0x}^2 - E_{0y}^2\right)}}}} \tag{2.28}$$

The sign of the square root determines the helicity of the electric field. The intensity $I$ can be also expressed by the sum of the squared electric field components:

$$I = E_{0x}^2 + E_{0y}^2. \tag{2.29}$$

### 2.2.3 Transformation $\{I, r, \gamma\} \Rightarrow \{E_{0x}, E_{0y}, \epsilon\}$

This transformation is similarly calculated from the equations 2.18 to 2.20. The electric field in horizontal $E_{0x}$ and vertical $E_{0y}$ direction is described by:

$$E_{0x/0y} = \sqrt{\frac{1}{2}\left(A_{major}^2 + A_{minor}^2 \pm \left(A_{major}^2 - A_{minor}^2\right) cos(2\gamma)\right)} \tag{2.30}$$

The positive sign corresponds to $E_{0x}$ and the negative sign to $E_{0y}$. The phase difference is given by

$$\epsilon = \frac{sin(2\gamma)}{|sin(2\gamma)|} arccos\left(\sqrt{\frac{\left(A_{major}^2 - A_{minor}^2\right)^2 \left(A_{major}^2 + A_{minor}^2\right)^2}{A_{major}^4 + A_{minor}^4 + A_{major}^2 A_{minor}^2 \left(cot^2(\gamma) + tan^2(\gamma)\right)}}\right). \quad (2.31)$$

Using the relations 2.14 and 2.15 equation 2.30 and 2.31 can be transformed to:

$$E_{0x} = \sqrt{\frac{1}{2} I \left(1 - \frac{r^2 - 1}{r^2 + 1} cos(2\gamma)\right)} \quad (2.32)$$

$$E_{0y} = \sqrt{\frac{1}{2} I \left(1 + \frac{r^2 - 1}{r^2 + 1} cos(2\gamma)\right)} \quad (2.33)$$

$$\epsilon = \pm arccos\left(\sqrt{\frac{\left(r^2 - 1\right)^2}{1 + r^4 + r^2 \left(cot^2(\gamma) + tan^2(\gamma)\right)}}\right) \quad (2.34)$$

Alternative but equivalent expressions for $E_{0x}$, $E_{0y}$ and $\epsilon$ can be obtained on the basis of geometrical considerations. Figure 2.1 depicts the ellipse in its bounding box and the relevant parameters. The angle of the diagonal in this bounding box $\chi$ can be used to describe the splitting of the intensity $I$ in the electric field components $E_{0x}$ and $E_{0y}$.

$$E_{0x} = \sqrt{I} cos(\chi) \quad (2.35)$$

$$E_{0y} = \sqrt{I} sin(\chi) \quad (2.36)$$

With the parameter

$$\chi = \frac{1}{2} arccos\left(cos(2\gamma) cos\left(2\, arctan(r)\right)\right) \quad (2.37)$$

the phase shift between the x and y component is calculated to

$$\epsilon = \pm arctan\left(\frac{tan\left(2\, arctan(r)\right)}{sin(2\gamma)}\right) \quad (2.38)$$

The sign is connected to the helicity of the light. The negative sign stands for left hand polarization and the positive for right hand polarization.

### 2.2.4 Projections of the polarization ellipse

In order to experimentally analyze the polarization state of light, the intensity can be measured after a polarizer. Depending on the orientation of the polarizer, the fraction which is projected on the axis of the polarizer and thus transmitted through the polarizer varies. These projections under different angles are used to determine the polarization state of the electric field. To exemplify this, the projection of an ellipse oriented at $\gamma$ on

the axis of the polarizer oriented at $\theta$ is depicted in figure 2.2. The projection is calculated solving the equation system of the Cartesian ellipse equation 2.16 and the equation of a linear slope ($y = tan(\alpha)x + d$). The general solution is a family of parallel linear functions. Two of these functions cut the ellipse only in one point. These are the tangents of the ellipse which are characterized by the parameter

$$d_{\pm} = \sqrt{\frac{A_{major}^2 + A_{minor}^2 + \left(A_{minor}^2 - A_{major}^2\right)\cos\left(2\left(\alpha - \gamma\right)\right)}{2\,cos^2(\alpha)}}. \tag{2.39}$$

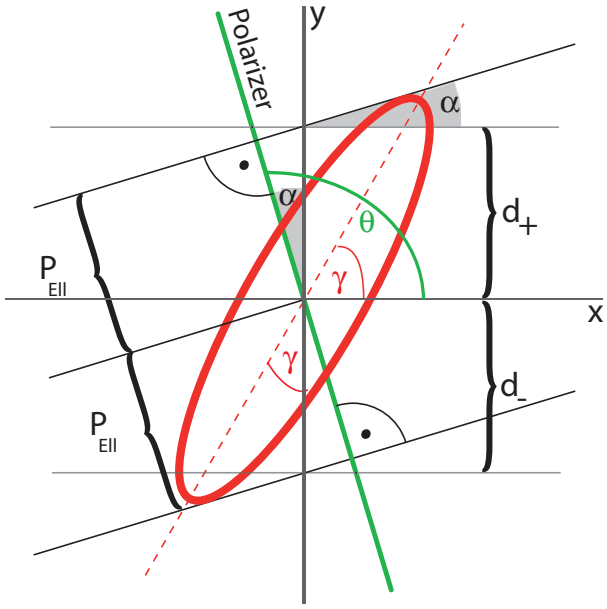


Figure 2.2: The transmitted light after a polarizer is calculated by the projection $P_{Ell}$ of the ellipse onto one axis. The orientation of the polarizer is given by $\theta$. The variables for calculating the projection are depicted.

The upper tangent corresponds to $d_+$ and the lower tangent to $d_-$. Using the expression for $d_{\pm}$ and the relation $cos(\alpha) = P_{Ell}/d$ the projection of the ellipse to the axis of the polarizer $P_{Ell}$ is calculated:

$$P_{Ell}(\alpha) = \frac{1}{\sqrt{2}}\sqrt{A_{major}^2 + A_{minor}^2 + (A_{minor}^2 - A_{major}^2)cos(2(\alpha - \gamma))} \tag{2.40}$$

The measured quantity after the polarizer is the intensity $P_{Int}$. Therefore, the equation has to be squared. Further, the angle of the slope $\alpha$ is replaced by the orientation of the polarizer ($\alpha = \theta - \frac{\pi}{2}$).

$$P_{Int}(\theta) = \frac{1}{2}I\left(A_{major}^2 + A_{minor}^2 + (A_{major}^2 - A_{minor}^2)cos(2(\gamma - \theta))\right) \tag{2.41}$$

This can be reformulated using the intuitive parameters intensity $I$ and ellipticity $r$.

$$P_{Int}(I, r, \gamma, \theta) = \frac{1}{2}I\left(1 - \left(\frac{r^2 - 1}{r^2 + 1}\right)cos(2(\gamma - \theta))\right) \tag{2.42}$$

In the following, this formula will be used to retrieve the polarization state of laser pulses. The intensity is connected to the power of the pulse which is measured after a polarizer for different orientations of the polarizer. At least three data points are required to determine the polarization state [20]. This set of data points is fitted using equation 2.42. The obtained fit parameters characterize the polarization state of the pulse. An analogous procedure is used in the detection of complex pulses with a time-dependent state of polarization. This is described in detail in section 3.3.

| **Polarization state** | **Jones vector** |
|---|---|
| linear, horizontal | $\begin{bmatrix} 1 \\ 0 \end{bmatrix}$ |
| linear, vertical | $\begin{bmatrix} 0 \\ 1 \end{bmatrix}$ |
| linear, oriented at $\gamma$ | $\begin{bmatrix} cos(\gamma) \\ sin(\gamma) \end{bmatrix}$ |
| circular, left-handed | $\frac{1}{\sqrt{2}} \begin{bmatrix} 1 \\ +i \end{bmatrix}$ |
| circular, right-handed | $\frac{1}{\sqrt{2}} \begin{bmatrix} 1 \\ -i \end{bmatrix}$ |
| elliptical, oriented in horizontal or vertical direction | $\frac{1}{\sqrt{a^2+b^2}} \begin{bmatrix} a \\ \pm ib \end{bmatrix}$ |
| elliptical, general | $\frac{1}{\sqrt{a^2+b^2+c^2}} \begin{bmatrix} a \\ b \pm ic \end{bmatrix}$ |

Table 2.1: Jones vectors: A summary of particular polarization states.

## 2.3 Jones formalism

The vectorial character of the electric field has already been discussed before. A convenient way to describe the polarization state of coherent light is the Jones formalism [21, 22]. Polarized light is represented by a 2×1 vector which is complex in general: the Jones vector. The effect of an optical element on the state of polarization of light is regarded as a linear operator acting upon the vector of the electric field. The optical elements are represented by unitary 2×2 matrices: the Jones matrices.

### 2.3.1 Jones vectors

The Jones vector is often represented in its normalized form. The general form of the Jones vector describing the polarization is:

$$\mathbf{E}_0 = \frac{1}{\sqrt{a^2+b^2+c^2}} \begin{bmatrix} a \\ b \pm ic \end{bmatrix} \tag{2.43}$$

The sign of the complex part determines the helicity. The positive sign stands for right-handed elliptical and the negative sign for left-handed elliptical polarization. The orientation of the ellipse is measured counter-clockwise starting from the x axis. A series of particular polarization states is presented in table 2.1.

### 2.3.2 Jones matrices

The polarization state of the electric field which has crossed an optical element $\mathbf{E}'$ can be calculated by multiplying the Jones matrix $\mathbf{J}$ of the element with the Jones vector $\mathbf{E}$ of the prior state of polarization. This general relation is written as

$$\begin{bmatrix} E'_x \\ E'_y \end{bmatrix} = \begin{bmatrix} j_{xx} & j_{xy} \\ j_{yx} & j_{yy} \end{bmatrix} \begin{bmatrix} E_x \\ E_y \end{bmatrix} \tag{2.44}$$

or

$$\mathbf{E}' = \mathbf{J} \cdot \mathbf{E}. \tag{2.45}$$

in which the components $j_{ii}$ of the Jones matrix determine the state of polarization of the resulting light field.

The optical elements can be classified into three groups: polarizers, attenuators, and phase retarders. Light of any polarization which has crossed a horizontally oriented polarizer is linearly polarized in horizontal direction. For an ideal polarizer, there is full transmission in horizontal direction and complete attenuation in vertical direction. The Jones matrix projects the electric field of the incoming Jones vector onto the the axis of the polarizer. Hence, the Jones matrix of a linear polarizer which is horizontally oriented is:

$$\mathbf{J}_{pol}^{0^\circ} = \begin{bmatrix} 1 & 0 \\ 0 & 0 \end{bmatrix} \tag{2.46}$$

A vertical polarizer is described by the Jones matrix $\mathbf{J}_{pol}^{90^\circ}$.

$$\mathbf{J}_{pol}^{90^\circ} = \begin{bmatrix} 0 & 0 \\ 0 & 1 \end{bmatrix} \tag{2.47}$$

The Jones matrix of any rotated optical element $\mathbf{J}'$ can be found by the rotation transformation

$$\mathbf{J}' = \mathbf{R}(-\theta) \cdot \mathbf{J} \cdot \mathbf{R}(+\theta). \tag{2.48}$$

Where $\mathbf{R}(\theta)$ is the universal rotation matrix and $\mathbf{J}$ is the unrotated Jones matrix.

$$\mathbf{R}(\theta) = \begin{bmatrix} cos(\theta) & sin(\theta) \\ -sin(\theta) & cos(\theta) \end{bmatrix} \tag{2.49}$$

The Jones matrix for a linear polarizer rotated by $\theta$ calculates to

$$\mathbf{J}_{pol}^{\theta} = \begin{bmatrix} cos(\theta) & -sin(\theta) \\ sin(\theta) & cos(\theta) \end{bmatrix} \begin{bmatrix} 1 & 0 \\ 0 & 0 \end{bmatrix} \begin{bmatrix} cos(\theta) & sin(\theta) \\ -sin(\theta) & cos(\theta) \end{bmatrix} \tag{2.50}$$

$$= \begin{bmatrix} cos^2(\theta) & cos(\theta)sin(\theta) \\ cos(\theta)sin(\theta) & sin^2(\theta) \end{bmatrix} \tag{2.51}$$

Experimentally, optical elements are not perfect and do not have complete transmission or full reflectivity. This loss can be described by a matrix which has the transmission (reflection) coefficients of the optical component on its diagonal.

$$\mathbf{J}_{att} = \begin{bmatrix} \sqrt{rP} & 0 \\ 0 & \sqrt{rS} \end{bmatrix} \tag{2.52}$$

In this, the transmission (reflectivity) coefficients in horizontal and vertical direction are $rP$ and $rS$. The condition $rP, rS \leq 1$ applies due to the dissipative character of the optical element. This matrix is also relevant for describing the evolution of the polarization state by passing through optical elements as the polarization state changes if $rP \neq rS$. When only considering the state of polarization, the relative transmission (reflectivity) between horizontal and vertical direction is relevant and the absolute transmission (reflectivity) can be neglected. For example: the reflectivity of a grating for horizontally polarized light is larger than the reflectivity for vertical components. This can be expressed by

$$\mathbf{J}^g = \begin{bmatrix} 1 & 0 \\ 0 & \sqrt{g} \end{bmatrix}. \tag{2.53}$$

The change of relative phase of the electric field in horizontal and vertical direction directly changes the polarization state as shown in section 2.2. The phase retarder introduces such a shift. Typically it is made of birefringent uniaxial crystals such as quartz, calcite, $MgF_2$, *et cetera*. In these crystals, the refractive index of one axis differs from the other two axes. This unique axis is called extraordinary axis or optical axis. If the refractive index of the optical axis is smaller than of the other axis, the phase velocity of the wave is larger and it is called fast axis. If the refractive index is larger, the phase velocity is smaller and it is called slow axis. Any phase retarder having its optical axis aligned in horizontal or vertical direction can be described by

$$\mathbf{J}_{ret} = \begin{bmatrix} e^{i\phi_x} & 0 \\ 0 & e^{i\phi_y} \end{bmatrix} \tag{2.54}$$

where $\phi_x$ and $\phi_y$ are the phases in horizontal and vertical directions. The phase retardance which is induced between the horizontal and vertical component of the electric field is the difference $\epsilon = \phi_y - \phi_x$. In optics, retardances of $\epsilon = \pi$ and $\epsilon = \pi/2$ are often used. They are referred to as half waveplate (HWP) and quarter waveplate (QWP). The Jones matrix of a quarter waveplate in horizontal and vertical direction are given by:

$$\mathbf{J}^{0^\circ}_{QWP} = e^{i\pi/4} \begin{bmatrix} 1 & 0 \\ 0 & -i \end{bmatrix} \tag{2.55}$$

$$\mathbf{J}^{90^\circ}_{QWP} = e^{i\pi/4} \begin{bmatrix} 1 & 0 \\ 0 & +i \end{bmatrix} \tag{2.56}$$

Quarter waveplates with the optical axis oriented 45° to linear polarization change the polarization state from linear to circular polarization and vice versa. The state of polarization is not changed if linear polarized light which is oriented parallel or perpendicular to the optical axis crosses the element. Elliptical polarization is obtained when the angle differs from multiples of 45°.

The phase retarder which induces a phase shift of $\pi$ is named half waveplate. The half waveplate acts as a rotator, which does not change the ellipticity of the electric field. The orientation of the polarization ellipse (or linear polarization) changes according to the relative angle of the optical axis of the half waveplate. It rotates the polarization ellipse by twice the angle of the optical axis in the opposite direction respective to the axis of the half waveplate. The Jones matrix of the half waveplate with its fast axis oriented at an angle $\alpha$ is expressed by

$$\mathbf{J}^{\alpha}_{HWP} = \begin{bmatrix} cos(2\alpha) & sin(2\alpha) \\ sin(2\alpha) & -cos(2\alpha) \end{bmatrix}. \tag{2.57}$$

Inspecting equation 2.57 it appears to be similar to the rotation matrix introduced in equation 2.49.

### 2.3.3 Jones theorems

On the basis of theoretical considerations of matrix multiplication and group theory R. C. Jones discussed a general system containing the optical elements discussed before: polarizers (also partial polarizers), retardation plates, and rotators. In 1941, he postulated and proved the following three theorems [21, 23, 24]:

- "For light of a given wavelength, an optical system containing any number of retardation plates and rotators is optically equivalent to a system containing only two elements – one a retardation plate and the other a rotator."
- "For light of a given wavelength, an optical system containing any number of partial polarizers and rotators is optically equivalent to a system containing only two elements – one a partial polarizer and the other a rotator."
- "For light of a given wavelength, an optical system containing any number of retardation plates, partial polarizers, and rotators is optically equivalent to a system containing four elements – two retardation plates, one partial polarizer, and one rotator."

### 2.3.4 Variable phase retarder: liquid crystal modulator

One of the most important tools used in this work is the spatial light modulator which employs two arrays of liquid crystals to alter the phase and state of polarization of the transmitted light. Liquid crystals combine the properties of liquid and solid crystals. They are regularly oriented in space while they can flow. There are many types of liquid crystal phases, which differ in their organization. Here, only the nematic phase is considered, which has a long distance orientation order.

The molecules used in liquid crystal modulators are elongated and birefringent. They are pre-aligned in one plane by small grooves in the cell containing the crystals. Due to their dipole moment the molecules can be rotated in this plane by applying an electric field. By rotating the liquid crystals the refractive index along the extra-ordinary axis is altered. The working principle is visualized in figure 2.3. The difference of the phase retardance $\varphi$ between the ordinary and extra-ordinary axis of a liquid crystal cell with the thickness $D$ for for a given wavelength $\lambda_0$ depending on the voltage $V$ is:

$$\varphi(V) = \frac{2\pi D}{\lambda_0} \left(n_e(V) - n_o\right). \tag{2.58}$$

Therefore, a liquid crystal can be used as a continuously controllable waveplate, which can precisely manipulate the polarization state of the electric field [25, 26]. The Jones matrix $\mathbf{J}_{lc}^{0^\circ}(\varphi)$ of such a device with the optical axis oriented horizontally can be expressed as

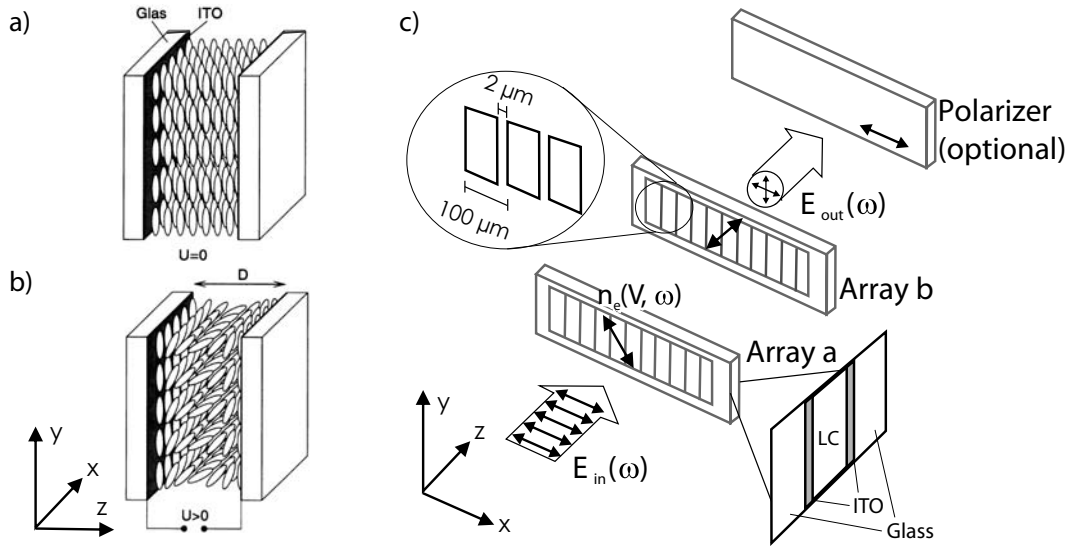


Figure 2.3: Functionality of a liquid crystal modulator. Two sides of the cell are coated with indium tin oxide (ITO), which is transparent for the used range of wavelengths and serves as an electrode. a) If no voltage is applied, the molecules in the liquid crystal are aligned parallel to the sides. The orientation of the molecules in the liquid crystal can be altered by applying a voltage as shown in b). In c), a schematic of a standard double liquid crystal modulator is depicted. It consists of two arrays of liquid crystal cells denoted as pixels, which can be controlled individually.

$$\mathbf{J}_{lc}^{0^\circ}(\varphi) = e^{i\frac{\varphi}{2}} \begin{bmatrix} e^{i\frac{\varphi}{2}} & 0 \\ 0 & e^{-i\frac{\varphi}{2}} \end{bmatrix} \tag{2.59}$$

One single array consisting of liquid crystals with this orientation can be utilized in a spatial light modulator (SLM) for shaping the phase of a laser pulse. Another commonly used orientation of the liquid crystal arrays is $+45^\circ$ or $-45^\circ$ respective to the horizontal axis. The Jones matrix $\mathbf{J}_{lc}^{\pm 45^\circ}$ of a liquid crystal with the optical axis oriented at $\pm 45^\circ$ is obtained by rotation transformation (cf. equation 2.48).

$$\mathbf{J}_{lc}^{\pm 45^\circ}(\varphi) = \mathbf{R}(\mp 45^\circ)\, \mathbf{J}_{lc}^{0^\circ}(\varphi)\, \mathbf{R}(\pm 45^\circ) \tag{2.60}$$

$$= e^{i\frac{\varphi}{2}} \begin{bmatrix} cos\left(\frac{\varphi}{2}\right) & \pm i\ sin\left(\frac{\varphi}{2}\right) \\ \pm i\ sin\left(\frac{\varphi}{2}\right) & cos\left(\frac{\varphi}{2}\right) \end{bmatrix} \tag{2.61}$$

The plus corresponds to an orientation of the optical axis at $+45^\circ$ and minus to $-45^\circ$. The Jones matrix $\mathbf{J}_{dlc}^{\pm 45^\circ}$ for a double liquid crystal modulator with the optical axes oriented at $\pm 45^\circ$ can be expressed as

$$\mathbf{J}_{dlc}^{\pm 45^\circ}(\varphi_a, \varphi_b) = \mathbf{R}(+45^\circ)\mathbf{J}_{lc}^{0^\circ}(\varphi_b)\,\mathbf{R}(-45^\circ)\mathbf{R}(-45^\circ)\mathbf{J}_{lc}^{0^\circ}(\varphi_a)\,\mathbf{R}(+45^\circ) \tag{2.62}$$

$$= e^{i\frac{1}{2}(\varphi_a+\varphi_b)} \begin{bmatrix} cos\left(\frac{\varphi_a-\varphi_b}{2}\right) & i\ sin\left(\frac{\varphi_a-\varphi_b}{2}\right) \\ i\ sin\left(\frac{\varphi_a-\varphi_b}{2}\right) & cos\left(\frac{\varphi_a-\varphi_b}{2}\right) \end{bmatrix}. \tag{2.63}$$

## 2.4 Mathematical description of laser pulses

The description of the electric field is now expanded to laser pulses. Laser pulses consist of a spectrum of many frequencies which all have a defined phase relation. The considerations in the following are carried out for a scalar electric field to simplify matters, but can be easily extended to vectorial fields. In this case, every vector component has to be treated separately.

The real electric field $E(t)$ of a laser pulse in the time domain can be written as a superposition of the complex frequency components $\tilde{E}(\omega)$, which is known as complex Fourier transformation.

$$E(t) = \frac{1}{\sqrt{2\pi}} \int_{-\infty}^{+\infty} \tilde{E}(\omega) e^{i\omega t}\, d\omega \tag{2.64}$$

The electric field in the frequency domain is obtained by the inverse Fourier transformation.

$$\tilde{E}(\omega) = \frac{1}{\sqrt{2\pi}} \int_{-\infty}^{+\infty} E(t) e^{i\omega t}\, dt \tag{2.65}$$

Negative frequency components cannot occur in reality and $\tilde{E}(\omega)$ has to be replaced by $\tilde{E}^{+}(\omega)$ with the condition $\tilde{E}^{+}(\omega) = 0$ for $\omega \leq 0$. The integration limits in equation 2.65 have to be changed to $[0, +\infty]$ resulting in $\tilde{E}^{+}(t)$. The negative complement $\tilde{E}^{-}(t)$ is calculated analogously. The real electric field $E(t)$ is the sum of $\tilde{E}^{+}(t)$ and $\tilde{E}^{-}(t)$. The complex Fourier transformation $\tilde{E}(\omega)$ reassembles $\tilde{E}(\omega) = \tilde{E}^{+}(\omega) + \tilde{E}^{-}(\omega)$. In the following, the complex field $\tilde{E}^{+}(\omega)$ is written as $E(\omega)$.

The pulse duration $\Delta\tau$ is directly connected to the spectral width of the pulse $\Delta\omega$. The width of the pulse in the frequency and the time domain is measured as the FWHM (full width at half maximum) of the pulse.

$$\Delta\omega \geq \frac{c_B}{\Delta\tau} \tag{2.66}$$

Assuming a Gaussian pulse shape, which describes laser pulses very well in the time and frequency domain, the constant is given as $c_B = 4\,ln(2) \approx 2.77$ [27].

### 2.4.1 Modulation in the time domain

The time-dependent complex electric field $\tilde{E}(t)$ of a laser pulse can be written as a product of a time-dependent envelope function $F(t)$ and a phase factor $\Gamma(t)$.

$$\tilde{E}(t) = F(t) \cdot e^{i\Gamma(t)} \tag{2.67}$$

The condition that the spectral width of the pulse is small compared to the carrier frequency allows for application of the slow varying envelope variation [19]. The phase factor $\Gamma(t)$ can be separated into the fast oscillating carrier frequency $\omega_0$ and a phase term $\phi(t)$:

$$\Gamma(t) = \omega_0 t + \phi(t) \tag{2.68}$$

With this the electric field can be written as:

$$\tilde{E}(t) = F(t) \cdot e^{i\omega_0 t} e^{i\phi(t)} \tag{2.69}$$

The derivative of the phase factor $\Gamma(t)$ defines the instantaneous frequency of the electric field $\omega(t)$:

$$\frac{d}{dt}\Gamma(t) = \omega(t) = \omega_0 + \frac{d}{dt}\phi(t) \tag{2.70}$$

**Temporal phase**

The temporal phase can be expanded in a Taylor series:

$$\phi(t) = a_0 + a_1(t - t_0) + \frac{1}{2}a_2(t - t_0)^2 + \frac{1}{6}a_3(t - t_0)^3 + \dots \tag{2.71}$$

The coefficients $a_n$ describe the change of the carrier frequency in time. They are calculated by:

$$a_n = \frac{d^n}{dt^n}\phi(t)\bigg|_{t=t_0} \tag{2.72}$$

The zero-order term $a_0$ induces a constant phase shift. The first order term $a_1$ shifts the carrier frequency to $\omega_0' = \omega_0 + a_1$. With the quadratic term $a_2$ the frequency changes linearly in time. This is called linear chirp. If $a_2$ is negative, the frequencies will become lower during the pulse, which is called down-chirp. In case of $a_2 > 0$, the frequency of the pulse increases during the pulse, which is called up-chirp or positive chirp. Higher order terms describe quadratic and higher order frequency changes in time.

Technically, the modulation of light pulses in the time domain is limited by the speed of the electronics. Pulses with durations of nanoseconds can be modulated directly in the time domain. Optical pulses with durations of a few nanoseconds can be chirped by ramping the current of the light emitting diode [28]. Controlled shaping of femtosecond laser pulses in the time domain is not directly possible. For ultrafast laser pulses, the modulation has to be indirectly applied to the spectral intensity in the frequency domain.

### 2.4.2 Modulation in the frequency domain

Similar to the temporal modulation, the spectral electric field can be separated in a term which describes the spectral amplitude $G(\omega)$ and one for the spectral phase $\phi(\omega)$.

$$\tilde{E}(\omega) = G(\omega) \cdot e^{i\phi(\omega)} \tag{2.73}$$

**Spectral phase**

The spectral phase can be expanded analogously to equation 2.71 in a Taylor series:

$$\phi(\omega) = b_0 + b_1(\omega - \omega_0) + \frac{1}{2}b_2(\omega - \omega_0)^2 + \frac{1}{6}b_3(\omega - \omega_0)^3 + \dots \tag{2.74}$$

with the Taylor coefficients $b_n$, which are expressed by:

$$b_n = \frac{d^n}{d\omega^n}\phi(\omega)\bigg|_{\omega=\omega_0} \tag{2.75}$$

The coefficients can be also attributed to physical properties. Similar to the temporal phase, $b_0$ shifts the phase of the electric field relative to the envelope, which is denoted as carrier envelope phase. The linear coefficient $b_1$ determines the position of the pulse in time. The quadratic term $b_2$ expresses analogously to the term $a_2$ in the frequency domain the linear chirp of the pulse. In case of a pulse with a Gaussian envelope, the coefficients $a_2$ and $b_2$ are equivalent. The linear chirp broadens the pulse in time maintaining the Gaussian envelope. Higher order terms are generally denoted as chirps of $(n-1)^{th}$-order. The coefficient $b_3$ corresponds to a quadratic chirp. The quadratic chirp results in an asymmetric pulse with an oscillatory envelope [29].

#### Frequency domain pulse shaping

The refractive index generally depends on the frequency of the light which crosses the optical medium. The frequency-dependent refractive index causes a frequency-dependent optical path length, which is known as group velocity dispersion (GVD). Similarly, the absorption coefficient, which is basically the complex refractive index, is frequency-dependent. The modulation which is induced by a medium can be described by multiplying a complex filter function $\tilde{H}(\omega)$ with the incoming electric field.

$$\tilde{E}_{out}(\omega) = \tilde{H}(\omega)\tilde{E}_{in}(\omega) \tag{2.76}$$

The modulation function $\tilde{H}(\omega)$ is composed of an amplitude filter $R(\omega)$ and a phase filter $\Phi(\omega)$.

$$\tilde{H}(\omega) = R(\omega)e^{i\Phi(\omega)} \tag{2.77}$$

The amplitude filter $R(\omega)$ is connected to the transmission $T(\omega)$ of the medium and determines the spectral intensity after modulation.

$$I_{out}(\omega) \propto \left|\tilde{E}_{out}(\omega)\right|^2 = \left|\tilde{H}(\omega)\tilde{E}_{in}(\omega)\right|^2 = \left|\tilde{E}_{in}(\omega)\right|^2 R^2(\omega) = \left|\tilde{E}_{in}(\omega)\right|^2 T(\omega) \tag{2.78}$$

The phase filter $e^{i\Phi(\omega)}$ is regarded as a frequency-dependent dispersion, which can be expressed by the Taylor coefficients $b_n$ derived in equation 2.74.

This modulation function can be used to describe pulse shapes using spatial light modulators in the Fourier plane of a 4-f-line. In this approach, the frequencies are spatially separated and can be individually controlled by the modulator. This is discussed in detail in section 3.2.

## 2.5 Light matter interaction

In this section, the theoretical foundations of molecular dynamics and the interaction of molecules with laser light are briefly restated. Firstly, the creation and propagation of

wavepackets are presented. Secondly, the interaction with a time-dependent electric field is described. Thirdly, the pump-probe technique – the standard tool for investigating molecular dynamics – is introduced. Further details can be found in various books, for example in [30] and [31].

### 2.5.1 Molecular wavepackets

The dynamics of an isolated molecule is given by the time-dependent Schrödinger equation

$$i\hbar\frac{\partial}{\partial t}\psi(\mathbf{r},t) = H_0\psi(\mathbf{r},t). \tag{2.79}$$

The Hamiltonian of the system is represented by $H_0$ and writes without an external field

$$H_0 = \frac{\hbar^2}{2m}\nabla^2 + V_M(\mathbf{r}). \tag{2.80}$$

The molecular potential $V_M(\mathbf{r})$ and the Hamiltonian are time-independent. The solution of the time-dependent Schrödinger equation can be expressed as

$$\psi(\mathbf{r},t) = \sum_{n=1}^{\infty} a_n\psi_n(\mathbf{r})e^{-\frac{i}{\hbar}E_n t}. \tag{2.81}$$

The coefficients $a_n$ are the weights of the respective wave functions $\psi_n(\mathbf{r})$. The time-independent states $\psi_n(\mathbf{r})$ are solutions of the time-independent Schrödinger equation

$$H_0\psi_n(\mathbf{r}) = E_n\psi_n(\mathbf{r}) \tag{2.82}$$

with the energy eigenvalues $E_n$. Equation 2.81 describes a propagating wavepacket. This becomes clear from calculating the probability density $|\psi(\mathbf{r},t)|^2$, which is interpreted as the position of the wavepacket:

$$|\psi(\mathbf{r},t)|^2 = \sum_{n=1}^{\infty}\sum_{m=1}^{\infty} a_m^* a_n\psi_m^*(\mathbf{r})\psi_n(\mathbf{r})e^{-\frac{i}{\hbar}(E_n-E_m)t} \tag{2.83}$$

The position of the wavepacket becomes time-dependent if more than one energy state with different energy is populated.

### 2.5.2 Interaction with an external field

The interaction of the molecule with an external electric field is expressed by the time-depending Hamilton operator $H$.

$$H = H_0 + H_1 \tag{2.84}$$

The time-independent Hamiltonian $H_0$, which is defined in equation 2.80, is purely molecular. The perturbation by the laser field is described by the time-dependent part $H_1$. For weak fields, it can be described by the dipole approximation

$$H_1 = -\mathbf{E}(t)\cdot\boldsymbol{\mu}. \tag{2.85}$$

At this point, the vectorial character of the interaction should be highlighted, which will be exploited in chapter 4 and 6. The electric dipole moment of the molecule is denoted as $\boldsymbol{\mu}$. For the excitation of a two-level system, the time-dependent Schrödinger equation can be written as

$$i\hbar\frac{\partial}{\partial t}\begin{bmatrix}\psi_a(\mathbf{r},t)\\ \psi_b(\mathbf{r},t)\end{bmatrix}=\begin{bmatrix}H_a & -\mathbf{E}^*(t)\cdot\boldsymbol{\mu}_{ab}\\ -\mathbf{E}(t)\cdot\boldsymbol{\mu}_{ba} & H_b\end{bmatrix}\begin{bmatrix}\psi_a(\mathbf{r},t)\\ \psi_b(\mathbf{r},t)\end{bmatrix}. \tag{2.86}$$

In this equation, $H_{a,b}$ defines the Hamiltonians which describe the dynamics of the different electronic states $a$ and $b$ in the Born-Oppenheimer approximation. For small perturbations, the first order perturbation theory can be applied, which yields

$$\psi^{(1)}(\mathbf{r},t)=\frac{1}{i\hbar}\int_0^t e^{-\frac{i}{\hbar}H_{0b}(t-t')}(-\mathbf{E}(t')\cdot\boldsymbol{\mu}_{ba})\ e^{-\frac{i}{\hbar}H_{0a}(t')}\psi_a(\mathbf{r},0)\ dt'. \tag{2.87}$$

This formula is interpreted as follows: before the interaction the system resides in the ground state and evolves according to the Hamiltonian $H_{0a}$. If the initial state is the vibrational ground state ($v=0$), no dynamic occurs.[2] At the time $t'$ the electric field $\mathbf{E}(t')=\mathbf{F}(t')e^{-i\omega t'}$ interacts with the transition dipole moment $\boldsymbol{\mu}_{ba}$ and population is transfered to the electronically excited state. Due to the broadband excitation pulse many vibrational states are populated and a vibrational wavepacket is formed, which evolves according to the Hamiltonian $H_{0b}$. The integration over $t'$ signifies that the interaction with the laser field has to be considered at all times $t'$. The final wavepacket is composed of the population of vibrational levels (including amplitudes and phases) which is created at different times of the pulse. This permits interaction of the electric field with the population which has been created by the same pulse at earlier times. Further, the population which has been transfered to the excited state can interfere with parts of the population which has been created by the same pulse. This permits to control the wavepacket using shaped pulses.

The wave function resulting from first-order perturbation theory given in equation 2.87 can be expressed in the basis of the vibrational eigenfunctions of the excited state $\psi_{b,v'}$:

$$\psi^{(1)}(\mathbf{r},t)=\sum_{v'}e^{-\frac{i}{\hbar}E_{b,v'}t}\psi_{b,v'}(\mathbf{r})\ c_{v',v''}\ I_{v',v''}(\omega,t) \tag{2.88}$$

With the time-dependent part

$$I_{v',v''}(\omega,t)=\int_0^\infty \mathbf{F}(t')e^{\frac{i}{\hbar}(E_{b,v'}-E_{a,v''}-\hbar\omega)t'}dt' \tag{2.89}$$

and a factor which is a product of two integrals. The first integral determines the orbital selection rules. The second integral is the vibrational overlap integral, also called the Franck-Condon factor.

$$c_{v',v''}=\int\psi_b(\mathbf{r}')\boldsymbol{\mu}_{ab}\psi_a(\mathbf{r}')dr'\int\psi_{v'}(\mathbf{r})\psi_{v''}(\mathbf{r})dr \tag{2.90}$$

[2]This condition holds for the molecules produced in a supersonic molecular beam, which is discussed in section 6.1

### 2.5.3 Pump-probe spectroscopy

The propagation of the wavepacket in the excited state can be observed with the pump-probe technique. A first pulse at $t''$ excites the molecule and creates a wavepacket in the excited state. This wavepacket propagates under the effect of the corresponding Hamiltonian $H_b$. At $t'$ after a time delay ($\Delta t = t'' - t'$) a second probe pulse follows and transfers the molecule into a detectable state. Depending on the position of the wavepacket the probability to excite and detect the molecule differs due to Franck-Condon factors. The detected signal reveals the molecular dynamic in the first excited state. The pump-probe scheme is illustrated in figure 2.4. This process is described by the solution of the Schrödinger equation in second order perturbation theory:

$$\begin{aligned}\psi^{(2)}(\mathbf{r},t) &= \left(\frac{1}{i\hbar}\right)\int_0^t\int_0^{t'} e^{-\frac{i}{\hbar}H_c(t-t')}(-\mathbf{E}(t')\cdot\boldsymbol{\mu}_{cb}) \\ & e^{-\frac{i}{\hbar}H_b(t-t'')}(-\mathbf{E}(t'')\cdot\boldsymbol{\mu}_{ba})e^{-\frac{i}{\hbar}H_a(t'')}\psi_a(\mathbf{r},0)dt'dt'' \end{aligned} \quad (2.91)$$

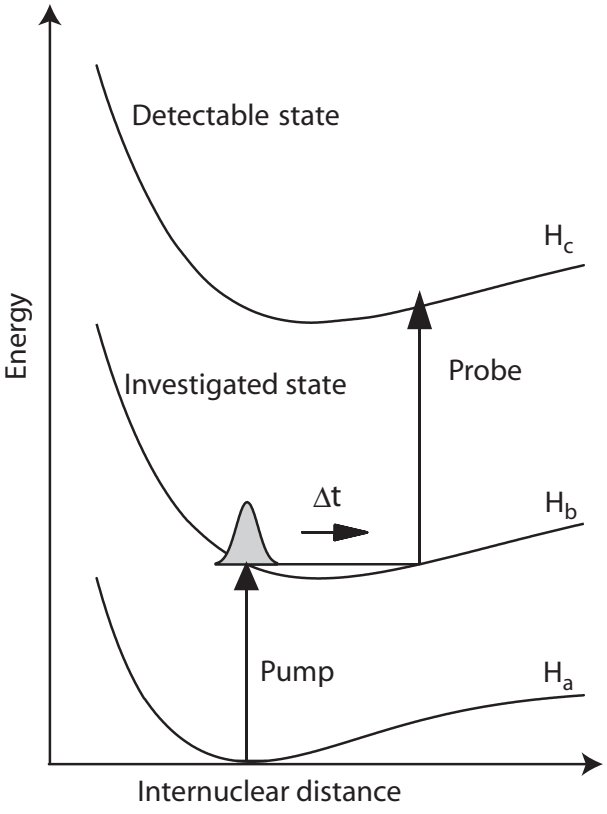


Figure 2.4: Pump-probe scheme: a first laser pulse excites a molecule and transfers population from the ground state a to the excited state b where a wavepacket is created. The wavepacket's evolution is influenced by the Hamiltonian $H_b$, which corresponds to a molecular oscillation. A second pulse – the probe pulse – excites this wavepacket to a detectable state c e.g. an ionic state. Due to the Franck-Condon factors, which depend on the internuclear distance, the dynamics of the wavepacket can be observed in the modulation of the detected signal. This modulations can reveal properties of the state b.

## 2.6 Coherent control

Chemists aim to influence reactions in order to maximize the outcome of reactions and to reduce any unwanted side products. In classical chemistry, the macroscopic parameters temperature, pressure, concentration, and the pH value are used to shift the equilibrium between initial reactants and the final product of the reaction in the desired direction.

This indirect approach is very limited since the microscopic reaction pathway is not under control. The use of light in classical photochemistry helped to overcome reaction barriers and changed the thermo-dynamical equilibrium. But due to the complex potential energy surfaces of molecules the final state of the product is determined by statistics.

The invention of lasers which provide light of a narrow frequency band or even of a single frequency gives access to the microscopic nature of molecules. By tuning the laser to the resonance frequency of a specific bond of a molecule energy is deposited in the vibration of the atoms in this specific bond. If enough photons are absorbed, the specific bond breaks up. The success of mode selective chemistry is limited due to the coupling of the molecular states. The energy which is deposited in one particular bond dissipates into the entire molecule, which is denoted as intra-molecular vibrational energy redistribution (IVR). This process prevents the accumulation of energy in the specific vibrational mode of the molecule and therefore avoids selective dissociation. Basically, the excitation of the molecule causes the heating of the irradiated sample.

The use of ultrafast pulses makes it possible to operate on timescales which are shorter than IVR. This allows for analysis and control of molecular dynamics, which is referred to as femto-chemistry. This new area of research was highly honored with the Nobel Prize for A. Zewail [32].

Due to the complexity of the energy surfaces of a molecule many reaction pathways exist. In order to control the reaction pathway of the quantum mechanical system an optimal trajectory has to be selected. The use of the coherence is the important concept of this approach, which is called coherent control or optimal control. Three concepts – each focusing on different aspects of the control mechanism – have been developed. These are introduced in the following.

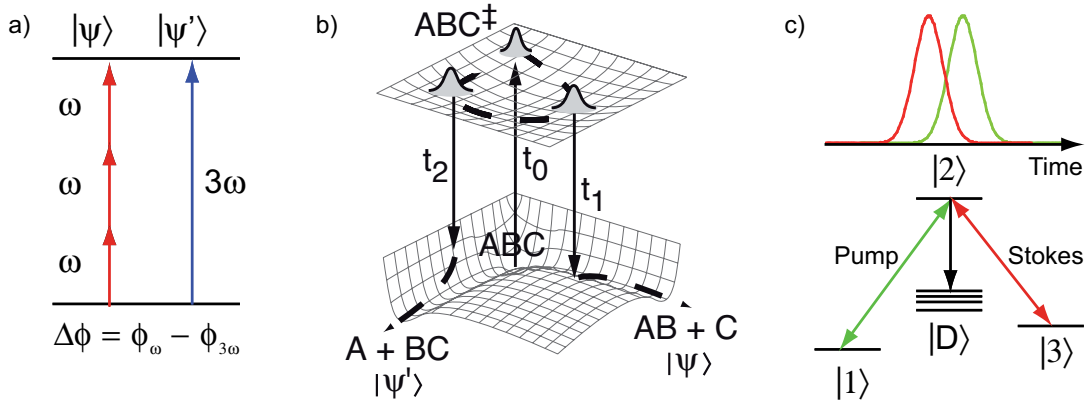


Figure 2.5: Three approaches in coherent control: a) phase control developed by P. Brumer and M. Shapiro. b) time control described by R. Kosloff, D. J. Tannor, and S. A. Rice. c) the STIRAP control of K. Bergmann. Adapted from [33]

### Phase control
### by P. Brumer and M. Shapiro

The scheme, which is depicted in figure 2.5a), operates in the frequency domain and uses interferences between different excitation paths [34]. Two continuous wave lasers with the

respective frequencies $\omega$ and $3\omega$ couple the initial state and the energetically degenerated final states ($|\psi\rangle$ and $|\psi'\rangle$) which are energetically separated by $3\hbar\omega$. By changing the relative phase $\Delta\phi = \phi_\omega - \phi_{3\omega}$ of the two laser fields the interference of the probability amplitudes of the two pathways leads to a modulation of the populations between the final states $|\psi\rangle$ and $|\psi'\rangle$. This scheme was successfully applied to atomic and simple molecular systems [35, 36].

### Time control
### by D. J. Tannor, R. Kosloff, and S. A. Rice

This approach discusses the selectivity of two reaction pathways in the time domain [37]. A triatomic molecule (ABC) which can fragment either into A+BC or into AB+C, illustrated in figure 2.5b), serves as an example. An ultrashort spectrally broad laser pulse creates a vibrational wavepacket in the electronically excited state at $t_0$ . This wavepacket propagates on the potential energy surface which corresponds to the classical oscillation of the atoms within the molecule. At $t_1$ the Franck-Condon overlap with the state $|\psi\rangle$ leading to the reaction channel AB+C is favorable. Classically, this corresponds to the situation where the bond between the atoms B and C is stretched the most. Then, a second ultrashort dump pulse can transfer the wavepacket back to the ground state into the dissociative reaction channel $|\psi\rangle$. Analogously, there is a time $t_2$ at which the position of the wavepacket is most probably excited to the other reaction channel $|\psi'\rangle$. The delay between pump and dump pulse can control the fragmentation of the molecules. This technique was successfully applied to the fragmentation of $XeI_2$ molecules [38].

### STIRAP
### by K. Bergmann

This control scheme is known as stimulated Raman adiabatic passage or, in short, STIRAP [39]. The goal is to transfer population from state $|1\rangle$ to $|3\rangle$ e.g. in a $\Lambda$-type system, which is depicted in figure 2.5c). Two pulsed lasers are used in this scheme. The pump laser couples the initial state $|1\rangle$ with the intermediate state $|2\rangle$. The second laser, called Stokes laser, couples the intermediate state $|2\rangle$ with the final state $|3\rangle$. With the counterintuitive time sequence and the Stokes pulse preceding the pump pulse population can efficiently be transferred from state $|1\rangle$ to $|3\rangle$. In this scheme, the laser pulses need to be intense enough to drive many Rabi-cycles. The analysis of the process shows that during the process no population is present in state $|2\rangle$. This avoids losses to the dissipative channel $|D\rangle$. In the meantime, many different variations of STIRAP have been developed and experimentally applied [40].

These three methods have one thing in common: they use one single parameter for control. But real quantum dynamical systems are often too complex for these simple control schemes. Larger and more complex molecules require many parameters for optimal control. The controllability and the calculation of excitation schemes with the attributed electric field is treated in the optimal control theory (OCT) [41, 42]. Often the results of these calculations lead to pulses with complex electric fields. These complex pulses can be produced by various pulse shaping techniques and tested on the respective system. This

approach, which is often denoted as an open loop, is limited to simple molecules since calculations require a precise knowledge of the potential energy surfaces.

### Closed loop control

The idea of R. S. Judson and H. Rabitz was to close the loop and involve the experimentally measured result directly in the optimization process [43]. A shaped pulse interacts with the quantum system. Then, the yield of the desired state is measured and serves as fitness. Based on this fitness, the optimization algorithm calculates a new pulse shape which is applied to the quantum system and should result in a larger fitness. The shape of the pulses adapts step by step to the quantum system without having any knowledge of the system itself. The procedure is denoted as feedback loop optimization, which is illustrated in figure 2.6. The evolution of the fitness is called learning curve. The analysis of the obtained pulse shapes can help to reveal the reaction pathway and the underlying processes.

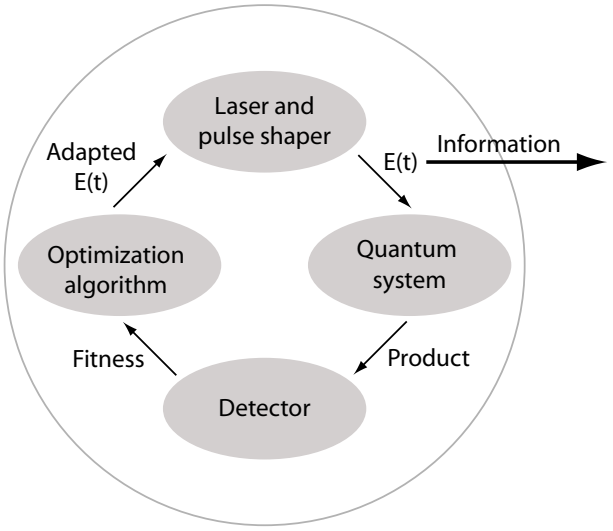


Figure 2.6: Schematic of the adaptive feedback loop optimization described by R. S. Judson and H. Rabitz. The electric field of the shaped laser pulses interacts with the quantum sytem. The resulting products are detected and the signal serves as a fitness. Based on this fitness, the optimization algorithm determines a new adapted electric field, which is produced by the pulse shaper and is again applied to the quantum system. In the course of the generations of the iteration procedure, the pulse shape converges to an optimal pulse form. The analysis of this optimal pulse form reveals information over the investigated system.

The progress made in femtosecond laser technique and the development of pulse shapers in particular, allowed for experimental implementation of the feedback loop. In the first experiment, the fluorescence yield of a dye was optimized [44] and many experiments followed. Nowadays, this technique is widely used in many fields of physics, chemistry, and biology. A few examples should give a representative impression of the versatile applications of this powerful method. In recent years, it was successfully applied to processes in atoms and molecules in the gas phase; e.g. in multi-photon processes [45], isomerization [46], selective bond breaking [47], and isotope separation [48]. The same holds for a large variety of different condensed phase quantum control experiments, among them dye molecules in solution [49], semiconductors [50], and molecular crystals [51]. Even complex biomolecules [52] and biological cells [53] as well as nanostructures [4] and lattice vibrations [54] have been controlled. Further, it was used in the generation of high harmonics [55] and soft x-rays [56].

## 2.7 Optimization algorithm

The algorithm which is used in feedback optimization procedures needs to comply with the following requirements. Firstly, the algorithm should apply a global search strategy to find a maximum in a huge search space. Secondly, it requires a robust convergence under experimental conditions where the fitness is afflicted with noise.

Deterministic algorithms such as the downhill Simplex or the gradient method fail in these conditions [57]. Thus, non-deterministic algorithms, which employ statistical methods, remain. In this group of algorithms, two search strategies have been developed. The first class of strategies searches for a local minimum (or maximum) in the multi-dimensional fitness landscape and the close environment is explored with statistical jumps. These strategies are called simulated annealing and were developed to describe the formation of crystals [58]. The other approach is to start at many points in the multi-dimensional fitness landscape to find many local minima (or maxima) whereby the point with the lowest (highest) fitness is then designated as the global maximum. These approaches utilize optimization strategies used in nature and are called genetic algorithms or evolutionary strategies [59, 60].

In the experiment, the search space can become unimaginably huge. When using spatial light modulators for phase and amplitude shaping, the number of possible solutions is in the order of $10^{2560}$. [3] Genetic algorithms or evolutionary strategies have proven to reach a better fitness and converge faster under these circumstances [61]. The difference between genetic algorithms and evolutionary strategies is the encoding of the optimization parameters. The genetic algorithm uses a binary encoding. In contrast to that, the parameters of the evolutionary strategies are encoded in a floating-point number. Since floating-point numbers are more suitable to encode physical values such as phases, evolutionary strategies were implemented in the algorithm for feedback loop optimization.

### 2.7.1 Evolutionary strategies

The evolutionary strategies are optimization procedures which are adapted from nature. Every individual is characterized by its genome. During evolution, different individuals adapt to the living conditions of the diverse environment. Individuals which are better adapted to the environment have higher probability to survive and reproduce. This process of the natural selection was termed *survival of the fittest* [62]. In reproduction, the genomes which are passed on to the next generation are slightly altered by *crossover* and *mutation*. Therefore, some of the individuals of the next generation are better adapted to the environment than their parents and siblings. Over the generations the genome of the individuals is better and better adapted to the environment. If the environment does not change, the genome can converge to an optimal configuration [59, 63].

This procedure is optimally suited to serve as an algorithm for the feedback-loop optimization presented in section 2.6. The employed evolutionary algorithm is illustrated in figure 2.7. The encoding of the genome and the implementation of the evolutionary steps in the experimentally used algorithm is presented in the following.

[3] In case of a modulator with 2×640 pixels using 100 steps for phase and amplitude modulation.

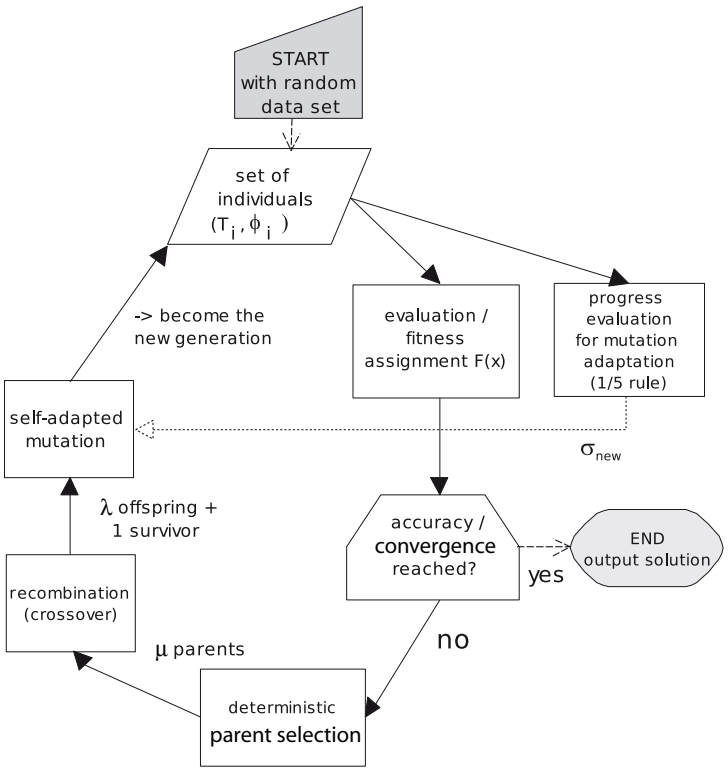


Figure 2.7: Flow chart of the experimentally implemented evolutionary algorithm. It illustrates the steps of each iteration of the feedback-loop optimization. Adapted from [64].

**Encoding of the individuals genome** Each pulse shape corresponds to an individual. The shape of the pulse is determined by the settings of the modulator, which are encoded in a vector $\mathbf{g}$. One example is a free phase optimization in which the phase values of the each pixel are independently optimized. The phases of the $N$ pixels are encoded in a vector $\mathbf{g}_\phi = \{\phi_1, \ldots, \phi_N\}$. In case of a free phase and amplitude optimization, the transmission $T_n$ of each pixel has to be added to the vector $\mathbf{g}_{\phi,T} = \{\phi_1, \ldots, \phi_N\, T_1, \ldots, T_N\}$. The vector can also consist of other parameters which encode the pulse. The value range of the parameters is mapped to the range $[0, 1]$.

**Initialization** The algorithm starts with a population of the size $\lambda = 30$ with a random number $[0, 1]$ for every component of the vector.

**Evaluation** Each individual is tested on its fitness. This could be the experimentally measured value or a cost function $f(\mathbf{g})$ which is assigned to the respective individual.

**Selection** In this step, $\mu$ parents are selected out of the population. In the used implementation, the best 11 individuals are chosen. The best individual is directly taken to be part of the next generation (elitist strategy), which improves the performance under noisy conditions. Since a noisy signal could accidentally kill some of the best individuals.

**Crossover** The selected parents are recombined to produce a $\lambda$-sized offspring. Two parents are selected randomly. Their genomes are arbitrarily shuffled by uniform crossover without changing the index.

**Self adapted mutation** A random number $n(\sigma)$ from a Gaussian distribution of the width $\sigma$ and the expectation value 0 is added to every gene $g_i' = g_i + n(\sigma)$. The mutation step size $\sigma$ is relevant for global convergence and is adapted by the 1/5 rule [65]. If 20% of the population achieves a better performance than the previous generation, the mutation step size $\sigma$ is increased by a factor of 1.25. In the other case, $\sigma$ is reduced by a factor of 0.8. This rule can be understood in the following way: when 1/5 of the generation is better than their ancestors, the algorithm is located in a section of the search landscape where progress is probable. It seems that the right way has been chosen and larger steps can be made.

After that, this generation is passed on to the next iteration step. This iteration is executed until the fitness converges. An indicator for convergence is the mutation parameter $\sigma$ which slowly approaches zero after passing a maximum.

# Chapter 3

# Experimental setup: pulse generation and detection

This chapter gives a short introduction to the generation and amplification of femtosecond laser pulses. In section 3.1.1, the femtosecond laser system which is used in this work is introduced and its specifications are summarized. The setup for manipulation of ultrashort laser pulses utilizing liquid crystal modulators is presented in section 3.2.2. Finally, the techniques for detecting shaped femtosecond laser pulses in the time and frequency domain are revised in section 3.3.

## 3.1 Femtosecond pulse generation

Nowadays, femtosecond lasers are a common tool. The ultrafast laser pulses are mainly generated by using Ti:sapphire crystals. The titanium-doped sapphire serves as the active medium. The crystal absorbs light in the range between 400 and 660 nm, whereby the broad emission spectrum is shifted to the red covering the range from 600 to 1000 nm having its maximum at 780 nm. The pumped crystal is placed in a cavity whose mode spectrum is determined by $L = \frac{n}{2}\lambda_M$ with the cavity length $L$ and $n \in \mathbb{N}$. Each mode is lasing with its wavelength $\lambda_M$ having an arbitrary phase. For pulsed operation, all laser modes have to stand in a fixed phase relation, which can be achieved by active or passive mode coupling. A passive mode coupling technique uses the Kerr-lens effect to introduce an intensity-dependent loss. Pulses which exhibit a higher intensity experience a more efficient amplification than the cw modes of the cavity which are suppressed. To correct for intra-cavity dispersion a prism compressor or chirp mirrors are often embedded. The cavity length of the oscillator defines the repetition rate as following: $f_{rep} = \frac{c}{2L}$. Commercial femtosecond oscillators can provide pulses with pulse durations below 10 fs. The pulse energy lies in the range of a few nJ at repetition rates in the order of 100 MHz.

To obtain larger pulse energies the seed pulses delivered from the oscillator are amplified. Damaging of the optics in the amplifier due to the high peak intensity is prevented by stretching the pulse in time before amplification. This scheme is called chirped pulse amplification (CPA). The stretched pulses gain energy by crossing – again – a pumped

| | **Mira** | **RegA** | **NOPA** |
|---|---|---|---|
| **Tunability** | 760–840 nm | 780–820 nm | 480–620 nm |
| **Spectral width (FWHM)** | 16–60 nm | 20–30 nm | 20–80 nm |
| **Pulse energy** | 10 nJ | 3–8 $\mu$J | $\leq$0.5 nJ |
| **Repetition rate** | 76 MHz | $\leq$300 kHz | same as pump |

Table 3.1: Specifications of the used femtosecond laser system. Taken from [20, 67, 69]

Ti:sapphire crystal. There are different concepts of amplification. In multi-pass amplifiers, the pulse crosses the crystal several times under different angles. In a regenerative amplifier, which is used in this work, the seed pulse is injected and amplified in a cavity. In every round trip the pulse gains energy. When the energy loss equals the gain, the amplified pulse is ejected. After amplification the pulse is compressed to recover an ultrashort pulse. Further information about the generation of laser pulses, their amplification, differences in pulse energy and repetition rates, limitations, and advantages or disadvantages can be found in [27, 66].

### 3.1.1 The femtosecond laser system

The femtosecond laser used in this work is a commercially available system from Coherent. The pulses are generated by a Mira Seed oscillator pumped by a diode-pumped solid state laser Verdi V5. The pulses delivered by the oscillator are not transform limited. For the direct use of the pulses, they are compressed in a prism compressor. For amplification, a regenerative amplifier RegA 9050 continuously pumped with 9-10 W power by a Millennia X (Spectra Physics) was used. Details of the respective system can be found in [67, 68, 69, 70]. The relevant specifications of the laser system are presented in table 3.1.

### 3.1.2 Non-colinear parametric amplification – NOPA

Pulses in the visible range can be obtained by non-colinear parametric amplification [71]. The non-colinear parametric amplifier (NOPA) used in this work is pumped by the pulses delivered from the regenerative amplifier. This NOPA is specifically designed to operate with pulses of a few microjoule [20, 72]. The single stage NOPA employs 90% of the pulse energy for second harmonic generation in a BBO crystal. The remaining pulse energy (10%) generates a white light continuum in a sapphire plate which is placed in the focus of a telescope (f=30 mm). The process of white light generation is highly non-linear and based on self focussing [73, 74] and self phase modulation [75, 76, 77]. The white light serves as a seed pulse in a second BBO crystal which is pumped by the frequency doubled light. Due to the temporal chirp originating from the white light generation the frequency band which is selected for amplification can be tuned by changing the time delay of the frequency doubled pump beam. Optimal parametric amplification is achieved by tilting the angle of the second BBO crystal for correct phase matching conditions.

When pumping with 4.5 $\mu$J at a central wavelength of 800 nm, the efficiency of the light conversion is maximal for wavelength around 510 nm and exceeds 12%. The pulses cover a broad spectral range of 480 to 620 nm. The spectral width amounts to 20–80 nm FWHM

depending on the central wavelength. Due to the process of generation the pulses are chirped with pulse durations around 600 fs, but can easily be compressed below 20 fs by using an external prism compressor.

## 3.2 Pulse shaper

The modulation of pulses in the frequency domain has already been theoretically discussed in 2.4.2. In this section, the experimental implementation is described. In order to spatially separate the individual frequencies of the pulse and to provide access to individual bands of the spectral intensity a zero-dispersion compressor is used [78]. It consist of a pair of gratings and cylindrical lenses or focussing mirrors. An example for the assembly with cylindrical lenses is depicted in figure 3.1. The optical elements are separated by the focal length f of the lenses. Hence, it is often called 4-f-setup or 4-f-line. The first grating disperses the broadband laser pulse. The subsequent lens parallelizes the laser beam and focusses the individual frequency components in a plane. This focal plane where the frequency components are mostly separated is called Fourier plane. The second lens and second grating are positioned in such a way that the 4-f-line is symmetric around the Fourier plane. They combine the frequency components to yield a short pulse again. The spatial resolution in the Fourier plane is connected to the size of the focus, which is determined by the beam diameter of the laser before entering the 4-f-line $w_i$, the wavelength of the light $\lambda_0$, and the focal length $f$:

$$w_0 = \frac{\lambda_0 f}{2\pi w_i}. \tag{3.1}$$

There are different variations in building a 4-f-line: folding the setup in the Fourier plane by inserting a mirror decreases the number of optical components and makes the setup more compact. Instead of gratings, prisms could be used as dispersing components. The lenses could be replaced by focussing mirrors [79].

In this work, the 4-f-line was built using a pair of lenses with a focal length of 200 mm or 250 mm. Gratings with 800, 1200 or 2000 grooves/mm were used. The combinations were chosen to obtain a maximal dispersed spectrum in the Fourier plane for a given spectral width to match the size of the modulator.

### 3.2.1 Spatial light modulator

The separation of the frequency components in the Fourier plane of the 4-f-line allows for their independent manipulation. The first modulations were carried out by placing static phase masks in the Fourier plane [80, 81]. A more versatile approach is to use spatial light modulators (SLM). Different techniques are used for modulation in the Fourier plane:

**AOM** Acoustic-optical modulators (AOM) utilize the density fluctuations of an acoustic wave in a medium. This technique can be either used for spatial light modulation in a Fourier plane or as a dispersive filter [82, 83, 84].

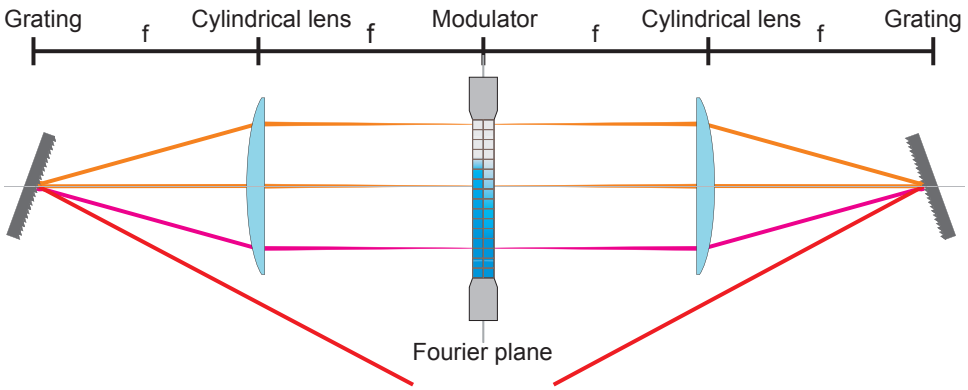


Figure 3.1: Pulse shaper setup. 4-f-line constructed with gratings and with cylindrical lenses separated by the focal length. The modulator is placed in the Fourier plane where the frequency components are spatially separated.

**MEMS** An array of micro mirrors (MEMS) provides the possibility of phase modulation combined with binary amplitude modulation [85, 86]. The advantage of this approach, which is still under development, is that it is not restricted to a certain frequency range.

**LC** Currently, the most sophisticated and widespread technique is based on liquid crystal (LC) modulators, which are optimally suited to modulate the frequencies in the near infrared provided by Ti:sapphire lasers. In this approach, arrays of liquid crystals are utilized. Each array consists of a number of pixels, which are individually addressed. The pixels control the phase and polarization of the transmitted frequency band $\omega_n$. [87].

### 3.2.2 Modulation by liquid crystal arrays

In this work, two different double liquid crystal array modulators, SLM-256 and SLM-640 (Cambridge Research Instruments) are used. The main difference between these two modulators is the size of the active area and the number of pixels. The SLM-256 provides 2×128 pixels and the SLM-640 2×640 pixels for shaping. The pixels measure 98 $\mu$m in width and are separated by 2 $\mu$m. Therefore, the active optical area amounts to 12.8 mm in case of the small shaper (SLM-256) and 64 mm in case of the large shaper (SLM-640). The optical axes of the pixels of each modulator are oriented at ±45°. The Jones matrix of a combination of two liquid crystals oriented at ±45° was derived in equation 2.63. To calculate the resulting electric field $\mathbf{E}_{out}(\omega)$ after passing the 4-f-line with one modulator the Jones formalism, which is introduced in 2.3, is used:

$$\mathbf{E}_{out}^{P+P}(\omega_n) = \mathbf{J}_{dlc}^{\pm 45^\circ}(\varphi_a^{\omega_n}, \varphi_b^{\omega_n}) \cdot E_0(\omega_n) \begin{bmatrix} 1 \\ 0 \end{bmatrix} \tag{3.2}$$

$$= E_0(\omega_n)\, e^{\frac{i}{2}(\varphi_a^{\omega_n} + \varphi_b^{\omega_n})} \begin{bmatrix} cos\left(\frac{\varphi_a^{\omega_n} - \varphi_b^{\omega_n}}{2}\right) \\ i\ sin\left(\frac{\varphi_a^{\omega_n} - \varphi_b^{\omega_n}}{2}\right) \end{bmatrix} \tag{3.3}$$

In this calculation, the input pulse is assumed to be linearly polarized oriented along the x axis with the amplitude $E_0(\omega)$. Each pixel is assigned to a frequency band $\omega_n$.

The resulting electric field $\mathbf{E}_{out}^{P+P}(\omega_n)$ can be separated into three parts. The first part, $E_0(\omega)$, contains the fast oscillating term and provides the initially available bandwidth. The second part describes the spectral phase and is determined by the sum of the phase retardances $\left(\frac{\varphi_a^{\omega_n}+\varphi_b^{\omega_n}}{2}\right)$. The third part, which is controlled by the difference of the phase retardances $\left(\frac{\varphi_a^{\omega_n}-\varphi_b^{\omega_n}}{2}\right)$, distributes the spectral intensity between the x and y component. This corresponds to a modulation of the ellipticity of the pulse which is determined by

$$r = tan\left(\frac{\varphi_a^{\omega_n} - \varphi_b^{\omega_n}}{2}\right). \tag{3.4}$$

The orientation of the electric field ellipse is fixed with the principal axes horizontally and vertically aligned. Phase and polarization can be modulated independently by controlling the sum and difference of $\varphi_a^{\omega_n}$ and $\varphi_b^{\omega_n}$.

Often, double liquid crystal array modulators are equipped with horizontally oriented polarizers. Thus, the electric field is linearly polarized and can be written as a scalar field in x direction, which is modulated in phase and amplitude.

$$\begin{aligned} E_{out}^{P+A}(\omega_n) &= E_0(\omega_n)\, e^{\frac{i}{2}\left(\varphi_a^{\omega_n}+\varphi_b^{\omega_n}\right)} cos\left(\frac{\varphi_a^{\omega_n} - \varphi_b^{\omega_n}}{2}\right) && (3.5)\\ &= E_0(\omega_n)\, e^{\frac{i}{2}\Phi(\omega_n)}\sqrt{T(\omega_n)} && (3.6) \end{aligned}$$

The spectral phase and the transmission of each frequency band can be controlled by $\Phi(\omega_n)$ and $T(\omega_n)$.

$$\begin{aligned} \Phi(\omega_n) &= \left(\frac{\varphi_a^{\omega_n} + \varphi_b^{\omega_n}}{2}\right) && (3.7)\\ T(\omega_n) &= cos^2\left(\frac{\varphi_a^{\omega_n} - \varphi_b^{\omega_n}}{2}\right) && (3.8) \end{aligned}$$

The phase retardances for each frequency component are determined by

$$\varphi_{a,b}^{\omega_n} = \frac{\pi}{2} + \Phi(\omega_n) \pm arccos\left(\sqrt{T(\omega_n)}\right). \tag{3.9}$$

The ambiguity in the *arccos* can be resolved by physical arguments, while the $\frac{\pi}{2}$ is added to obtain only positive retardances. These have to be in the modulation range from $-\pi$ to $+\pi$. When applying phase functions, which exceed this range, this function has to be wrapped to this range. Mathematically, applying a phase shift of $n \times 2\pi$ makes no difference.

### 3.2.3 Serial setup for phase, amplitude, and polarization shaping

In some parts of this work, polarization shaped laser pulses are required. For this purpose, either the setup which is described in section 4.2 can be used or if a restricted polarization control is sufficient the serial setup [20, 88]. The serial setup makes use of a 4-f-line with

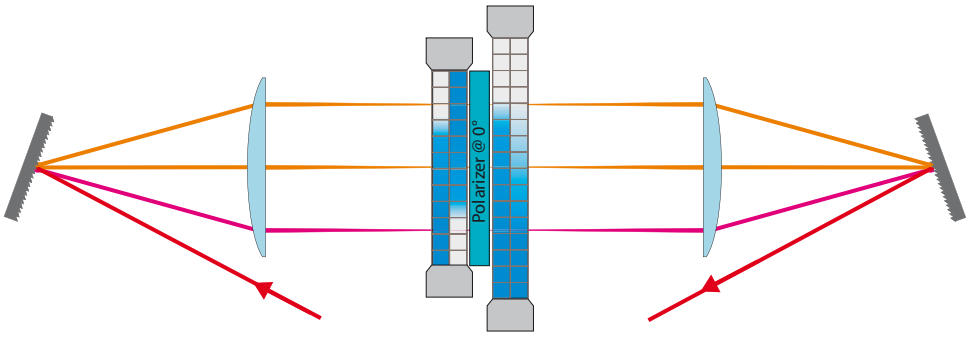


Figure 3.2: Serial setup for restricted phase, amplitude, and polarization shaping in single pass configuration. For the modulation of the pulse, two double liquid crystal modulators which are separated by a polarizer are placed in the Fourier plane of a zero-dispersion compressor. The functionality of this setup is identical to the setup presented in figure 4.1c).

one double liquid crystal modulator, which is crossed twice at different locations of the liquid crystal arrays. A schematic of this setup is depicted in figure 4.1c). In the first pass through the modulator, the amplitude is modulated. Then, in the second pass the phase and polarization is set. The double pass through the 4-f-line was developed because at that time only one liquid crystal modulator was available. In some of the experiments in this work, a pulse shaper is used which is similar to the serial setup. It was modified since two double liquid crystal modulators (SLM-256 and SLM-640) were used. Both modulators are placed in the Fourier plane of the 4-f-line. Therefore, no double pass configuration is required. The first arrays are denoted as array $a$ and $b$. These are followed by a polarizer and the two arrays of the second modulator array $c$ and $d$. The layout of the setup is presented in figure 3.2. The electric field of this setup can be calculated by the product of the Jones matrix of the first modulator, the horizontal polarizer, and the second modulator.

$$\mathbf{E}_{out}^{serial}(\omega_n) = \mathbf{J}_{dlc}^{\pm 45^\circ}\left(\varphi_c^{\omega_n}, \varphi_d^{\omega_n}\right) \cdot \mathbf{J}_{pol}^{0^\circ} \cdot \mathbf{J}_{dlc}^{\pm 45^\circ}\left(\varphi_a^{\omega_n}, \varphi_b^{\omega_n}\right) \cdot E_0(\omega_n) \begin{bmatrix} 1 \\ 0 \end{bmatrix} \tag{3.10}$$

$$= E_0(\omega_n)\, e^{i\frac{\varphi_a^{\omega_n}+\varphi_b^{\omega_n}+\varphi_c^{\omega_n}+\varphi_d^{\omega_n}}{2}} cos\left(\frac{\varphi_a^{\omega_n}-\varphi_b^{\omega_n}}{2}\right) \begin{bmatrix} cos\left(\frac{\varphi_c^{\omega_n}-\varphi_d^{\omega_n}}{2}\right) \\ i\ sin\left(\frac{\varphi_c^{\omega_n}-\varphi_d^{\omega_n}}{2}\right) \end{bmatrix} \tag{3.11}$$

$$= E_0(\omega_n)\sqrt{T(\omega_n)} e^{i\frac{\varphi_c^{\omega_n}+\varphi_d^{\omega_n}}{2}} \begin{bmatrix} cos\left(\frac{\varphi_c^{\omega_n}-\varphi_d^{\omega_n}}{2}\right) \\ i\ sin\left(\frac{\varphi_c^{\omega_n}-\varphi_d^{\omega_n}}{2}\right) \end{bmatrix} \tag{3.12}$$

The intensity of a spectral band $\omega_n$ is determined by the differences of the retardances of the first modulator $\varphi_a^{\omega_n}$ and $\varphi_b^{\omega_n}$. The transmission is calculated by comparing the spectral intensity of the shaped field to the spectral intensity of the incident field:

$$T(\omega_n) = cos^2\left(\frac{\varphi_a^{\omega_n}-\varphi_b^{\omega_n}}{2}\right) = \frac{|E_{out}^x(\omega_n)|^2 + |E_{out}^y(\omega_n)|^2}{|E_0(\omega_n)|^2} \tag{3.13}$$

The retardances are calculated analogously to equation 3.9 by

$$\varphi_{a,b}^{\omega_n} = \frac{\pi}{2} \pm arccos\left(\sqrt{T(\omega_n)}\right) \tag{3.14}$$

The phase and the state of polarization is controlled by the retardances of the second double liquid crystal modulator. The polarization modulation is limited to ellipses with a fixed major and minor axis oriented in horizontal and vertical direction. This is due to the orientation of the optical axes of the liquid crystals. The difference of $\varphi_c^{\omega_n}$ and $\varphi_d^{\omega_n}$ couples the horizontal and vertical component of the electric field. The retardances of the second modulator $\varphi_c^{\omega_n}$ and $\varphi_d^{\omega_n}$ are calculated by inversion of equation 3.12:

$$\varphi_{c,d}^{\omega_n} = \Re\left(-i\ ln\left(\frac{E_{out}^x(\omega_n) \pm E_{out}^y(\omega_n)}{E_0(\omega_n)\sqrt{T(\omega_n)}}\right)\right) \tag{3.15}$$

The real part has to be taken because the liquid crystals can induce only a real retardance. The consequence of this restriction is the appearance of sub-pulses. The calculation of the retardances as well as the limitations of the setup and their consequences are discussed in detail in [64].

#### Calibration

The modulators consist of two liquid crystal arrays with the optical axes at different orientations. Both liquid crystal arrays induce a retardance of $n \times \pi + \varphi$. Since the arrays are glued together, they cannot be investigated separately. The light crosses both arrays before it can be analyzed. Therefore, the retardance of both arrays cannot be determined absolutely. The relative retardance is the only parameter which is determined in the calibration. Each pixel of the modulator is controlled by 2048 voltage steps. The voltage is assigned to a phase retardance by calibration. This procedure employs equation 3.9 and is described in detail in [29].

### 3.2.4 Deviations from optimally shaped pulses

#### Space-time coupling

Fourier optical analysis of the waveform after the modulation in the 4-f-line reveals deviations from an ideal pulse shaper. The pulse shaper does not only modify the temporal and spectral properties of the laser pulse but also changes its transversal spatial distribution. This phenomenon is known as space-time coupling and is in detail analyzed in [89]. The modulation with a spectral phase shifts the spatial position of the emerging beam. In case of a double pulse sequence, the emerging beam consists of two spots which are spatially separated in horizontal direction. More complex pulse shapes like a spectral sinusoid phase result in a spectral fringes across the spot. In the experiment, a spatial average of the pulse shape drives the excitation process. The deviation from the optimal pulse shape is very often negligible, which was demonstrated for different example systems [90]. The deviations in the focus can be reduced by controlling the divergence of the laser with a telescope [84].

#### Issues of pixelation

The use of an array of individual liquid crystal cells for pulse shaping is associated with several artefacts which could occur. The pixels of the modulators are separated by 2 $\mu m$. In this part of the modulator, the light passes unshaped. A pulse with a striped amplitude pattern results in a pulse train. This interferes with the shaped pulse. Due to this fact, it is not possible to fully remove spectral components by amplitude shaping in the standard configuration. This could be overcome by placing the modulator between two crossed polarizers.

The liquid crystals in the inter-pixel gaps are interacting with the electric fields of the adjacent pixels. This prevents an abrupt phase change between these pixels, which occurs for example when wrapping the phase function. This smoothes the wrapped phase function leading to errors in the effectively applied phase, which is discussed in detail in [91].

The Fourier transformation of a discrete pixel mask reveals that replica pulses separated by $\Delta t = \frac{2\pi}{\Delta\omega}$ appear before and after the main pulse [29, 92]. Further, the width of the frequency band transmitted through one pixel defines the shaping window which limits the length of the modulated pulses. It is determined by a sinc-function and spans between the two nearest replica pulses. For the experimentally used calibration coefficient of 0.3415 nm/pixel,[1] it results in a free time window of 5.9 ps for pulse shaping.

The complexity or slope of the function written on the modulator is limited by the Nyquist theorem [29, 93]. Sampling of a curve requires at least two sampling points per period. This means that the difference of the retardances of two adjacent pixels has to be smaller than $\pi$: $\varphi_n - \varphi_{n-1} \leq \pi$.

## 3.3 Pulse detection

The shaped pulses as well as the pulses delivered from the femtosecond laser system have to be characterized. Methods for pulse characterization which are used in this work are presented in this section.

#### Spectrometer

In the frequency domain, the spectral intensity ($I(\omega) \propto |E(\omega)|^2$) is the parameter of interest. The spectra were typically recorded by two standard fiber spectrometers (Ocean Optics). One of the spectrometers is sensitive in the infrared ranging from 696 to 964 nm. It has a resolution of 0.5 nm FWHM. The other spectrometer covers the spectral range from 302 to 1683 nm and works with a resolution of 2.7 nm FWHM. For better resolution, a grating monochromator HRS2 (Jobin YVON) was used in combination with a photodiode. This bulky device provides a much higher resolution, but has the drawback of a long acquisition time ($\approx$ hours).

[1] This value corresponds to the configuration of the 4-f-line which uses the gratings with 1200 grooves/mm and lenses with f=200 mm

The intensity evolution of the pulse in the time domain is not directly accessible, since opto-electronic devices are too slow for sampling a signal in the femtosecond regime. Indirect methods for characterization are applied which measure the pulse by correlation with another pulse.

### Auto-correlation

The auto-correlator is the simplest device for measuring the pulse duration of short pulses. It creates two copies of the incoming pulse which are superimposed in a non-linear medium (non-linear crystal, two-photon diode, etc.). By changing the time delay between these pulses the response signal of a non-linear medium is recorded. The second order intensity auto-correlation can be expressed as

$$I_{AC}(\tau) = \int_{-\infty}^{+\infty} |E(t) \cdot E(t-\tau)|^2 dt \tag{3.16}$$

The autocorrelation signal is by definition symmetric in $\tau$. Therefore, the temporal shape of the measured pulse is ambiguous. However, if the shape of the pulse is known (e.g. a gaussian or hyperbolic secant squared) the pulse length can be determined [27]. To measure the pulse length of unshaped pulses the autocorrelator Mini from APE was used. This autocorrelator is able to measure pulse lengths ranging from 50 fs to 3.5 ps.

### Cross-correlation

Due to their larger complexity shaped pulses require a slightly different detection scheme. In the cross-correlation measurement the shaped pulse is correlated with a short pulse. This pulse which is called reference pulse is split off before being shaped by a beamsplitter. The shaped pulse and the reference pulse are non-collinearly overlapped in a non-linear $\beta$-barium borate crystal (BBO). The reference pulse is time delayed by a mechanical delay stage (PI-Instruments). The sum-frequency, which is generated in the non-linear crystal, is measured with a photomultiplier tube. A schematic of the used homebuilt sum-frequency cross-correlation (SF-XC) is depicted in figure 3.3. The SF-XC signal is calculated by

$$I_{SF-XC}(\tau) = \int_{-\infty}^{+\infty} |E_{shaped}(t) \cdot E_{ref}(t-\tau)|^2 dt. \tag{3.17}$$

The $I_{SF-XC}$ represents the intensity trace of the shaped pulse convoluted by the short reference pulse. This intensity trace provides information about the time evolution of the shaped pulse, but its features are broadened due to the convolution. The intensity evolution of the shaped pulse could be obtained by deconvolution. But this would require precise knowledge of the shape (amplitude $|E(t)|$ and phase $\phi$(t)) of the reference pulse, which was not accessible at the time of the experiments. Further, the deconvolution process would additionally introduce errors.

Therefore, the pulses depicted in this work are presented as cross-correlation traces. This fact should be kept in mind when estimating sub-pulse durations. The sub-pulse distance is not affected by the convolution.

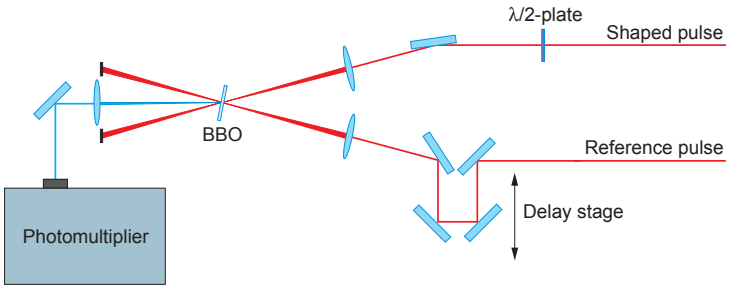


Figure 3.3: Layout of the sum-frequency cross-correlation setup. The shaped pulse and the reference pulse are non-collinearly overlapped in a BBO-crystal. The generated sum-frequency is detected by a photo multiplier tube (Hamamatsu R212). To resolve the polarization state of the shaped pulse several projections of the intensity are selected by the half waveplate.

### 3.3.1 Retrieval of polarization shaped pulses

This setup can be extended to measure polarization shaped pulses. To retrieve the polarization state of a pulse the intensity along different orientations needs to be measured (cf. equation 2.42). In order to measure the intensity cross-correlation of the pulse in a dedicated orientation, a half waveplate is inserted in the path of the shaped pulse. The half waveplate rotates the state of polarization of the whole pulse and the BBO, which is highly polarization-sensitive, selects the intensity components along the desired direction. By this time-dependent ellipsometry scheme the state of polarization can be determined for each time-step.

The retrieval process is illustrated in figure 3.4. In this work, 10 cross-correlation traces covering the orientations within 180° were measured for the characterization of the polarization-shaped pulse. For each time step, this data is fitted to the function given in equation 2.42 to determine the parameters of the instantaneous polarization ellipse. The angle of the half waveplate is related to the orientation by $\theta_{HWP} = -2\theta_{Pol}$. Repeating this procedure for every time step retrieves the time-dependent intensity as well as the time-dependent polarization state, which is characterized by the ellipticity and orientation.

In the course of this work, the time evolution of polarization shaped pulses is presented in a graph in which the intensity over time is presented along with the corresponding polarization state. The intensity curve is plotted in a solid red line. The polarization parameters ellipticity and orientation are plotted by a dashed green line and a dotted blue line. All three curves are depicted in the same graph. The polarization is undefined at times of no intensity. Therefore the polarization state is determined by the noise of the measurement outside the pulses. Again, these curves are not deconvoluted. This fact has to be considered when pulse durations are determined. Further, a three-dimensional representation is calculated from this data, which provides an intuitively understandable picture of the pulse.

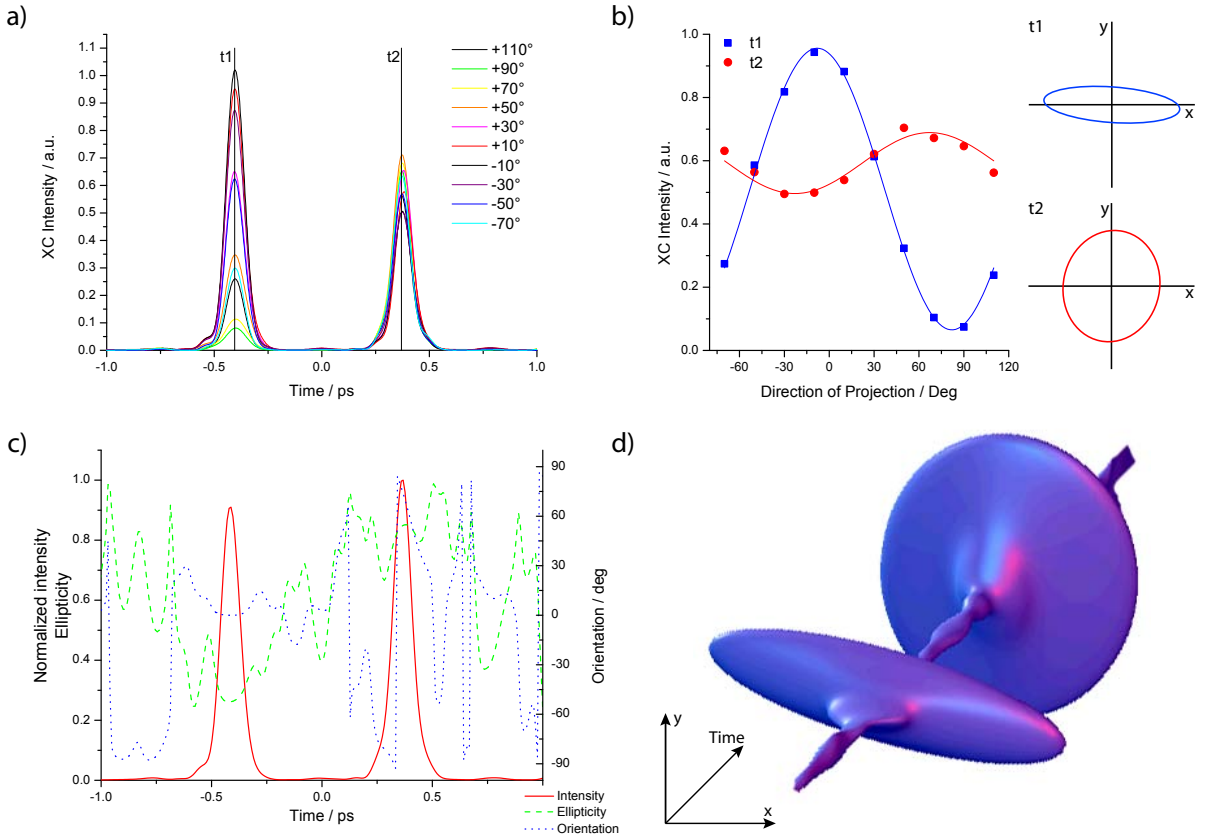


Figure 3.4: Retrieval process for polarization-shaped pulses. First, a set of 10 cross-correlation traces is measured in different orientations, which are depicted in a). Then, for each time step an ellipse is fitted to determine the state of polarization. In part b), this is exemplarily shown for two points in time: t1 and t2. The polarization state and the intensity of all time steps are stringed together and produce a graph which presents the time-dependent pulse parameters intensity $I$, orientation $\gamma$, and ellipticity $r$. The resulting curves are shown in c). For an easy accessible illustration, the fitted ellipses are assembled to a three-dimensional representation of the pulse, which is depicted in d).

# Chapter 4

# Unrestricted polarization pulse shaping

In the field of coherent control, mainly the scalar parameters amplitude and phase were used for shaping laser pulses in order to control the outcome of reactions. Until a few years ago, the vectorial character of the electric field was neglected. Since the transition dipole moment consists of the vector product $\boldsymbol{\mu} \cdot \mathbf{E}$ the vectorial character of the light and therefore the polarization is relevant and important in the excitation process of quantum systems. First experiments have demonstrated that the controllability of excitation processes can benefit from the implementation of the polarization [2, 45]. Moreover, the analysis of polarization shaped pulses obtained by feedback loop optimizations provides more information over the molecular dynamics. This observation propelled the new field of ultra fast polarization shaping.

After a review of the progress in polarization shaping in section 4.1 a new setup is introduced in section 4.2. This non-interferometric setup is capable of simultaneous phase, amplitude, and polarization shaping. It allows for the independent and unrestricted control of the electric field. The mathematical fundament is developed and the functionality of the device is tested in section 4.4. In section 4.6.2, a parametric encoding is developed which allows for producing pulse sequences consisting of independently shaped sub-pulses. Experimentally generated and measured double-pulse sequences are shown in section 4.8 and demonstrate the capabilities of independent control of the sub-pulse parameters. More complex pulse sequences are presented in section 4.9. The implementation of the setup in a closed feedback loop optimization of second harmonic generation is demonstrated in section 4.11 and shows the advantages of the parametric sub-pulse encoding. Section 4.12 concludes and gives an outlook.

## 4.1 History of polarization pulse shaping

The first publication regarding to polarization shaping of laser pulses was written by M. M. Wefers and K. A. Nelson in 1995 [94]. They introduced a newly developed double liquid crystal modulator in which the optical axes of the two arrays were oriented at $\pm 45°$. This device was designed for phase and amplitude shaping and is still used in this

configuration today. In their publication, they also highlight the capability of generating ultrafast polarization profiles. Equations 3.3 and 3.5 describe the electric field shaped by this type of modulator in phase and polarization mode or phase and amplitude mode respectively. In their setup, they used a 4-f-line with gratings of 1800 grooves/mm with very strong polarization-dependent reflection efficiency. The efficiency of the reflection in vertical direction was about 120 times smaller than in horizontal direction. This issue made the generation and application of the polarization modulated pulses impossible.

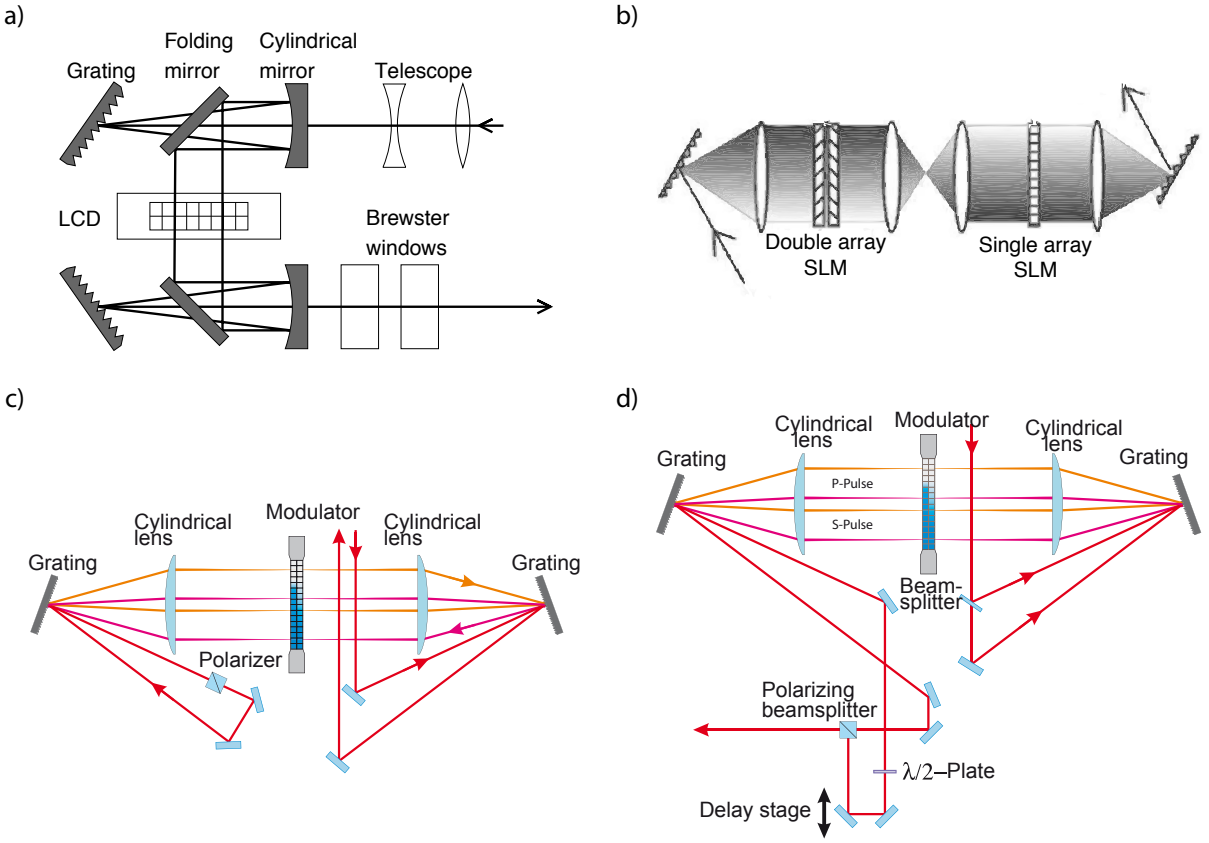


Figure 4.1: Significant concepts and setups in the development of femtosecond polarization pulse shaping. a) the setup developed by T. Brixner *et al.*. b) the setup introduced by L. Polachek *et al.*. The setups from our group: c) the serial setup and d) the parallel setup. Taken from [88, 95, 96, 97].

A few years later, T. Brixner *et al.* introduced a similar setup where he used the standard double liquid crystal array modulator in combination with gratings which attenuated the y component of the laser intensity only three times stronger than the x component. This difference in reflectivity was compensated by inserting a stack of Brewster plates in the beam path after the last grating. The Brewster plates attenuated the horizontal component of the pulses more than the vertical component, which enabled to compensate for the polarization-dependent grating reflectivity with the drawback of reducing the overall transmission of the pulse shaper. Nevertheless, this setup which is depicted in figure 4.1a), was able to generate and control polarization shaped pulses [95]. Further, it was successfully applied in feedback loop experiments on $K_2$ [2] and $I_2$ [45]. These first experiments revealed the importance of a polarization change within the optimal pulse in the process of multi-photon ionization. Many experiments on different systems followed

[3, 4, 5, 98]. New developments in the design of holographic volume gratings made the balancing of the grating reflectivity obsolete [98, 99]. The polarization modulation of this type of setup is restricted due to the fixed orientation of the optical axes in the double liquid crystal arrays. The analysis of the resulting electric field (equation 3.3) reveals that the principal axes of the spectral polarization ellipse are fixed in horizontal and vertical direction. Thus, the polarization modulation of this setup is restricted to a variation of the ellipticity.

This restriction was overcome by L. Polachek *et al.* [96] using a double liquid crystal modulator followed by a single liquid crystal modulator in an 8-f configuration, which is depicted in figure 4.1b). By the use of a third array with the optical axes oriented at 0° in the second Fourier plane the controllability of the spectral polarization was extended. This combination allows for independent control of the ellipticity and the orientation and therefore every desired polarization state can be reached.

In the field of optical fiber communication, pulse shapers have been applied to compensate the distortion of the state of polarization. A sequence of liquid crystal arrays with their optical axes oriented at 90°/−45° or 0°/+45°/0°/90° allowed for the correction of the polarization mode distortion, which is the limiting factor in high speed optical communication [100, 101, 102].

All these setups have one thing in common: the lack of amplitude control. Our group introduced the first setup – the serial setup – which is capable of independent and simultaneous phase, amplitude, and polarization shaping [88]. This original setup, shown in figure 4.1c), utilizes a standard double liquid crystal array modulator in a 4-f-line which is passed twice. The number of grooves of the grating and the incident angle at which the pulse enters the 4-f-line were chosen to illuminate only one half of the modulator with the dispersed incident pulse. After recombination at the second grating the pulse crosses a polarizer. In this first pass, the pulse is shaped in amplitude. For the second pass, the pulse is reflected back in to the 4-f-line under a different incident angle. Therefore, the pulse crosses the modulator on the other half where it is shaped in phase and polarization. The double pass configuration divides the resolution in half and results in a reduced overall transmission. It was chosen because of the availability of one shaper only. A similar setup is described in section 3.2.3 and used for some experiments in this work.

Due to the orientation of the optical axes at ±45° in the double pass setup the polarization control is also limited to ellipses with fixed principal axes (cf. section 3.2.3). This setup was successfully applied to the multi-photon ionization of NaK [103]. The provided amplitude modulation is essential for the generation of parametric pulse sequences [104]. The application of these parametric pulses to the molecular model system NaK revealed the important features of the ionization process. Further, the amplitude modulation allowed for a pre-calculated compensation of the difference in the grating reflectivity which induces a polarization shift. The concept of shaping the pulse in different parts of a modulator in order to provide more controllability was also used in combination with a 2D modulator [105].

For unrestricted control of the electric field, we employed a different approach to pulse shaping. Up to this point, the pulses were modulated by subsequently passing through liquid crystal arrays with diverse orientations. The new concept for generating phase, amplitude, and polarization shaped pulses is very intuitive. The arbitrary shaped electric

field is described by a vector (cf. equation 2.6), which can be separated in a x and y component. Each component can be described as an electric field which is shaped in phase and amplitude. This approach is transferred to the parallel setup [97] which utilized a modulator in each arm of a Mach-Zehnder interferometer for pulse shaping. The setup is displayed in figure 4.1d) and operates as follows: the incident pulse is split into two parts by a beam splitter. The two sub-pulses enter a 4-f-line under different incident angles. Therefore, they are modulated at different locations of the double liquid crystal array modulator. After the 4-f-line the two pulses are still spatially separated and the polarization state of one of the pulses is rotated by 90° using a half waveplate. Then, the two pulses are overlapped in a polarizing beam splitter. In this polarizing beam splitter the desired spectral components are directed in one direction which provides amplitude modulation whereas the others leave the other channel and are disregarded. When the pulses are perfectly overlapped in time and space, the polarization and time evolution of the pulse can be arbitrarily controlled by the phases and amplitudes of the horizontal and vertical components. Parametrically shaped pulse sequences illustrated the capabilities of this setup [106]. The details of the experimental layout, the alignement procedure to find the perfect overlap in space and time and an analysis of the stability can be found in [20, 107].

The stability of this interferometric setup was improved by M. Sato *et al.* with an active stabilization [108]. The idea of this pulse shaping approach was adopted by M. Ninck *et al.* [109] and O. Masihzadeh *et al.* [110]. They conceptualized a common optic design by using a Wollaston prism in order to passively improve the stability.

The spectral range of these setups is limited from 400 to 1800 nm in which the liquid crystals are transparent. This range was extended to the mid-infrared by C.T. Middleton *et al.* [111]. They used an acousto-optical modulator in a setup which is similar to the parallel setup. The extension to the shorter wavelength of the ultra-violet was developed by P. Nürnberger *et al.* [112]. In their scheme, they produce phase- and polarization-shaped pulses with the pulse shaper depicted in figure 4.1a). This polarization-shaped light passes two BBO crystals with perpendicularly oriented optical axes. Due to the polarization dependence of the second harmonic generation the two components of the pulse are frequency-doubled in either one of the two crystals. The components of the frequency doubled light are perfectly overlapped since they originate from one shaped pulse.

These developments of polarization shaping setups can be divided in two groups. In one approach, the polarization shaped pulse is interferometrically constructed out of two orthogonal components which are shaped in phase and amplitude. This approach can generate unrestricted pulse shapes but involves complicated alignment procedures and interferometrically stable setups, which are often bulky. In the other approach, the frequency components are modulated sequentially by a series of liquid crystal arrays. Therefore, the stability of the setup is no matter of concern. However, all setups of this approach, which have been introduced until now, are restricted in the modulation. The intention when designing a new polarization pulse shaper must be the complete control without the drawback of instability and complicated optical setups.

## 4.2 Full control over the electric field using four liquid crystal arrays

A setup which is able to generate arbitrarily shaped pulses is described in this chapter. The generation of arbitrary pulse shapes requires complete and independent control of the phase, the amplitude, and the polarization of the electric field. For this purpose, four independent parameters for the manipulation of the electric field are necessary. The phase and amplitude modulation requires one parameter each. The control of the polarization state demands a parameter for the ellipticity and another one for the orientation of the polarization ellipse. The helicity can be regarded as the sign of the ellipticity.

A modulator with a sequence of four liquid crystal arrays with an appropriate orientation of the optical axes and with a polarizer in between fulfills the requirements. One possible sequence of arrays with the orientation of the optical axis would be $+45°/-45°/\mathrm{POL}/+45°/0°$.

The Jones matrix of this sequence is calculated by multiplication of the Jones matrices of the respective optical components (cf. section 2.3):

$$\mathbf{J}^{mod4} = \mathbf{J}_{lc}^{0°}\left(\varphi_e^{\omega_n}\right)\mathbf{J}_{lc}^{+45°}\left(\varphi_c^{\omega_n}\right)\ \mathbf{J}_{pol}^{0°}\ \mathbf{J}_{lc}^{-45°}\left(\varphi_b^{\omega_n}\right)\mathbf{J}_{lc}^{+45°}\left(\varphi_a^{\omega_n}\right). \tag{4.1}$$

The Jones matrix for this modulator $\mathbf{J}^{mod4}$ and a Jones matrix $\mathbf{J}^{G}$ which takes the difference in the grating reflectivity into account determine the resulting modulated electric field. Assuming a linearly horizontally polarized incoming laser pulse which is described by $\tilde{\mathbf{E}}_{in}(\omega)$ the modulated electric field is calculated by

$$\begin{aligned}\tilde{\mathbf{E}}_{out}^{mod4}\left(\omega_n\right) &= \mathbf{J}^{G}\ \mathbf{J}^{mod4}\ \tilde{\mathbf{E}}_{in}(\omega) &(4.2)\\ &= \tilde{E}_{in}\left(\omega_n\right)e^{\frac{i}{2}\left(\varphi_a^{\omega_n}+\varphi_b^{\omega_n}+\varphi_c^{\omega_n}\right)}\\ &\quad\times cos\left(\frac{\varphi_a^{\omega_n}-\varphi_b^{\omega_n}}{2}\right)\begin{bmatrix} cos\left(\frac{\varphi_c^{\omega_n}}{2}\right)\\ i\ e^{i\varphi_e^{\omega_n}}sin\left(\frac{\varphi_c^{\omega_n}}{2}\right)\sqrt{g}\end{bmatrix}. &(4.3)\end{aligned}$$

The equation shows that the resulting electric field $\tilde{\mathbf{E}}_{out}^{mod4}\left(\omega_n\right)$ can be arbitrarily modulated by the combination of the individual retardances $\varphi_a^{\omega_n}$, $\varphi_b^{\omega_n}$, $\varphi_c^{\omega_n}$, and $\varphi_e^{\omega_n}$.

A detailed analysis of this equation reveals the responsibility of each factor. $\tilde{E}_{in}\left(\omega_n\right)$ contains the fast oscillating term and describes the bandwidth of the pulse. The exponential term includes the phase on the shaped pulse. The cosine controls the amplitude and the vector expresses the polarization state of the respective frequency band $\omega_n$.

## 4.3 Experimental realization using three double liquid crystal array modulators

The modulator described by equation 4.1 in the previous section is not commercially available. Therefore, an alternative solution which uses only standard optical components was

considered. The use of three double liquid crystal modulators allowed for finding a combination which exibits the same potential for control. The optical axes of these modulators are fixed at an orientation of ±45°. In a setup which is capable of full polarization control at least one axis has to be in a different orientation, desirably at 0° or 90°. This can be achieved by placing one modulator between two half waveplates.

$$\mathbf{J}_{lc}^{90^\circ}\ \mathbf{J}_{lc}^{0^\circ} = \mathbf{J}_{HWP}^{22.5^\circ}\ \mathbf{J}_{lc}^{-45^\circ}\ \mathbf{J}_{lc}^{+45^\circ}\ \mathbf{J}_{HWP}^{22.5^\circ} \tag{4.4}$$

The Jones matrix of the modulator with the optical axes at 0° and 90° is identical to the Jones matrix of the standard ±45° modulator situated between two half waveplates with their optical axes oriented at 22.5°.

For the full control of the electric field the second half waveplate is not necessary. However, it is implemented to illustrate the equality of the ideal setup which utilizes four arrays and the setup which uses six arrays. Furthermore, it simplifies the mathematical description of the six array setup. The ideal sequence of four arrays can be mimicked by the following sequence of three double liquid crystal modulators a polarizer and two waveplates.

$$\begin{aligned}\mathbf{J}^{mod6} \;=\;& \mathbf{J}_{HWP}^{22.5^\circ}\ \mathbf{J}_{lc}^{-45^\circ}\left(\varphi_f^{\omega_n}\right)\ \mathbf{J}_{lc}^{+45^\circ}\left(\varphi_e^{\omega_n}\right)\ \mathbf{J}_{HWP}^{22.5^\circ} \\ & \mathbf{J}_{lc}^{-45^\circ}\left(\varphi_d^{\omega_n}\right)\ \mathbf{J}_{lc}^{+45^\circ}\left(\varphi_c^{\omega_n}\right) \\ & \mathbf{J}_{pol}^{0^\circ}\ \mathbf{J}_{lc}^{-45^\circ}\left(\varphi_b^{\omega_n}\right)\ \mathbf{J}_{lc}^{+45^\circ}\left(\varphi_a^{\omega_n}\right). \end{aligned} \tag{4.5}$$

The resulting electric field is found by Jones matrix multiplication:

$$\begin{aligned}\tilde{\mathbf{E}}_{out}^{mod6}\left(\omega_n\right) &= \mathbf{J}^G\ \mathbf{J}^{mod6}\ \tilde{\mathbf{E}}_{in}(\omega) && (4.6)\\ &= \tilde{E}_{in}\left(\omega_n\right) e^{\frac{i}{2}\left(\varphi_a^{\omega_n}+\varphi_b^{\omega_n}+\varphi_c^{\omega_n}+\varphi_d^{\omega_n}\right)} \\ &\quad \times cos\left(\frac{\varphi_a^{\omega_n}-\varphi_b^{\omega_n}}{2}\right)\begin{pmatrix} e^{i\varphi_f^{\omega_n}} cos\left(\frac{\varphi_c^{\omega_n}-\varphi_d^{\omega_n}}{2}\right) \\ i\, e^{i\varphi_e^{\omega_n}} sin\left(\frac{\varphi_c^{\omega_n}-\varphi_d^{\omega_n}}{2}\right)\sqrt{g}\end{pmatrix} && (4.7)\end{aligned}$$

The equations for the modulator consisting of four arrays (4.3) and the one which utilizes six arrays (4.7) are equal when setting $\varphi_d^{\omega_n}$ and $\varphi_f^{\omega_n}$ to zero. Due to the physical dimensions, the liquid crystals have an intrinsic offset retardance. This is not identifiable since the arrays are fixed to each other and only relative changes of the retardance matter. Therefore, it is not possible to experimentally set each the retardance of each individual array to zero or to a multiple of $2\pi$. Further, the modulation function of this setup is overdetermined. It uses six arrays to control the four parameters phase, amplitude, ellipticity, and orientation. In order to reduce the number of parameters and ensure uniqueness, the following transformation is implemented.

$$\begin{aligned}\varphi_a^{\omega_n}-\varphi_b^{\omega_n}=\varphi_{Dab}^{\omega_n}\ ; \quad \varphi_a^{\omega_n}+\varphi_b^{\omega_n} &= \varphi_{Sab}^{\omega_n} \\ \varphi_c^{\omega_n}-\varphi_d^{\omega_n}=\varphi_{Dcd}^{\omega_n}\ ; \quad \varphi_c^{\omega_n}+\varphi_d^{\omega_n} &= \varphi_{Scd}^{\omega_n}=0 \\ \varphi_e^{\omega_n}-\varphi_f^{\omega_n}=\varphi_{Def}^{\omega_n}\ ; \quad \varphi_e^{\omega_n}+\varphi_f^{\omega_n} &= \varphi_{Sef}^{\omega_n}=0\end{aligned} \tag{4.8}$$

Using this substitution, the formula for the six array equation 4.7 setup simplifies to

$$\tilde{\mathbf{E}}_{out}^{modSD}(\omega_n) = \tilde{E}_{in}(\omega_n)\, e^{\frac{i}{2}\varphi_{Sab}^{\omega_n}} cos\left(\frac{\varphi_{Dab}^{\omega_n}}{2}\right) \begin{pmatrix} e^{\frac{i}{2}\varphi_{Def}^{\omega_n}} cos\left(\frac{\varphi_{Dcd}^{\omega_n}}{2}\right) \\ i\, e^{-\frac{i}{2}\varphi_{Def}^{\omega_n}} sin\left(\frac{\varphi_{Dcd}^{\omega_n}}{2}\right)\sqrt{g} \end{pmatrix}. \tag{4.9}$$

## 4.4 Experimental implementation

The last section has demonstrated the possibility to achieve the full control utilizing three standard double liquid crystal modulators, a polarizer, and two half waveplates. This sequence of optical elements is incorporated in a standard 4-f-line as shown in figure 4.2. For organizational reasons two different 4-f-lines were used. In section 4.5, gratings with 600 grooves/mm and cylindrical lenses with a focal length of 250 mm are used. This leads to a calibration coefficient of 0.570 nm/pixel. In the other experiments, a slightly different configuration used gratings of 1200 grooves/mm and cylindrical lenses of 200 mm focal length leading to a calibration coefficient of 0.3415 nm/pixel. The double liquid crystal modulators (2× SLM-640 and SLM-256) have the same pixel width of 98 $\mu$m separated by gaps of 2 $\mu$m. The small modulator with 128 pixels limits the resolution of the setup. Each modulator is mounted on a high precision stage for transverse alignment and pixel assignment. After the first modulator a horizontal polarizer is placed followed by the second modulator. Then, the third modulator follows which is placed between two half waveplates with the optical axis oriented at +22.5°. Due to the broad spectral width of the pulses achromatic zero order waveplates are used. The overall transmission of this setup including all optical elements amounts to 27%.

## 4.5 Demonstration of functionality

### 4.5.1 Extended Fourier plane

The first concern that arises when these optics are put into a 4-f line is the possible decrease in resolution because of the displacement of the first and the last liquid crystal arrays from the Fourier plane. To keep this displacement small, the polarizer and the first waveplate are very thin and fixed in a particularly flat mount. Further, the modulators are positioned in such a way that the first and the last one have their liquid crystal array located on the side of the box facing the inner modulator. The whole sequence of the three double liquid crystal arrays, the polarizer, and the first waveplate is about 51 mm thick.

To investigate the effect of a displacement of the liquid crystal arrays from the Fourier plane several spectra were measured with a high-resolution monochromator. As a test function an amplitude pattern of alternating attenuating and transmitting pixels is applied to a single double liquid crystal array with a polarizer. This modulator was displaced along the beam out of the Fourier plane by up to 50 mm. The corresponding spectra are presented in figure 4.3. Even with a displacement of 50 mm, which is twice the displacement of the optical elements from the Fourier plane, the spectrum does not show

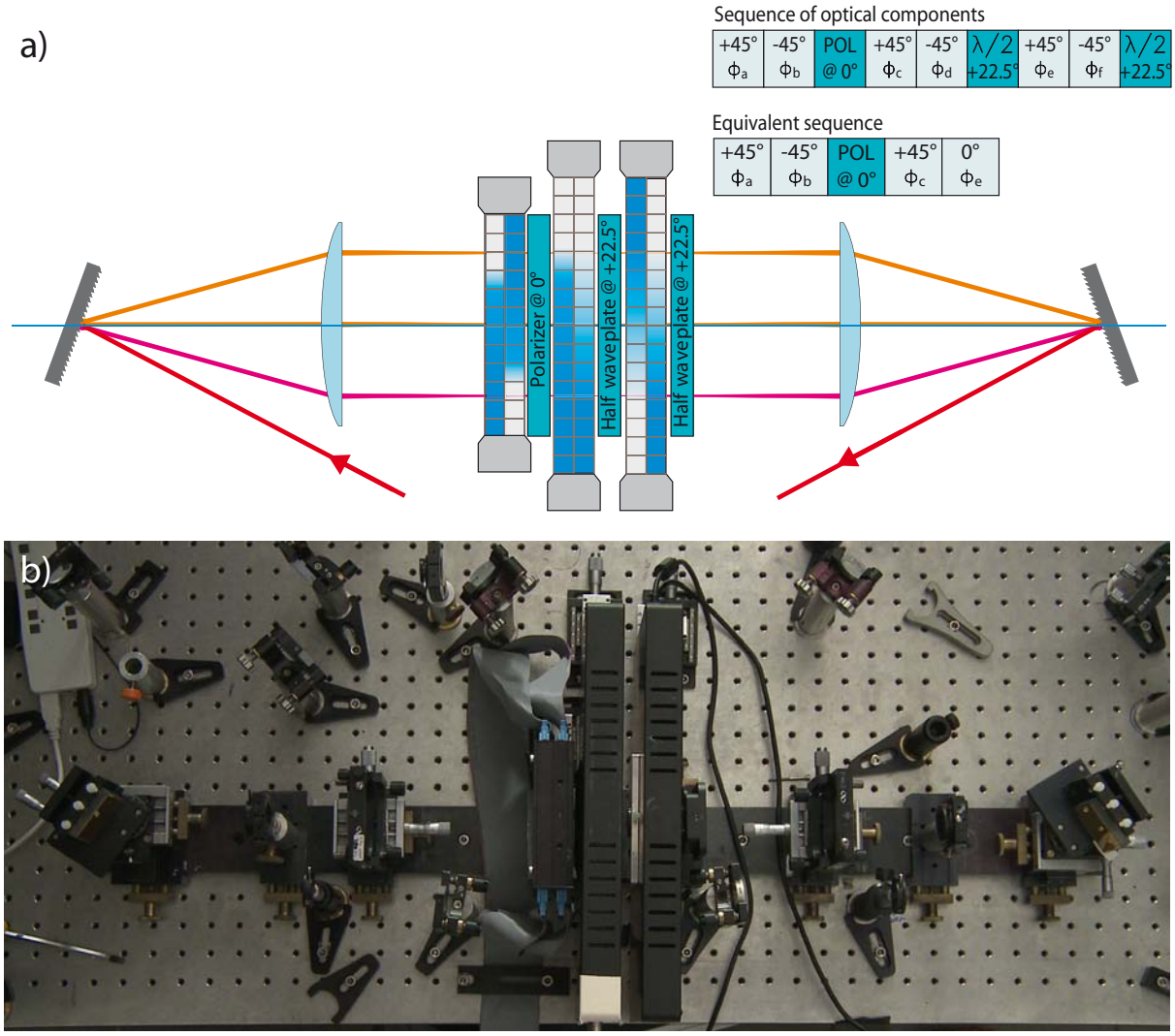


Figure 4.2: Pulse shaper capable of unrestricted phase, amplitude, and polarization shaping. In a), the schematic layout is depicted. The inset in the upper right explains the used and ideal sequence of optical elements. In b), a photograph from the lab illustrates the experimental realization. In both cases, the 4-f-line – consisting of a pair of gratings and lenses – is visible. The three modulators, the polarizer, and the waveplates are placed in the center of the 4-f-line.

a decrease in resolution. This ensures that even complex patterns can be produced and complicated pulse sequences can be shaped with this setup.

### 4.5.2 Independent control of the polarization state

#### Calculation of retardances

To verify the capabilities of the polarization modulation the retardances, which are written on the modulator, are expressed by the parameters of an ellipse. The polarization ellipse of the electric field is characterized by the physical intuitive parameters intensity $I$, ellipticity $r$, and orientation $\gamma$. By using the equations 2.32, 2.33, and 2.34, which are derived in

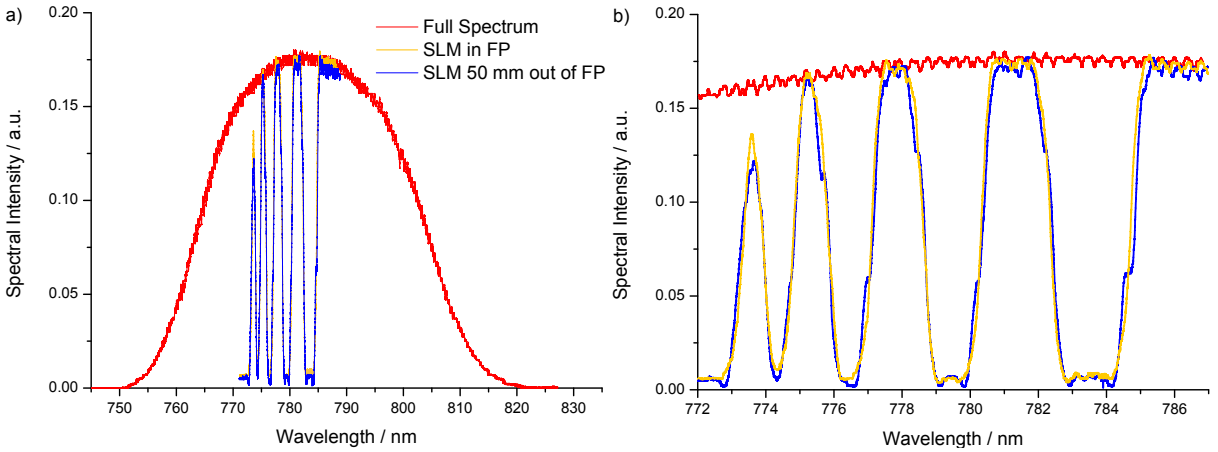


Figure 4.3: High-resolution spectrum of a binary amplitude pattern of ...0101100111000111100001... around the central wavelength. The measurement was carried out for different displacements of the modulator out of the Fourier plane. In this figure, the spectrum in which the modulator is placed in the Fourier plane is compared to one in which the modulator is displaced by 50 mm. a) depicts the whole spectrum and b) the shows a detailed zoom. The resolution is not affected by a displacement in this range.

section 2.2.3, the retardances for each array are calculated. The first modulator controls the spectral intensity by the difference of the retardances of array a and array b analogous to the standard phase and amplitude shaping setups (equation 3.5).

$$\varphi_{Dab}^{\omega_n} = 2\,arccos\left(\sqrt{E_{0x}^2 + E_{0y}^2}\right) \tag{4.10}$$

$$= 2\,arccos\left(\sqrt{I}\right) \tag{4.11}$$

The grating reflectivity can be implemented by attenuating the x component of the electric field by the factor $\sqrt{g}$.

$$\varphi_{Dab}^{\omega_n} = 2\,arccos\left(\sqrt{g\,E_{0x}^2 + E_{0y}^2}\right) \tag{4.12}$$

$$= 2\,arccos\left(\sqrt{\frac{I}{2}\left(1 + g - \frac{(g-1)(r^2-1)\,cos(2\gamma)}{1+r^2}\right)}\right) \tag{4.13}$$

This in not a necessary requirement for the analytical polarization control since it does not change the polarization state, but ensures equal intensity for every polarization state. The sum of the retardances of the first modulator $\varphi_{Sab}^{\omega_n}$ gives the total phase $\Phi(\omega_n)$ of the pulse.

$$\varphi_{Sab}^{\omega_n} = \Phi(\omega_n) \tag{4.14}$$

The second modulator distributes the spectral intensity to horizontal and vertical direction. The ratio of the electric field in horizontal and vertical direction is expressed

by

$$r = \frac{E_y}{E_x} = \frac{\sqrt{g}\, sin\left(\frac{\varphi_{Dcd}^{\omega_n}}{2}\right)}{cos\left(\frac{\varphi_{Dcd}^{\omega_n}}{2}\right)}. \tag{4.15}$$

By solving this equation the difference retardances $\varphi_{Dcd}^{\omega_n}$ of the second modulator are found to be

$$\varphi_{Dcd}^{\omega_n} = 2\, arctan\left(\sqrt{\frac{1 + r^2 + (r^2 - 1)cos(2\gamma)}{g(1 + r^2 - (r^2 - 1)cos(2\gamma))}}\right). \tag{4.16}$$

The arrays $e$ and $f$ of the third modulator introduce a phase shift between the x and y component of the electric field which defines the final polarization state.

$$\varphi_{Def}^{\omega_n} = -\epsilon - \frac{\pi}{2} \tag{4.17}$$

$$= -\frac{\pi}{2} \pm arccos\left(\sqrt{\frac{2(r^2 - 1)^2\, sin(2\gamma)^2}{1 + 6r^2 + r^4 - (r^2 - 1)^2\, cos(4\gamma)}}\right) \tag{4.18}$$

**Continous variation of the polarization state**

By controlling the retardances of the individual pixels of the arrays it is possible to generate any desired polarization state. In this section, the equations 4.13, 4.16, and 4.18 are implemented for the experimental demonstration of the arbitrary control of the polarization state. To analyze the capabilities of the setup the polarization parameters are scanned while measuring the power transmitted through a polarizer.

Figure 4.4a) presents the case in which the polarization ellipse is rotated by 180°. This experiment is carried out for different ellipticity, from r=0.0 (linear) to r=1.0 (circular) in steps of 0.1. In case of the linear pulse, a cosine modulation is observed. In the minimum of the curve no intensity is transmitted. The position of the maximum denotes the orientation of the polarizer. The modulation depth decreases with larger ellipticity. For a circular pulse (r=1.0) no modulation is visible and the curve has a constant amplitude of half the maximal transmitted power.

Figure 4.4b) depicts the variation of the ellipticity of the polarization ellipse while the orientation is kept constant. Each curve represents a different orientation of the polarization ellipse ranging from 0° to 90° in steps of 15°. For circular polarization (r=1.0) all curves start at half of the maximal transmitted power. In case of linear polarization, the intensity of the transmitted light is connected to the orientation of the polarization ellipse. It is maximal for the orientation parallel to the polarizer and minimal if the polarization ellipse is perpendicularly oriented to the polarizer.

Both sets of measurements show the expected behavior and demonstrate the ability of this pulse shaper setup to continuously and independently control the parameters of the polarization.

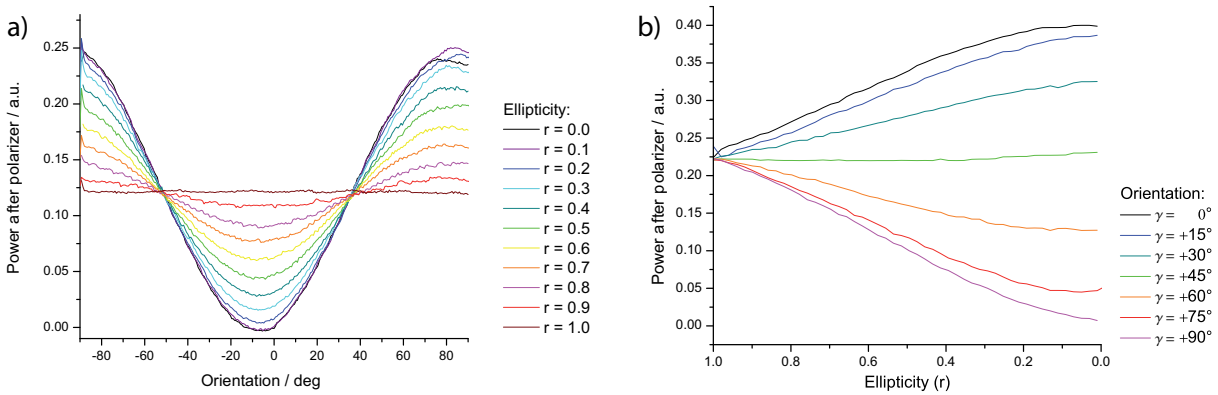


Figure 4.4: Systematic variations of the polarization parameters of the pulse. The power is measured after a polarizer while the polarization of the pulse is varied. In a), the rotation of the ellipse for different ellipticity is depicted. In b), the variation of the ellipticity is shown. It is continuously changed from circular (r=1.0) to linear (r=0.0) while the orientation is kept constant at different angles.

### Polarization shaped single pulses

For pulse shaping it is important that the manipulation of the polarization state is independent from a modulation of the amplitude and phase. The spectral amplitude and especially the phase determine the intensity evolution of the pulse in time. Four example pulses with a determined state of polarization are generated and measured with the time-resolved ellipsometry scheme which was introduced in section 3.3.1. In figure 4.5, the polarization state ellipticity and orientation as well as the intensity over time is presented for four single pulses with different polarization states. The set and measured pulse parameters are summarized in table 4.1. In all cases, the intensity curves exhibit a perfect Gaussian shape with a corresponding cross-correlation length of 87 fs, which corresponds to a pulse length of 62 fs. The polarization parameters – ellipticity and orientation – of the pulse are nearly constant. Before and after the pulse where virtually no intensity is present these values are no longer well-defined. This proves that this setup allows for the independent and unrestricted polarization control of defined ultrashort laser pulses.

| | shown in | **Fig. 4.5a)** | **Fig. 4.5b)** | **Fig. 4.5c)** | **Fig. 4.5d)** |
|---|---|---|---|---|---|
| **Orientation** | set | 0° | +30° | +45° | not |
| | measured | +4° | +31° | +45° | defined |
| **Ellipticity** | set | 0.00 | 0.00 | 0.40 | 1.00 |
| | measured | 0.13 | 0.12 | 0.41 | 0.88 |
| **Pulse length** | set | short | short | short | short |
| | measured | 86±1 fs | 86±1 | 88±1 fs | 86±1 fs |

Table 4.1: Set and measured parameters of the ultrafast polarization shaped single pulses which are presented in figure 4.5.

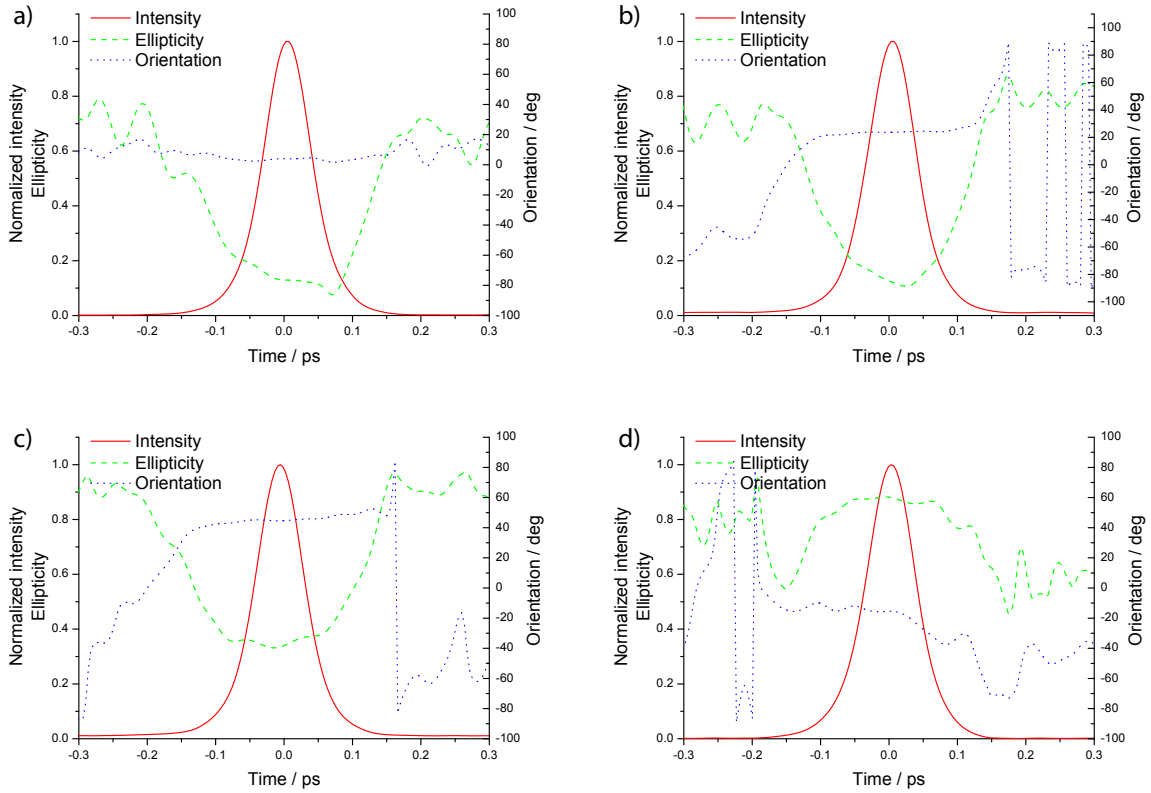


Figure 4.5: Examples of polarization shaped single pulses. Each graph displays the time-dependent parameters intensity, ellipticity, and orientation of the polarization ellipse. In a), a linearly polarized pulse is depicted which is horizontally oriented. In b), a linearly polarized pulse oriented at 30° is shown. In c), an elliptical pulse with a major axes ratio of 0.4 oriented at +45° is presented. In d), a circular pulse is shown.

## 4.6 Parametric pulse shaping

The control over the individual pixels of the modulators spans an unimaginably huge search space. Despite the fact that evolutionary strategies can handle such a huge search space the optimal pulses found in feedback loop optimizations are often very complex. Further, the algorithm converges to different optimal solutions with similar fitness. Due to this fact it is very difficult to extract the underlying processes which are driven by the optimally shaped pulse. To simplify the result of the optimizations the dimensionality of the search space can be reduced. This has the additional advantage that the number of generations which are necessary to reach convergence of the pulse to the optimum is smaller. This in turn makes the feedback loop optimization applicable to experiments which have a limited runtime.

### 4.6.1 Developments in parameterization

The first concepts applied to the restriction of the search space were parameterizations of the phase function, that is written on the modulator. The control parameters of the acoustic wave, which is generated by a acoustic optical modulator (AOM), restricted the search space to a few parameters [44]. Merging of pixels was also successfully applied as a simple way to decrease the size of the search space with the drawback of a limited resolution. A coarse raster of the phase steps from more than 1000 steps, which corresponded to the voltage range, to 32 possible settings reduced the search space without decreasing the obtained fitness [113]. This was pushed to the extreme limit of a binary phase function [114]. The use of the spectral Taylor terms (cf. section 2.4.2) is ideally suited to compensate the chirp of a pulse to obtain a short pulse [113, 115, 116]. The application of periodic phase functions in the frequency domain, constructed by one or several sine functions, corresponds to a train of sub-pulses in the time domain, which was successfully put into operation [117].

Parameterization of amplitude shaping was also developed. Analog to phase modulations, periodic amplitude patterns in the frequency domain also lead to a periodic pulse structure in time, which was used to track coherences in a dissipative environment [118]. Gaussian peaks in the transmission pattern allowed to find the relevant frequencies for transitions. This technique revealed relevant vibrational transitions in NaK [119] and exposed the electronic excitation pathway in ultracold rubidium dimers (cf. section 7.6) [120].

A different approach is to parametrize the pulse in the time domain, transfer it to the spectral domain, and write the corresponding pattern on the modulator. First temporal encodings controlled the envelope and the phase of pulses [121]. This scheme was extended to manipulate the individual pulse parameters of a pulse sequence. The sub-pulses were controlled by the physically intuitive parameters intensity, position in time, phase, and chirps [119]. The optimization of these scalar sub-pulse properties was succesfully applied to the multi-photon ionization of NaK [119]. In connection with the development of the serial setup, this approach was extended to the polarization of the sub-pulses [64, 106]. An experiment on the multi-photon ionization of NaK revealed the importance of the alternating polarization state within a pulse as well as the oscillation period in the excited state of the system [104]. A parametrization in the von Neuman picture describes the shaped pulses in the a joint time-frequency representation [122].

The review of the diverse parameterizations and restrictions of the search space shows that different physical systems need a diverse pulse encoding. Especially for molecular systems the parameterization of a pulse sequence in which the parameters of the individual sub-pulses are controlled is particularly suited. This type of parameterization reduces the search space tremendously to a few dimensions. The resulting sequence of pulses is less complex than the one obtained by a free optimization of the parameters of each pixel. Therefore, the pulse sequence which consists of a few sub-pulses can be interpreted more easily. The individual sub-pulses can be often attributed to excitation steps in the molecular dynamics.

### 4.6.2 Parameterization of a pulse sequence

For the parameterization of a pulse sequence, each sub-pulse is individuallly controlled in its physically intuitive parameters. These parameters are: intensity $I$, position in time, zero order phase, chirps as well as the polarization state orientation $\gamma$, ellipticity r, and helicity. These parameters are defined in section 2.2.1.

The polarization state of each sub-pulse is converted to the spectral vectorial components of the electric field $\tilde{\mathbf{E}}(\omega)$. It is determined by the amplitudes in horizontal (X) and vertical (Y) direction and the phase difference between these spectral components $\epsilon$. The spectral amplitude in horizontal and vertical direction can be expressed by:

$$X = \sqrt{I}\ cos\left(\frac{1}{2} arccos\left(cos\left(2\gamma\right) cos\left(2 arctan\left(r\right)\right)\right)\right) \tag{4.19}$$

$$Y = \sqrt{I}\ sin\left(\frac{1}{2} arccos\left(cos\left(2\gamma\right) cos\left(2 arctan\left(r\right)\right)\right)\right) \tag{4.20}$$

The phase difference $\epsilon$ between the X and Y component determines the ellipticity of the polarization ellipse. It is

$$\epsilon = \phi_y - \phi_x = \pm arctan\left(\frac{tan\left(2\ arctan\left(r\right)\right)}{sin\left(2\gamma\right)}\right) \tag{4.21}$$

in which the sign determines the helicity. Plus stands for right hand polarization and minus for left hand polarization.

The phase $\Phi(\omega)$ of the sub-pulse is constructed by the spectral Taylor terms $b_n$, which are introduced in section 2.4.2. The zero order term regulates the relative phase between the sub-pulses. It also sets the carrier envelope phase (CEP) if a CEP-stabilized laser provides the input pulses. The first order term $b_1$ shifts the pulse in time and, therefore, determines the position in time. The quadratic term generates the linear chirp of the sub-pulse and higher order terms are connected to higher order chirps. The overall pulse sequence is composed of the superposition of $N$ sub-pulses. The complex vectorial electric field in the frequency domain is described by

$$\tilde{\mathbf{E}}^{par}(\omega) = \tilde{E}_{in}(\omega) \sum_N \begin{pmatrix} X_N e^{i\Phi_N(\omega)} \\ Y_N e^{i(\Phi_N(\omega)+\epsilon_N)} \end{pmatrix} \tag{4.22}$$

$$= \tilde{E}_{in}(\omega) \cdot \tilde{\mathbf{H}}^{par}(\omega) \tag{4.23}$$

where $\tilde{E}_{in}(\omega)$ is the electric field of the linearly polarized input pulse, which serves as a prototype and specifies the available overall pulse energy and spectral width. The output electric field can be expressed as a product of the input electric field and an modulation function $\tilde{\mathbf{H}}^{par}(\omega)$.

$$\tilde{\mathbf{H}}^{par}(\omega) = \frac{\tilde{\mathbf{E}}^{par}(\omega)}{\tilde{E}_{in}(\omega)}. \tag{4.24}$$

The modulation function is complex and can be expressed by its real and imaginary part of the horizontal x and vertical y component, respectively.

$$\tilde{\mathbf{H}}^{par}(\omega) = \begin{pmatrix} ReH_x^{\omega} + i\, ImH_x^{\omega} \\ ReH_y^{\omega} + i\, ImH_y^{\omega} \end{pmatrix} \tag{4.25}$$

### 4.6.3 Arbitrarily shaped pulses

The construction of the modulation function is not restricted to the introduced parameterization of sub-pulse sequences. A modulation function of any desired electric field can be calculated within the limits of the available laser pulses. The electric field can be obtained by different types of parametrizations or theoretical considerations. A construction of the electric field in the time domain as $\tilde{\mathbf{E}}(t)$ is also possible, since it is directly connected to the frequency domain $\tilde{\mathbf{E}}(\omega)$ by Fourier transformation.

### 4.6.4 Calculation of the retardances from the modulation function

In order to calculate the individual retardances of the arrays for the pulse shaper setups, which are introduced in section 4.2 and 4.3 the expression of the corresponding electric field is recalled. It can be transformed to a product of the incoming electric field $\tilde{E}_{in}(\omega)$ and a modulation function $\tilde{\mathbf{H}}^{mod}$

For the ideal setup, which utilizes four liquid crystal arrays for the modulation of the electric field, it writes

$$\begin{aligned} \tilde{\mathbf{E}}_{out}^{mod4}(\omega_n) &= \tilde{E}_{in}(\omega)\, e^{\frac{i}{2}\left(\varphi_a^{\omega_n}+\varphi_b^{\omega_n}+\varphi_c^{\omega_n}\right)} \\ &\quad \times cos\left(\frac{\varphi_a^{\omega_n}-\varphi_b^{\omega_n}}{2}\right) \begin{bmatrix} cos\left(\frac{\varphi_c^{\omega_n}}{2}\right) \\ i\; e^{i\varphi_e^{\omega_n}} sin\left(\frac{\varphi_c^{\omega_n}}{2}\right)\sqrt{g} \end{bmatrix} && (4.26) \\ &= \tilde{\mathbf{H}}^{mod4} \cdot \tilde{E}_{in}(\omega), && (4.27) \end{aligned}$$

which is derived in section 4.2. In case of the alternative setup, which uses three double liquid crystal modulators, it can be expressed as:

$$\begin{aligned} \tilde{\mathbf{E}}_{out}^{modSD}(\omega_n) &= \tilde{E}_{in}(\omega_n)\, e^{\frac{i}{2}\varphi_{Sab}^{\omega_n}} cos\left(\frac{\varphi_{Dab}^{\omega_n}}{2}\right) \begin{pmatrix} e^{i\frac{\varphi_{Def}^{\omega_n}}{2}} cos\left(\frac{\varphi_{Dcd}^{\omega_n}}{2}\right) \\ i\, e^{-i\frac{\varphi_{Def}^{\omega_n}}{2}} sin\left(\frac{\varphi_{Dcd}^{\omega_n}}{2}\right)\sqrt{g} \end{pmatrix} && (4.28) \\ &= \tilde{\mathbf{H}}^{modSD} \cdot \tilde{E}_{in}(\omega) && (4.29) \end{aligned}$$

In order to transfer the retardances of the modulation function from the calculated desired field to the modulator, the frequency band of the pulse needs to be resampled to the discrete frequency bands $\omega_n$ corresponding to the pixels of the modulator.

Then, the modulation function of the desired field is identified with the modulation function of the modulator.

$$\tilde{\mathbf{H}}^{par}(\omega_n) = \tilde{\mathbf{H}}^{mod}(\omega_n) \tag{4.30}$$

When considering the real and imaginary part of each vector component, this leads to a system of four coupled linear equations. It relates the retardances of the liquid crystal arrays to the components of the modulation function $\tilde{\mathbf{H}}^{mod}$. In the following, it is solved for both setups. First, for the ideal setup which utilizes four arrays. Then, it is analogously carried out for the setup which utilizes three standard double liquid crystal modulators.

### Pulse shaper which uses four liquid crystal arrays

The linear system of equations for the setup which uses four liquid crystal arrays:

$$\begin{aligned}
ReH_x^{\omega_n} &= \frac{1}{4}(cos\left(\varphi_a^{\omega_n}+\varphi_e^{\omega_n}\right)+cos\left(\varphi_b^{\omega_n}+\varphi_e^{\omega_n}\right) \\
&\quad +cos\left(\varphi_a^{\omega_n}+\varphi_c^{\omega_n}+\varphi_e^{\omega_n}\right)+cos\left(\varphi_b^{\omega_n}+\varphi_c^{\omega_n}+\varphi_e^{\omega_n}\right)) && (4.31)\\
ImH_x^{\omega_n} &= \frac{1}{4}(sin\left(\varphi_a^{\omega_n}+\varphi_e^{\omega_n}\right)+sin\left(\varphi_b^{\omega_n}+\varphi_e^{\omega_n}\right) \\
&\quad +sin\left(\varphi_a^{\omega_n}+\varphi_c^{\omega_n}+\varphi_e^{\omega_n}\right)sin\left(\varphi_b^{\omega_n}+\varphi_c^{\omega_n}+\varphi_e^{\omega_n}\right)) && (4.32)\\
ReH_y^{\omega_n} &= \frac{1}{4}(-cos\left(\varphi_a^{\omega_n}\right)-cos\left(\varphi_b^{\omega_n}\right) \\
&\quad +cos\left(\varphi_a^{\omega_n}+\varphi_c^{\omega_n}\right)cos\left(\varphi_b^{\omega_n}+\varphi_c^{\omega_n}\right))\sqrt{g} && (4.33)\\
ImH_y^{\omega_n} &= \frac{1}{4}(-sin\left(\varphi_a^{\omega_n}\right)-sin\left(\varphi_b^{\omega_n}\right) \\
&\quad +sin\left(\varphi_a^{\omega_n}+\varphi_c^{\omega_n}\right)sin\left(\varphi_b^{\omega_n}+\varphi_c^{\omega_n}\right))\sqrt{g} && (4.34)
\end{aligned}$$

This system of equations can be solved for the retardances:

$$\begin{aligned}
\varphi_a^{\omega_n} &= \pm ACOS - ACOT - ATAN && (4.35)\\
\varphi_b^{\omega_n} &= \mp ACOS - ACOT - ATAN && (4.36)\\
\varphi_c^{\omega_n} &= 2\ ACOT && (4.37)\\
\varphi_e^{\omega_n} &= ACOTX + ATAN && (4.38)
\end{aligned}$$

For $\varphi_a^{\omega_n}$ and $\varphi_b^{\omega_n}$ two solutions can be found, which is indicated by $\pm$ and $\mp$ respectively.

### Pulse shaper which uses three double liquid crystal modulators

The analogous equation system for the six array modulator is:

$$ReH_x^{\omega_n} = cos\left(\frac{\varphi_{Dab}^{\omega_n}}{2}\right) cos\left(\frac{\varphi_{Dcd}^{\omega_n}}{2}\right) cos\left(\frac{\varphi_{Def}^{\omega_n} + \varphi_{Sab}^{\omega_n}}{2}\right) \tag{4.39}$$

$$ImH_x^{\omega_n} = cos\left(\frac{\varphi_{Dab}^{\omega_n}}{2}\right) cos\left(\frac{\varphi_{Dcd}^{\omega_n}}{2}\right) sin\left(\frac{\varphi_{Def}^{\omega_n} + \varphi_{Sab}^{\omega_n}}{2}\right) \tag{4.40}$$

$$ReH_y^{\omega_n} = cos\left(\frac{\varphi_{Dab}^{\omega_n}}{2}\right) sin\left(\frac{\varphi_{Dcd}^{\omega_n}}{2}\right) sin\left(\frac{\varphi_{Def}^{\omega_n} - \varphi_{Sab}^{\omega_n}}{2}\right) \sqrt{g} \tag{4.41}$$

$$ImH_y^{\omega_n} = cos\left(\frac{\varphi_{Dab}^{\omega_n}}{2}\right) sin\left(\frac{\varphi_{Dcd}^{\omega_n}}{2}\right) cos\left(\frac{\varphi_{Def}^{\omega_n} - \varphi_{Sab}^{\omega_n}}{2}\right) \sqrt{g} \tag{4.42}$$

The sums and differences of the retardances of the setup which utilizes six liquid crystal arrays are found by similar consideration as in the previous case.

$$\varphi_{Sab}^{\omega_n} = ACOTX - ATAN \tag{4.43}$$

$$\varphi_{Dab}^{\omega_n} = \pm 2\, ACOS \tag{4.44}$$

$$\varphi_{Dcd}^{\omega_n} = 2\, ACOT \tag{4.45}$$

$$\varphi_{Def}^{\omega_n} = ACOTX + ATAN \tag{4.46}$$

For a more compact presentation, the following abbreviations have been used:

$$ACOS = arccos\left(\sqrt{1 + \frac{(ImH_x^{\omega_n})^2}{(ReH_x^{\omega_n})^2}}\, ReH_x^{\omega_n} \sqrt{1 + \frac{(ImH_y^{\omega_n})^2 + (ReH_y^{\omega_n})^2}{\left((ImH_x^{\omega_n})^2 + (ReH_x^{\omega_n})^2\right) g}}\right) \tag{4.47}$$

$$ACOT = arccot\left(\frac{\sqrt{1 + \frac{(ImH_x^{\omega_n})^2}{(ReH_x^{\omega_n})^2}}\, ReH_x^{\omega_n}\, ImH_y^{\omega_n} \sqrt{1 + \frac{(ReH_y^{\omega_n})^2}{(ImH_y^{\omega_n})^2}}\, \sqrt{g}}{(ImH_y^{\omega_n})^2 + (ReH_y^{\omega_n})^2}\right) \tag{4.48}$$

$$ACOTX = arccot\left(\frac{ReH_x^{\omega_n}}{ImH_x^{\omega_n}}\right) \tag{4.49}$$

$$ATAN = arctan\left(\frac{ReH_y^{\omega_n}}{ImH_y^{\omega_n}}\right) \tag{4.50}$$

A necessary condition results from energy conservation. The shaped pulse, which leaves the setup, cannot have a higher energy than the short pulse, which enters the setup. The condition

$$\left|\tilde{\mathbf{E}}_{out}\left(\omega_n\right)\right| \leq \left|\tilde{\mathbf{E}}_{in}\left(\omega_n\right)\right| \tag{4.51}$$

must be valid for all $\omega_n$. Since the first two arrays control the spectral amplitude the retardances of these arrays ($\varphi_a$ and $\varphi_b$, or $\varphi_{Dab}$) become complex if this condition is violated. Therefore, the spectral amplitude has to be normalized to fulfill this condition. Including the grating correction in the equations in which the parameter $g$ takes the difference in reflectivity into account leads to a slightly different normalization. It depends

on the polarization state of the pulse. The correction focuses on the parameters of the first arrays. The term within the *arccos* (equation 4.47) needs to be in the range of $-1$ to $+1$ to result in a real number, which is also achieved by normalization of $\tilde{\mathbf{H}}^{par}$ with its maximal value.

$$\tilde{\mathbf{H}}^{par}_{norm} = \frac{\tilde{\mathbf{H}}^{par}}{\sqrt{(ReH_x^{max})^2 + (ImH_x^{max})^2 + ((ReH_y^{max})^2 + (ImH_y^{max})^2)/g}} \tag{4.52}$$

The terms ACOT, ACOTX, and ATAN and, therefore, the states of polarization of a pulse sequence are not altered by the normalization because the normalization factor cancels out. This normalization can be also performed to obtain the maximal overall pulse energy for the pulse-sequence of particular interest.

## 4.7 Generation of double pulses

In this section, the generation of multi-pulses is illustrated with simulated double pulse sequences. The variation of one parameter exemplifies the implication on the electric field of the pulse sequence. The purpose of this series of double pulses is to give an impression of the appearance of the electric field in the time and frequency domain.

The electric field of a double pulse is composed by superposition of the electric fields of the sub-pulses. Due to the complex character of the electric field interferences appear. A variation of the phase or amplitude of the electric field of one sub-pulse changes the interference condition and, therefore, the field of the overall pulse sequence. The variation of the parameters intensity, position in time, chirps, and the polarization state, which describe the pulse in the time domain, transfers to a characteristic behavior in the spectral domain. In each example one single parameter is modified. The amplitudes and phases of the electric field in horizontal and vertical direction and the corresponding pattern of the liquid crystal arrays are displayed. The resolution of the frequency width per pixel is chosen to be equal to the one in the experiment.

In figure 4.6, the orientation of the linearly polarized second sub-pulse is different in each sub-set. The sub-pulses are equal in energy and separated by 200 fs. The distance in time is chosen to be smaller than in the examples of the experimental pulses, which are presented later, because the features in the spectrum of the pulses are easier to identify.

In figure 4.6a), both pulses are linearly horizontally polarized. The temporal and spectral field in the vertical direction is zero. The spectrum of this pulse sequence in horizontal direction exhibits an oscillatory structure. This structure is the interference pattern of two pulses. The distance of the fringes is inverse to the sub-pulse distance in time. This pulse is produced using only the arrays of the first double liquid array modulator. The arrays with the retardances $\varphi_{Dcd}$ and $\varphi_{Def}$ are not required for this linearly polarized pulse sequence.

If the sub-pulses are perpendicularly polarized (as illustrated in figure 4.6b)), the interference disappears. The spectral amplitude in both directions is a Gaussian. The phase of the x component is a linear function with a positive slope. It shifts this sub-pulse to a negative position in time. The phase of the y component is also linear but with a negative

slope shifting the sub-pulse in positive time direction. The corresponding retardances are presented on the right part of the figure.

In example 4.6c), the second sub-pulse is linearly polarized oriented at 30°. This sub-pulse has spectral components in horizontal and vertical direction, which are distributed by $\frac{E_x}{E_y} = tan(30°)$. The spectral components in horizontal direction interfere while in vertical direction only the undistorted Gaussian spectrum is present. The interference fringes in the horizontal components have a lower amplitude. Due to the different intensities of the sub-pulse components in y direction complete destructive interference is not possible.

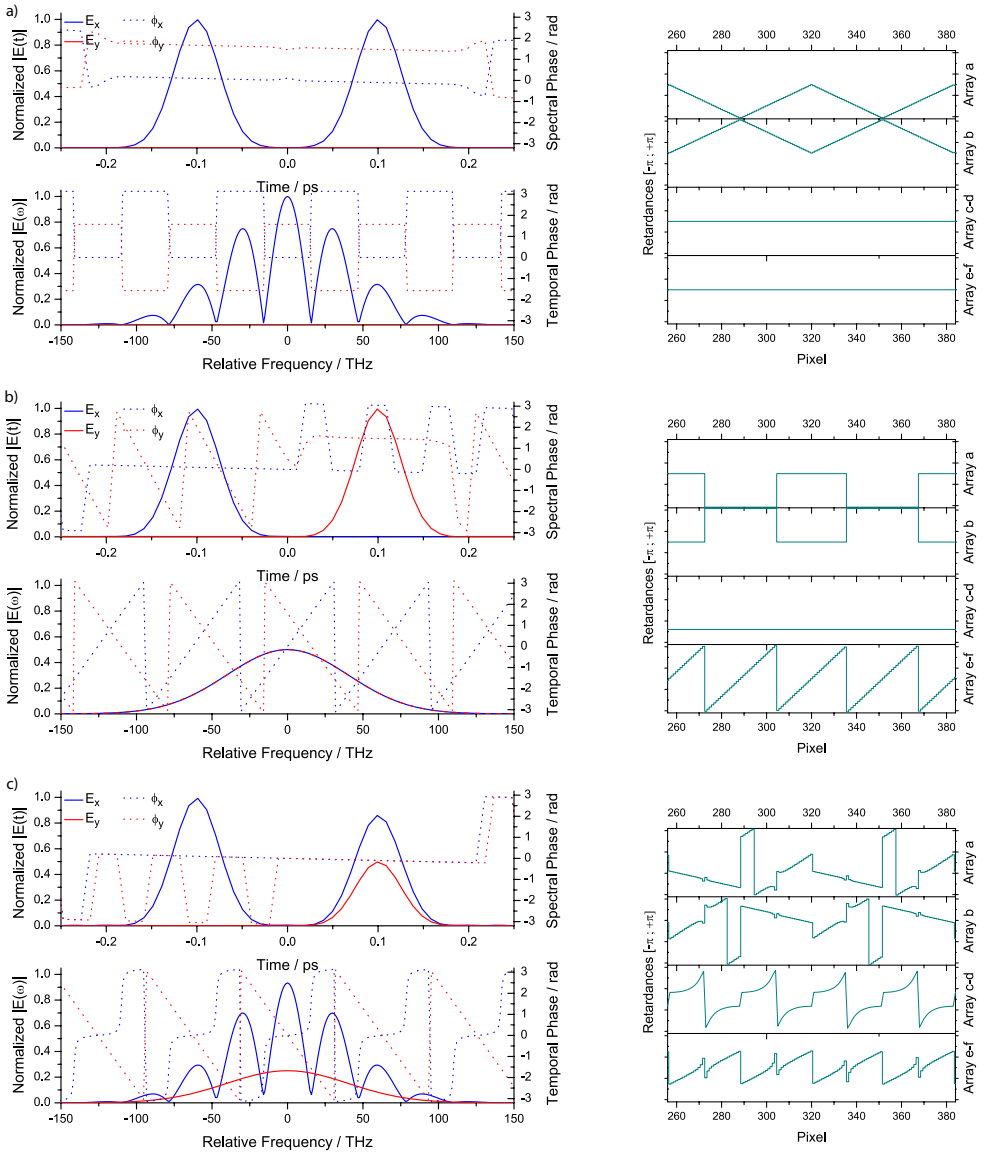


Figure 4.6: The electric field in the time and frequency domain for simulated double pulse sequences. It is represented for a series of linearly polarized double pulses along with the corresponding retardance pattern of the liquid crystal arrays, which would produce the particular pulse sequence. In example a), the sub-pulses are both horizontally oriented. In example b), the sub-pulses are orthogonally polarized. In example c), a pulse sequence of a sub-pulse oriented at 0° and 30° is depicted.

In figure 4.7, the parameters ellipticity, intensity, position in time, and linear chirp of the first sub-pulse are varied. The corresponding retardances of the liquid crystal arrays are shown on the right. The double pulse which is presented in figure 4.6c) serves as an initial example.

In figure 4.7a), the ellipticity of the first sub-pulse is set to $r$=0.5. This distributes intensity to both components of the electric field vector and results in interference in horizontal and vertical direction in the frequency domain. Due to the phase shift between x and y component of the elliptical sub-pulse, the fringes in the y component are likewise shifted.

In part b) of figure 4.7, the relative intensity of the first sub-pulse is tripled. This can be observed in both representations of the electric field. The effect on the modulation depths in the x component is also visible.

In figure 4.7c), the distance in time between the sub-pulses is doubled. This is realized by increasing the slope of the linear phase function in the frequency domain. It leads to a higher modulation frequency of the interference pattern in the spectral amplitude.

The application of a linear chirp to the first sub-pulse is demonstrated in figure 4.7d). The chirp of 2000 $fs^2$ is clearly expressed in a prolonged time duration of the electric field. The temporal phase of the sub-pulse shows the characteristic parabolic shape. In the frequency domain, the spacing of the interference fringes increases for larger frequencies. This is comprehensible when considering the timing of the frequency components. The higher frequencies are first present in the sub-pulse. The lower frequencies arrive later. Therefore, these low frequencies in the tail of the sub-pulse interfere with the following second sub-pulse. The modulation frequency of the interference decreases for higher frequencies.

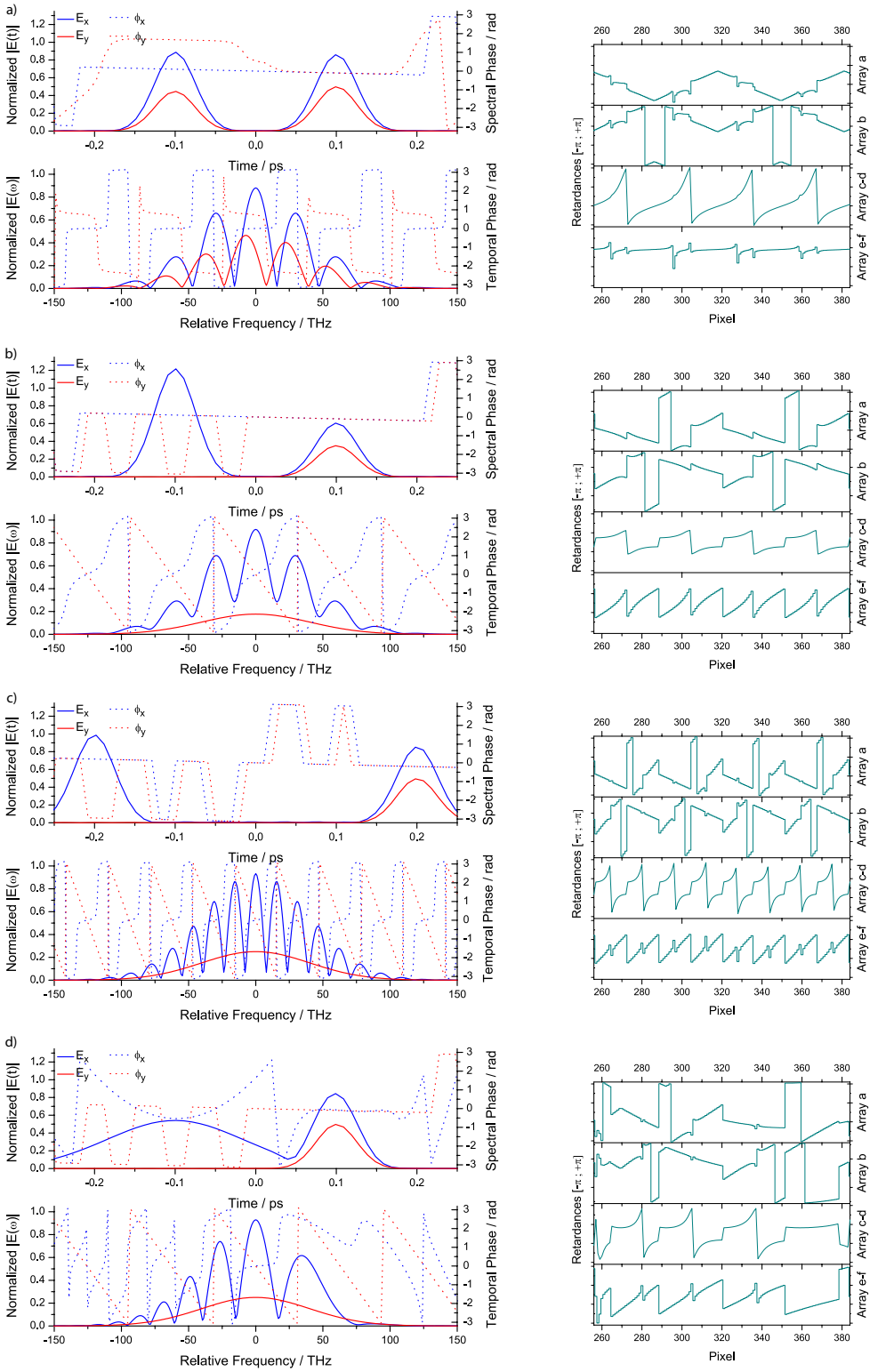


Figure 4.7: The electric field in the time and frequency domain for a series of simulated double pulse sequences is represented with the corresponding retardance pattern which would produce the respective pulses. In each example, one parameter of the first sub-pulse is changed compared to the pulse sequence presented in figure 4.6c). In part a), the first sub-pulse is elliptical polarized (r=0.5). In part b), the intensity of the first sub-pulse is increased by a factor of three. In part c), the sub-pulse distance is increased to 400 fs. In part d), a linear chirp of 2000 $fs^2$ is applied.

## 4.8 Systematic variation of a single parameter in a double pulse sequence

In this section, the functionality of the parameterization in combination with the introduced setup which uses six arrays is experimentally demonstrated. To prove that it is possible to control each parameter of every individual sub-pulse independently a series of double pulses is generated, measured, and retrieved. This provides information about the time-dependent pulse parameters: the polarization including orientation and ellipticity as well as intensity. The intensity graph, which is basically the integrated SFG-XC signal, reveals the distance and chirps of the measured pulses. For a systematic investigation, a single parameter of the double pulse sequence is varied while the others are kept constant. The particular parameter under investigation is plotted. The same parameter of the other sub-pulse is additionally plotted to serve as a reference. To illustrate this scan two double pulses are exemplarily choosen from each series in order to show the evolution of the intensity and the polarization parameters. These are presented along with a three-dimensional representation of the pulse, which is calculated from the measured data.

Figure 4.8 depicts the variation of the sub-pulse energy. In figure 4.9, the distance between the sub-pulses is changed. By linearly chirping the first sub-pulse a prolongation of its pulse duration can be observed while the second sub-pulse remains short. This is depicted in figure 4.10. The focus of this setup is on the full control of the polarization. Therefore, the variation of the polarization parameters orientation and ellipticity is demonstrated in two sets of figures each. In figure 4.11, the second sub-pulse is rotated while maintaining its linear polarization. In figure 4.12, an elliptical sub-pulse with a constant ellipticity of $r = 0.5$ is rotated while the first sub-pulse remains unchanged. The change of the ellipticity of the second sub-pulse is depicted in the two following figures. The orientation of the polarization ellipse is set to $+30°$ in figure 4.13 and to $+60°$ in figure 4.14 while the ellipticity is varied from linear (r=0.0) to circular (r=1.0). The set paramters and statistics regarding the measured parameters which were kept constant are presented in table 4.2.

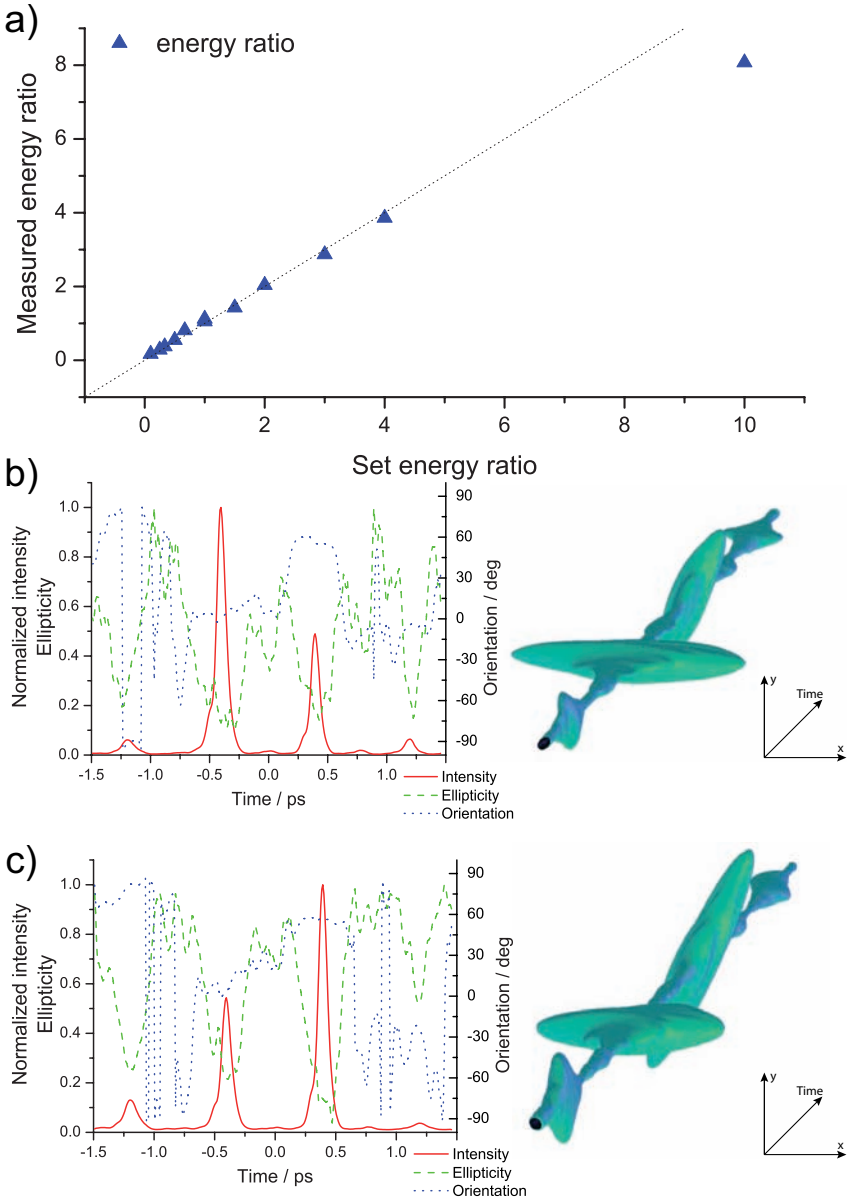


Figure 4.8: Variation of the sub-pulses' energy. a) shows the change of the relative energy between the two sub-pulses from 1:10 to 10:1. The other sub-pulse parameters are kept constant. Both sub-pulses are linearly polarized. The first sub-pulse is oriented at 0° and the second one at +60°. The distance between the sub-pulses amounts to 800 fs. In b), the first sub-pulse has twice the energy of the second one. In pulse c) it is the opposite.

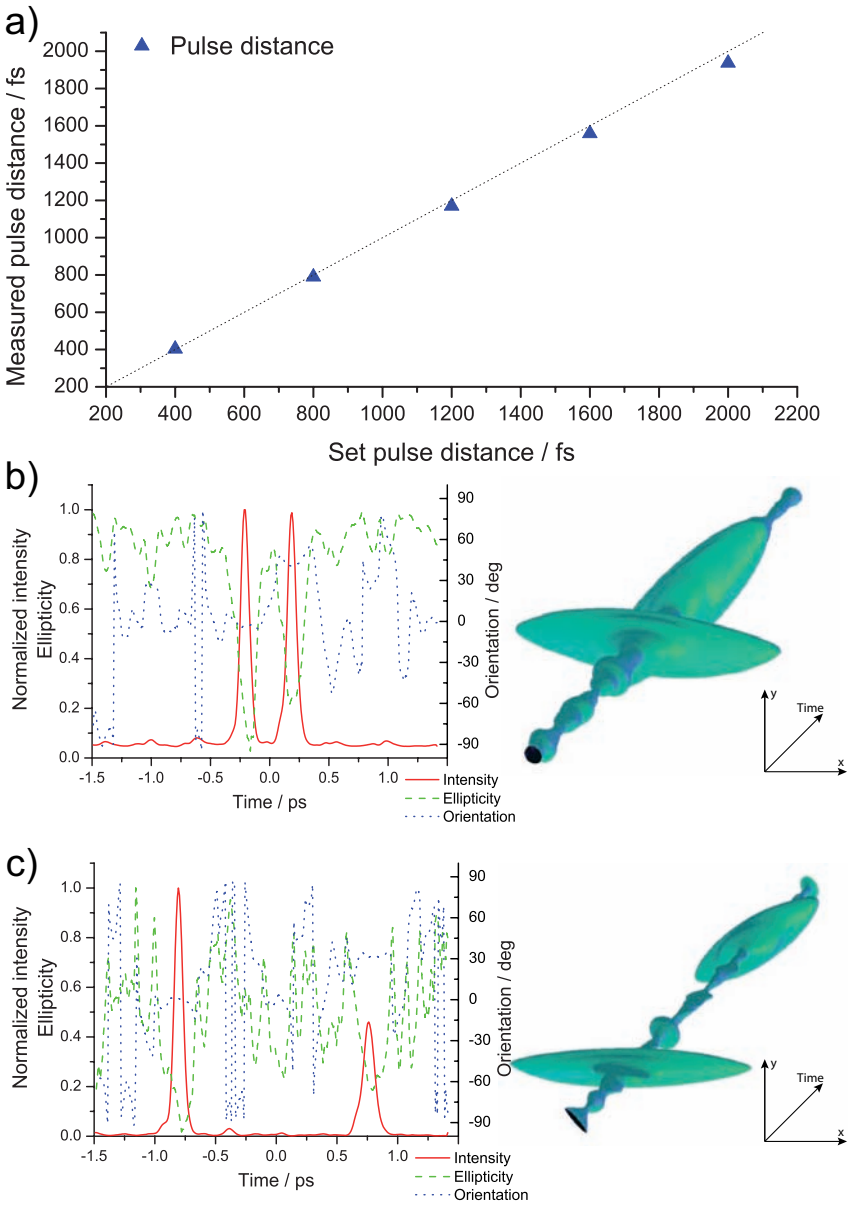


Figure 4.9: Variation of the distance between the sub-pulses from 400 fs to 2000 fs. The double pulse consists of two linear sub-pulses oriented at 0° and +45°, respectively. In b), the sub-pulse distance amounts to 400 fs. In c), the sub-pulse distance is set to 1600 fs.

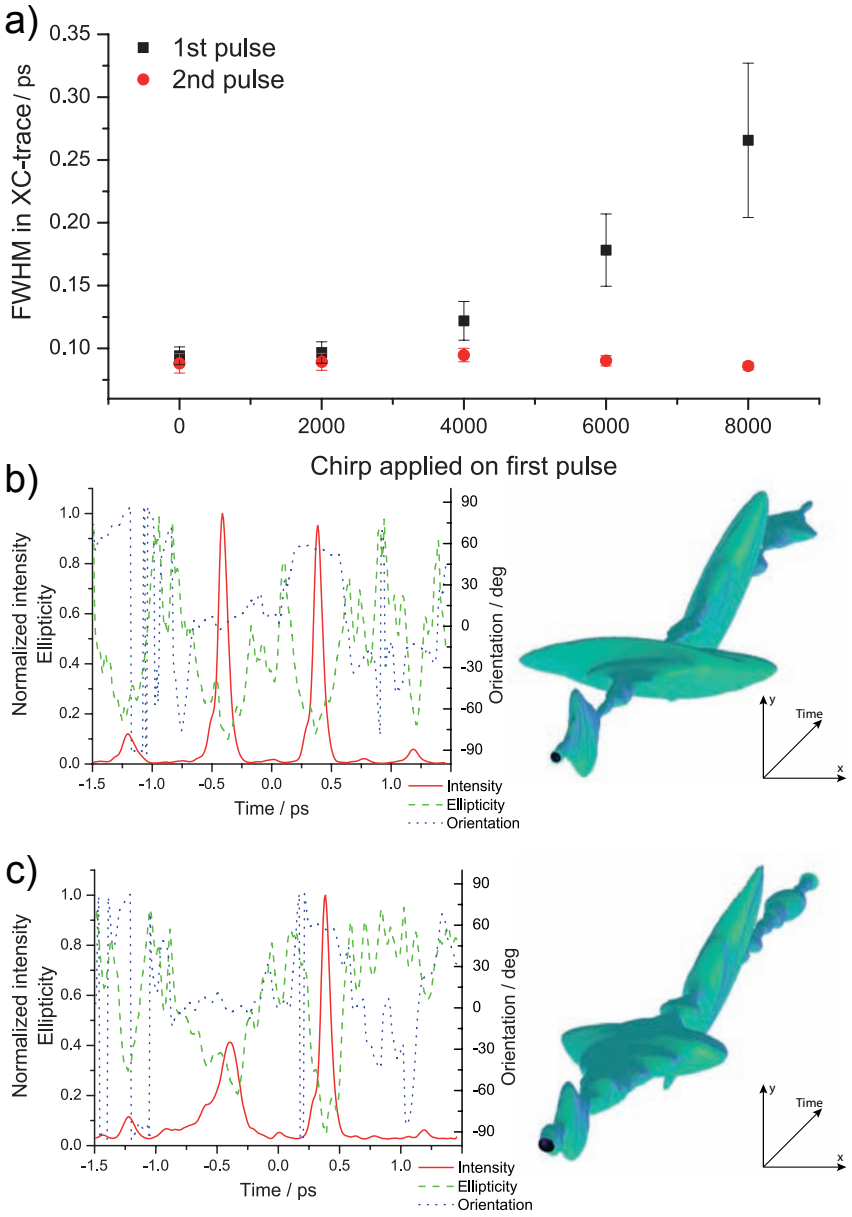


Figure 4.10: In this series, the effect of applying a linear chirp to the first sub-pulse is demonstrated. The intensity trace of every curve is fitted with a Gaussian. In a), the FWHM of the intensity trace of the first sub-pulse is plotted depending on its chirp. The pulse length would be obtained by deconvolution with the reference pulse. The length of the first sub-pulse increases with larger chirps and the peak intensity is reduced. The duration of the second sub-pulse remains constant at about 90 fs. Both sub-pulses are linearly polarized oriented at 0° and +60°, respectively. In b), the example of two short sub-pulses is depicted. In c), the first sub-pulse is chirped by +6000 $fs^2$.

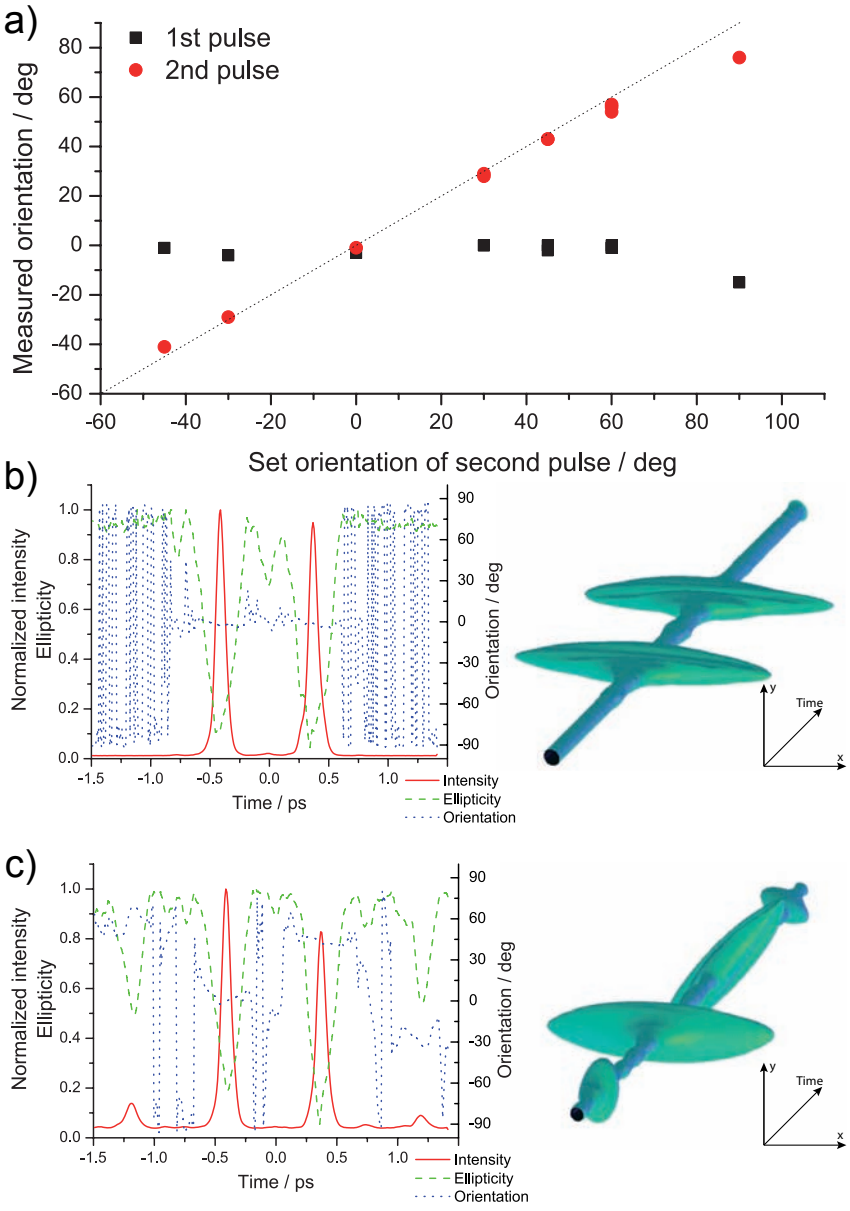


Figure 4.11: The variation of the orientation is demonstrated in figure a). The two sub-pulses having the same energy, are linearly polarized and are separated by 800 fs. The first sub-pulse is fixed at 0° whereas the orientation of the second sub-pulse is rotated counter clockwise. Two examples of this series are shown in part b) and c) in which the orientation of the second sub-pulse is 0° and +45°, respectively.

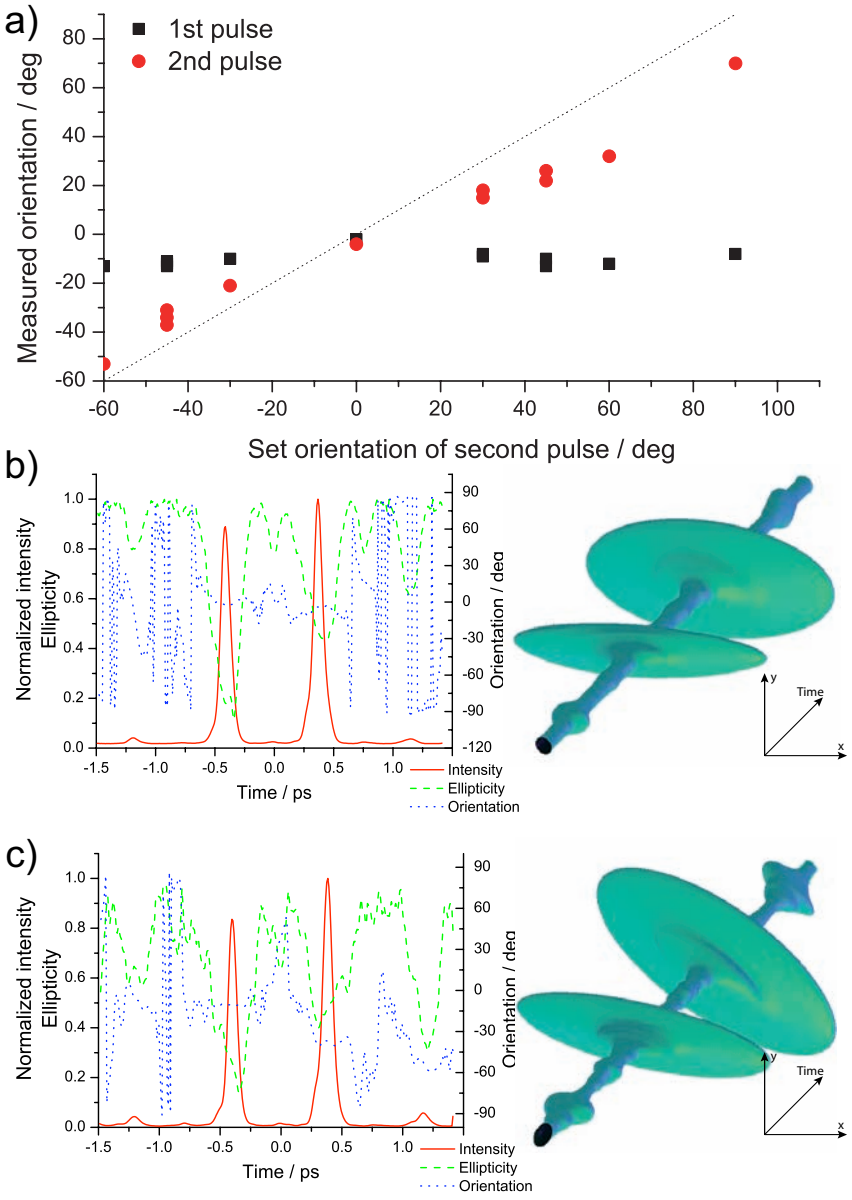


Figure 4.12: The variation of the orientation is demonstrated for a double pulse sequence of a linear sub-pulse followed by an elliptical sub-pulse with r=0.5. The two sub-pulses have the same energy are separated by 800 fs and have the same energy. The first sub-pulse is fixed at 0° whereas the orientation of the second elliptical sub-pulse is rotated counter clockwise. Two examples of this series are shown in part b) and c) in which the orientation of the second one is set to 0° and −45°, respectively.

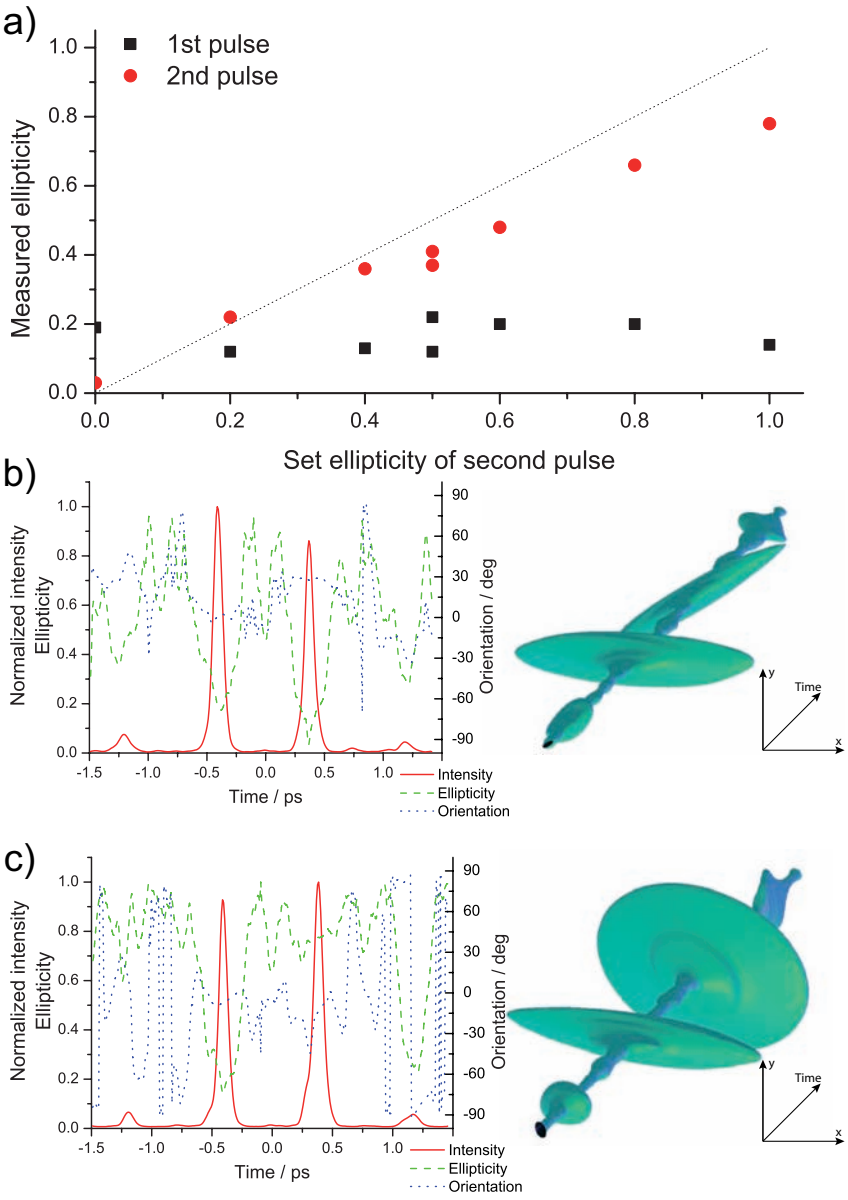


Figure 4.13: The variation of the ellipticity is illustrated. A sequence of double pulses with equal energy separated by 800 fs serves as an example. The orientation of the first sub-pulse is set to 0° and of the second one is set to +30°. The polarization of the first sub-pulse is kept linear whereas the ellipticity of the second sub-pulse is varied from linear (r=0.0) via elliptical to circular (r=1.0). In b), the two sub-pulses are linearly polarized. In part c), the linear sub-pulse is followed by a circular one.

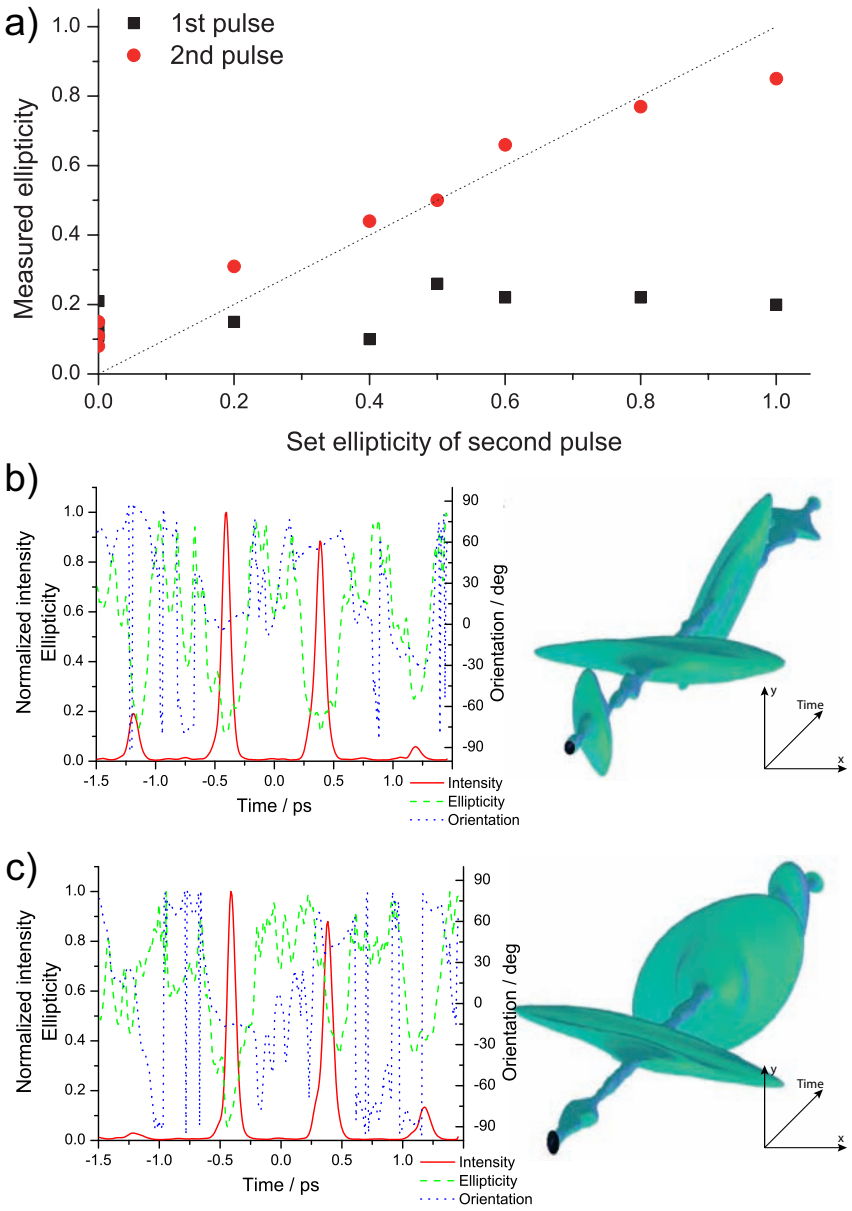


Figure 4.14: In this figure, another example of the independent variation of the ellipticity is presented. A double pulse in which sub-pulses of equal energy are separated by 800 fs serves as an example. The orientation of the first sub-pulse is 0° and of the second sub-pulse it is +60°. The ellipticity of the first sub-pulse is kept linear whereas the ellipticity of the second one is varied from linear (r=0.0) via elliptical to circular (r=1.0). In b), the two sub-pulses are linearly polarized. In part c), the linear sub-pulse is followed by an elliptical with an ellipticity of r=0.4.

| | shown in | **Energy** Fig. 4.8 | **Distance** Fig. 4.9 | **Chirp** Fig. 4.10 | **Orientation** Fig. 4.11 | **Orientation** Fig. 4.12 | **Ellipticity** Fig. 4.13 | **Ellipticity** Fig. 4.14 |
|---|---|---|---|---|---|---|---|---|
| **Energy** | set | varied | 1.0 | 1.0 | 1.0 | 1.0 | 1.0 | 1.0 |
| | measured | | 1.5±0.5 | 0.8±0.2 | 1.2±0.2 | 1.1±0.2 | 1.0±0.1 | 1.1±0.1 |
| **Distance** | set | 800 fs | varied | 800 fs | 800 fs | 800 fs | 800 fs | 800 fs |
| | measured | 796±3 fs | | 798±16 fs | 785±10 fs | 782±5 fs | 788±7 | 791±13 fs |
| **Pulse length** | set | short | short | varied | short | short | short | short |
| 1st pulse | measured | 92±1 fs | 83±1 fs | | 89±4 fs | 89±4 fs | 85±4 fs | 85±5 fs |
| **Pulse length** | set | short | short | short | short | short | short | short |
| 2nd pulse | measured | 83±1 fs | 95±1 fs | 105±3 fs | 90±2 fs | 93±2 fs | 93±2 fs | 93±2 fs |
| **Orientation** | set | 0° | 0° | 0° | 0° | 0° | 0° | 0° |
| 1st pulse | measured | +2±6° | −2±2° | 0±5° | −2±4° | −7±7° | −7±3° | −7±6° |
| **Orientation** | set | +60° | +45° | +60° | varied | varied | +30° | +60° |
| 2nd pulse | measured | +56±1° | +38±6° | +55±3° | | | +22±6° | +52±6° |
| **Ellipticity** | set | 0.00 | 0.00 | 0.00 | 0.00 | 0.00 | 0.00 | 0.00 |
| 1st pulse | measured | 0.20±0.09 | 0.21±0.11 | 0.24±0.06 | 0.18±0.06 | 0.21±0.05 | 0.16±0.04 | 0.17±0.06 |
| **Ellipticity** | set | 0.00 | 0.00 | 0.00 | 0.00 | 0.50 | varied | varied |
| 2nd pulse | measured | 0.17±0.04 | 0.21±0.06 | 0.17±0.06 | 0.14±0.09 | 0.55±0.16 | | |

Table 4.2: Parameters of the double pulses which are depicted in figure 4.8 to 4.14. Each column represents a series of double pulses. The set parameters and statistics on measured parameters which are kept constant in the respective series are displayed. For the determination of the orientation, only sub-pulses with an ellipticity larger than 2/3 are considered because of the uncertainty in the determination of the orientation for nearly circular pulses.

## 4.9 Complex pulse sequences

In the last section, the intended control of sub-pulse parameters in a double pulse sequence was systematically demonstrated. In this section, the parametrically shaped pulse sequences are extended to more complex pulses. These example pulses are parametrically generated, measured, and retrieved by time-resolved ellipsometry (cf. section 3.3.1). The resulting time-dependent parameters intensity, ellipticity and orientation of the pulse are presented along with a three-dimensional representation of the pulse. The example pulses presented in this section shall demonstrate the level of complexity which is accomplishable with this parameterization procedure and the utilized setup. This shows that this method is universal and not restricted to double pulses. In the pulse sequences the parameter of any sub-pulse can be individually controlled.

The control of the linear chirp, which results in a symmetrically stretched pulse in time, was presented for a double pulse sequence in figure 4.10. Higher order chirps also can be applied to the individual sub-pulse. The application of a quadratic chirp is demonstrated on double and triple pulse sequences in figure 4.15. The quadratic chirp causes an asymmetric broadening with an oscillatory envelope of the pulse. The sign of the chirp determines the order in time of the steep increase and the slab tail of the pulse. In example a) and c) of figure 4.15, the characteristic shape of the quadratic chirp can be clearly observed. In case b), the inward directed tails of the pulses overlap. In figure 4.15c), a short linear pulse is situated between two quadratically chirped pulses of opposite sign. In all three examples the polarization state of the sub-pulses is not afflicted by the applied chirp. Details of the state of polarization, distances in time, energy as well as the magnitude of the chirps are denoted in the caption of the figure.

In figure 4.16, the pulse sequences consist of six sub-pulses. In a), the pulse sequence consists of six linear sub-pulses whereby the orientation of each sub-pulse is rotated by +30° relative to the previous sub-pulse. In b), the ellipticity of each subsequent sub-pulse is increased by 0.2. Starting with a linearly polarized sub-pulse it ends with a circularly polarized sub-pulse. The polarization ellipses are all oriented in the same direction at 0°. The variation of the orientation as well as the ellipticity can be combined, which is presented in figure 4.16c) and d). In figure 4.16c), the orientation of each sub-pulse is rotated by +30° while the ellipticity is increased in steps of 0.2. In example d), three linear sub-pulses with an increasing orientation angle of 0°,+45°, and 90° are separated by circular sub-pulses.

So far, only sub-pulses in which the state of polarization is constant during the pulse duration have been presented. In figure 4.17, single pulses with a changing state of polarization are shown. These pulses are generated by superimposing two pulses of a different chirp or state of polarization in which the pulse distance is small compared to the pulse duration. Figure 4.17a) represents a short pulse with an increasing ellipticity while the orientation of the pulse stays constant. This pulse is constructed by two sub-pulses separated by 50 fs. One of the sub-pulses is linearly polarized at 0° while the other pulse is circularly polarized. In figure 4.17b), a longer pulse is shown. During the pulse duration of approximately 350 fs the ellipticity changes four times from circular to linear and back. It is also constructed by two differently polarized pulses. The first pulse is linearly polarized oriented at 0° and is followed by a linearly polarized pulse oriented

at 90° after a time delay of 200 fs. Both pulses are linearly chirped by $+1.5\times10^4$ fs$^2$. The counterpart of the changing ellipticity is the rotation of the oscillation plane of the electric field during the pulse. This is exemplified in figure 4.17c). The pulse is nearly linearly polarized while it rotates by more than 450°. It is constructed by two circularly polarized pulses of different helicity which are separated by 200 fs. Both pulses are linearly chirped by $+1.5\times10^4$ fs$^2$. The three dimensional shape of the pulse in the last example of figure 4.17d) appears to be non-physical. Yet, at a second glance it turns out to be a pulse with an oscillating state of polarization. The orientation of the polarization ellipse oscillates between $-60°$ and $+60°$ while the ellipticity changes in between 0.2 to 0.5. This results in a cross-shaped profile of the pulse. The pulse sequence which causes this behavior is composed of two linearly polarized pulses oriented at 0° and 90°. They are separated by 400 fs and chirped by $+1.5\times10^4$ fs$^2$.

### Chirped pulses

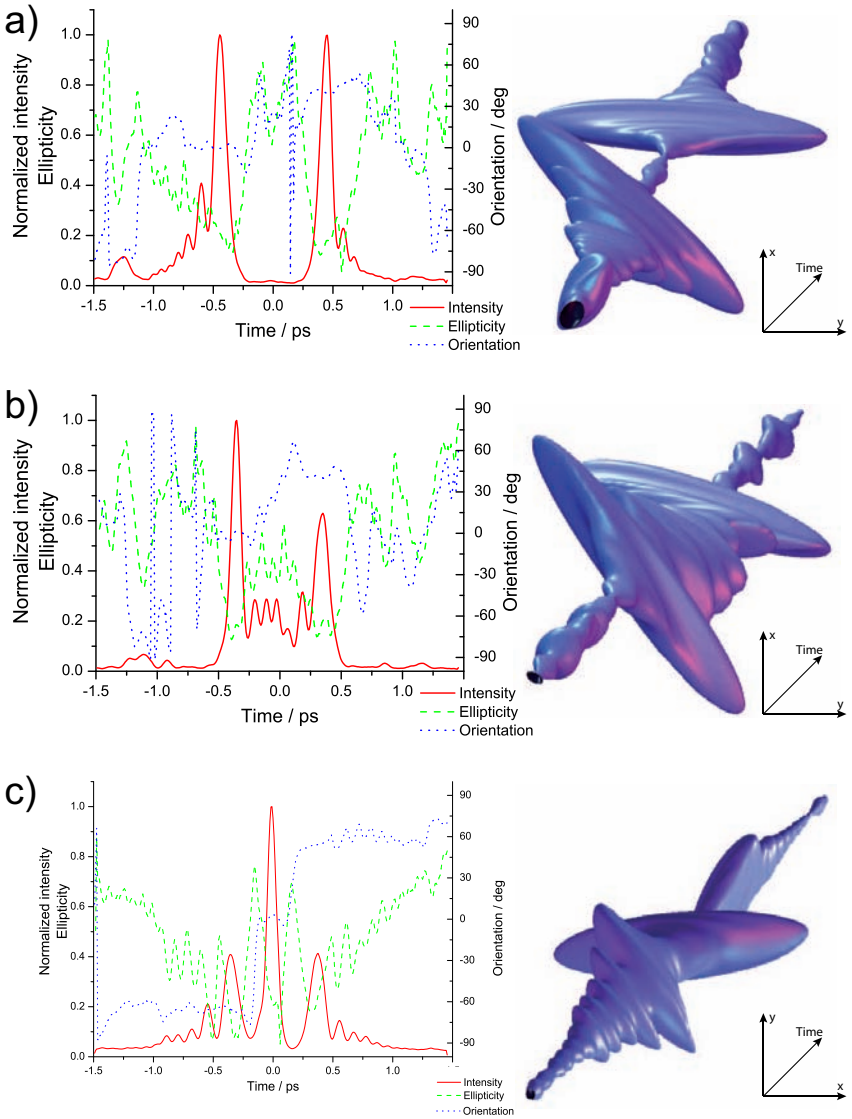


Figure 4.15: Pulse sequences with a third order chirp. In a), a double pulse sequence is depicted. The distance amounts to 800 fs. Energy is equally distributed to the linear sub-pulses. The first pulse is oriented at 0° and the second one at +45°. The first pulse is chirped by $-5\times10^5$ fs$^3$ and the second one by $+5\times10^5$ fs$^3$. The pulse sequence in b) is identical to the one in a) except for the signs of the quadratic chirp, which is reversed. Therefore, the tail of the sub-pulses points towards the other sub-pulse. In c), a pulse sequence of three pulses separated by 300 fs is presented. The linearly polarized sub-pulses are oriented at −60°, 0°, and +60°. The two outer pulses are quadratically chirped by $\pm1\times10^6$ fs$^3$ whereas the inner one is not chirped in order to remain short.

## Multi-pulse sequences

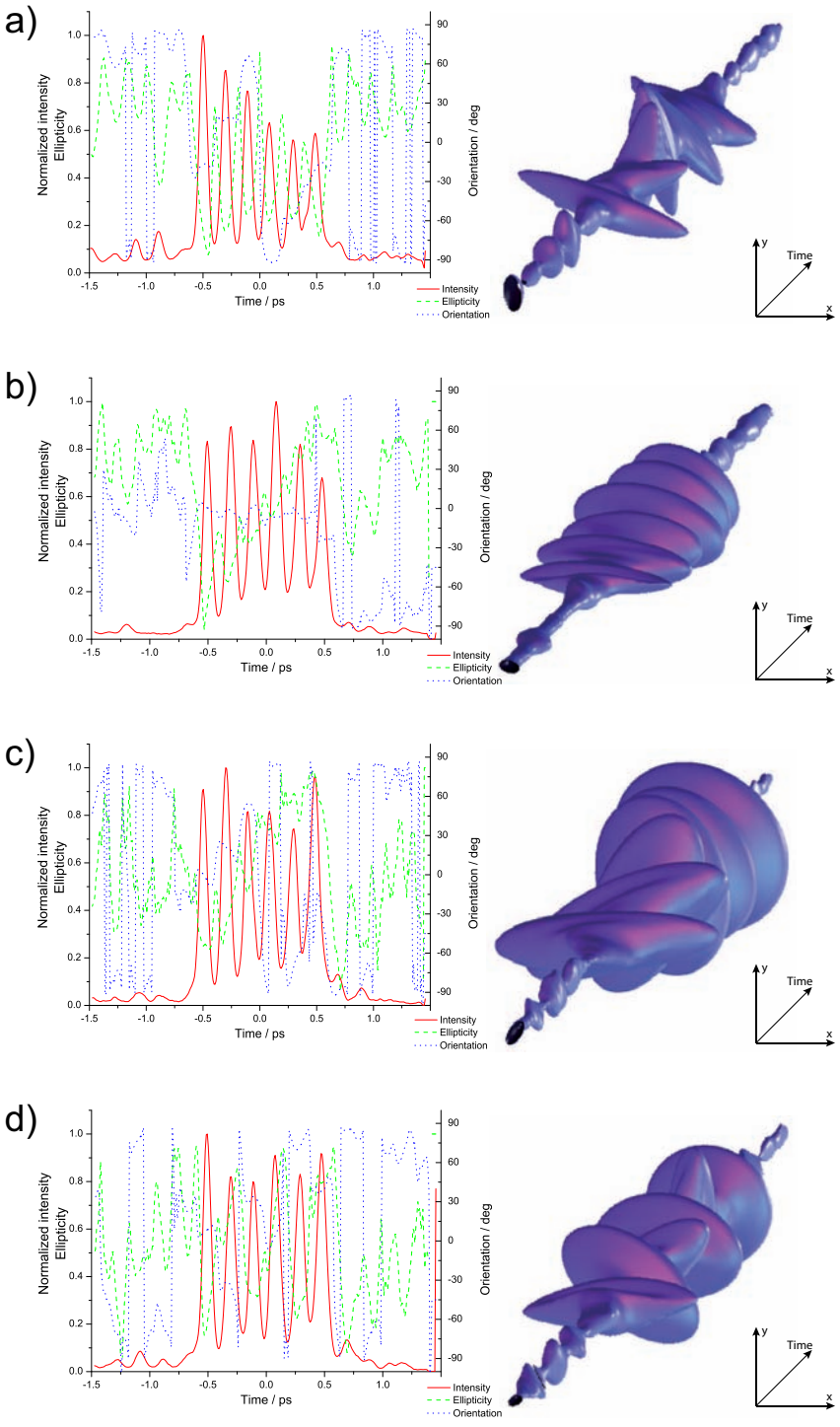


Figure 4.16: Complex pulse sequences consisting of six sub-pulses with different polarization states. In a), the orientation of the linearly polarized sub-pulses is systematically varied from $-30°$ to $+120°$ in steps of $30°$. In b), the ellipticity of the individual sub-pulses is increased from linear to circular in steps of 0.2. In c), the orientation and ellipticity changes from sub-pulse to sub-pulse. In d), an alternation of circular and linear sub-pulses with different orientations is shown.

### Single pulses with changing state of polarization

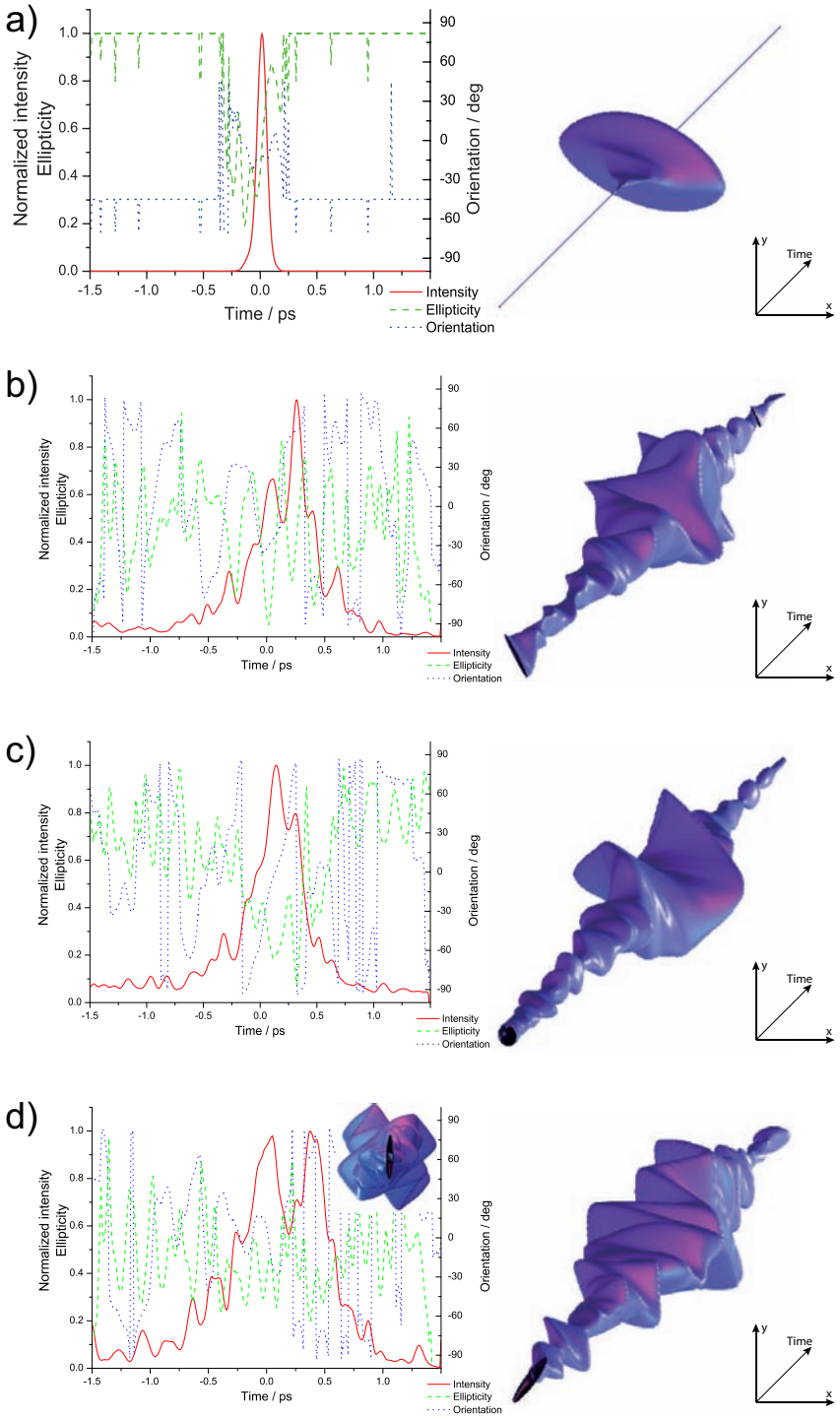


Figure 4.17: Polarization shaped single pulses. During the pulse the state of polarization changes. In a) and b), the ellipticity of the pulse changes. In c), the orientation of the polarization ellipse changes within the pulse. In d), the state of polarization – the ellipticity and the orientation – oscillates resulting in a cross-shaped pulse, which is depicted in the inset.

## 4.10 Discussion of capabilities

The complexity and the duration of the pulse sequence is limited by the bandwidth provided by the laser pulses, the resolution of the 4-f-line, and the number of pixels of the employed liquid crystal arrays. These factors also determine the rotation speed of an ellipse or the required time to change from linear to perpendicular linear polarization. The change of the helicity of a circular polarized pulse from left-handed to right-handed is another example. The limit of an instantaneous change of the polarization state or a drop-off in the intensity is given by Fourier transformation. Sharp features in the time domain require a continuum or at least a broad band of frequencies. Therefore, the bandwidth of the laser pulse determines the pulse length as well as the speed in the change of a pulse parameter. A detailed analysis on the speed of polarization changes is carried out in [123]. In figure 4.17, it can be seen that the time which is required for the change of ellipticity or orientation are in the range of the pulse duration of the unshaped pulse. Within these limits every desired pulse shape can be produced with this setup, since it provides the capability for unrestricted control of the electric field.

The appearance of side pulses due to a restriction of the polarization modulation as in the case of the serial setup is excluded [64, 104]. The appearance of side pulses, which can be observed in the measured double pulses shown in the previous sections, must have a different origin. The origin of the deviations of the measured pulse from the intended pulse shape are discussed in the next section.

### 4.10.1 Deviations and errors

An error analysis is based on the statistics on measured and set parameters of the series of single and double pulses. The errors are summarized in table 4.3. Comparing the deviations in single and double pulses reveals that the deviations of the pulse parameters increase when more complex pulses are generated.

| | **Error in detection** | **Error in single pulses** | **Error in double pulses** |
|---|---|---|---|
| **Energy** | ±0.04 | – | ±0.2 |
| **Distance** | ±4 fs | – | ±9 fs |
| **Pulse length** | ±1 fs | ±1 fs | ±3 fs |
| **Orientation** | ±2° | ±4° | ±5° |
| **Ellipticity** | ±0.03 | ±0.05 | ±0.08 |

Table 4.3: Errors in the parameters of phase, amplitude, and polarization shaped pulses. The errors which have their origin in the detection are presented in the first column. The deviations of the measured pulse parameters from the set values are listed for single and double pulses. In the determination of the ellipticity a systematic error of 0.1 has to be added due to the detection procedure.

Deviations of the pulse shape from the intended pulse shape result from imperfections of the setups for generation and measurement of the polarization shaped pulses. A high quality of the implemented optical elements is essential. They must be suitable for the

broadband frequencies of the used pulses. Although the used waveplates are of a zero order and achromatic they have minimal variation over the wavelengths, which are present in the pulse. In case of the half waveplates, which act as a rotator, the lower frequencies are rotated a bit further than the higher frequencies or vice versa. In case of the last modulator, it plays a crucial role for the polarization control. A double liquid crystal array modulator with the optical axis oriented at 0° and 90° is mimicked by a modulator with the orientation of the optical axes at ±45° placed in between two half waveplates oriented at +22.5°. A deviation in the retardances of the waveplates results in an effective orientation of greater or lesser than 0° and 90°. This results in unintentional changes of the state of polarization within the pulse. The frequency components which pass a sequence of the last arrays in which the relative orientation of the optical axes of the subsequent arrays is not effectively 45° results in a systematically different polarization of the generated pulses. A similar effect results from a poor alignment of the orientation of the optical axes of the waveplates and liquid crystal arrays as well as the orientation of the polarizer. An improper calibration of the liquid crystal arrays results in imprecise pulse parameters. When using very broadband laser pulses or even a super continuum, the pixels have to be calibrated separately to include the frequency dependence of the retardances [124]. In the presented work, this was not necessary since the error in calibration dominates. The accuracy of the modulator was determined to be better than 3%. The extinction ratio of the polarizer has to be high to enable to write sharp patterns on the spectral amplitude.

Further issues which have an impact on the shaped pulse are connected to the technique of spatial light modulators which utilize liquid crystal arrays. These effects originating from pixel quantization, gap-to-stripe ratio, and phase resolution are discussed in detail in section 3.2.4.

All the above mentioned errors have an impact on the accuracy of the produced pulse shapes. The errors induced by improper alignment, poor calibration, and additional noise on the retardances were simulated and examined. All this leads to a less precise control of the pulse parameters. The effect of the errors and the resulting deviations from the desired pulse form depend on the polarization states of the sub-pulses of the pulse sequence. The deviations which occur are in the order of the error which provoked them. All in all, they are in the range of a few percent, which also can be observed in the deviation of the retrieved parameters of the presented pulses. The errors of each parameter are determined by statistics on a number of single pulses and double pulses. A summary is presented in table 4.3.

A more crucial point is the pixel overlap in the succeeding arrays. A simulation of this error reveals that if every n-th pixel does not precisely modulate the same frequency band $\omega_n$, side pulses will occur. These side pulses can be observed in some of the pulses presented before. This is exemplary illustrated for a double pulse. The double pulse consists of two linearly polarized short pulses of equal energy separated by 800 fs. The first pulse is oriented at 0° and the second at +30°, which was already presented in figure 4.13b). The time-dependent intensity and polarization state is calculated for the ideal pulse shaper without errors and the case in which the first array is shifted in the Fourier plane by one pixel. In figure 4.18b), the simulated data is compared with the data of the experimental pulse. The side pulses including their polarization state are well reproduced by this simulation. In the experiment, this might be due to the use of three modulators – one of which being of a different type.

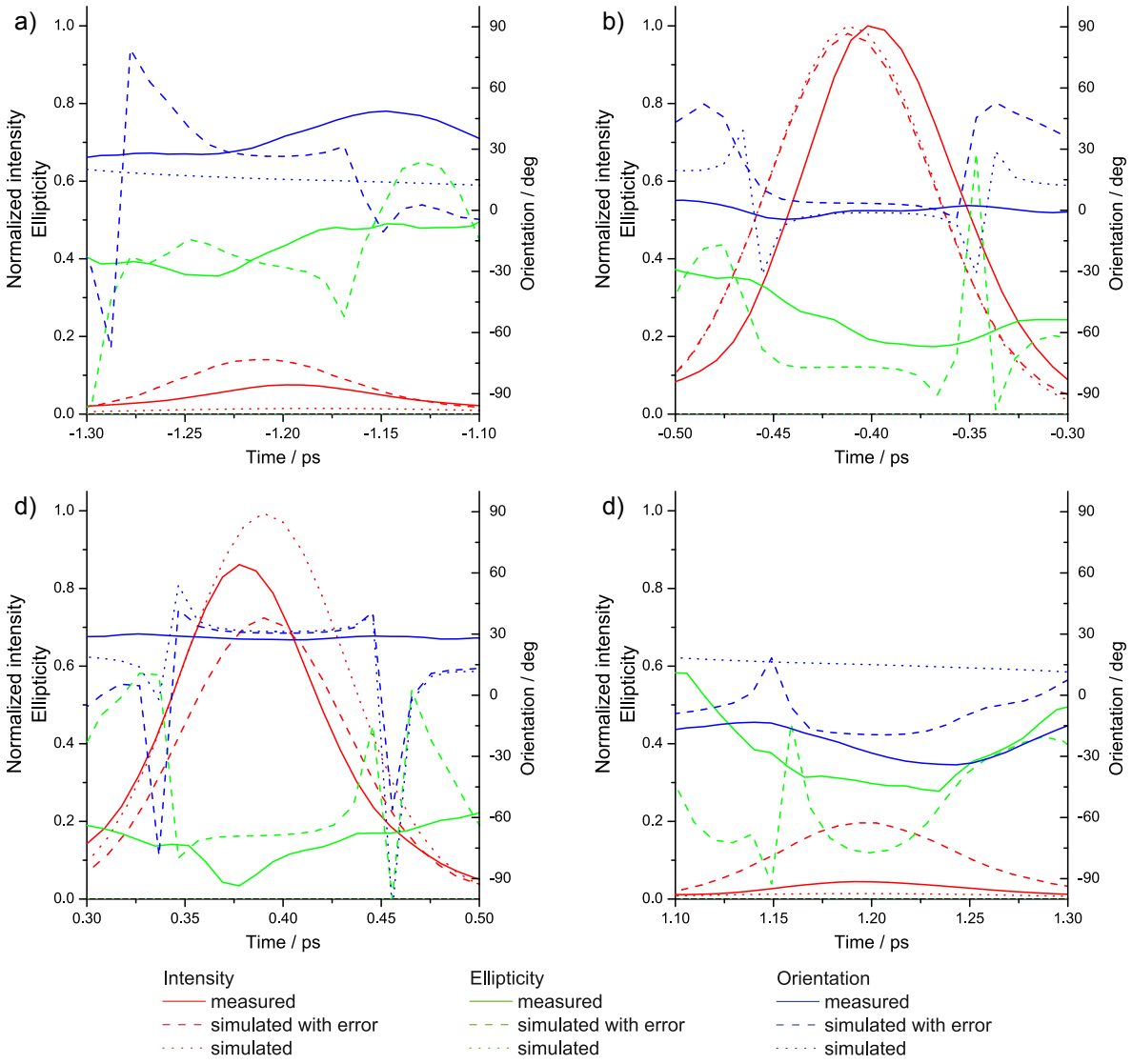


Figure 4.18: A theoretical investigation of the deviations in the pulse sequence induced by shifting the first double array by one pixel with respect to the others. The double pulse from figure 4.13c) serves as an example. The sub-pulses which are intended and the ones which are due to the error are investigated separately in figure a) to d). The intensity (red), ellipticity (green), and orientation (blue) over time are plotted for each sub-pulse. Each graph of the measured pulse (solid line) is compared to the simulated one with (dashed line) and without (dotted line) the error in pixel overlap taken into account. The graph resulting from the experiment is very similar to the one obtained by simulation in which a shift of one pixel on the first double array is applied.

Employing a device which consists of only four arrays of identical dimensions would certainly prevent this error and produce side pulse free pulse sequences. Further, the reduced number of optical elements will decrease the imprecision and yield a higher fidelity of the generated pulse shapes.

### 4.10.2 Issues in the detection of polarization-shaped pulses

As any measurement, the used detection and retrieval scheme for polarization shaped pulses, which is introduced in 3.3.1, is afflicted with errors. To estimate the error which can be attributed to the detection a double pulse sequence was measured ten times. Statistics on the error is presented in table 4.3 and gives an impression to which proportion the error is induced by the inaccuracy of the detection method.

A few remarks on typical concerns and errors shall be given here. The quality of the optical elements especially of the half waveplate is also important. Further, the optics used for guiding the shaped pulses to the detector have to be chosen carefully. Some of the dielectric mirrors, which are commonly used in laser optics, have a different reflectivity for vertical and horizontal polarization components. An alternative are metallic mirrors, which do not prefer a specific polarization state. However, there is the drawback of lower reflectivity and higher sensitivity to physical damage. Reflections always have an impact on the state of polarization. The helicity of the electric field vector is changed from left- to right-handed after reflection. In addition, each reflection mirrors the orientation of the electric field ellipses at the plane perpendicular to the plane of propagation. Therefore, the number of reflections and the relative orientation of the mirrors is important to consider.

The retrieval procedure is based on a fit of the ellipses in time. A larger number of data points increases the quality of this determination. A problem in the fitting procedure is that the fitted curve could partly imply a negative intensity, which is not physical. To correct this, an overall offset has to be applied. This could impact the polarization state and result in an increased ellipticity. The consequence is that the ellipticity of all pulses is overvalued. The ellipticity which were retrieved for linearly polarized single pulses are approximately r=0.1. This is in the same order of the linearity which is provided from the laser. In case of the RegA 9050, the contrast of the polarization is 500:1, which corresponds to an ellipticity of 0.05. In case of circularly polarized laser pulses, the ellipticity is always underestimated by the fitting procedure.

Further, the parameters are all convoluted with the reference pulse, which has a finite width and smoothes every sharp feature in the detected pulse. This should be exemplified for a pulse which changes its ellipticity from circular via linear to circular of a different helicity. The pulse is perfectly linear for one point in time. The detected state of polarization for a given position in time will be convoluted with the ellipticity next to this point which will be elliptical. This results in a detected pulse which is not linear in the particular point. This must be kept in mind especially for pulses with a variation of the polarization over time as shown in figure 4.17b).

A disadvantage of this procedure is that the helicity as well as temporal phases cannot be retrieved. In the thesis of S. M. Weber, a proposal is made to additionally use the spectrum in different directions [64]. With this set of curves – spectra and cross-correlations – the

pulse shape is retrieved using a multi-objective evolutionary algorithm. It has been proven to work for theoretical pulses, but up to now this method has not yet been experimentally implemented.

Other detection schemes are suggested for the detection of polarization shaped pulse rely on spectral interference (SI). An example is POLLIWOG, which stands for "POLarized Light Interference versus Wavelength of Only a Glint" [125]. It determines the absolute phase and the amplitude of a pulse in x and y direction. Therefore, the complete state of polarization can be reconstructed. This approach requires a well-characterized reference pulse and an interferometric setup.

## 4.11 Feedback loop optimization on second harmonic generation

The implementation of the novel shaper setup which utilizes three double liquid crystal modulators in a close feedback loop experiment is demonstrated in this section. The optimization of second harmonic generation (SHG) serves as a test for the functionality of the setup. The power of the frequency-doubled light serves as a fitness which has to be maximized. In this section, two types of optimizations are performed that differ in the encoding of the parameters. In the first example, the retardances of the individual pixels of each array are independently optimized. In the second example, the parametric encoding, which is presented in section 4.6.2, is used and the pulse parameters are optimized.

### 4.11.1 Second harmonic generation

Frequency doubling is a phenomenon of non-linear optics. In this process, two photons interact with a non-linear material and form a new photon of twice the energy. Some materials which are not symmetric in inversion have a non-linear dielectric susceptibility. For strong electric fields the polarization $\mathbf{P}$ of the medium cannot be restricted to the linear term and higher order terms have to be considered.

$$\mathbf{P} = \epsilon_0 \sum_n \chi^{(n)} \mathbf{E}^n \tag{4.53}$$

In case of the second harmonic generation, only the second order term $\chi^{(2)}$ is relevant. For an electric field $\mathbf{E}(t) = \mathbf{E}_0 sin(\omega t)$ and with the use of the trigonometric identity $sin^2(\omega t) = \frac{1}{2}(1 - cos(2\omega t))$ the polarization can be expressed as

$$\begin{aligned} |\mathbf{P}^{(2)}| &= \epsilon_0 \chi^{(2)} \mathbf{E}^2 \\ &= \epsilon_0 \chi^{(2)} \mathbf{E}_0^2 \sin^2(\omega t) \\ &= \frac{\epsilon_0 \chi^{(2)} \mathbf{E}_0^2}{2} - \frac{\epsilon_0 \chi^{(2)} \mathbf{E}_0^2}{2} \cos(2\omega t). \end{aligned} \tag{4.54}$$

The second order of the polarization can be separated in two terms. One term is static and the other oscillates with twice the frequency of the driving electric field. This oscillating polarization of the medium generates the radiation which is doubled in frequency. The

intensity of the frequency doubled light depends quadratically on the intensity of the incident light.

$$I_{2\omega} \propto I_{\omega}^{2} \tag{4.55}$$

A requirement for efficient second harmonic generation is the phase matching of the fundamental wave and the second harmonic wave. Generally they have a different phase velocity in any medium. Without phase matching second harmonic generation still occurs but the emission of the frequency doubled light is suppressed by interference and down-conversion. Therefore, often birefringent crystals like BBO ($\beta$-barium borate) are used for SHG. For type I second harmonic generation, two photons of the fundamental frequency polarized in the ordinary plane of the crystal form one photon of twice the frequency in the extraordinary plane. This plane has to be selected by the right polarization of the incident light. If the polarization of the light is not in the plane, only the projection to the plane is relevant for the process. Thus, second harmonic generation is very sensitive on the polarization of the incident light. The high sensitivity of second harmonic generation on the intensity, which is controlled by the pulse energy and pulse duration as well as the polarization, qualifies it for the demonstration of the capabilities of the setup in the feedback loop optimization.

### 4.11.2 Setup for optimization of SHG

In this experiment the pulses of the oscillator were used. The central wavelength was set to 780 nm and the spectral width to 23 nm. The 4-f-line with the gratings of 800 lines/mm and the lenses with a focal length of 250 mm were used. After the modulation in phase, amplitude, and polarization the pulses were focussed with a thick lens with a focal length of 100 mm on a BBO crystal. The remaining light of the fundamental frequency is spatially separated from the emerging beam by a high reflective dielectric mirror which is designed for the fundamental wavelength. The frequency doubled light was detected with a photo-multiplier tube (Hamamatsu R212). As an obstacle a half waveplate (HWP) was inserted before the BBO to distort the polarization state. The experimental setup is depicted in figure 4.19.

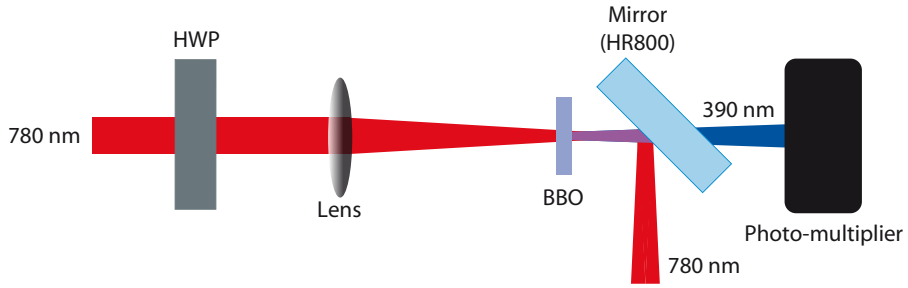


Figure 4.19: Setup for second harmonic generation. The polarization of the shaped pulse is modified by a half waveplate. Then the beam is focussed on a BBO. Before detection with a photo-multiplier the residual fundamental frequencies are reflected out of the beam.

### 4.11.3 Optimization of second harmonic generation

In the feedback loop optimization, the goal is to find the optimally shaped pulse which yields the largest intensity of the frequency-doubled light. For optimal SHG the algorithm has to set the right polarization state and to maximize the intensity in the BBO. To obtain the maximum intensity in the BBO the transmission has to be maximized. In addition, any chirps, originating from imperfect alignment of the 4-f-line and the use of thick lenses have to be compensated.

Two encodings are used for the optimization. The free optimization where the algorithm controls the retardances of the individual pixels of each array and the case where the pulse parameters of a single pulse are controlled.

In the free optimization the encoding of the retarcances of every 4×128 pixels ($\varphi_a^{\omega_n}, \varphi_b^{\omega_n}, \varphi_{Dcd}^{\omega_n}, \varphi_{Def}^{\omega_n}$) is varied in the range of $[-\pi, +\pi]$. This leads to a huge search space of 512 parameters. The learning curve of this optimization is depicted in figure 4.20a). The first generation starts with a fitness of 0.002 to 0.006. It takes about 800 generations to the convergence of the fitness, which corresponds to a run time of 16 hours. Finally, the fitness is improved by nearly four orders of magnitude to 1.7.

In the parametric optimization, the pulse parameters intensity, position in time, phase, linear chirp, and quadratic chirp, as well as the polarization state with the orientation, ellipticity and helicity have been optimized. All in all these are 8 parameters. The learning curve of the parametric optimization is shown in figure 4.20b). It starts in the first generation with fitness values ranging from 0.009 to 2.528. The fitness shows a steep increase of the fitness and converges after about ten generations to a maximum of about 5.2.

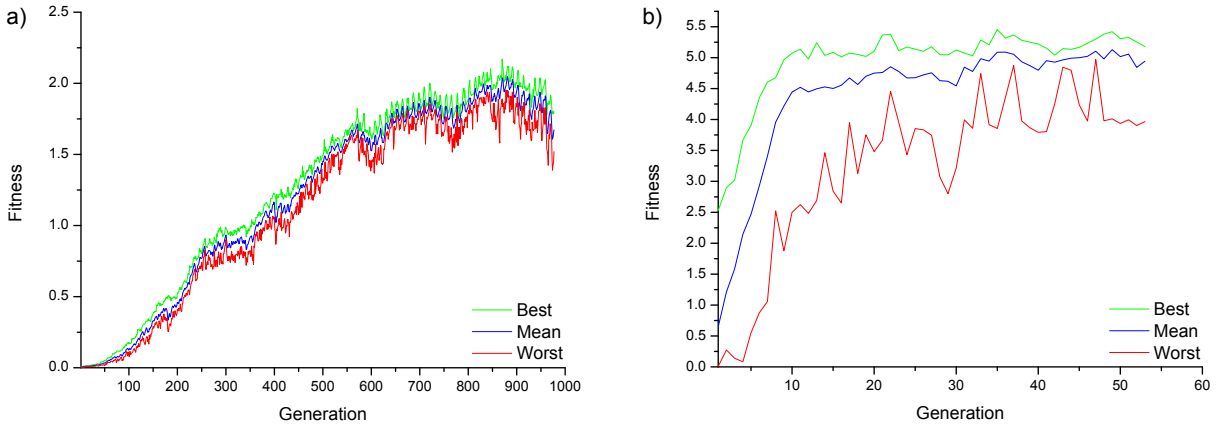


Figure 4.20: Learning curves of feedback loop optimizations of the second harmonic generation. Each graph depicts the best, the worst, and the average fitness of the generation. In a), the learning curve for a free optimization is shown. In b), the leaning curve of the parametric optimization is presented.

### Free versus parametric optimization

The comparison of the learning curves in figure 4.20 show that the parametric optimization converges much faster than the free optimization. This enormous difference is expected and is due to the difference in the size of the search space. The starting fitness of the parameterized pulse is already in the same order of magnitude as the final fitness. This is due to the fact that by the parameterization already a single pulse interacts with the BBO. In case of the free optimization, the random retardance pattern results in a very long irregular pulse with varying polarization states and very low peak intensity.

Moreover, the difference in the achieved fitness is suspicious. The fitness reached by the parametric optimization is larger than in the free optimization, although the final pulse of the parametric optimization is in principle accomplishable by the free optimization. This can be explained by the very complex structure of the search space. If the polarization modulation of the n$^{th}$-pixel (set by $\varphi_{Dcd}^{\omega_n}$ and $\varphi_{Def}^{\omega_n}$) is not suitable for second harmonic generation, the transmission and phase (controlled by $\varphi_{a}^{\omega_n}$ and $\varphi_{b}^{\omega_n}$) of set by this pixel is irrelevant and vice versa. The retardance pattern of the parametric optimization is – due to the encoding in pulse parameters – very smooth and only some steps are visible which result from the phase wrapping into the range from $-\pi$ to $+\pi$. Further, in the retardance pattern on array $a$ and $b$, which are presented in figure 4.21a), a parabolical shape indicates the negative linear chirp that compensates the chirp induced by the transversed glass. In contrast to this, the retardance pattern of the optimal pulse of the free optimization, which are depicted in figure 4.21a), are very structured. At the end of the optimization the fitness cannot be enhanced any further. The improvement which might be obtained by a little shift in the retardance is lost in the noise and cannot be observed any longer. Although there would be potential for many of this little optimization steps. This can be exemplified with the transmission pattern, which is depicted in figure 4.21b). It is beyond question that full transmission of all pixels would give the optimal result. But the experimentally obtained transmission pattern exhibits single pixels which permit a transmission clearly below one. The increase of the transmission of these pixels does not seem to be detected. Furthermore, the algorithm might get stuck in a local minimum from where it cannot escape due to a missing prospect of significantly larger fitness values. The patterns of the parametric optimization are very smooth because the pixels were controlled as a unit. This allows for generating a larger fitness possible.

The feedback loop optimizations on the second harmonic generation demonstrated the functionality of the developed pulse shaper. Due to the large and complex search space the brute force method of the free optimization is not well-suited. In contrast to that, the parametric optimization which employed a pulse parameter encoding was very successful. In terms of convergence speed and the reached fitness value it was superior compared to the free optimization.

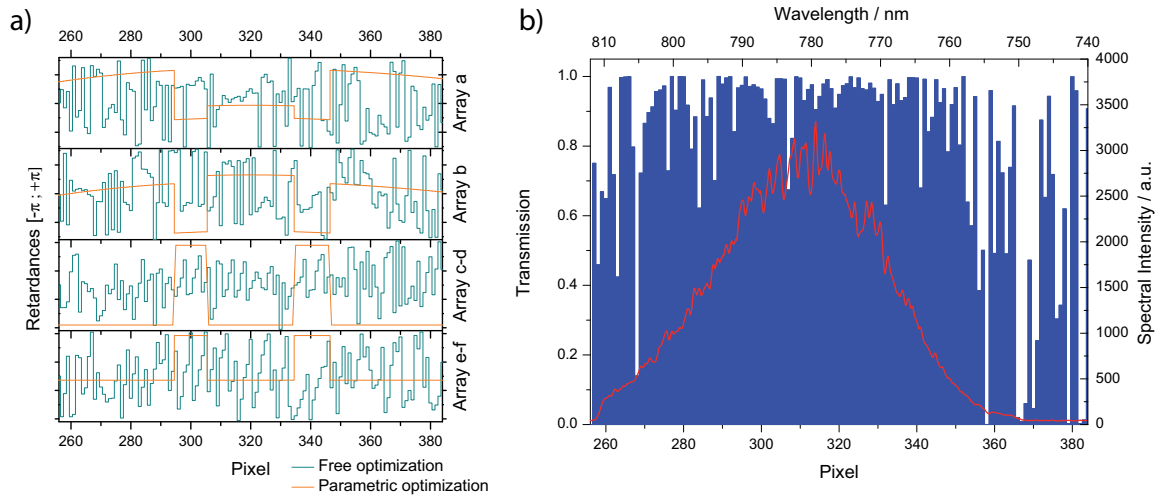


Figure 4.21: Resulting optimized retardance pattern on the liquid crystal arrays. In a), the retardances of the arrays are depicted. The retardances $\varphi_a^{\omega_n}$, $\varphi_b^{\omega_n}$, $\varphi_{Dcd}^{\omega_n}$ and $\varphi_{Def}^{\omega_n}$ determine the state of the spectral field according to 4.9 The green patterns represent the optimized pulse shape obtained by a free optimization. The orange patterns correspond to the parametric optimization. In b), the transmission pattern of the free optimization, which is calculated by equation 3.8, is presented. The spectrum of the unshaped pulse is additionally plotted to visualize which pixel controls which amount of spectral intensity.

## 4.12 Conclusion and outlook

In this chapter, a newly developed pulse shaper was introduced. The invented pulse shaper utilizes four subsequent liquid crystal arrays for pulse shaping and is therefore non-interferometric. This setup is capable of simultaneous phase, amplitude, and polarization shaping. It allows for the full and unrestricted control of the electric field. Since the ideal modulator consisting of four arrays was not available an alternative was developed using standard optical elements. The experimentally implemented modulator consisting of six arrays, two half waveplates, and a polarizer mimics the ideal modulator. The mathematical description of this setup was presented and the experimental feasibility was demonstrated. A procedure that determines the required retardances for any desired pulse shape was introduced.

Further, a parameterization scheme was developed. Using this parameterization a sequence of sub-pulses can be produced. The sub-pulse parameters energy, delay from zero, phase, chirps, and the state of polarization can be individually controlled. The functionality of this procedure was exemplified with a series of double pulses. In each series, one of the possible sub-pulse parameters was varied while the other parameters were kept constant. This systematic variation showed the independent control of the sub-pulse's parameters. A selection of complex pulse sequences was presented in order to exhibit the level of control and prove that the procedure can be extended to an arbitrary complex level.

The implementation of the setup in a feedback loop experiment on the second harmonic generation showed the capabilities for coherent control. The parametric encoding was

compared with the conventional free optimization. The use of the parametric sub-pulse encoding reduces the number of required generations and results in solutions which are easy to interpret.

Moreover limits and errors of this setup have been discussed. A theoretical analysis revealed that additionally appearing sub-pulses could be explained by an imprecise assignment of the subsequent pixels. These artifacts will not appear when using a modulator which is constructed of four identical arrays.

Such a commercially built modulator would easily provide the capabilities of unrestricted polarization shaping for scientists in various fields without the need for complicated setups. Recently, we got informed that CRi got some request for four-array modulators. Due to the discard in the production of a four array modulator this device might be too cost intensive at the moment. Therefore, they decided to offer a special two array modulator with the optical axes oriented at 45° and 0°. With this additional new modulator scientists would be able to fully control the electric field by placing this modulator behind the standard double liquid crystal modulator. This solution follows exactly the idea which is described in this chapter.

Polarization shaping will have an impact in various fields and many experiments will possibly benefit from the new level of control. At this point, a few examples should be discussed.

The use of the polarization of ultrashort laser pulses allows for controlling the population of degenerate states and the distribution of the angular momentum [3]. Polarization-shaped pulses could be used to distinguish between the specific conformers. The conversion of enantiomers [126] or the control of isomerization [46] would be a fantastic application. This is especially demanded in drug design were different structures have different properties.

In high-harmonic generation, the trajectory of the accelerated electron can be controlled with the use of polarization-shaped pulses. This allows for controlling efficiency of the harmonic generation. An ultrashort pulse with an ellipticity changing from circular to linear and back to circular is suggested to be ideal for a short burst of high harmonic frequencies [6]. Further, the pulses could be used for polarization gating, which offers an interesting alternative to the use of a carrier-envelope phase stabilized source [127]. The combination of polarization shaping techniques with nano structures allows for generating longitudinal components of the electric field vector in the near field. It has been shown that the resolution obtained by this near field is beyond the diffraction limit in the order of nanometers combined with femtosecond time resolution. This could be used in near field imaging techniques as well as for quantum information processing [4, 128].

Recently, shaped pulses were used for ultrafast computing. Quantum interferences in a diatomic molecule which were created by shaped femtosecond laser pulses are used to implement a classical Fourier transformation [129]. Here, polarization shaped pulses could be beneficial for extending this method to more complex molecules and to carry out a sequence of operations.

The electron dynamics driven by circular polarized laser pulses in porphyrin rings or even atoms result in a ring current. The theoretical considerations of this process predict a

resulting magnetic field of enormous strength [10, 130]. Shaping of the pulse which drives this process could probably switch these ring currents and the associated magnetic field.

# Chapter 5

# Guiding shaped pulses through optical fibers

The control of femtosecond laser pulses in phase, amplitude, and polarization was already introduced in chapter 4. These shaped pulses have numerous applications in various fields of research. Some of these applications might require transportation of the light by optical fibers, since the objects under investigation are not directly accessible. In this chapter, a method is presented for generating parametrically polarization shaped ultrafast pulses which are available after propagation through an optical fiber. This allows a flexible application of shaped pulses for example through endoscopes. Especially biophysics and medicine would benefit from *in vivo* employment. The generation of pulses which are parametrically shaped in phase, amplitude, and polarization after transmission through a fiber is demonstrated for two different types of optical fibers: a single-mode step-index fiber (section 5.5) and a microstructured hollow core photonic crystal fiber (section 5.6).

## 5.1 History of fiber optics

The guiding of light was first demonstrated by J.-D. Colladon in 1884 [131]. In his experiment, which is depicted in figure 5.1, he showed that light can be guided in a water jet. The underlying principle is the total internal reflection. Light-guiding techniques were developed in the late $18^{th}$ century on the basis of this effect. First, inelastic glass rods were used to guide light. The progress in glass processing promoted the production of flexible glass fibers. These first fibers were used for illumination of inner organs in medicine. A detailed overview about the early developments in fiber optics can be found in [132].

The application of fibers for communication started in the 1950s. The advantage of optical fibers compared to the coaxial cables used until then was the broader frequency range, which increased the transmission bandwidth. The attenuation over long propagation distances was the main problem. Fundamental considerations of C. K. Kau revealed the possible causes of losses. He suggested the use of fibers which consist of a core surrounded by a cladding of different refractive index. Silica glass of high purity is perfectly suited for this purpose. The size of the core of these fibers is ideally in the range of

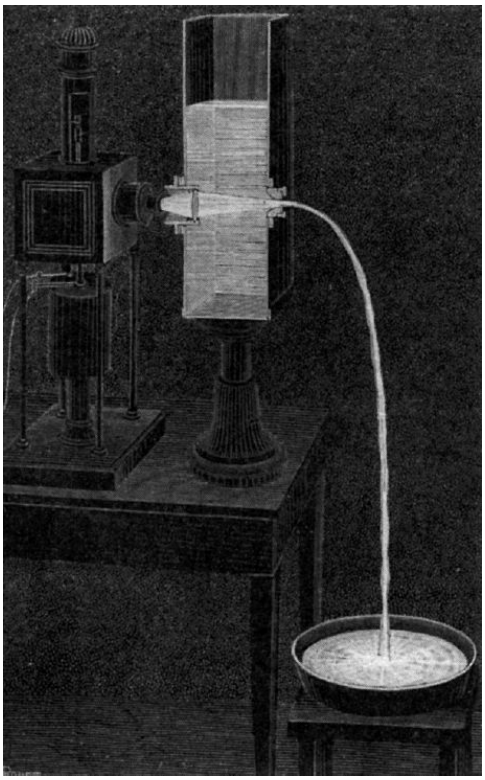

Figure 5.1: Colladon's fountain of light. The first demonstration of light-guiding by total internal reflection. Taken from [131].

the wavelength used. Further, single-mode operation is optimal for transmitting signals. For these contributions, he was awarded with the Nobel Prize in 2009. Today, modern communication – especially the internet – demands transmission of extremely huge data rates which is based on fiber optics.

As the demand for higher bit rates and larger distances increases, distortions in the propagation are the limiting factor in high-speed transmission. In the field of telecommunication research, pulse shapers are used to compensate for effects such as polarization mode dispersion (PMD) [101, 102].

The generation of ultrashort laser pulses after propagation through an optical fiber was achieved by compensating the group velocity dispersion by pre-chirping [133]. In this approach, the peak intensity of the pulses is limited by self-phase modulation (cf. section 5.3.6). The limit in pulse energy could be increased by inserting a glass rod after the fiber. With this trick, the pulse is still slightly chirped when it leaves the fiber and the final compression of the remaining chirp is achieved within the glass rod. In the glass rod, the beam diameter is larger and therefore the intensity is smaller [116].

In the 1990s a new class of optical fibers was invented: photonic crystal fibers (PCF) [134]. The light-guiding mechanism of the microstructured fibers is determined by the properties of an arrangement of very tiny and closely spaced air holes which go through the whole length of the fiber.

In some types of photonic crystal fibers, the microstructures form a hollow core. This special type of photonic crystal fibers are particularly suited for guiding ultrashort laser pulses with larger energy since the pulses propagate predominantly in air [135]. The appearance of self-phase modulation in the hollow core photonic crystal fiber was investigated with amplified pulses. Further, amplified pulses guided by the fiber were used for

two-photon microscopy [11]. For the investigation of group velocity dispersion and net group delay induced by the photonic crystal fiber [136] pulse shaping with fixed phase masks was used.

## 5.2 Optical fibers

The two different types of fibers which are used in this work are introduced in this section: the step-index fiber and the microstructured hollow core photonic crystal fiber. The guiding mechanisms, the characteristic properties, and the specifications of the respective fibers are presented. Further, the effects which occur when transmitting pulses through optical fibers are discussed.

### 5.2.1 Step-index fibers

The light-guiding in conventional fibers relies on total internal reflection which occurs at the boundary of two media with different refractive index $n_1$ and $n_2$. When a ray of light strikes this boundary, it is refracted. The refraction angle is determined by Snellius' law

$$n_1 sin(\theta_1) = n_2 sin(\theta_2). \tag{5.1}$$

When increasing the incident angle $\theta_1$ and assuming that $n_1 > n_2$ at one point, the refracted light propagates parallel to the boundary. This angle is called the critical angle $\theta_c$.

$$\theta_c = arcsin\left(\frac{n_2}{n_1}\right) \tag{5.2}$$

For incident angles larger than the critical angle, the light is completely reflected at the boundary of the two media. Total internal reflection can only occur on a boundary from large to low refractive index as in passing from glass to air. In a fiber, the transmission depends on the incident angle of the light respective to the fiber core and whether it is guided through the fiber or enters the cladding and is lost.

Optical fibers can have different refractive index profiles. Step-index fibers are the simplest and most widely used fibers. The refractive index is constant across the core and larger than in the cladding. The difference in the refractive index is achieved by doping the silica glass with elements such as titanium, germanium, or boron.

#### Single-mode fibers

Generally, a fiber supports many modes in which the light can be guided. The $V$-number is a parameter which determines the optical properties of step-index fibers.

$$V = \frac{2\pi}{\lambda} a \sqrt{n_{core}^2 - n_{cladding}^2} \tag{5.3}$$

This parameter is determined by the radius of the core $a$, the difference of the refractive index between core and cladding, and the vacuum wavelength of the considered light $\lambda$. It determines the number of modes which can propagate through the fiber. For $V$ being smaller than 2.405, the fiber supports only one mode per polarization direction [137].

**Specification of the step-index fiber**

The first fiber described in this work is a standard silica single-mode step-index fiber tagged as SM750 and produced by Fibercore Limited. It has a 0.10 to 0.14 numerical aperture, a 5.3 $\mu$m mode field diameter, and a 125 $\mu$m cladding diameter surrounded by a coating of 245 $\mu$m diameter. There is only a small birefringence in this single-mode fiber due to random waveguide imperfections, which can be characterized by polarization mode dispersion (cf. 5.3.4); a typical value is 0.05 ps/km or less. The beat length corresponding to this fiber is in the order of 100 m. The fiber patchcord is 115 cm long and has FC/PC connectors at both ends.

### 5.2.2 Microstructured photonic crystal fibers

A fundamentally different approach for guiding light employs two-dimensional photonic crystals. In photonic crystals, the light is trapped by a photonic band gap. The application of this technique for the construction of optical fibers was pioneered by P. Russel who realized the first photonic crystal fiber in 1996 [134, 138]. In photonic crystal fibers, this band gap is created by a periodically microstructured cladding. Such a band gap can confine the light in a core which has a lower refractive index than the surrounding cladding. If the mode of the core finds no states in the cladding to which it is phase-matched, light cannot leak out and the light is confined in the core. The core material determines the loss and the non-linearity of the fiber. The use of a hollow – air-filled – core surrounded by a structure of micro holes permits for guidance of a single-mode without restrictions imposed by the core material [139].

The fabrication of these fibers is done in a stack and draw procedure. Glass capillaries and glass rods of about 1 mm diameter are stacked into a preform. The structure of the preform already corresponds to the desired fiber structure. This preform is inserted into a glass tube and then drawn into the fiber. The manufacturing process is controlled by temperature, pressure, feeding velocity, and drawing velocity. The scaling in size of the preform to the fabricated fiber exceeds $10^4$. As all fibers, the fabricated photonic crystal fibers are coated with a polymer jacket for improving the mechanical strength. A micrograph of the cross-section of the hollow core photonic crystal fiber used in this work is depicted in figure 5.2b).

The properties of the fiber can be controlled by the design of the microstructure. The transmission band and the dispersion landscape can be varied over a wide range. Furthermore, the guidance through the air-filled core results in very low non-linearity which allows propagating ultra short laser pulses of high energy. This is the key point why this type of fiber is perfectly suited for the transmission of femtosecond laser pulses which makes it interesting for this work [135].

Today, photonic crystal fibers find their application in different areas including communication, high-power transmission, non-linear devices (super-continuum generation), and fiber sensors. Inside the hollow core of some fibers, small particles can be trapped and guided along a curved path [140]. A broad overview over these fibers and their range of application is given in [141].

### Specification of the hollow core photonic crystal fiber

The hollow core photonic crystal fiber used in this work is manufactured by Blaze Photonics which is the only company that produces these fibers on a commercial basis. The fiber is identified with HC-800-1. It is produced of undoped silica. The core of the fiber is formed by removing 7 hexagonal unit cells of the cladding. In this particular fiber, the core is slightly asymmetric and measures 9.5 $\mu$m and 9.2 $\mu$m for the long and short axis, respectively. The diameter of the holey region amounts to 40 $\mu$m which is embedded in a silica cladding of 135 $\mu$m diameter. More than 95% of the optical power is located in this air-filled core or the surrounding holes. A micrograph of the core is depicted in figure 5.2b). This geometry is optimized for a broad wavelength range of over 70 nm centered at 830 nm. The loss at this operation wavelength is specified to be smaller than 0.3 dB/m. The zero dispersion wavelength is situated around 810 nm. The dispersion curve and the transmission curve are depicted in figure 5.2a). The length of the fiber is 110 cm. To avoid damaging of the ends or contamination of the microstructure, the fiber is spliced to silica glass rods of 100 $\mu$m thickness at both ends. Furthermore, the ends of the fiber are terminated with standard FC/PC plugs for easy handling.

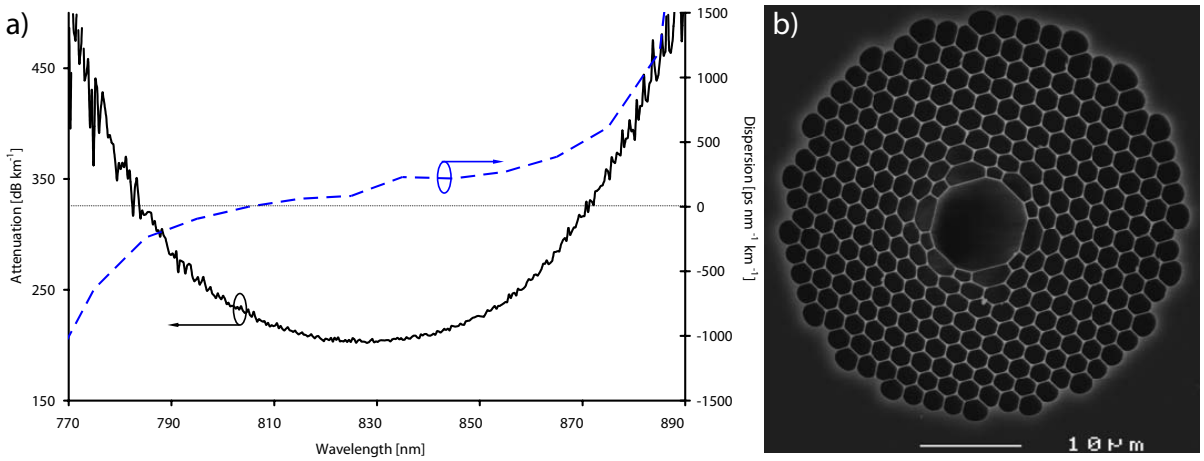


Figure 5.2: Properties of the hollow core photonic crystal fiber. In a), the transmission spectrum (black solid line) and the chromatic dispersion (blue dashed line) are depicted. In b), a micrograph of the cross-section of the core of the fiber is shown. Taken from [142].

## 5.3 Fiber characteristics

When light is guided through optical fibers, it is affected by its intrinsic properties. Thereby, the properties of the light are altered. In this section, the effects which need to be considered when propagating ultrashort laser pulses through optical fibers are discussed. A summary of all possible effects can be found, for example, in the standard book of G. P. Agrawal [137].

### 5.3.1 Chromatic dispersion

When light propagates through a dielectric, its electric field interacts with the bound electrons of the medium. In general, the response of the medium depends on the optical frequency. Therefore, the parameters of the medium, such as the refractive index, are frequency-dependent. This effect is called chromatic dispersion. It plays a critical role in pulse propagation, since pulses – in particular femtosecond laser pulses – have a broad frequency spectrum. After propagation through a dispersive medium, the lower and higher frequencies are shifted in time respective to each other. The dispersion is described by the Taylor terms which were discussed in section 2.4.2. After the fiber, the originally short pulse is stretched in time, which is known as chirp. In telecommunication, the dispersion induced by fibers is compensated by integrating dispersion compensating fibers [143] or fiber Bragg gratings [144]. For shorter pulses, the compensation achieved by pre-chirping the pulse by prism or grating compressors was shown [145, 146]. Another approach utilizes a pulse shaper to compensate for the chromatic dispersion by inducing a phase which is adapted to the specific fiber [116, 147].

### 5.3.2 Birefringence

Even in a single-mode fiber two degenerate modes which are linearly polarized in two orthogonal directions are supported. In a real fiber, this degeneracy is broken due to imperfections of the fiber. These could be induced by core asymmetries, impurities of the material, imprecision in the manufacturing process, or density fluctuations caused by mechanical stress. This results in different refractive indices for the two orthogonal components. The strength of the modal birefringence $B_m$ is defined for the length in which the refractive indices are constant.

$$B_m = |n_f - n_s| = \frac{|\beta_f - \beta_s|}{\mathbf{k}} \tag{5.4}$$

In this equation $n_{f/s}$ are the refractive indices and $\beta_{f/s}$ are the propagation constants of the two orthogonally polarized modes. For a given value of $B_m$, the overall polarization state in the fiber changes periodically. The periodicity of the polarization change is called beat length $L_B$. The variation of the state of polarization along the fiber is visualized in figure 5.3a). The beat length is determined by

$$L_B = \frac{2\pi}{|\beta_f - \beta_s|} = \frac{\lambda}{B_m}. \tag{5.5}$$

The axis along which the refractive index is lower is called fast axis – analogous to the nomenclature for waveplates. In real optical fibers, the modal birefringence $B_m$ is not constant over the length of the fiber and the modal birefringence changes when the fiber is stressed by bending, twisting, or by changes in temperature. This alters the polarization state of the light after the fiber [148].

Fibers can be classified by their modal birefringence. Fibers with a modal birefringence less than $10^{-6}$ are denoted as low birefringent fibers. Fibers with modal birefringence larger than $10^{-5}$ are named high birefringent fibers. The modal birefringence of standard

single-mode fibers is situated in between. A special type of fiber is the polarization maintaining fiber. In this fiber, the birefringence is drastically increased by inducing core asymmetries. This can be achieved by mechanical stress in the production process. Another way is to implement rods of different material close to the core in the preform which breaks the symmetry of the fiber. Such fibers are often named according to the shape of the cross-section, for example panda- or bow-tie-fibers. In these fibers, the random birefringence induced by imperfections or mechanical stress due to bending is insignificant compared to the inherent birefringence. Therefore, the linear polarization of the light which is oriented parallel to the optical axis of the fiber is maintained.

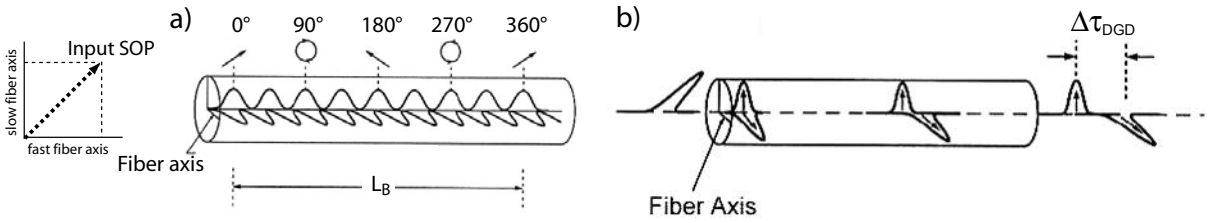


Figure 5.3: a) The difference in the refractive index results in a phase shift between the components along the two axes which changes the state of polarization along the fiber. The distance in which the phase shift accumulates to $2\pi$ is called beat length $L_B$. In b), the temporal splitting of a pulse with components of the electric field along both axes of the fiber due to difference group delay is depicted. Taken from [149].

### 5.3.3 Principal axes of the fiber

The fiber can be approximated as a sequence of waveplates with step-wise constant birefringence and orientation. According to Jones' theorems, this series of waveplates can be substituted by one single waveplate and a rotator (cf. section 2.3). Light which enters the fiber linearly polarized along one of the two axes of the waveplate, which characterizes the whole fiber, remains linearly polarized. The two components of the electric field are orthogonal respective to each other whereas the overall orientation can be altered. The corresponding axes are denoted as principal axes of the fiber. The phase between the two components is in general also shifted.

### 5.3.4 Polarization mode dispersion

In case of laser pulses with a broad frequency spectrum, the situation gets more complex. When the pulse is coupled into both polarization modes of the fiber, the two components experience different frequency-dependent refractive indices ($n_{f/s}(\omega)$) which lead to different group velocity dispersions and chirps. The pulse becomes temporally broader at the end of the fiber. This effect is known as polarization mode dispersion (PMD). In fibers with a symmetric core, this effect is averaged out because of its random origin. For fibers with a core asymmetry, the polarization mode dispersion causes a temporal splitting of the pulses that travel along the two axes which is known as difference group delay (DGD). This effect is illustrated in figure 5.3b). The time delay between the pulses

which propagate on the two different axis in a fiber of the length $l$ can be calculated by

$$\Delta\tau_{DGD} = \frac{d}{d\omega}(\beta_f - \beta_s). \tag{5.6}$$

This is valid for the hollow core photonic crystal fiber which is used in this work. Moreover, the asymmetry results in different zero dispersion wavelengths for the respective axis. For the frequencies which are situated in between the two zero dispersion wavelengths, this results in anomalous dispersion for one axis and normal dispersion for the other axis.

### 5.3.5 Non-linear effects in optical fibers

In any medium, non-linear effects occur for high intensities of the electric field. These effects are particularly relevant when ultrashort pulses with high peak intensities propagate through optical fibers where the entire intensity is confined in their small core. The bound electrons of the dielectric medium interact with the electromagnetic field. For large intensities, the response to the applied electric field becomes non-linear due to the anharmonic motion of the electrons. The polarization of the medium is no longer proportional to the electric field and higher-order terms have to be considered.

$$\mathbf{P} = \epsilon_0 \sum_n \chi^{(n)} \mathbf{E}^n \tag{5.7}$$

This equation has already been discussed in the context of second harmonic generation (cf. 4.11.1). In optical fibers, second harmonic generation or the sum-frequency generation does not occur since $SiO_2$ is a symmetric molecule and $\chi^{(2)}$ vanishes for silica glass. This type of second-order non-linear effect can be only caused by electric quadrupole fields, by fiber defects, or impurities and can therefore be regarded to be very weak. The lowest order of observed non-linear effects originates from the third order susceptibility $\chi^{(3)}$. The generation of new frequencies by third-harmonic generation or four-wave mixing is very inefficient due to the lack of phase-matching and is considered to be very weak. Another process which is determined by $\chi^{(3)}$ is the non-linear optical refraction. For larger intensities, the refractive index depends on the intensity of the electric field

$$\tilde{n}(\omega, |E|^2) = n(\omega) + n_2|E|^2 \tag{5.8}$$

in which $n_2$ is the non-linear refractive index coefficient which is related to $\chi^{(3)}$.

This non-linear refractive index leads to a number of effects. In optical fibers, the dominant effect is self-phase modulation (SPM) which is discussed in detail in section 5.3.6. Other effects occuring in fiber optics are cross-phase modulation (XPM), stimulated Raman scattering (SRS) and stimulated Brillouin scattering (SBS). These effects are discussed in detail in [137].

### 5.3.6 Self-phase modulation

To discuss the effect of intensity-dependent refractive index a pulse with Gaussian envelope is considered. Its time-dependent intensity is written as

$$I(t) = I_0 e^{-\frac{t^2}{\tau^2}} \tag{5.9}$$

in which $I_0$ is the peak intensity and $\tau$ the pulse length. The refractive index in equation 5.8 can be written as a function of the intensity of the electric field.

$$\tilde{n}(I) = n_0 + n_2 \cdot I \tag{5.10}$$

In case of a Gaussian laser pulse, the intensity rises and falls as the pulse passes. This results in a time-dependent refractive index.

$$\frac{d}{dt} n\left(I(t)\right) = n_2 \frac{d}{dt} I(t) = -n_2 I_0 \frac{2t}{\tau^2} e^{-\frac{t^2}{\tau^2}} \tag{5.11}$$

This variation creates a phase shift in the instantaneous phase of the pulse which is denoted as self-phase modulation [76, 137].

$$\phi(t) = \omega_0 t - \frac{2\pi}{\lambda_0} n\left(I(t)\right) l \tag{5.12}$$

Here, $l$ is the distance the pulse has propagated, $\omega_0$ and $\lambda_0$ are the carrier frequency and the vacuum wavelength. This phase shift results in a variation of the instantaneous frequency

$$\omega(t) = \frac{d}{dt}\phi(t) = \omega_0 - \frac{2\pi l}{\lambda_0} \frac{d}{dt} n\left(I(t)\right) = \omega_0 + \frac{4\pi l n_2 I_0}{\lambda_0 \tau^2}\ t\ e^{-\frac{t^2}{\tau^2}}. \tag{5.13}$$

The frequency components in the leading part of the pulse are detuned to lower frequencies and in the trailing part to higher frequencies. In short pulses, this effect generates new frequencies in the pulse and broadens its spectrum. This can be utilized in the generation of a supercontinuum in fibers [150]. For pulses which are strongly negatively chirped, the spectral width is narrowed [151].

## 5.4 Experimental setup

The guiding of femtosecond laser pulses through optical fibers is investigated using a setup which consists of three main parts: a source of phase, amplitude, and polarization shaped pulses, optical fiber, and devices for characterization of the transmitted pulses. The setup is presented in figure 5.4.

If not stated differently, the laser pulses are delivered by the oscillator (Mira). In case of the hollow core photonic crystal fiber, the regenerative amplifier (RegA) is used for testing the energy limits. A fraction of 10% of the laser pulses is separated before the shaper by a beam splitter and serves as a reference beam for the detection in a cross-correlation setup. The major part is shaped in phase, amplitude, and polarization using two or three liquid crystal modulators which are situated in the Fourier plane of a zero dispersion compressor. The setup which utilizes three liquid crystal modulators and the construction of parametrically shaped pulses is described in detail in chapter 4. For a number of the experiments, only pulses with a fixed orientation of the principal axis of the electric field are required. For the generation of these pulses, two double liquid crystal array modulators are sufficient. This setup is described in section 3.2.3 and uses the SLM-256 and one SLM-640 separated by a polarizer for modulation of the pulses. The major and minor axes of the electric field ellipse produced by this pulse shaper are fixed in

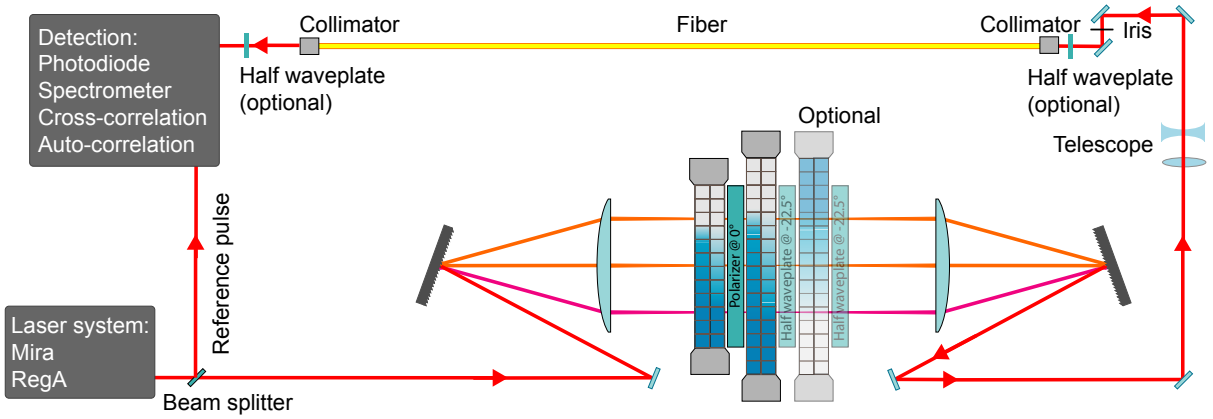


Figure 5.4: Experimental setup for the generation of phase, amplitude, and polarization shaped pulses after propagation through a fiber. The laser pulses are shaped in a 4-f-line using liquid crystal modulators. Either two or three double liquid crystal modulators are used for modulation. Then, they are launched into the fiber by collimation optics. Finally, the pulses are characterized by different detectors.

horizontal and vertical direction. These axes of the electric field ellipse can be aligned to the principal axes of the fiber using a half waveplate. The intensity of the laser pulses is controlled by attenuation. The coarse adjustment is performed by using neutral grey filters and the fine-tuning by using the shaper. The polarization shaped laser pulses are guided by silver mirrors or dielectric mirrors, which have the same reflectivity for both components of the electric field.

Before the laser pulses are launched into the fiber, they pass a telescope to optimize the divergence of the beam for the collimator. With an iris before the fiber the beam profile can be improved. This increases the amount of light coupled into the fiber. The collimator consists of a lens system which focuses the light in the core of the fiber. The collimator is a standard collimator from Newport with the type specification F-C5-F3-780. It is optimized for wavelengths around 780 nm and is compatible with the FC/PC plugs of the fibers. The collimator of the fiber is held by a mirror mount for adjusting the coupling of the laser pulses into the fiber. For precise alignment, the last mirror before the fiber is placed very close to the collimator.

The other end of the fiber is equipped with the same collimator. Further, the end is fixed in a rotating mount to allow for inducing a torsion independent of the position of the fiber. If not stated differently, the fiber is straight and fixed in space by an acrylic glass tube.

The pulses which are transmitted through the fiber are characterized by a spectrometer and a photodiode which are placed behind a rotatable polarizer. The pulse duration of a single pulses is determined by auto-correlation measurements. The time evolution of more complex pulses is recorded by a cross-correlation measurement in a time-resolved ellipsometry scheme. The devices and methods for pulse characterization are described in section 3.3.

## 5.5 Femtosecond laser pulses guided by a step-index fiber

The measurements using the step-index fiber were performed with pulses from the oscillator. These pulses have a spectral width of 23 nm at a central wavelength of 780 nm. The power of the laser before the fiber amounts to 80 mW. After transmission through the fiber, a maximal intensity of 36 mW was measured. This corresponds to a pulse energy of 4.7 nJ. The efficiency of the coupling into the fiber amounts to approximately 45%. This value is relatively small because after shaping the beam profile deviates from a perfect symmetric Gaussian (cf. 3.2.4).

### 5.5.1 Characterization of the step-index fiber

Since the light is guided through the silica core of the fiber, dispersion and non-linear effects are induced. The impact and the magnitude of these effects on the femtosecond laser pulses have to be specified to allow for determined control of the pulse parameters after the fiber. The dispersion which is induced by the fiber has to be compensated to achieve a short pulse after the fiber. Furthermore, the limits of the suitable pulse energy needs to be investigated to ensure operation in the linear regime.

#### Dispersion compensation and intensity limits

Both parameters, the pre-chirp and the pulse energy regulate the occurrence of non-linear effects. Self-phase modulation is determined by the peak intensity of the pulse. When a short pulse enters the fiber, self-phase modulation occurs in the first part of the fiber which results in a broadening of the pulse spectrum. At the end of the fiber the pulse is strongly chirped due to self-phase modulation and the inherent dispersion in silica. When the pulse is temporally stretched by a negative pre-chirp, the peak intensity at the beginning of the fiber is reduced. Due to the dispersion of the fiber, the pulse is compressed during the propagation and the chirp is compensated. At the end of the fiber, the pulse is short and non-linear effects occur only in the last part of the fiber. But, the negative chirp at the beginning of the fiber results in spectral narrowing due to self-phase modulation. Therefore, the pulse duration finally obtained is limited by the reduced spectral width. These two effects of spectral broadening and spectral narrowing are illustrated in figure 5.5. In this example, the unattenuated beam was launched into the fiber. The pulse energy in the fiber amounts to approximately 0.4 nJ. The spectral width before the fiber amounts to 23 nm. After propagation through the fiber the spectral width is changed. In case of a short un-chirped pulse, the spectral width is increased to approximately 40 nm. In case of a negative pre-chirp of $-48\ 000\ \mathrm{fs}^2$, the spectral width is decreased to 6 nm.

In the following, the effect on the spectrum of the pulse which has been transmitted through the fiber is systematically investigated in experiment and simulation. The spectral width is measured depending on the chirp of the pulse which is varied from

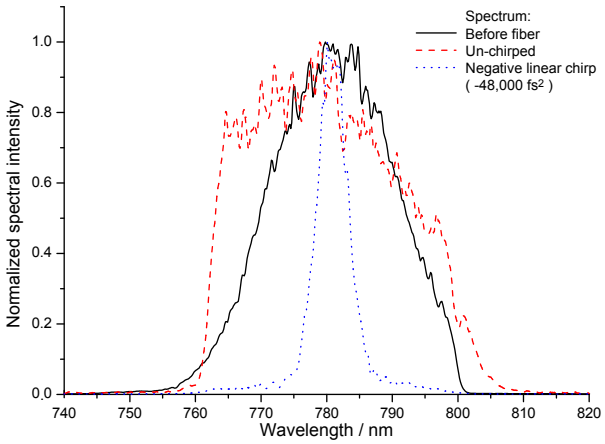


Figure 5.5: The effect of spectral narrowing and spectral broadening by self-phase modulation is illustrated. It depends on the pre-chirp of the pulse which is transmitted through the step-index fiber. A solid black line depicts the spectrum of the pulse before the fiber. A red dashed line shows the spectrum of an un-chirped short pulse after transmission through the fiber. The spectrum of a pulse with a negative pre-chirped of $-48\ 000\ \mathrm{fs}^2$ after transmission through the fiber is represented by a dotted blue line.

$-100\ 000\ \mathrm{fs}^2$ to $+100\ 000\ \mathrm{fs}^2$ using the pulse shaper. This is done for different intensities. Neutral grey filters of 50%, 25%, 10%, 5%, and 2% attenuation are used for reducing the intensity of the pulses. The results are depicted in figure 5.6a).

This effect is simulated with the help of the Lab2 packet which is a virtual femtosecond laser lab in the LabView environment [152, 153]. The simulation is carried out for the same parameters as in the experiment. The resulting curves are presented in figure 5.6. The shape of the curves obtained by simulation is very similar to the experimentally obtained curves. There are only little deviations in the position of the maxima and minima as well as in the spectral width in these points.

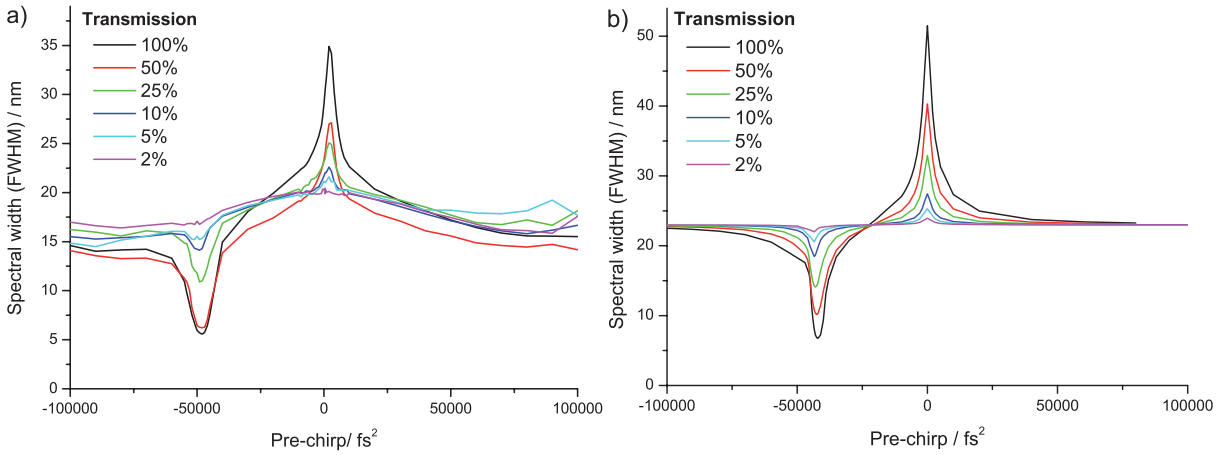


Figure 5.6: The effect of self-phase modulation on the spectrum of the pulse which is transmitted through the fiber. The spectral width is investigated depending on the chirp of the pulse before the fiber and its intensity. The experimentally obtained curves are depicted in a). The corresponding simulations are depicted in b).

The curves – obtained by experiment and simulation – reveal the effect on the spectrum induced by self-phase modulation. For this specific fiber, the spectral width is broadened if the pulse which enters the fiber is not chirped. In case of a negative pre-chirp of about $-48\ 000\ \mathrm{fs}^2$ ($-42\ 000\ \mathrm{fs}^2$ in the simulation), the spectral width is drastically reduced. The effect of self-phase modulation strongly depends on the peak intensity of the pulse.

The alteration of the spectral width is reduced for lower intensities. For pulses having only 2% of the maximal power used, the effect nearly disappears.

A short pulse is dispersed by propagation through the fiber. In case of the fiber used in the experiments, the pulse is stretched from an initial pulse length of 60 fs to over 3.5 ps. In order to obtain a short pulse after propagation through the fiber, the dispersion which is induced by the fiber needs to be compensated. The pulse length of the transmitted pulse is determined by auto-correlation measurements. The auto-correlation time of the transmitted pulses is measured for different pre-chirps. The negative pre-chirps are changed by the shaper up to $-100\ 000\ \mathrm{fs}^2$ while the corresponding auto-correlation time is determined. Similar to the investigation of the spectral width, this is performed for different intensities. Due to the poor sensitivity of the auto-correlator, this measurement was only possible with intensities down to 25%. The data is depicted in figure 5.7a). The auto-correlation time of the pulse is shorter when the magnitude of the negative chirp is increased. At a linear chirp of $-53\ 000\ \mathrm{fs}^2$ the curve of the measured auto-correlation time has its minimum. For larger chirps beyond this point, the auto-correlation time increases again. The simulation of the pulse duration depending on the linear chirp of the input pulse generates very similar curves which are depicted in figure 5.7b).

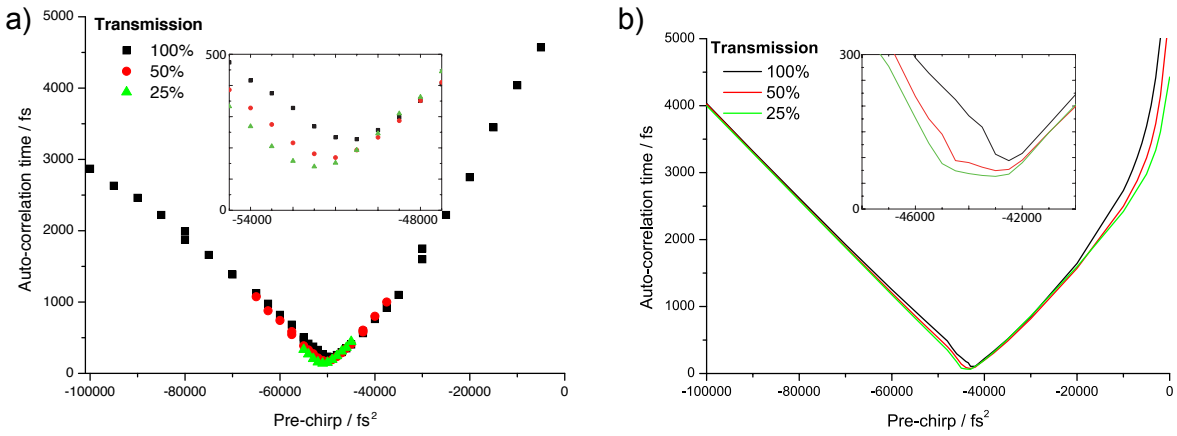


Figure 5.7: a) Auto-correlation measurements of the pulse which is transmitted through the fiber. The magnitude of the linear pre-chirp is varied and determines the pulse length. In b), the auto-correlation time is simulated. In both graphs, the inset shows the detail of the minima.

The graphs obtained by experiment and simulation reveal that shorter pulse durations are possible for reduced intensities. This is due to non-linear effects. Further, the reduction of the intensity shifts the minimum of the curve towards larger amounts of linear pre-chirp. In order to reduce the non-linear effects, the intensity is set to 2% in the following experiments using the step-index fiber.

The auto-correlation time is a measure for the length of the pulse. However, it does not provide sufficient information about the shape of the pulse. Therefore, higher order chirps which result in a temporal asymmetry are investigated by cross-correlation measurements. The pulse length was minimized by variation of the linear and second order chirp starting from the value which was determined in the auto-correlation measurement. The optimal values were found to be $-53\ 000\ \mathrm{fs}^2$ for the linear chirp and $-110\ 000\ \mathrm{fs}^3$ for the second order chirp. The phase function consisting of these values for linear and quadratic chirp

compensates the dispersion of the fiber. Using this compensation, the duration of the pulse after propagation through the fiber amounts to 67 fs. In the following experiments with the step-index fiber, these parameters serve as an offset pre-chirp.

Including the quadratic chirp into the compensation corrects for small asymmetries in the time evolution of the pulse. The cross-correlation traces, shown in figure 5.8, illustrate the effect of the chirp compensation. In a), the cross-correlation trace of the compensated pulse is compared to the trace of an uncompensated pulse. The effect of adding the quadratic chirp to the compensation is demonstrated in b). When only a linear chirp is applied, the cross-correlation trace has a little shoulder on the leading part of the pulse. This asymmetry vanishes when the quadratic phase is added to the compensation.

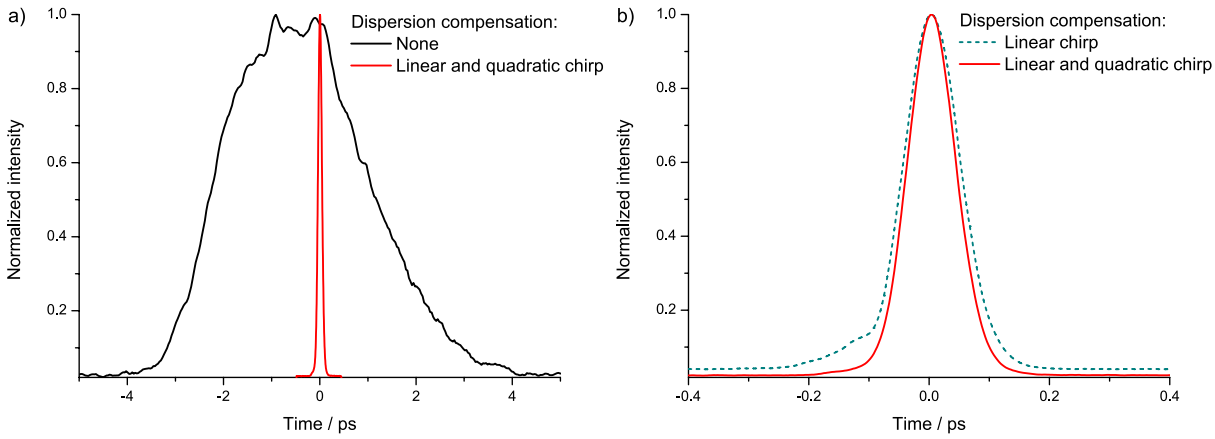


Figure 5.8: Cross-correlation trace of the pulse after propagation through the step-index fiber. In a), the trace of an uncompensated pulse (black line) is compared to the one with the optimal compensation factors of $b_2$=−53 000 fs$^2$ and $b_3$=−110 000 fs$^3$ (red line) for the linear and quadratic chirp respectively. The pulse duration for the uncompensated pulse amounts to 3.5 ps. The compensation of linear and quadratic chirp compresses the transmitted pulse to 67 fs. In b), the effect of adding the third order chirp to the compensation is illustrated. The cross-correlation trace of a pulse compensated with linear and quadratic chirp (red line) is compared to one that is compensated only with a linear chirp (dashed green line).

### Principal axes and birefringence

After the evaluation of the appropriate energy range and the determination of the optimal chirp compensation, the impact of the propagation through the fiber on the state of polarization is investigated. The change in the polarization is analyzed by comparing the polarization state of the input and output pulse.

Within this analysis the pulses are reduced in intensity and are pre-chirped by the compensation values which were found in the previous experiments. The polarization of the incoming pulses is linear whereby the orientation can be changed by a half waveplate. The state of polarization after propagation through the fiber is determined via an intensity measurement. The intensity of the pulse is measured in different directions after an analyzing polarizer. The orientation of the analyzing polarizer is varied covering the

range of 180° in steps of 10°. This procedure is carried out for a series of different orientations of the incoming linearly polarized pulse. The measured intensities depending on the orientation of the polarizer are depicted in figure 5.9a). The curves exhibit a sinusoidal modulation with fixed position of zero crossing. The modulation amplitude varies for different orientations of the linear polarization of the incoming pulse.

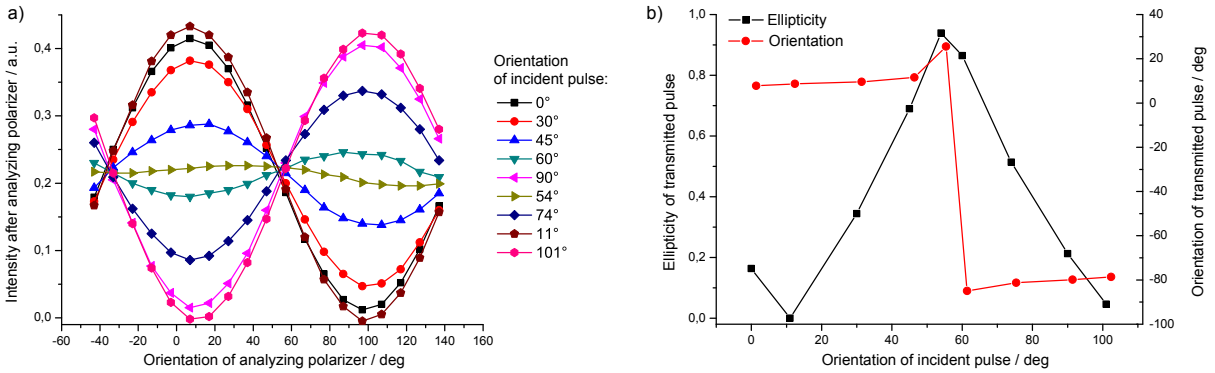


Figure 5.9: Analysis of the birefringence of the step-index fiber. The intensity in different directions is measured with an analyzing polarizer and a photodiode. The intensity traces in different directions are measured for different linear polarizations of the incident pulse which is shown in a). Using this data the polarization state of the transmitted pulse is determined depending on the orientation of polarization of the incident pulse: b).

On the basis of this data, the state of polarization of the pulse after transmission through the fiber is determined. This is achieved by a fit using the function 2.42 derived in section 2.2.4. The polarization parameters of the pulse which is transmitted through the fiber are presented in figure 5.9b). The graph shows the ellipticity $r$ and orientation $\gamma$ of the transmitted pulse depending of the orientation of the incident pulse. For two orientations of the incoming linear polarization, the polarization of the transmitted pulse is also linear. This is the case for pulses which enter the fiber linearly polarized with an orientation of 11° and 101°. These angles indicate the principal axes of the fiber. As expected, the principal axes are perpendicular respective to each other.

The difference in the phase retardance along the two principal axes of the fiber can be determined by an incident pulse which is linearly polarized and oriented at 45° with respect to the principal axes. The ellipticity of the pulse which is transmitted through the fiber is $r$=0.94, which is close to circular polarization. This characterizes the retardance to $(2n + 0.48)\pi$ with $n \in \mathbb{Z}$. The offset n cannot be determined by this measurement. The maximal achievable beat length is obtained for $n = 0$ which corresponds to a beat length of about 4 m. This maximal value is far below the specified beat length of 100 m. This means that the fiber used has a stronger birefringence than expected. This could be due to stress which might have been induced by the attachment of the connectors. Another possible source of this increased birefringence is stress induced by bends or twists of the fiber during transportation. The fiber was straightly lined up during the experiments but might have been slightly twisted.

### 5.5.2 Control of the orientation of linearly polarized single pulses after the fiber

In the previous section, the ellipticity of the transmitted pulse was controlled by the orientation of the linearly polarized incident pulse. The analysis of change in the polarization revealed the principal axes of the fiber and the retardance. In this section, the reversed approach is used to control the orientation of the transmitted pulses which are linearly polarized. Hereby, the incident pulse needs to be elliptical polarized with different orientations. The angle of the transmitted light is determined by

$$\gamma_{out} = \frac{1}{2} arctan\left(\frac{2E_{major}E_{minor}}{E_{major}^2 - E_{minor}^2} cos(\epsilon)\right) \tag{5.14}$$

which was derived in section 2.2.2. Since the retardance between the fast and slow principal axes of the fiber amounts to nearly $\frac{\pi}{2}$ this can be compensated by the retardance of a quarter waveplate which is likewise $\frac{\pi}{2}$. The overall retardance which is induced by the quarter waveplate and the fiber is almost zero and therefore the cosine is equal to one. By rotation of the quarter waveplate before the fiber the intensity distribution to the major and minor axis of the electric field ellipse is controlled. Then, the major and minor axes are aligned parallel to the principal axes of the fiber by a subsequent half waveplate. The orientation of the polarization of the pulse which is transmitted through the fiber correlates with the orientation of the quarter waveplate.

The control of the linear polarization after propagation through the fiber is demonstrated with a series of different incident pulses which are characterized by the orientation of the quarter waveplate. The state of polarization of the transmitted pulse is analyzed with an intensity measurement after an analyzing polarizer as in the experiment before. The measured data is presented in figure 5.10a). The graph depicts a series of curves which have a sine modulation. Each curve represents the state of polarization of a transmitted pulse. The maximum of each curve is shifted compared to the neighboring curve. This corresponds to a change in the orientation of the polarization ellipse. The modulation goes down to nearly zero transmitted intensity which indicates linear polarization. The orientation and ellipticity of the polarization ellipse are determined by a fit using equation 2.42. The parameters which correspond the measurements in figure 5.10a) are shown in part b).

The data points which represent the orientation of the electric field ellipse lie all on a straight line with a slope of 1.002±0.003. The values for the ellipticity lie in the range between 0.04 and 0.15 which describes linear polarization.

### 5.5.3 Generation of parametrically shaped pulse sequences after propagation through the step-index fiber

In this section, a pulse shaper is used to generate pulses which are shaped in phase, amplitude, and polarization after propagation through the fiber. The pulses are shaped using the parametric encoding which is, except for the lack of orientation control, identical to the one presented in section 4.6.2. In combination with a suitable compensation of the

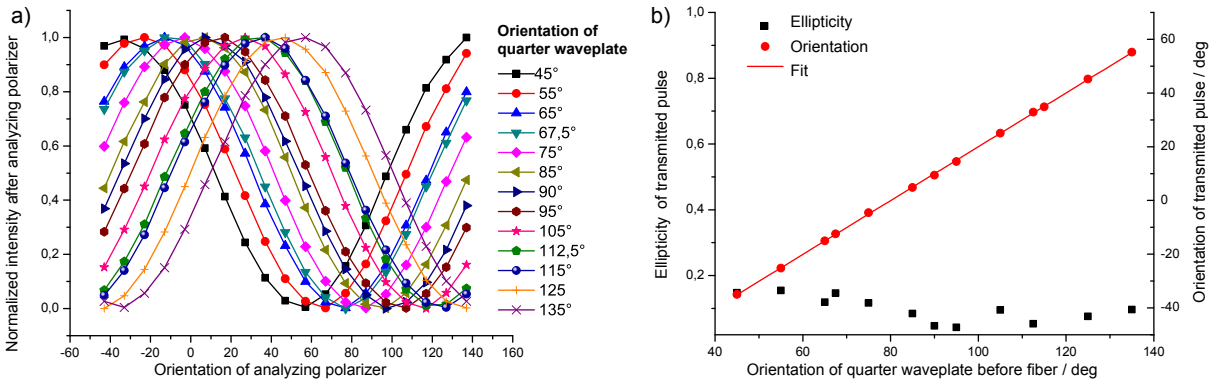


Figure 5.10: Generation of linearly polarized single pulses after the propagation through the step-index fiber. The control is achieved by changing the ellipticity of the entering pulse which is done by the rotation of a quarter waveplate. In a), the polarization the transmitted pulses is analyzed by an analyzing polarizer and a photodiode. The corresponding ellipse parameters which are obtained by a fitting procedure are presented in b).

effects induced by the fiber, this method allows for generation of pulse sequences in which the physically relevant parameters of each sub-pulse are individually controlled. In the first part, the serial setup which utilizes two liquid crystal modulators is employed to generate the shaped pulses (cf. section 3.2.3). This setup is restricted to ellipses with a fixed orientation of the principal axes in the modulation of the electric field. Due to this limitation, the pulses which are transmitted through the fiber are restricted analogously. Unfortunately, a third modulator was not available at this time of the experiments.

The experimental procedure for determination of the compensation is described, before the introducing the generation of complex pulse sequences. This compensation is verified with three short example pulses which are produced after propagation through the fiber. A series of double pulses illustrates the functionality of the shaper setup in combination with the parameterization and the compensation of chirps and polarization effects. This is followed by the application of the shaper which uses three modulators for modulation of the pulse and has the capability to fully control the electric field without any restrictions. The functionality of the setup and the calculation of dedicated pulse sequences are described in chapter 4.

### 5.5.4 Compensation of the birefringence by the pulse shaper

By using the shaper, it is possible to compensate the birefringence of the fiber more precisely than with a waveplate, since the difference retardance can be adjusted in fine steps. In case of the serial setup, the second modulator controls the polarization by the difference between the retardances $\varphi_c^{\omega_n}$ and $\varphi_d^{\omega_n}$. Therefore, the optical axes of this modulator have to be aligned parallel to the principal axes of the fiber. This is achieved by a half waveplate which is placed directly before the fiber. The experiment in section 5.5.1 showed that the fiber induces a difference retardance of about $\frac{\pi}{2}$. This is the initial value for the optimization of the compensation. This compensation value is symmetrically split and added to the retardances of the two last liquid crystal modulators ($\varphi_c^{\omega_n}$ and $\varphi_d^{\omega_n}$).

The orientation of the half waveplate and the offset difference retardance are iteratively aligned. The test pulse is a circularly polarized pulse which is produced and measured after the fiber. As an optimal offset for the polarization compensation a difference retardance of $0.42\pi$ was found. The time-dependent pulse parameters were determined by the time-resolved ellipsometry procedure described in section 3.3.1. For the example pulse which were intended to be linearly polarized, an ellipticity of $r$=0.04 was measured. The corresponding curves are depicted in figure 5.11a). The elliptical state of polarization with a set ellipticity of $r$=0.5 is depicted in b). For this pulse, the measured ellipticity was $r$=0.55. In figure 5.11c), the example of the circularly polarized pulse is presented with a measured ellipticity of r=0.94. All pulses show a Gaussian intensity curve which is characteristic for short pulses. The pulse duration of these three pulses amounts to about 70 fs. The coordinate system of the transmitted pulse is rotated by $-61°$ with respect to the horizontal axis.

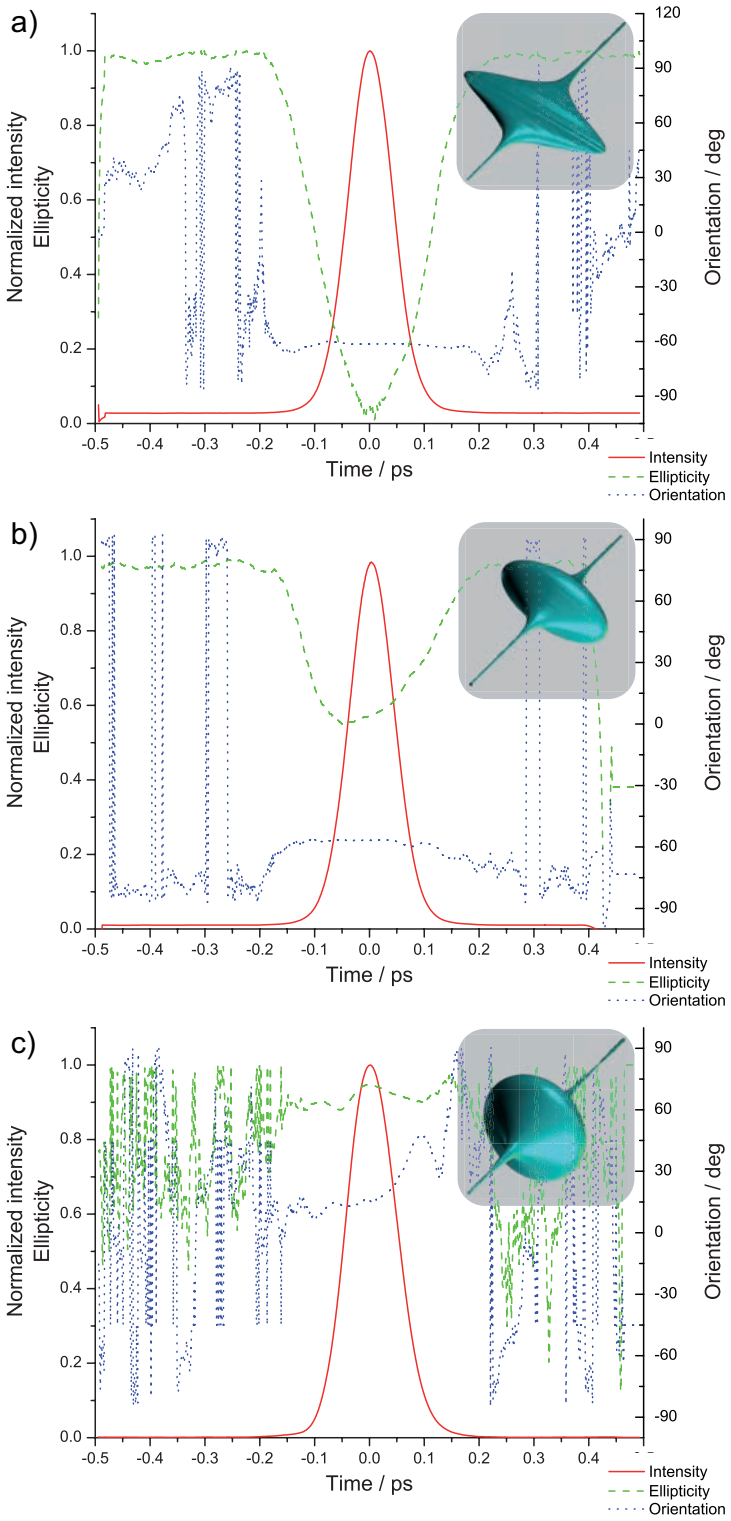


Figure 5.11: Single pulses for testing the compensation of chirps and birefringence. The pulses are short and have a different state of polarization: a) linear (r=0.0), b) elliptical (r=0.5), and c) circular (r=1.0).

### 5.5.5 Illustration of the compensation for a double pulse sequence

The preparation of parametrically polarization shaped pulses after propagation through the fiber is demonstrated in this section. The procedure of the generation of a double pulse is illustrated in figure 5.12. This double pulse sequence consists of two linearly polarized short sub-pulses separated by 600 fs which are oriented perpendicular to each other. A short linearly polarized pulse which is depicted in figure 5.12a) enters the serial setup (cf. section 3.2.3). The desired pulse sequence is calculated by superposition of sub-pulses with individually controllable sub-pulse parameters. For the resulting electric field, which is represented in the frequency domain, the phase and amplitude as well as the difference retardance, which determines the state of polarization, is calculated. The phase function of the chirp compensation is superimposed upon the phase of the pulse. The value obtained for the polarization correction is added to the corresponding difference retardance of array $c$ and $d$. The resulting pixel pattern which is written on the modulators is depicted in figure 5.12b). In the pixel pattern of array $a$ and $b$, the quadratic phase function of the chirp compensation is clearly visible. The retardances in array $c$ and $d$ are shifted by $0.42\pi$ respective to zero, which is due to the polarization compensation. After the pulse shaper, the pulse is very long and highly structured. This is can be seen in figure 5.12c). This pulse is launched into the step-index fiber. During propagation through the fiber the shaped pulse is modulated again due to the optical properties of the fiber. After transmission through the fiber the pulse obtains the desired shape. Figure 5.12d) clearly shows the desired double pulse sequence. The side pulses are an inherent feature of the application of the serial setup which is discussed in [64].

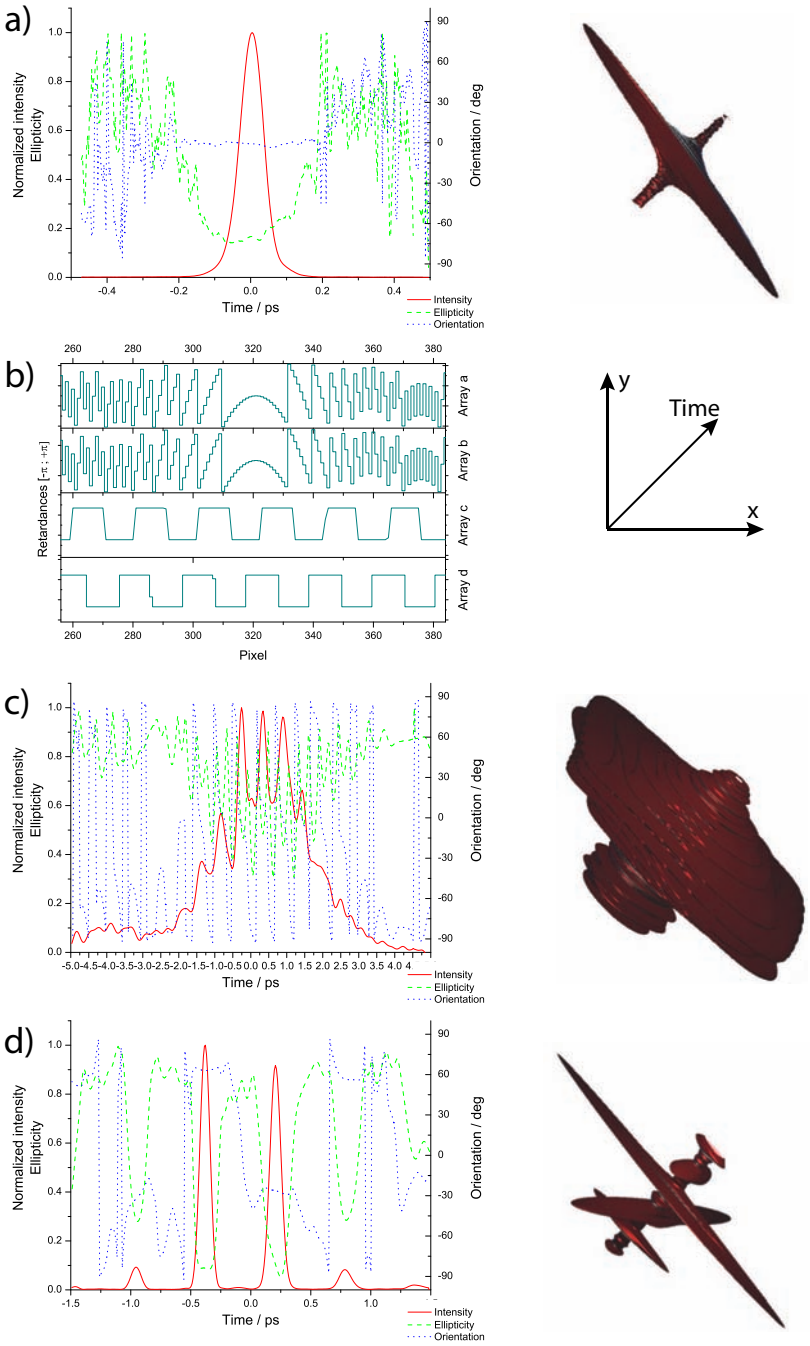


Figure 5.12: Procedure of the dedicated control of a pulse sequence after transmission through the step-index fiber. As an example, a double pulse is chosen that consists of two perpendicular linearly polarized sub-pulses which are separated by 600 fs. In a), c), and d) the pulse shape at different positions is depicted. a) before the shaper. c) after shaper. d) after fiber. In b), the pixel patterns are depicted which are written on the liquid crystal arrays of the serial setup.

### 5.5.6 Systematic variation of the ellipticity in a double pulse sequence

The capability of generating a polarization shaped double pulse has been shown in the previous section. In this section, the control over the ellipticity of the pulses which are transmitted through the fiber is systematically investigated. The limitation to an ellipticity change in the produced ellipses of the electric field is due to the restriction of the shaper setup (cf. section 3.2.3). The ellipticity is controlled by inducing a difference in the phase retardances of the two electric field components. In this analysis, the difference retardance is used since it maps the control space more uniformly. The ellipticity is connected to the difference retardance via

$$r = tan\left(\frac{\varphi_c - \varphi_d}{2}\right) \tag{5.15}$$

which was derived in section 3.2.2. A series of double pulses with a systematically changed difference retardance of the second sub-pulse is generated. Each double pulse is retrieved and the ellipticity of each pulse is calculated. The ellipticity is transformed to the corresponding difference retardance. The set and measured values of difference retardances are plotted in figure 5.13. The values range from $\pm 1.0$ – corresponding to vertical linear polarization – via elliptical polarization to 0 – corresponding to horizontal linear polarization. The positive sign of the difference retardances corresponds to right-handed helicity the negative to left-handed helicity. The difference retardance of the first sub-pulse remains constant with values close to zero, which describes horizontally linear polarization. The measured difference retardance of the second sub-pulse matches the set value.

### 5.5.7 Triple pulses with different states of polarization

The independent control of the ellipticity of one sub-pulse of a double pulse sequence has been demonstrated in the previous section. Here, the variation of the other pulse parameters is demonstrated, including distance, energy, chirp, and polarization of the individual sub-pulses. This variation of the parameters is illustrated in a series of triple pulses depicted in figure 5.14. In this series of triple pulses, various changes in the sub-pulse parameters are presented. In figure 5.14a), a sequence of three pulses with an inter-pulse distance of 600 fs is depicted. All three sub-pulses have the same pulse energy and are linearly polarized in the same direction. In 5.14b), the pulse parameters are equal to the pulse in a) apart from the orientation of the first and last sub-pulse which is changed to 90°. In the example shown in figure 5.14c), the pulse distances are changed to 400 fs and 600 fs. Further, in pulse c), the polarization of the last sub-pulse is set to circular. In d), the pulse energy of the central sub-pulse is reduced to one half. In example e), the last sub-pulse is quadratically chirped by $8{\times}10^5$ fs$^3$ and has an energy three times larger than the energy of the first two sub-pulses.

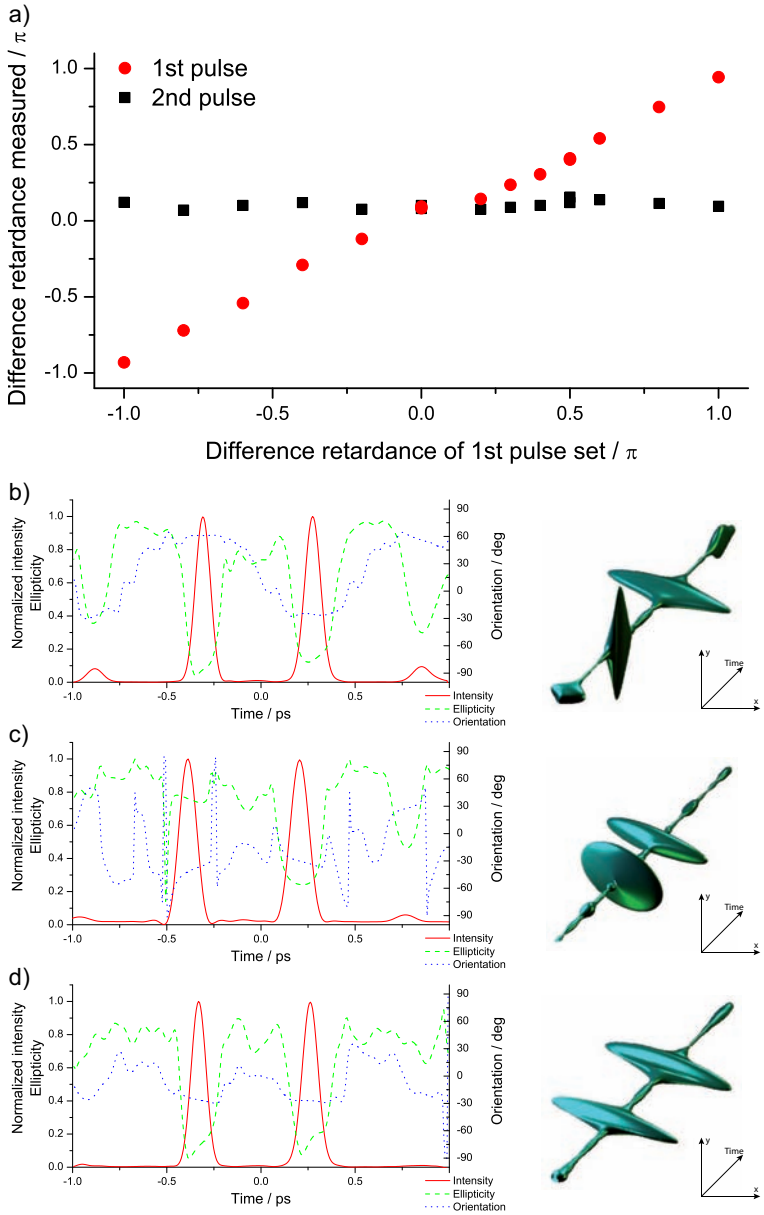


Figure 5.13: Control of the ellipticity in a double pulse sequence. The second sub-pulse is constantly linearly polarized in horizontal direction. In a), the ellipticity of the first sub-pulse is changed from vertical polarization ($1.0\pi$), via elliptical and circular polarization ($0.5\pi$) to horizontal polarization ($0.0\pi$) and back. The sign of the difference retardance changes the helicity from left to right hand polarization. In b), c), and d) the time evolution and the three-dimensional representation of the corresponding double pulses is shown.

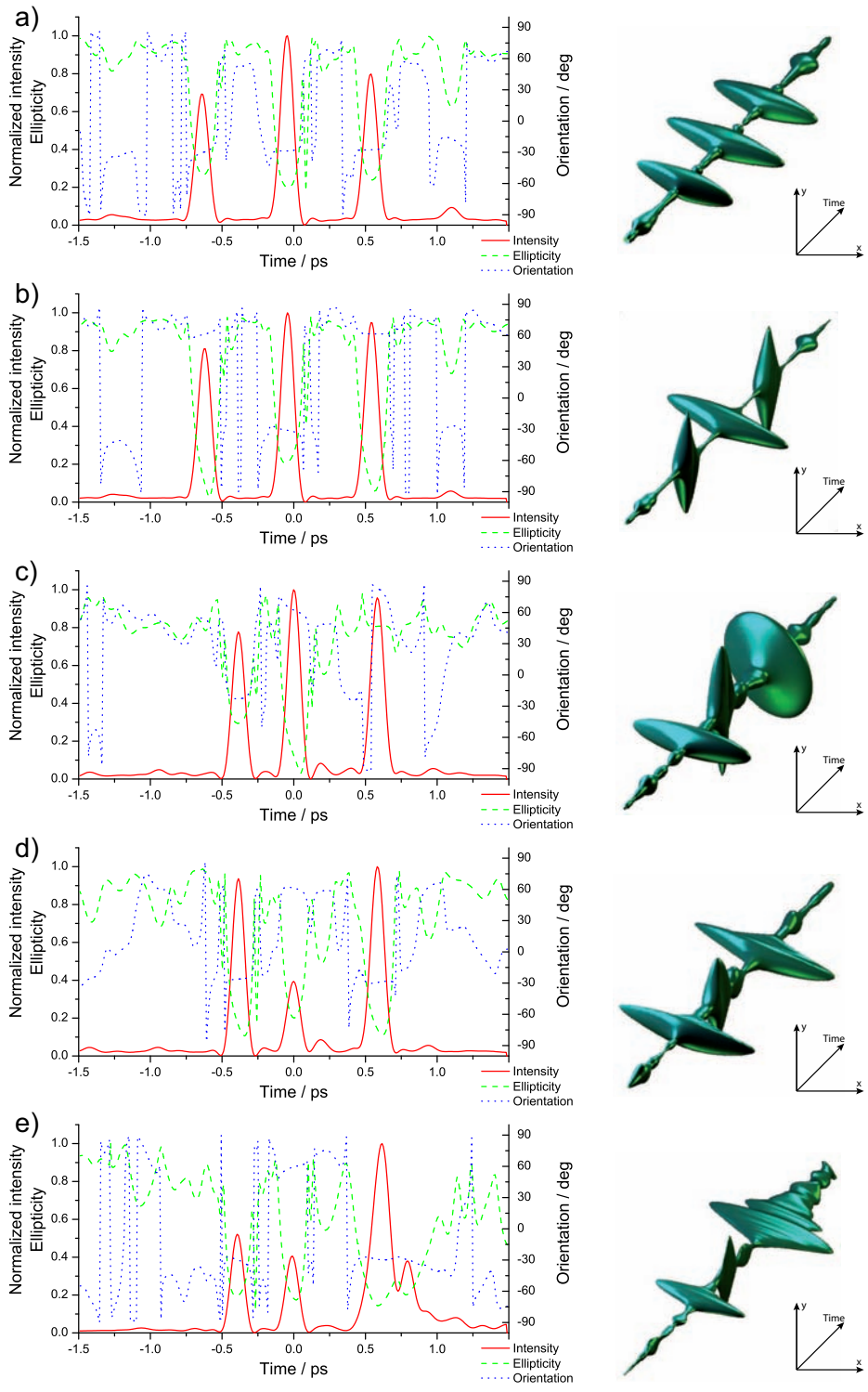


Figure 5.14: This figure illustrates the generation of parametrically shaped pulse sequences after transmission through a step-index fiber by modulation with the serial setup. In the series of triple pulses, the variation of the individual sub-pulse parameters is shown. See the text for detailed description of the pulses.

### 5.5.8 Polarization pulse shaping after the fiber with full control over the electric field

In this section, the shaper setup described in chapter 4 is employed for generating the pulses. This setup is able to produce arbitrary electric fields without any restriction in polarization control. Therefore, the modulation of the pulses which are transmitted through the fiber is also not restricted. The half waveplate which was, in the previous experiments, located in front of the fiber is not required because the shaper is able to control the orientation of the pulse respective to the optical axes of the fiber. The capabilities of this shaper in combination with the fiber is illustrated with single pulses as well as double pulse sequences.

#### Arbitrary polarized single pulses

The prospects of the polarization control are tested with single pulses of different polarization states. A single pulse with a determined state of polarization which is characterized by the orientation $\gamma$, the ellipticity $r$ and the helicity (left- or right-handed) is transmitted through the fiber. After propagation through the fiber, the state of polarization is determined by measuring the intensity with a photodiode after a rotatable polarizer which serves as analyzer.

This is done for a large number of example pulses. The orientation of the incident pulses is changed from $-90°$ to $+90°$ in steps of $5°$. For each orientation, the ellipticity of the pulses varied from $r$=0.00 to $r$=1.00 in steps of 0.05. This measurement was carried out for both helicities. In total, these are more than 1500 different polarization states. The intensity of the transmitted pulse was measured over the whole range of $360°$ in steps of $5°$. This measurement was accomplished by an automatic procedure in which the diode signal was processed by a computer controlling the pulse shaper and a motorized rotator mount with a polarizer. During the 15 hours of the measurement more than 500 000 data points were taken.

The polarization state of the transmitted pulse, which is assigned to the polarization state of the incident pulse, is determined by processing this massive data set with an automated fitting procedure. The result presented in figure 5.15 consists of a set of curves. Each curve represents one series of polarization states with a constant ellipticity. Along one curve, the orientation of the polarization ellipse is rotated by $180°$. Due to periodicity, the curves are closed loops and the polarization state of the first point of the curve is reached again after $180°$. The color code for the helicitiy and ellipticity is specified in the legend. The curves cover all possible polarization states. This is the experimental proove that any state of polarization can be generated after transmission through the fiber.

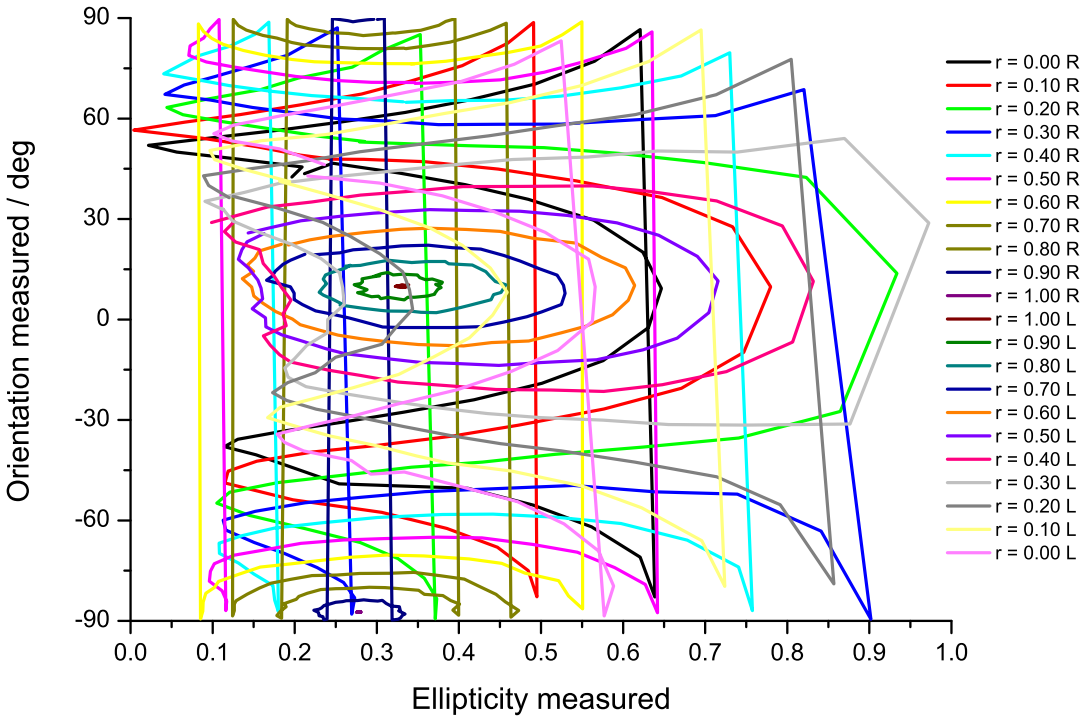


Figure 5.15: Generation of arbitrary parametrically shaped pulses after transmission through a step-index fiber by modulation using the pulse shaper which employs three double liquid crystal array modulators. This graph was generated by an automated procedure described in the text. It illustrates that any desired state of polarization can be produced after propagation through the fiber.

### Systematic variation of the polarization state for single pulses

The independent control of the polarization parameters is demonstrated with single pulses. A series of pulses is generated in which one polarization parameter is kept constant while the other parameter is modified. The pulses are transmitted through the fiber and are measured and detected in the time-resolved ellipsometry scheme. This data was used to determine the state of polarization. The analysis reveals that variations in the orientation of the polarization ellipse are independent of the ellipticity and vice versa. This is depicted in figure 5.16a) for an elliptical pulse of $r$=0.5 and in figure 5.16b) for linear pulses. The opposite is shown in figure 5.16c): the ellipticity is varied from linear to circular while the orientation of the polarization ellipse is horizontally oriented. The set and measured polarization parameters are equal within the range of the measurement and the fitting accuracy.

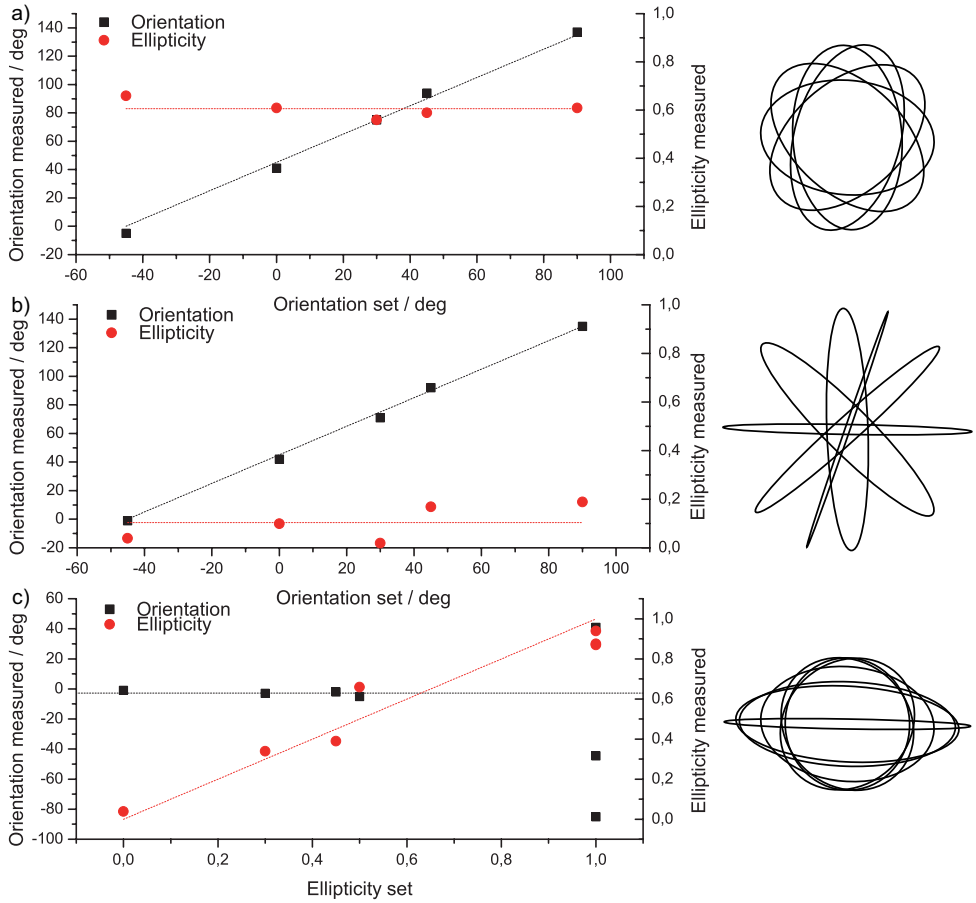


Figure 5.16: Systematic variation of the polarization state of a single pulse which is defined by the ellipticity and orientation after transmission through the step-index fiber. In the series, one of the parameters is kept constant while the other parameter is changed. The left column depicts the graph of the polarization parameters. The corresponding ellipses of the electric field is shown on the right. In a), the pulse with an ellipticity of $r$=0.5 is rotated. In b), the orientation of a linear pulse is changed. In c), the ellipticity is changed while the pulse is horizontally polarized.

### Double pulses with independent and unrestricted control over the polarization state

In the previous sections, the full control of the electric field after transmission through the step-index fiber was presented for single pulses. Here, this capability is extended to double pulse sequences in which the orientation of each sub-pulse is individually controlled. In the series which is depicted in figure 5.17, the orientation of the individual sub-pulses is demonstrated. All double pulses in this series are separated by 600 fs and have the same pulse energy. The series starts with example a) in which the relative orientation of two linearly polarized sub-pulses amounts to 45°. The relative orientation of the two pulses is changed to 20° in figure 5.17b). In figure 5.17c), the first sub-pulse is elliptical polarized with an ellipticity of $r$=0.5 followed by a linear polarized sub-pulse. The relative orientation of the principal axes of the two pulses is turned by 65°. In figure 5.17 d), a double pulse which consists of two elliptical sub-pulses with ellipticity of $r$=0.3 and $r$=0.5 is presented. The orientation of the two sub-pulses is −5° and 70°.

Together with the double pulses of figure 5.13, this series illustrates the individual and independent control of the polarization state of sub-pulses within a pulse sequence.

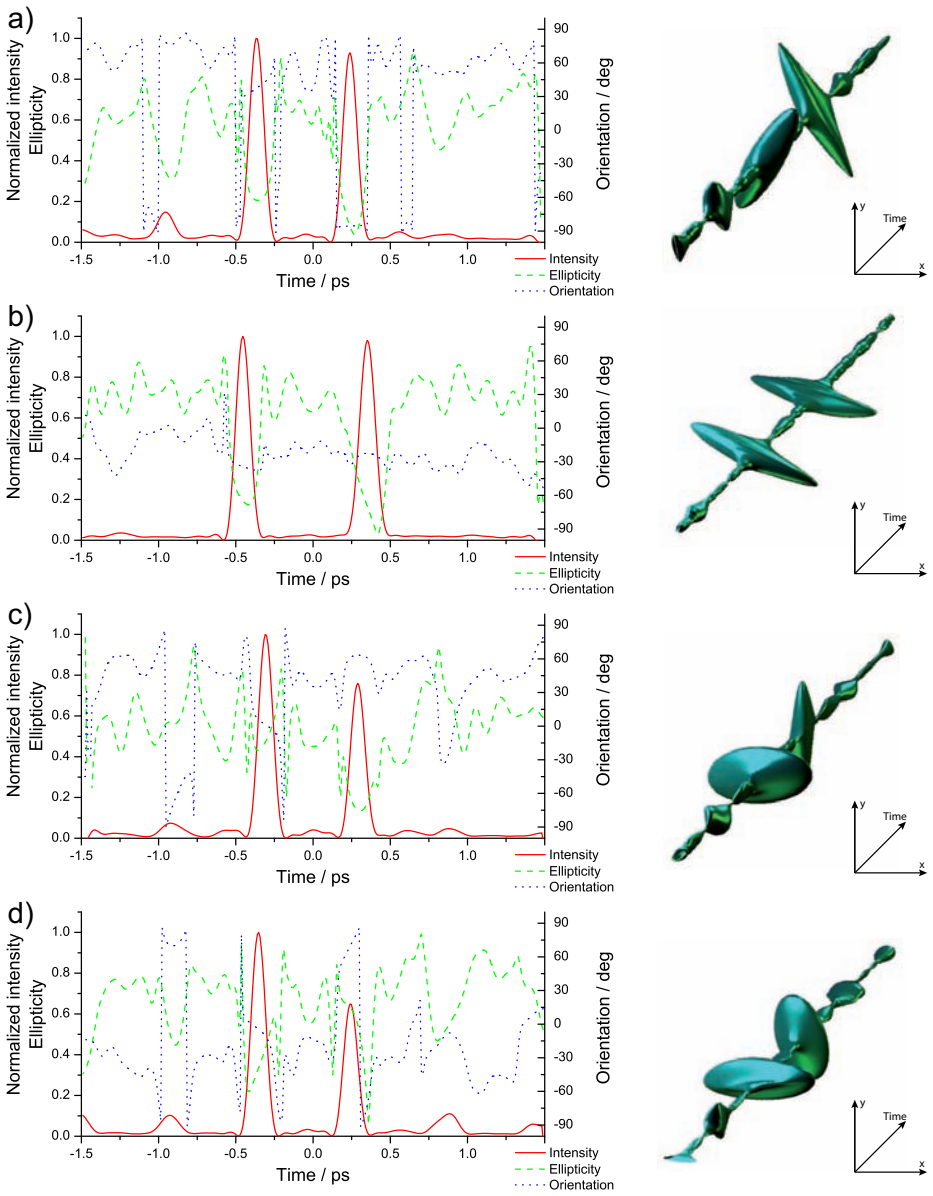


Figure 5.17: The individual control of the relative orientation is demonstrated by a double pulse sequence. The time-dependent intensity and polarization state as well as a three-dimensional representation is shown. The sequence in a) consists of two linear sub-pulses with a orientation of 45° and 90°, respectively. In b), the relative orientation between the sub-pulses amounts to 20°. In c), the first sub-pulse is elliptical polarized ($r$=0.5) and the second sub-pulse linear polarized, wherein the relative orientation is 60°. In d), both sub-pulses are elliptical polarized with $r$=0.3 and 0.5 in which the relative orientation amounts to 75°.

### 5.5.9 Impact of external mechanical stress on the pulse shape

Twisting and bending induces mechanical stress in the fiber. This results in a change of the birefringence of the fiber. The effect on the state of polarization of the transmitted pulse is investigated. First, the change of the polarization of single pulses depending on the torsion is systematically investigated. Linear polarization oriented at 0° and 45° as well as left- and right-handed circular polarization are chosen for pulses in the investigation. Then, the different torsions and bends of the fiber are compensated by the modulator. A series of double pulses tests the compensation.

#### Continuous torsion of the fiber

One end of the fiber is fixed in a rotatable mount which allows for twisting the fiber. The twist is characterized by the rotation angle between the fiber ends. The polarization state of the transmitted pulse is determined by an intensity measurement with a photodiode after an analyzing polarizer at different orientations.

The effect on the polarization of the transmitted pulse is tested with linearly polarized pulses. The orientation of the polarization is chosen to be aligned at 0° and 45° respective to the untwisted fiber. The end of the fiber is rotated in both directions up to 400°. The polarization of the pulse is characterized by the ellipticity and the orientation which are plotted depending on the twist. The results are depicted in figure 5.18.

The curves for the ellipticity show an oscillatory behavior. The ellipticity varies from linear to circular. For a straight fiber (zero twist), the pulse that is oriented parallel to the principal axes of the fiber is linear before and after the fiber. The transmitted pulse which corresponds to the incident pulse with the polarization rotated to 45° to the principal axes of the fiber is circularly polarized. This is similar to the experiment described in section 5.5.1.

The curves corresponding to the incident polarization of 0° and 45° show a diametrical behavior of the ellipticity. This is due to a change of the principal axes of the fiber. The transmitted pulses are only linearly polarized when the incident polarization is parallel to the principal axes of the fiber. A birefringence of $n \times \pi$ with $n \in \mathbb{Z}$ has the same effect. This case is discussed below. In case of linearly polarized incoming light oriented at 45°, the transmitted pulse gets linear at twist angles of approximately ±135°. This suggests that for these twist angles the axes of the fiber are rotated by 45°. This means that for twists of ±135° the principal axes of the fiber are oriented at 45° to the polarization of the incident pulse which is oriented at 0°. Therefore, the state of polarization of these pulses is close to circular.

The inspection of the corresponding orientation of the electric field ellipse of the transmitted pulses supports this interpretation. The angle of the transmitted pulse shifts linearly with the twist of the fiber. The slope of the linear fit is $-0.59$.

Analogous investigations are carried out with circular polarization of different helicity. For circular polarization, the orientation of the principal axes of the fiber is not relevant. The change in the polarization of the transmitted pulse due to the twist is produced by a change of the birefringence. Both pulses – left- and right-handed circularly polarized

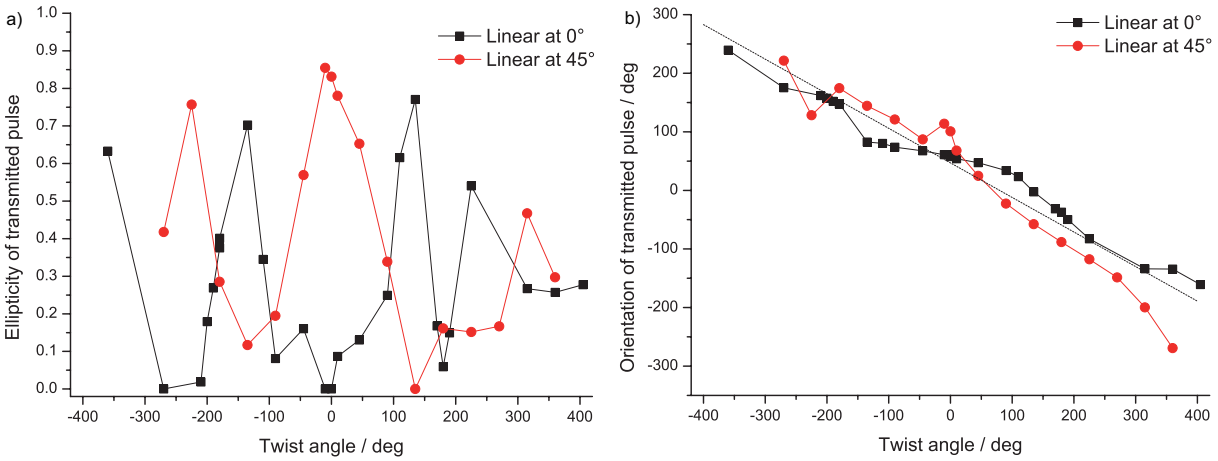


Figure 5.18: Variation of the polarization state after the step-index fiber due to mechanical stress. The stress is induced by twisting the fiber. This is investigated using linearly polarized pulses which enter the fiber oriented at 0° and 45° respective to its principal axes. The state of polarization is characterized by the ellipticity which is depicted in a) and the orientation which is depicted in b).

– experience the same amount of birefringence. Therefore, the two curves obtained for the ellipticity depicted in figure 5.19a) are parallel. The same holds for the curve for the orientation of the polarization which is presented in figure 5.19b). The only difference is a shift of the orientation by 90° which is due to the different helicity. An interesting point

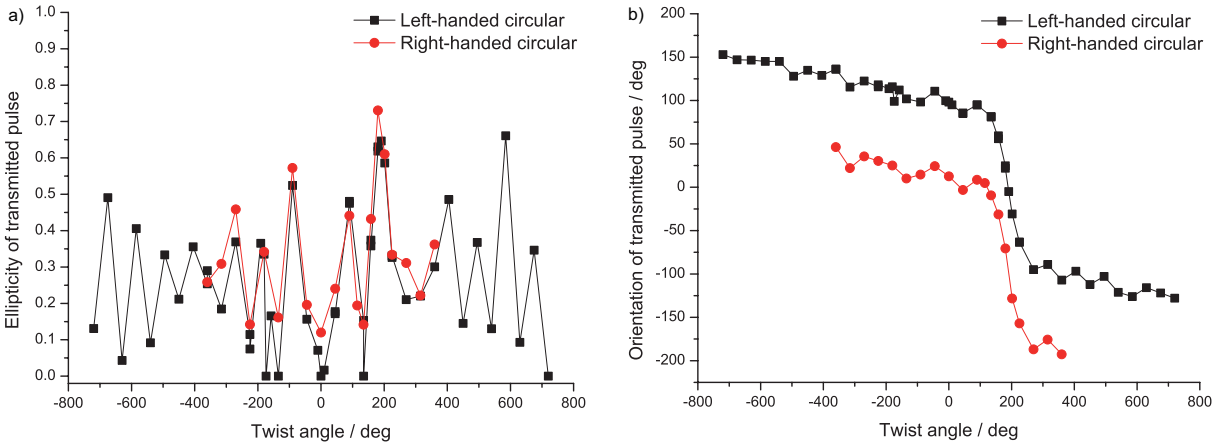


Figure 5.19: Variation of the polarization state after the step-index fiber due to mechanical stress. The stress is induced by twisting the fiber. This is investigated using left- and right-handed circular polarized pulses. The state of polarization is characterized by the ellipticity which is depicted in a) and the orientation which is depicted in b).

in the curve is the twist of 180°. At this point, both transmitted pulses are circularly polarized and the ellipticity is not changed. This also applies for the linear pulses which are presented in figure 5.18. This means that in this point the birefringence induces a difference in the phase retardance of $n \times \pi$ ($n \in \mathbb{Z}$). Further, the orientation of the polarization ellipse changes at this point by 180°, which can be observed in figure 5.19b). This happens if the difference in the phase retardance crosses $n \times \pi$.

In conclusion, the stress induced by twisting the fiber changes the orientation of the principal axes of the fiber and its birefringence. A twist of 180° changes the birefringence by more than $\pi/2$.

### Distorison of the fiber and its compensation

Distortion of the fiber impacts the state of polarization of the transmitted pulse. In the following, it is discussed if distortions can be compensated by the pulse shaper. Distortions can be induced by external mechanical stress. The twist of the fiber induces shear forces and was already explained above. The bending of the fiber stretches the material in the outer and compresses it in the inner perimeter. The bending can be realized by looping the fiber. The relevant parameter is the radius of the loop. Any pathway of the fiber can be described by a combination of bending and twisting. An example of a complex combination of twists and loops with changing radii is a knot in the fiber.

Different distortions of the fiber were tested:

- Twist by +180°
- Twist by −45°
- Loop of 17 cm in diameter
- Loop of 11 cm in diameter and twist of −60°
- Knot in the fiber (cf. figure 5.20)

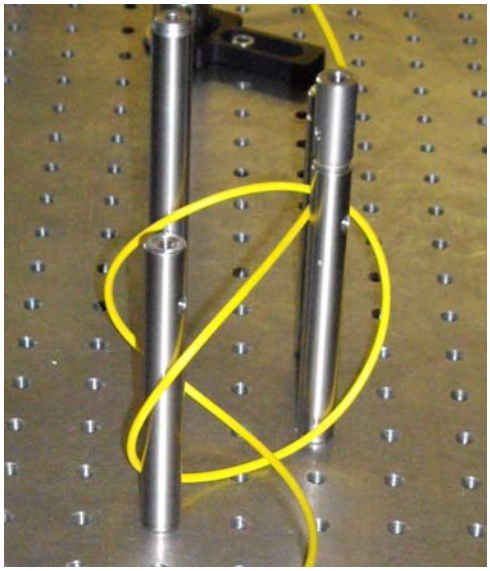

Figure 5.20: Photograph of the step-index fiber with a knot. The metal posts hold the fiber in place. The size of the knot can be estimated by the hole spacing of the table which amounts to 25 mm.

After distortion of the fiber, new parameters for the polarization compensation have to be determined. The dispersion compensation remains unaffected. With the adapted compensation parameters test pulses are transmitted through the fiber. A series of six double pulses with different combinations of pulse parameters were used. These pulses are characterized by the time-resolved ellipsometry. The parameters of the pulses – set and measured – are summarized in table 5.1. These parameters are compared to the measured parameters of the respective pulses which are not transmitted through the fiber which are

also listed in the table. The comparison reveals that the accuracy of the pulse parameters after transmission is not worse than for pulses which are not propagated through the fiber. The origin of the deviations is the precision of the pulse shaper which is analyzed in section 3.2.4. In case of the pulses transmitted through the fiber, the pattern which are written on the liquid crystal arrays are even more complicated since a large linear chirp is superimposed upon the phase of the pulses. This results in phase masks close to the Nyquist limit of the shaper.

| | | **Set value** | **Straight fiber** | **Twist +180°** | **Twist −45°** | **Loop** | **Loop+ Twist** | **Knot** | **No fiber** |
|---|---|---|---|---|---|---|---|---|---|
| **Pulse 1** | $\Delta t$ | 600 fs | 600 fs | 557 fs | 574 fs | 583 fs | 591 fs | 600 fs | 600fs |
| | $\Delta\gamma$ | 0° | 1° | 2° | 2° | 2° | 0° | 1° | 1° |
| | $r_1$ | 0.00 | 0.13 | 0.14 | 0.08 | 0.04 | 0.12 | 0.09 | 0.08 |
| | $r_2$ | 0.00 | 0.15 | 0.15 | 0.14 | 0.11 | 0.13 | 0.10 | 0.09 |
| **Pulse 2** | $\Delta t$ | 600 fs | 582 fs | 583 fs | 572 fs | 574 fs | 583 fs | 582 fs | 600 fs |
| | $\Delta\gamma$ | 90° | 89° | 93° | 87° | 89° | 90° | 88° | 90° |
| | $r_1$ | 0.00 | 0.10 | 0.19 | 0.06 | 0.18 | 0.08 | 0.06 | 0.12 |
| | $r_2$ | 0.00 | 0.09 | 0.15 | 0.10 | 0.02 | 0.16 | 0.17 | 0.08 |
| **Pulse 3** | $\Delta t$ | 1200 fs | 1154 fs | – | 1165 fs | 1157 fs | 1157 fs | 1157 fs | 1208 fs |
| | $\Delta\gamma$ | 90° | 91° | – | 89° | 93° | 88° | 87° | 89° |
| | $r_1$ | 0.00 | 0.15 | – | 0.12 | 0.10 | 0.11 | 0.14 | 0.06 |
| | $r_2$ | 0.00 | 0.23 | – | 0.18 | 0.16 | 0.11 | 0.22 | 0.28 |
| **Pulse 4** | $\Delta t$ | 600 fs | 586 fs | 582 fs | 574 fs | 582 fs | 591 fs | 591 fs | 600 fs |
| | $\Delta\gamma$ | – | (1°) | (17°) | (15°) | (10°) | (13°) | (13°) | (24°) |
| | $r_1$ | 0.00 | 0.25 | 0.15 | 0.08 | 0.16 | 0.22 | 0.24 | 0.25 |
| | $r_2$ | 1.00 | 0.75 | 0.86 | 0.86 | 0.76 | 0.74 | 0.77 | 0.78 |
| **Pulse 5** | $\Delta t$ | 600 fs | 588 fs | 591 fs | 574 fs | 574 fs | 574 fs | 583 fs | 600fs |
| | $\Delta\gamma$ | – | (85°) | (85°) | (87°) | (65°) | (70°) | (87°) | (75°) |
| | $r_1$ | 1.00 | 0.88 | 0.87 | 0.87 | 0.89 | 0.86 | 0.88 | 0.77 |
| | $r_2$ | 1.00 | 0.89 | 0.85 | 0.88 | 0.89 | 0.93 | 0.81 | 0.85 |
| **Pulse 6** | $\Delta t$ | 600 fs | – | 574 fs | 574 fs | 574 fs | 583 fs | 574 fs | 600 fs |
| | $\Delta\gamma$ | – | – | (61°) | (60°) | (6°) | (3°) | ( 5°) | (41°) |
| | $r_1$ | 0.50 | – | 0.51 | 0.50 | 0.43 | 0.37 | 0.35 | 0.30 |
| | $r_2$ | 1.00 | – | 0.88 | 0.87 | 0.78 | 0.84 | 0.88 | 0.85 |

Table 5.1: Pulse parameters of a series of double pulses transmitted through the fiber which is distorted by torsion and bending. The parameters are determined by the procedure described in section 3.3.1. Presented are pulse distance $\Delta t$, relative orientation $\Delta\gamma$, and the ellipticity $r_{1/2}$ of the first and second sub-pulse. For circularly polarized pulses, the orientation is not defined. Therefore, the measured parameters are put in brackets in case of nearly circular polarization. All parameters are compared to the set parameters and the parameters which are measured without fiber.

## 5.6 Guiding shaped pulses through a hollow core photonic crystal fiber

In this chapter, a hollow core photonic crystal fiber is employed for guiding polarization shaped femtosecond laser pulses. The goal is – analog to the previous section – to parametrically control the phase, amplitude, and polarization of the pulses after the fiber. The properties of the photonic crystal fiber are entirely different compared to a standard silica step-index fiber because the light is guided in a slightly asymmetric air-filled – hollow – core. In order to characterize the fiber, several experiments were carried out to determine its birefringence and dispersion. It is expected that the pulse energy can be larger compared to standard glass fibers. The limit of the usable pulse energy is investigated with amplified pulses. To obtain parametrically shaped pulses after propagation through the fiber, a compensation and construction scheme which takes its characteristic birefringence and the dispersion into account is developed. For the modulation of the pulse, the serial setup is used in which its inherent limitation in polarization control is not obstructive. The functionality is illustrated by several series of double pulses.

### 5.6.1 Characterization of the photonic crystal fiber

For the experiments with the photonic crystal fiber, the optimal central wavelength has to be determined. The spectrum and the intensity of the transmitted pulse as well as the auto-correlation are measured for central wavelengths between 780 and 840 nm while the spectral width of the input pulse is kept constant at 21 nm. Within the range from 800 to 835 nm, the transmitted intensity is nearly constant. When going to larger or lower wavelength, the attenuation increases. The auto-correlation measurement shows a minimal pulse length of the transmitted pulse at 805 nm. This differs slightly from the data given in the specification of the fiber presented in 5.2a). In the following experiments, the central wavelength is set to 805 nm. The spectrum of the pulse before and after propagation through the fiber is displayed in figure 5.21a). It does not show significant modification induced by the fiber for the unattenuated pulses from the oscillator.

### 5.6.2 Birefringence

The chirp which is induced by the photonic crystal fiber is expected to be lower than in the step-index fiber since the major fraction of the light propagates through the hollow air-filled core. This becomes noticeable when setting up the path of the reference beam for the cross-correlation which is approximately half a meter shorter compared to the step-index fiber. Further, a larger birefringence is expected due to the asymmetric shape of the core. This results in different properties of the fiber compared to the step-index fiber.

Due to its birefringence, the fiber can be described by its two perpendicular principal axes. A short pulse which enters the fiber linearly polarized and oriented at an angle of 45° to the principal axes is split in two sub-pulses. This can be observed in figure 5.21b). Both sub-pulses are linearly polarized and perpendicularly oriented to each other. The

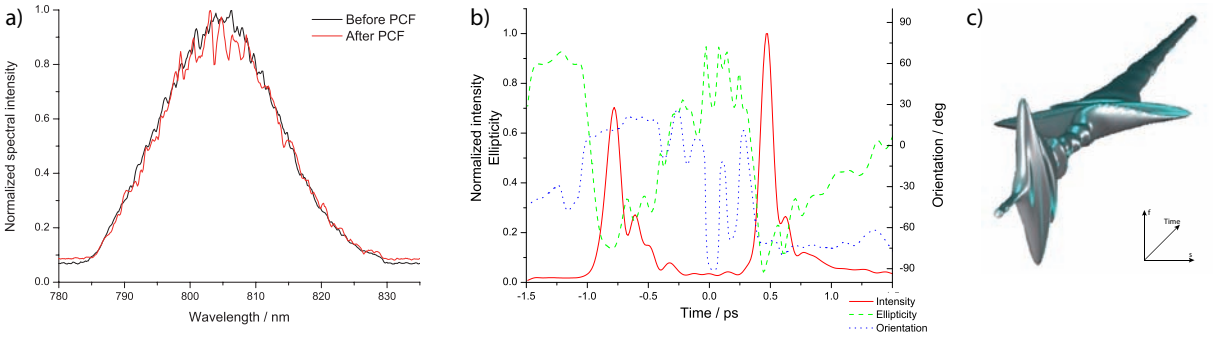


Figure 5.21: Spectrum and cross-correlation of an initially short pulse after propagation through the hollow core photonic crystal fiber. In a), the spectrum of the pulse after propagation through the fiber is compared to its spectrum before the fiber. In b), the time-dependent polarization state is shown. It pictures two linearly polarized pulses which are perpendicularly oriented. The three-dimensional representation of the pulse is portrayed in c).

two sub-pulses are separated by 1.16 ps. This splitting is denoted as difference group delay (cf. section 5.3.4) and is induced by the strong birefringence.

This measured separation corresponds to a spatial separation of 0.35 mm or 434 times the wavelength of 805 nm. Together with the length of the fiber of 110 cm this results in a beat length of 2.7 mm. Fibers of this beat length belong to the group of polarization maintaining fibers.

To address both principal axes of the fiber, these are oriented parallel to the axes of the electric field ellipses which are produced by the serial setup. This alignment is achieved by rotating the polarization of the shaped pulses using a half waveplate. If a pulse is transmitted along one principal axis of the fiber, it is not affected by the birefringence and only one pulse is detected after the fiber. This pulse is depicted in figure 5.22a). The pulse which travels along the fast axis through the fiber is denoted as f pulse. The pulse which corresponds to the slow axis of the fiber is denoted as s pulse. The s pulse is delayed relatively to the f pulse by approximately 1.16 ps, which can be observed in figure 5.22b). Both pulses are rotated after transmission through the fiber. This is due to a rotation of the reference system of the fiber. The lab frame is rotated respective to the coordinate system of the fiber by $-65°$.

Each sub-pulse is treated separately for the investigation of the energy scaling and the dispersion compensation.

### 5.6.3 Dispersion

After transmission, both pulses are asymmetric in time. The leading slope is steep while the trailing part of the pulse has a long tail. This indicates that the dispersion is dominated by the quadratic chirp. Due to the asymmetric geometry of the fiber, the dispersion along each axis is different. The chirp of each polarization component is compensated separately with the shaper by using the Taylor terms of the linear, quadratic, and third order chirp

($b_2$, $b_3$, and $b_4$). The parameters were iteratively adapted in order to find the shortest pulse by cross-correlation measurements. The values found for the f pulse are $b_2$=−7900 fs$^2$ for the linear chirp, $b_3$=−7.6×10$^5$ fs$^3$ for the quadratic chirp, and $b_4$=−9.9×10$^6$ fs$^4$ for the third order chirp. In case of the s pulse, the parameters are determined to: $b_2$=+7000 fs$^2$, $b_3$=−3.2×10$^5$ fs$^3$, and $b_4$=+7.3×10$^6$ fs$^4$. The sign of the linear chirp is different for the f and s pulse. For the s pulse, a positive linear chirp is required which means that along this axis dispersion is anomalous. The two pulses seem to have different dispersion curves with a different zero dispersion wavelength. The manufacturer provided only one curve which might be the average of both (cf. figure 5.2).

When a pulse which consists of equal components along both principal axes of the fiber in which each component is provided with its respective chirp compensation, two short pulses are measured after the fiber. This is portrayed in figure 5.22c).

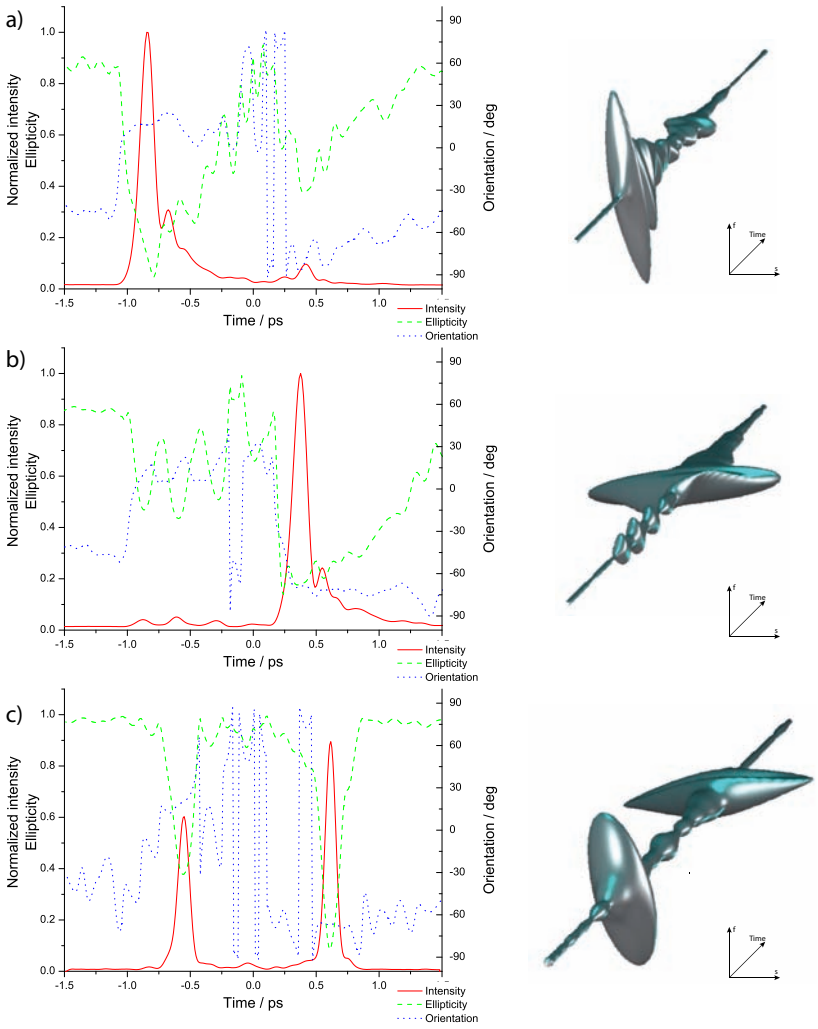


Figure 5.22: Pulses which are propagated along the principal axes of the hollow core fiber. In a), a linearly polarized short pulse is transmitted along the fast axis of the fiber. In b), the linearly polarized short pulse is oriented parallel to the slow axis. In c), a double pulse is produced having a sub-pulse in direction of each axis. The corresponding chirp compensation is used for the respective principal axis of the fiber.

### 5.6.4 Intensity range

The spectrum shown in figure 5.21a) proves that for the laser pulses of the oscillator (Mira) no self-phase modulation occurs. In order to analyze the limitations of the pulse energy, the pulses are amplified by the regenerative amplifier (RegA). The average power after transmission through the fiber amounts to 18 mW, which is comparable to the average power of the oscillator, but the pulse energy is about 300 times larger due to the reduced repetition rate of 250 kHz. For full power, the pulse energy amounts to 0.24 nJ for the oscillator and 72 nJ for the amplified pulses. The quality of the beam profile and linearity of the polarization for the amplified pulses is worse than for the pulses of oscillator. Further, the pulse length is slightly increased due to gain narrowing in the amplification process and spatial chirp induced by the stretcher/compressor. It is determined to be 77 fs by auto-correlation measurements. This leads to a slightly reduced quality of the pulse shapes produced after the fiber for the amplified pulses of the RegA.

To investigate the occurrence of self-phase modulation, the spectrum of the amplified pulses is measured for different linear pre-chirps. The chirp is varied by the shaper in the range from $-20\ 000\ \mathrm{fs}^2$ to $+20\ 000\ \mathrm{fs}^2$. This measurement is carried out separately for both principal axes of the fiber with a f pulse and s pulse. The series of spectra is presented in figure 5.23. The spectrum changes depending on the pre-chirp of the pulse.

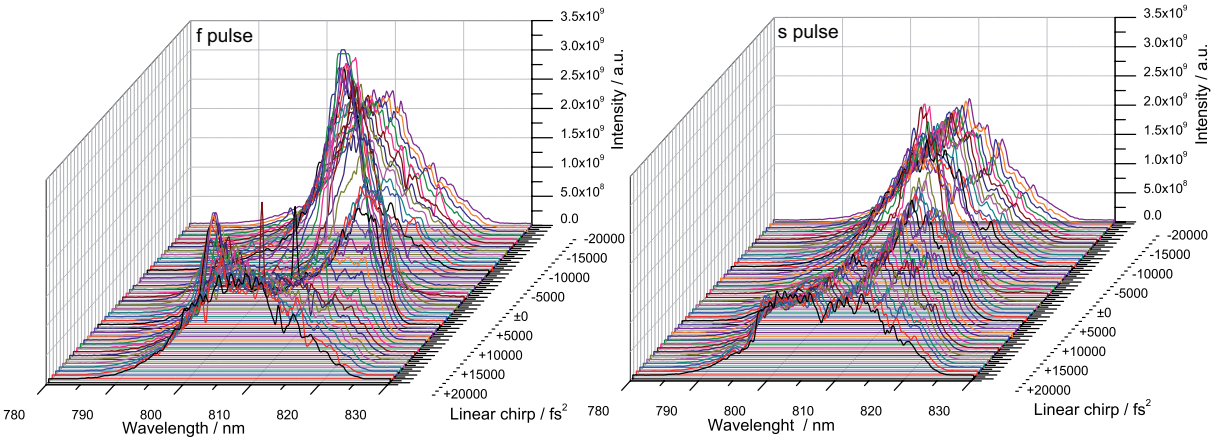


Figure 5.23: Spectrum pulse after transmission through the hollow core photonic crystal fiber depending on the pre-chirp. This measurement is carried out separately for both principal axes of the fiber.

Since the spectral intensity is not affected by chirping, the changes in the spectrum can be attributed to self-phase modulation. It is noticable that the shapes of the spectra for the respective axes are changed differently. This is probably due to different dispersions of the fiber along the two axes.

The power dependence of the self-phase modulation is investigated by the spectrum and the length of the pulse. The power is varied by changing the transmission of the shaper. This measurement is carried out for the f pulse, the s pulse and one pulse which consists of an f and s pulse which perfectly overlap in time and form a pulse oriented at 45° to the f or s pulse respectively (cf. section 5.7.1). The length of the auto-correlation trace of the pulse after propagation through the fiber is depicted in figure 5.24a).

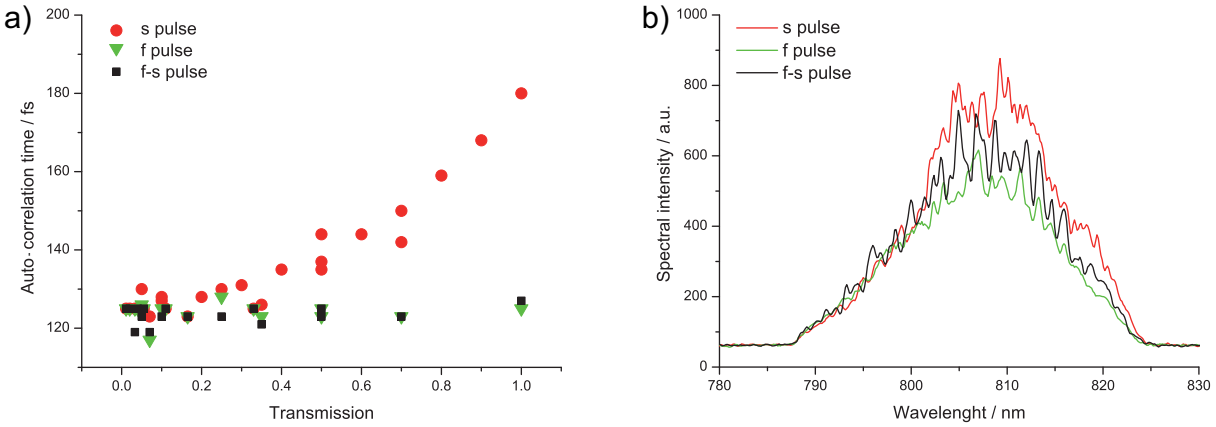


Figure 5.24: Power dependence of the pulse duration. In a), the power is controlled by the transmission of the shaper and the corresponding auto-correlation time is shown. The pulses are linearly polarized and oriented along the principal axes of the fiber, which is denoted as f and s pulse. f-s pulse specifies a pulse which is composed of an f and s pulse. Therefore, the intensity of the pulse is distributed to both axes. In b), the spectra for a transmission of T=0.3 are presented for s, f, and f-s pulses.

The pulse length, which is directly connected to the auto-correlation time, is shorter when the power is decreased. The auto-correlation time of the s pulse is most sensitive to the power. In contrast to this, the f pulse does not depend on the power of the pulse. The f-s pulse is less sensitive to the variation of the total power in this range since it consists of two sub-pulses and the peak intensity is distributed to both principal axes of the fiber.

For a transmission smaller than T=0.3, the pulse duration of the three pulses is equal within the errors. The corresponding spectra of all three pulses – f, s, and f-s – for the transmission of T=0.3 are shown in figure 5.24b). The shape of the spectrum is hardly distorted by self-phase modulation. However, there is one striking aspect: the spectral width of the pulses after propagation through the fiber is reduced to 17 nm. Before the fiber, it was measured to 20 nm. This can be explained by the beam profile and a spatial chirp of the amplified pulses, which degrades the focus of the pulse. Therefore, the bandwidth of the pulse is not coupled completely into the fiber. Due to the narrowed spectrum, the pulses are also slightly longer.

These measurements revealed the limitations in the propagation of short pulses through the fiber. The energy of the individual sub-pulses in a pulse sequence must be smaller than 24 nJ for pulses of 77 fs duration. This is taken into account for the following experiments. In case of multi-pulses, the pulse energy is distributed to the individual sub-pulses which decreases the peak intensity of each sub-pulse. When the polarization states of the sub-pulses have components in the same direction, the intensity is further reduced since amplitude modulation is required (this fact is illustrated in section 4.7).

## 5.7 Parametrically shaped pulses after propagation through the photonic crystal fiber

The generation of parametrically shaped pulses after transmission through the hollow core photonic crystal fiber is discussed in this section. In case of sub-pulses which are purely linearly polarized and oriented in one direction, the construction is straightforward. In this case, the pulse can be designed analogous to the case without fiber using a standard double liquid crystal array. The orientation of the linear polarization has to be aligned parallel to one of the principal axes of the fiber. For compensating the chirp induced by the fiber, the corresponding phase function which consists of the Taylor terms found in section 5.6.3 has to be added to the phase of the shaped pulse. The pulse after the fiber will also be linear and of the same shape as it would have directly after the shaper (without the additional chirp). This procedure for scalar pulse shaping works for all polarization maintaining fibers.

For polarization shaped pulses, the procedure is more complex since the fiber is strongly birefringent and the difference group delay splits the pulses into two components unless they are parallel to one of the principal axes.

### 5.7.1 Construction of single pulses with arbitrary polarization states

The concept of polarization control after strongly birefringent fibers becomes clear when the composition of the electric field vector is considered. This vector consists of two components oriented in x and y direction. The polarization state of the vector is given by the amplitude ratio between the x and y component and their relative phase. The mathematical basis is in detail described in section 2.2.

Two linearly perpendicularly polarized pulses of equal energy, spectrum, chirp, and phase which are perfectly overlapped in time compose a single pulse which is also linearly polarized but oriented at $+45°$ to the two original pulses. By changing the energy ratio, the orientation can be changed while the pulse remains linearly polarized. If the relative phase $\epsilon$ is changed, the resulting pulse becomes elliptical polarized. In case of equal energies and a phase shift of $\pm\frac{\pi}{2}$, the pulse is circularly polarized. The manipulation of the state of polarization by the variation of the relative phase and the amplitude ratio is in detail described in section 2.2.3.

This is transferred to the two pulses which are linearly polarized along the two principal axes of the fiber. In order to ensure the temporal overlap, both pulses need to be shifted in time. Further, the phase of the pulses needs to be equal to ensure constructive interference between the pulses in order to produce a linearly polarized pulse. These requirements are very crucial. The compensation of the chirps of the transmitted pulses was already carried out for the f and s pulse (cf. section 5.6.2). This was sufficient to achieve a short pulse in both directions but for full interference of the two pulses this is not precise enough. Furthermore, it is very tedious since it involves the adjustment of ten parameters ($0^{th}$, $1^{st}$,$2^{nd}$,$3^{rd}$, and $4^{th}$ order phase for both components). In general, the relative intensity

| Parameter | s pulse | f pulse |
|---|---|---|
| **Position in time** | $-400$ fs | $+766$ fs |
| **Phase** | $-0.92\times\pi$ | $-0.67\times\pi$ |
| **Linear chirp** | $-7\ 000$ fs$^2$ | $+8\ 827$ fs$^2$ |
| **Quadratic chirp** | $-7.30\times10^5$ fs$^3$ | $-3.90\times10^5$ fs$^3$ |
| **Cubic chirp** | $-5.50\times10^6$ fs$^4$ | $+2.48\times10^6$ fs$^4$ |

Table 5.2: Compensation parameters for a perfect overlap of the f and s pulse which produces a linearly polarized pulse oriented at 45° with respect to the principal axes of the fiber. These parameters are determined by a feedback loop optimization.

between f and s pulse has also be adapted for equal distribution. However, for the straight fiber and small distortions this was not required.

In order to equalize the phase of the two pulses and to find the correct temporal overlap, a closed feedback loop optimization is carried out. The intensity measured with a photodiode behind a polarizer oriented at 45° respective to the f and s pulse after the fiber serves as fitness. The position and chirps of the f pulse are set to the values determined in the preceding experiments and are fixed during the optimization. This optimization is performed in order to produce a short pulse fixed in time. The chirps (linear, quadratic and third order), position in time, the phase of the s pulse, and the phase of the f pulse are optimized by the algorithm. The fitness can be minimized or maximized to find a linearly polarized pulse at $-45°$ or $+45°$, respectively. The resulting parameters of the best optimization is presented in table 5.2. The pulse which corresponds to these values is measured by time-resolved ellipsometry. The time-dependent intensity, ellipticity, and orientation of this pulse as well as a three-dimensional representation of the pulse are depicted in figure 5.25a). The pulse is linear with a measured ellipticity of $r$=0.07. The pulse length is measured to 63 fs. The state of polarization is set to circular when a phase shift of $0.5\pi$ is applied between the f and s component. This is exemplified in figure 5.25b). The measured ellipticity of this pulse amounts to $r$=0.83. The pulse is equally short with a length of 61 fs.

The parameters obtained by the optimization are used in all following experiments. The only parameter which has to be adjusted on a day to day basis is the relative phase (Taylor term $b_0$) between the two components. Since a circular pulse is the most difficult pulse shape to achieve it is used as an indicator for the re-adjustment of the relative phase.

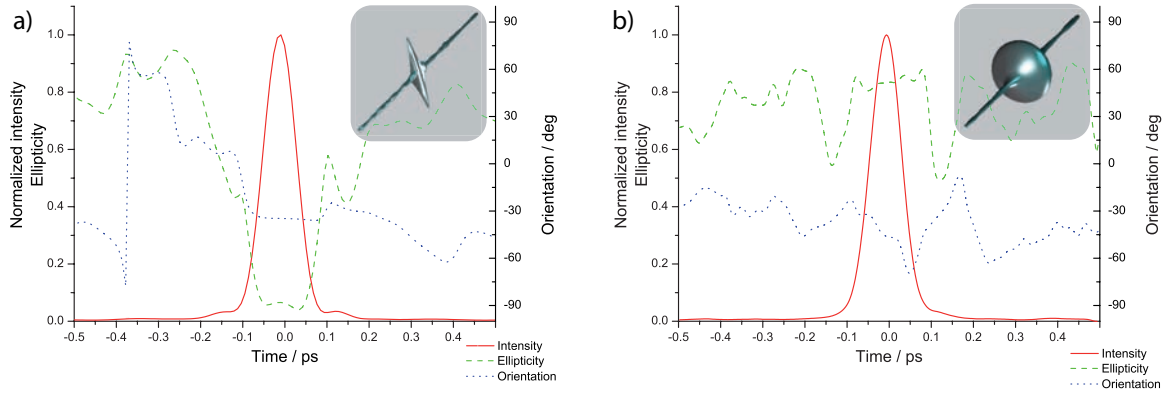


Figure 5.25: Polarization shaped pulses after propagation through the hollow core photonic crystal fiber. Both pulses are constructed by superposition of two perpendicular short sub-pulses using the values from table 5.2. The relative phase is set to zero to obtain a linearly polarized pulse which is portrayed in a) and to $0.5\pi$ for generation of a circular pulse which is shown in b).

### 5.7.2 Systematic control of the polarization state

Using these optimized offset parameters, the state of polarization of a single pulse after transmission through the fiber can be arbitrarily controlled. The independent control of orientation and ellipticity is illustrated in figure 5.26.

In figure 5.26a), the rotation of a pulse is presented while the ellipticity remains linear. The measured orientation increases linearly with the set orientation (slope of the fit is $0.96 \pm 0.02$). An offset of the orientation angle is due to a rotated overall coordinate system of the transmitted pulse. The ellipticity is constantly close to linear for all different orientations (average $0.10 \pm 0.03$).

In figure 5.26b), the counterpart is shown: the ellipticity is varied from linear, via elliptical, to circular while the orientation is kept constant. The measured ellipticity for circular pulses and linear pulses deviates from the set value (slope of the fit $0.79 \pm 0.05$). This is due to the complexity of generating circular and linear pulses. In this series, the orientation is constant at $53° \pm 3°$. A strong deviation occurs for the circular pulse for which no orientation can be defined.Therefore, it is not considered in the calculation of the average.

Interestingly, the state of polarization of the pulse after the photonic crystal fiber can be arbitrarily controlled although the pulse shaper – the serial setup – is restricted in the polarization control. This seems to be odd. However, the additional control is gained by the interferometric construction of the pulse on the basis of two perpendicularly polarized prototype pulses. This increases the complexity of the pulse patterns. Further, in the generation of more than one pulse side pulses are produced which result from the limited modulation of the serial setup. However, these side pulses are very small and are separated by more than 1 ps from the main pulse.

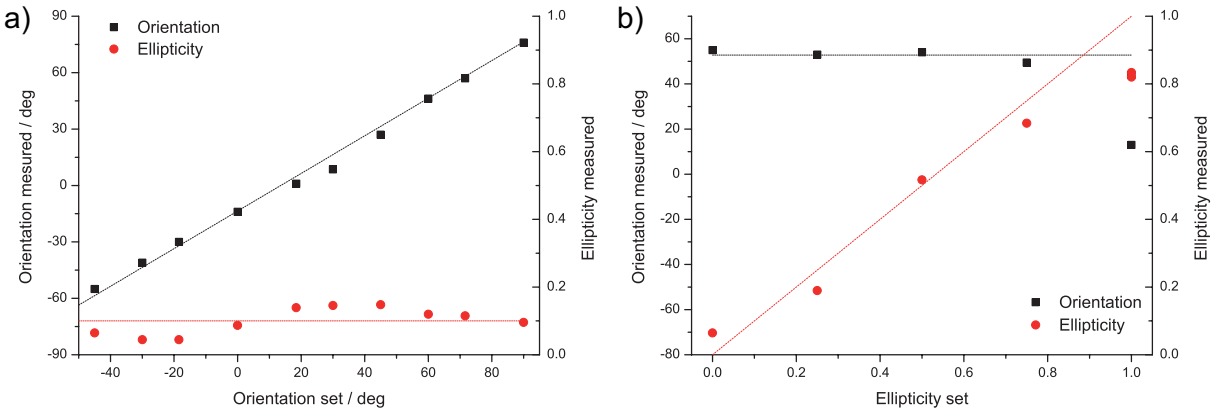


Figure 5.26: Independent variation of the polarization state of a single pulse after transmission through the hollow core photonic crystal fiber. In a), a series of pulses is shown in which a linearly polarized pulse is rotated. In b), the ellipticity is varied while the orientation of the pulse is kept constant at 45°.

### 5.7.3 Parametrically polarization shaped multi-pulses

In the last section, the polarization control of single pulses was demonstrated. Here, this procedure is extended to pulse sequences. The f and s pulses including their associated compensation parameters serve as prototype pulses. The pulse parameters of each sub-pulse are transferred to these prototype pulses. In this process, the parameters of the phase function are added to the phase function of both pulses. This includes the distance (linear phase), the linear chirp (quadratic phase), the quadratic chirp (cubic phase), and the third order chirp ($4^{th}$order phase). The remaining sub-pulse parameters energy, ellipticity, orientation, and helicity determine the distribution of the energy and the relative phase of the f and s pulse. The energy and the relative phase of the f and s pulse is calculated by the equations 2.32, 2.33, and 2.34. The construction of the pulse sequence is explained in section 4.6.2. The only difference is that the spectral phase of the compensation for f and s pulse which was obtained by the feedback loop optimization optimization has to be added to the respective phase of the pulse component which are oriented along the axes of the fiber.

In this procedure, the desired pulse sequence is composed – in general – by the superposition of twice the number of prototype pulses. In case of a linearly polarized pulse, which is oriented along one of the fiber's principal axes, only one pulse is required. These pulses overlap due to the difference in group velocity dispersion and interfere to produce the desired pulse sequences. This interference is ultra stable since the pulses are guided by the same optics and have an identical pathway.

#### Systematic variation of double pulses

The independent control of sub-pulses in a pulse sequence is illustrated by a series of double pulses. This is presented in a similar way as in the demonstration of the capabilities of the setup which utilizes four liquid crystal arrays (cf. section 4.8). In the following examples, which are shown in figure 5.27 to 5.33, the double pulses are constructed of three

prototype pulses. The first sub-pulse in these pulse sequences is always an s pulse: a short linearly polarized pulse. Two prototype pulses compose the second sub-pulse. In each series, one sub-pulse parameter of this pulse is varied independently. The parameters of the pulse sequence are given in the respective caption. Statistics of the parameters which are not varied are summarized in table 5.3.

The change of the energy distribution between the two sub-pulses is demonstrated in figure 5.27. The distance between the double pulses is systematically varied from 200 to 1200 fs, which is shown in figure 5.28. The application of a linear chirp on the second sub-pulse and the associated increase in pulse duration is presented in figure 5.29. The polarization control is visualized by two series each for the orientation and ellipticity variation. The rotation of a sub-pulse is demonstrated for linear and elliptical polarization which is shown in figure 5.30 and 5.31. The control of the ellipticity is visualized for two different orientations. The respective pulse is oriented at 30° in figure 5.32 and −45° in figure 5.33 respective to the slow axis of the photonic crystal fiber.

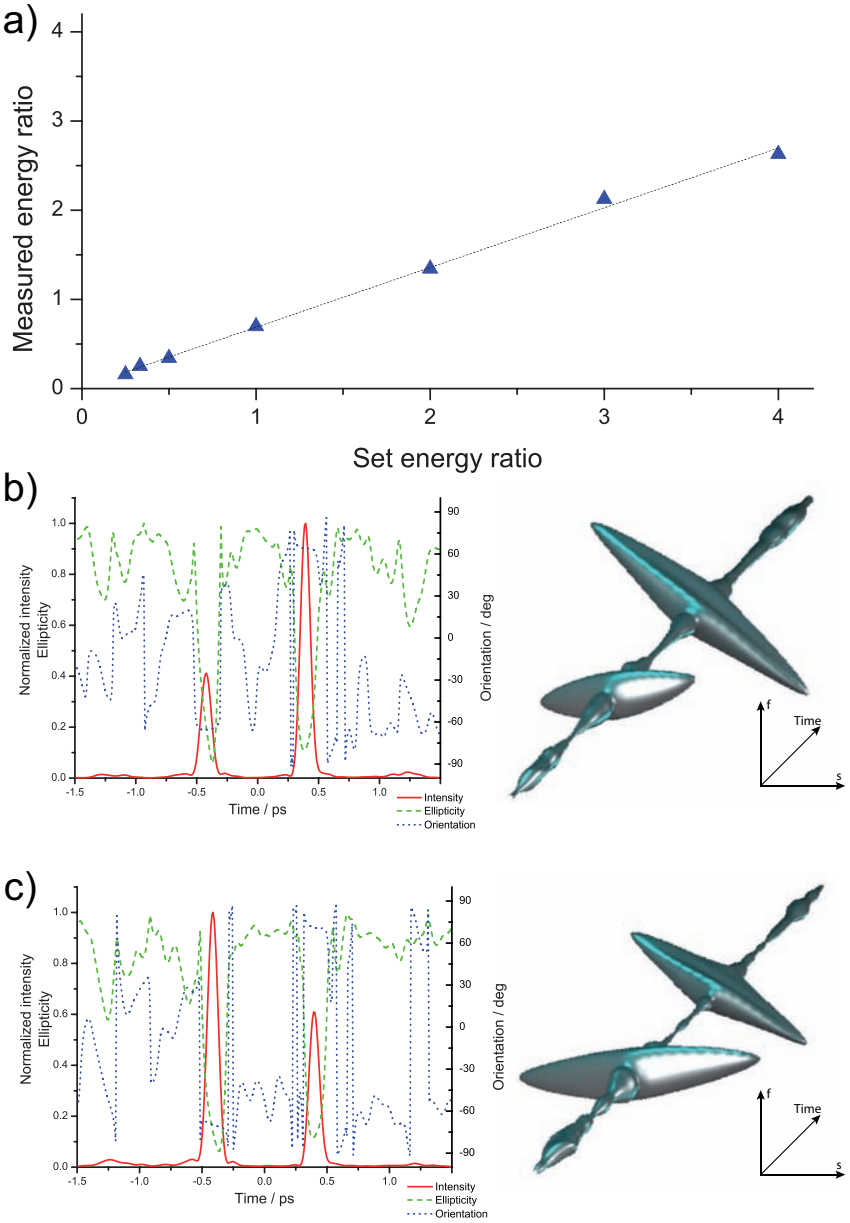


Figure 5.27: Variation of the energy between the two sub-pulses. This is carried out for ratios between 1:4 an 4:1 presented in a). The examples in b) and c) pictures the ratios of 1:2 and 2:1. The measured energy is proportional to the set value. The fit of the data has a slope of 0.67. This can be explained by the construction of the pulse sequence. The first sub-pulse is one single pulse transmitted along one principal axis of the fiber. The second sub-pulse consists of two pulses, which determine its polarization state. Therefore, the energy ratio between the first and the second sub-pulse is altered by 2/3. The state of polarization is kept constant. The first sub-pulse is linearly oriented along the slow axis of the fiber and the second one is linearly polarized oriented at $-60°$.

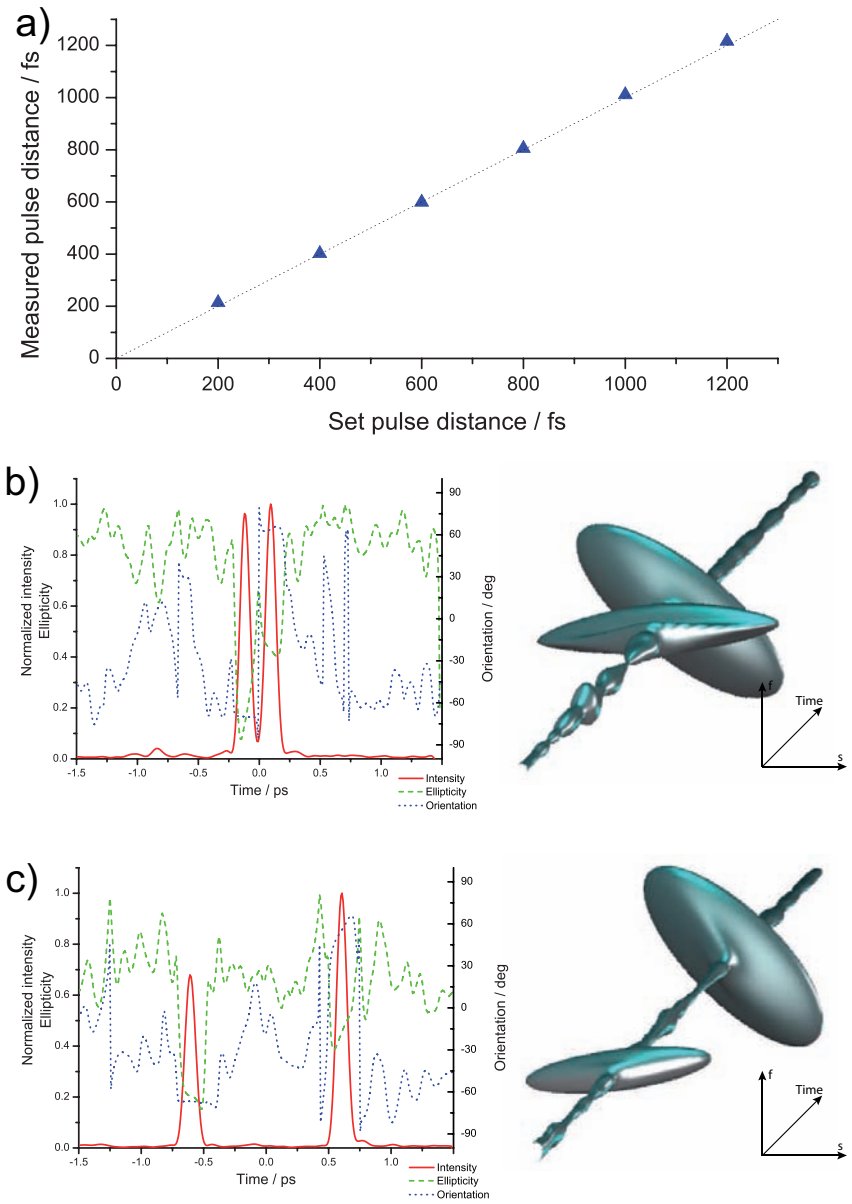


Figure 5.28: Independent control of the distance between two sub-pulses is demonstrated. It is changed from 200 fs (figure b)) to 1200 fs (figure c)) in steps of 200 fs. The small deviations from the ideal line show the high precision in the control of the pulse distance. The polarization of the sub-pulses is kept constant in this series. The fist sub-pulse is linearly and the second elliptical ($r$=0.5) polarized. The relative orientation of the two sub-pulses is set to 60°.

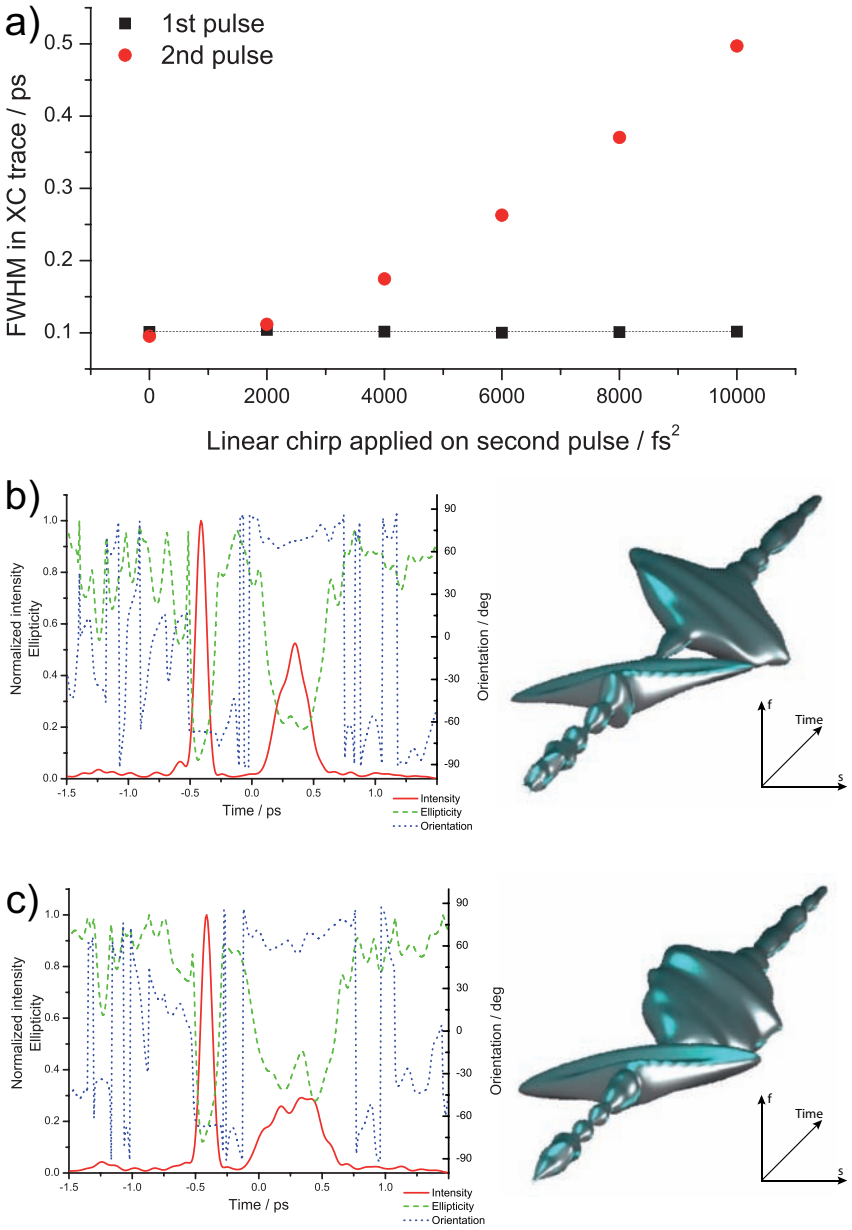


Figure 5.29: The variation of the pulse duration depending on the chirp is presented. The second sub-pulse is linearly chirped while the first sub-pulse is kept short. The curve in a) shows that the length of the second sub-pulse increases with larger chirps. The curve represents the shape expected for linearly chirped pulses characterized by cross-correlation measurement. The pulse duration of the other pulse remains constant at 72 fs. The examples in b) and c) show different linear chirps of +6 000 $fs^2$ and +10 000 $fs^2$, respectively. The state of polarization of the two pulses is kept constant. Both pulses are linearly polarized. The first sub-pulse is oriented along the s axis of the fiber. The second sub-pulse is oriented at $-45°$ relative to the first sub-pulse.

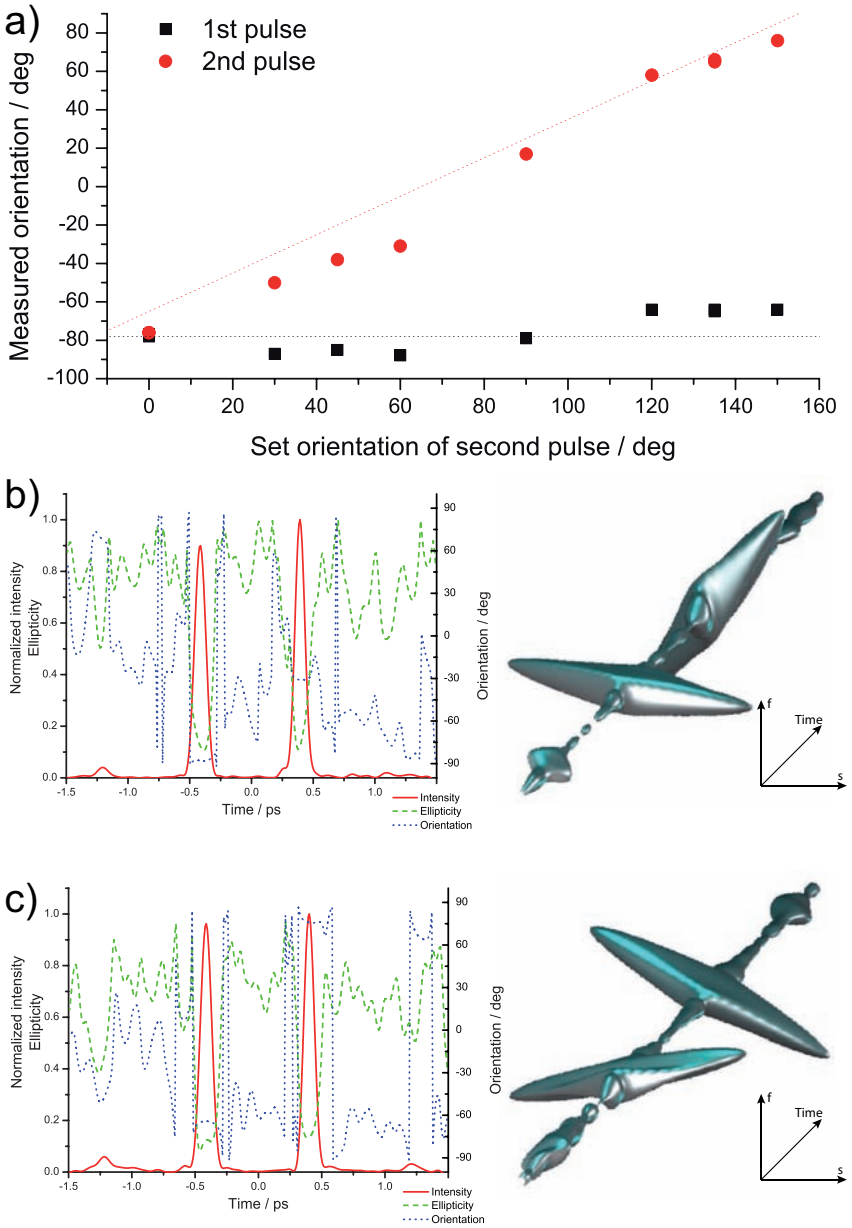


Figure 5.30: Variation of the orientation in a double pulse sequence. The second sub-pulse is rotated with respect to the first sub-pulse. In a), the orientation of the second sub-pulse is changed from 0° to 150°. Both sub-pulses are linearly polarized and have the same energy. The distance is set to 800 fs. In b), and c) two examples are selected where the relative orientation amounts to +60° and −45°, respectively.

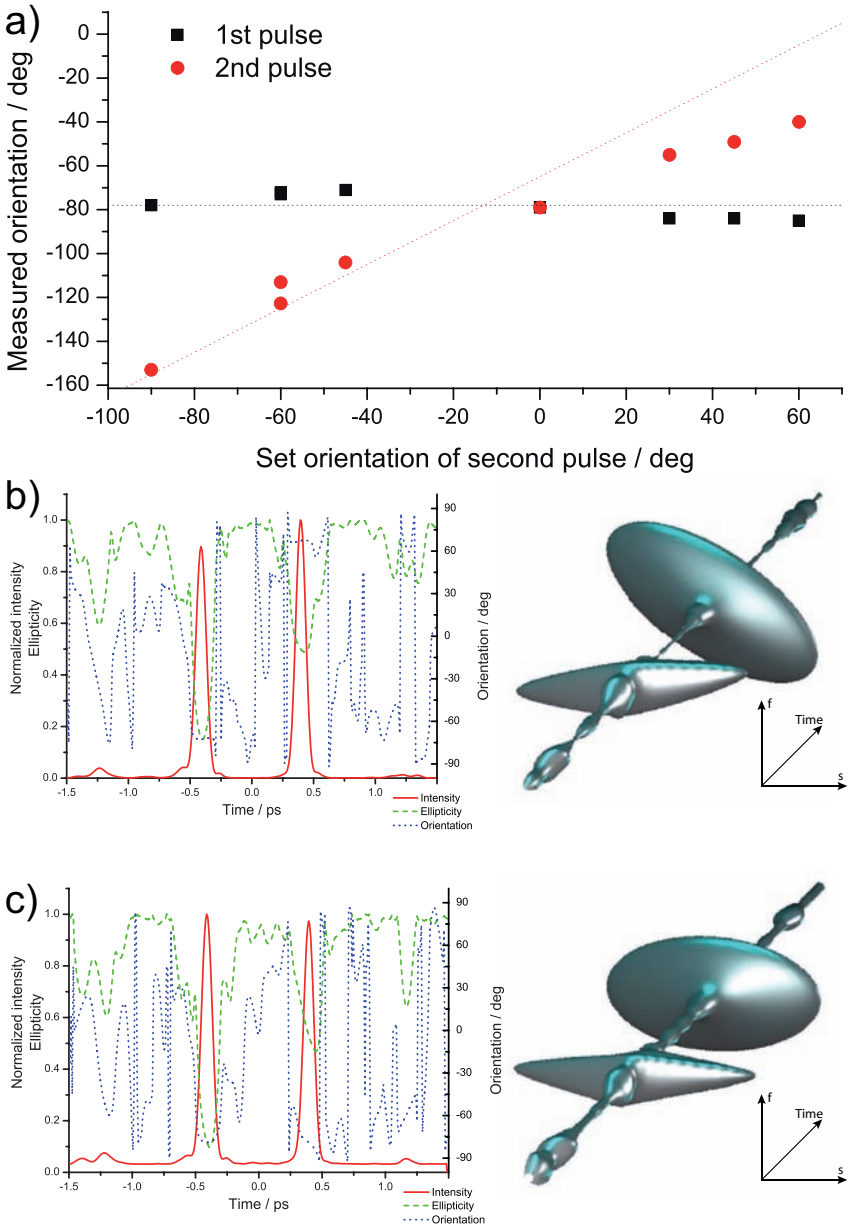


Figure 5.31: Another example for the independent control of the sub-pulse orientation. The first sub-pulse is linearly polarized with fixed orientation along the slow axis of the fiber. The second sub-pulse is elliptical polarized with $r$=0.5 and rotated. The deviation from the ideal values (indicated by the dotted line) is due to the larger uncertainty in the experimental determination of the orientation for elliptical polarized pulses. In a), the orientation of both pulses is depicted. Two examples are selected from this series: b) with a relative orientation of $-60°$ and c) in which the second sub-pulse is oriented parallel to the first one.

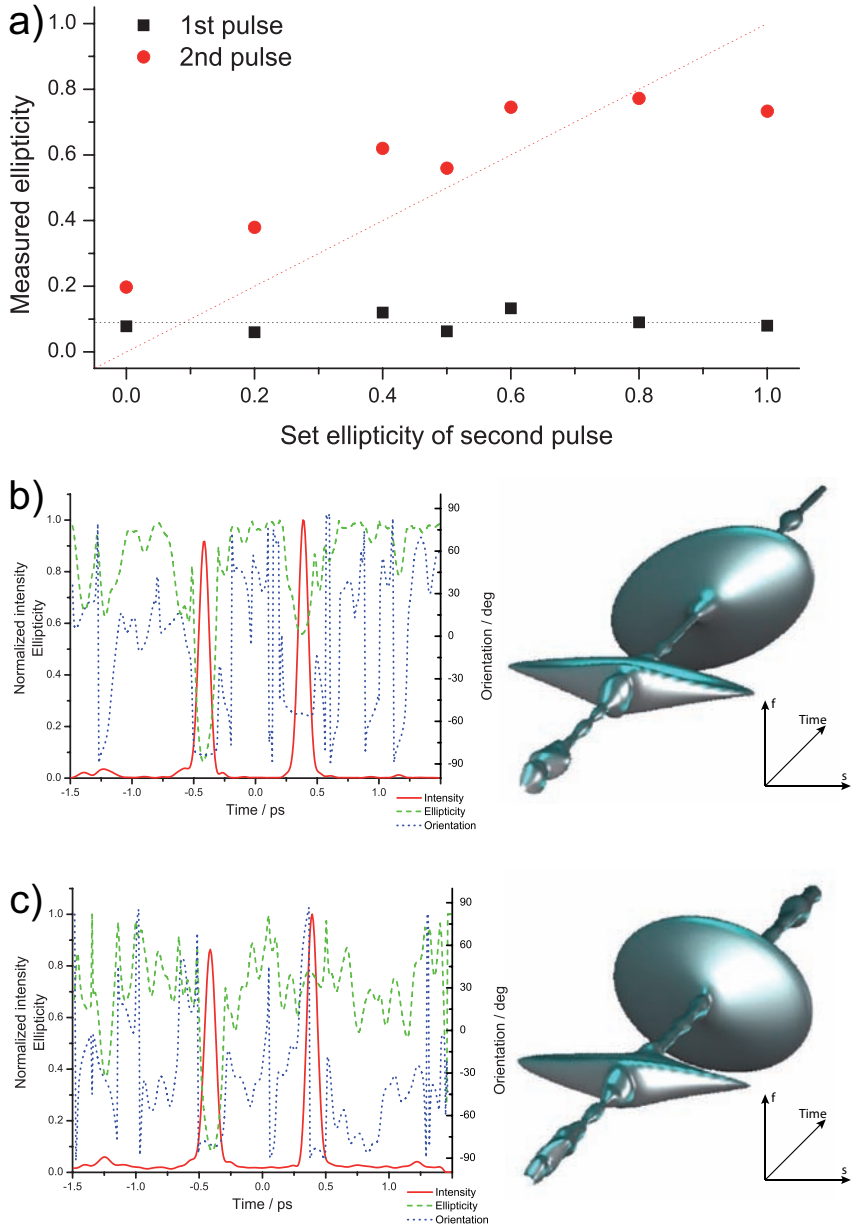


Figure 5.32: Independent variation of the ellipticity in a double pulse sequence. In a), the ellipticity of both sub-pulses is depicted. The first sub-pulse is linearly polarized while the ellipticity of the second sub-pulse is increased from linear ($r$=0.0) via elliptical to circular ($r$=1.0). The deviations from the ideal ellipticity are due to the inherent over/under estimation of the ellipticity for linearly/circularly polarized pulse by the retrieval procedure (cf. 3.3.1). The orientation of the two pulses is constant at 0° and +30° respective to the slow axis of the fiber. In b), the second sub-pulse is elliptical polarized with $r$=0.5. Part c) shows an example in which the second sub-pulse is elliptical polarized with $r$=0.8.

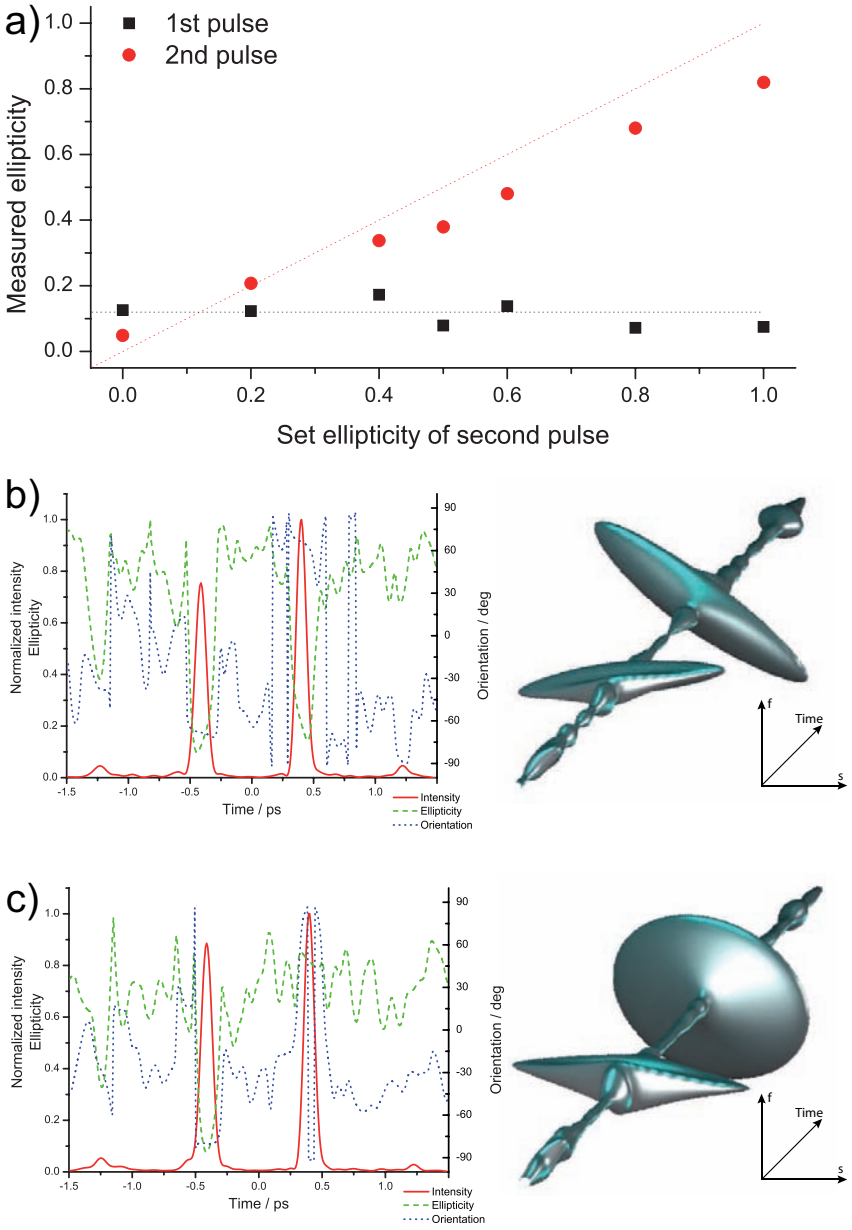


Figure 5.33: The control of the ellipticity shown for a double pulse sequence. The set and measured ellipticity of both pulses is presented in a). The first sub-pulse is linearly polarized and oriented parallel to the slow axis of the fiber. The second sub-pulse is constantly oriented at $-45°$ relative to the first pulse while the ellipticity is increased from linear to circular. In b), the ellipticity of the second sub-pulse is set to $r$=0.2. In c), an example with circular polarization ($r$=1.0) is shown.

| | shown in | **Energy** fig. 5.27 | **Distance** fig. 5.28 | **Chirp** fig. 5.29 | **Orientation** fig. 5.30 | **Orientation** fig. 5.31 | **Ellipticity** fig. 5.32 | **Ellipticity** fig. 5.33 |
|---|---|---|---|---|---|---|---|---|
| **Energy** | set | varied | 1.0 | 1.0 | 1.0 | 1.0 | 1.0 | 1.0 |
| | measured | | 0.77±0.12 | 0.77±0.05 | 0.94.±0.27 | 0.91.±0.11 | 0.85.±0.05 | 0.76.±0.05 |
| **Distance** | set | 800 fs | varied | 800 fs | 800 fs | 800 fs | 800 fs | 800 fs |
| | measured | 810±5 fs | | 779±25 fs | 809±6 fs | 804±6 fs | 804±3 fs | 810±5 fs |
| **Pulse length** | set | short | short | short | short | short | short | short |
| 1st pulse | measured | 65±4 fs | 66±5 fs | 68±4 fs | 65±5 fs | 64±5 fs | 63±6 fs | 63±2 fs |
| **Pulse length** | set | short | short | varied | short | short | short | short |
| 2nd pulse | measured | 63±6 fs | 64±4 fs | | 65±4 fs | 64±5 fs | 63±4 fs | 63±3 fs |
| **Orientation** | set | −65° | −65° | −65° | −65° | −65° | −65° | −65° |
| 1st pulse | measured | −68±3° | −70±3° | −66±2° | −75±10° | −78±6° | −83±4° | −72±6° |
| **Orientation** | set | +70° | +55° | +70° | varied | varied | −35° | +70° |
| 2nd pulse | measured | +67±3° | +60±5° | +64±4° | | | −50±12° | +67±2° |
| **Ellipticity** | set | 0.00 | 0.00 | 0.00 | 0.00 | 0.00 | 0.00 | 0.00 |
| 1st pulse | measured | 0.16±0.03 | 0.17±0.03 | 0.13±0.03 | 0.09±0.02 | 0.12±0.04 | 0.09±0.03 | 0.12±0.04 |
| **Ellipticity** | set | 0.00 | 0.50 | 1.00 | 0.00 | 0.50 | varied | varied |
| 2nd pulse | measured | 0.12±0.03 | 0.43±0.05 | 0.22±0.13 | 0.13±0.05 | 0.55±0.16 | | |

Table 5.3: Summary and statistics of the parameters of the double pulses transmitted through the hollow core photonic crystal fiber. The corresponding graphs of the variations are depicted in figure 5.27 to 5.33. Each column represents a series of double pulses. The set parameters and statistics on measured parameters which are kept constant in the respective series are displayed. For the determination of the orientation, only pulses with an ellipticity smaller than 2/3 are considered because of the uncertainty in the determination of the orientation for nearly circular pulses.

### Complex multi-pulses

The systematic variation of the sub-pulse parameters in the last section confirmed that it is possible to parametrically design and measure double pulses of the desired state. This procedure is not limited to double pulses and can be extended to a larger number of sub-pulses and higher complexity. A few examples are shown in figures 5.34 and 5.35. In figure 5.34, the oscillator is used and in figure 5.35 the amplifier is used for pulse generation.

In figure 5.34a), a triple pulse sequence is depicted. The two outer sub-pulses are quadratically chirped by $\pm 6\times10^5$ fs$^3$. The difference in the sign of the chirp results in different orientations of the elongated tail. The first sub-pulse is linearly polarized along the slow axis of the fiber. Its pulse energy is two times larger relative to the other sub-pulses. The third sub-pulse is linearly polarized along the fast axis of the fiber. The sub-pulse in between is short and circularly polarized. In figure 5.34b), the control of the orientation of linearly polarized sub-pulses is demonstrated. The first sub-pulse is oriented in direction of the slow axis of the fiber. The two subsequent sub-pulses are rotated by 23°. The sub-pulse distances are set to 400 fs. In figure 5.34c), a sequence of four short linearly polarized sub-pulses are shown. The orientation of each subsequent sub-pulse is rotated by +45°. The distances are set to 400 fs. In figure 5.34d), a similar pulse sequence is depicted in which the polarization of the first and third sub-pulse is set to elliptical polarization with $r = 0.5$. This pulse sequence is construced by the superposition of eight prototype sub-pulses which interfere to this pulse sequence.

The results presented in figure 5.35 demonstrates that full control is also achieved for amplified pulses. In figure 5.35a), a sequence of three linearly polarized sub-pulses separated by 400 fs is shown. The first and second sub-pulse are oriented along the slow and the fast axes of the fiber. The third sub-pulse is oriented at −45° to the slow axis of the fiber. In figure 5.35b), a sequence of three short, linearly polarized sub-pulses is shown. The two outer sub-pulses are oriented along the slow axis of the fiber. The sub-pulse in between is polarized along the fast axis of the fiber. The distance between the first and second sub-pulse is set to 400 fs and the distance between the second and third sub-pulse is set to 800 fs. The sub-pulse in between is set to twice the intensity of the outer ones. In figure 5.35c), a triple pulse sequence is presented in which the two outer sub-pulses are quadratically chirped. The first sub-pulse is linearly polarized along the slow axis of the fiber and has a quadratic chirp of $-8\times10^5$ fs$^3$. The third sub-pulse is perpendicular to the first one and its chirp has the opposite sign. The sub-pulse in between is short and circularly polarized. The sub-pulse distances are set to 300 fs and 500 fs. In figure 5.35d), the polarization is changed compared to c). The two outer sub-pulses are now circularly polarized and the sub-pulse in between is linearly polarized oriented along the slow axis.

The quality of the sub-pulses decreases with an increasing number of sub-pulses because each sub-pulse is generated by two prototype pulses. For a larger number of sub-pulses, the shaping function gets more complex and the errors resulting from differing f and s prototype pulses accumulate. For the amplified pulses shown in figure 5.35, this is more crucial since the pulse quality before the shaper is already lower.

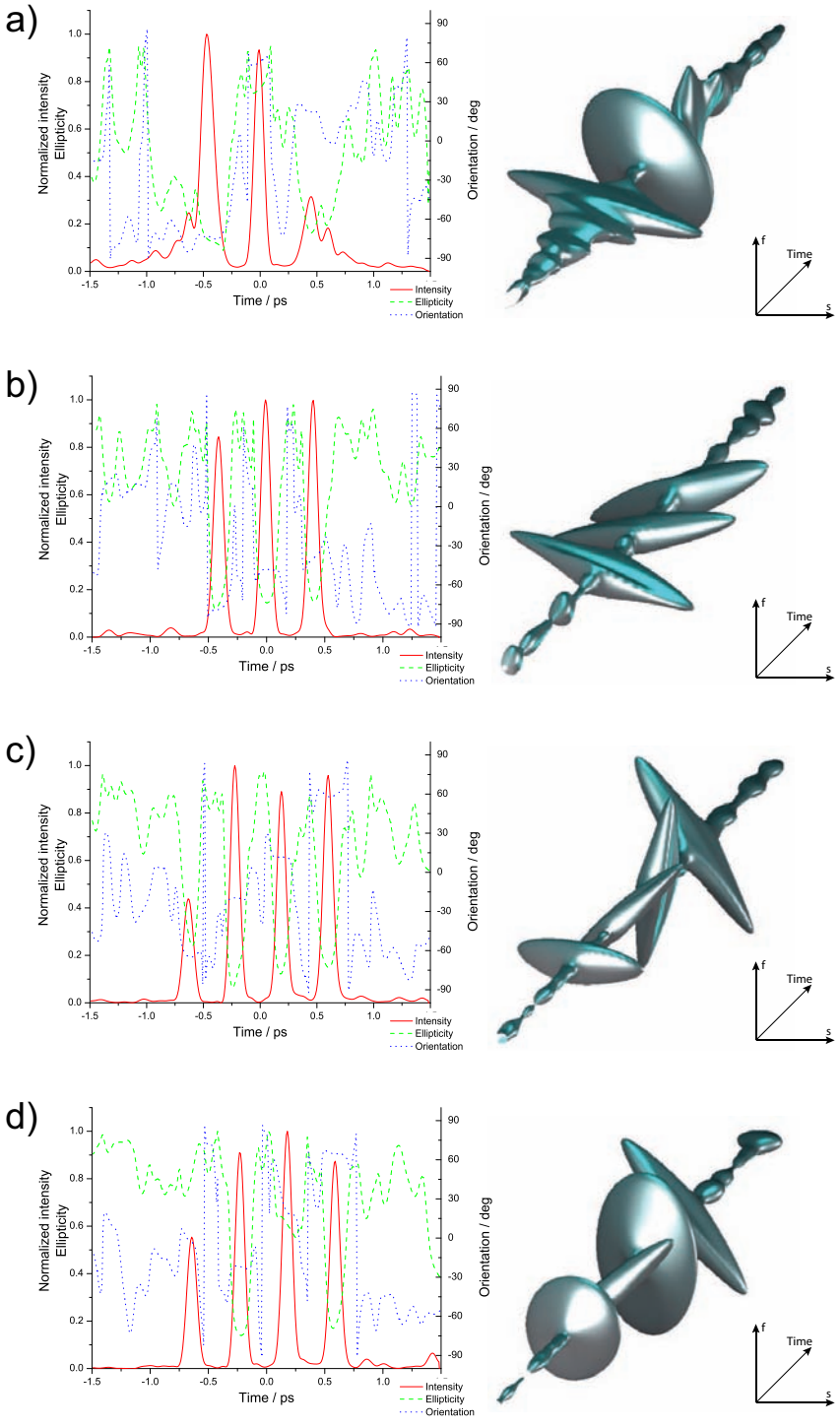


Figure 5.34: Multi-pulse sequences after the hollow core photonic crystal fiber generated by the oscillator. With these examples the capability of controlling the orientation, in combination with a variation of ellipticity and chirps is demonstrated. Details of the pulse shapes are given in the text.

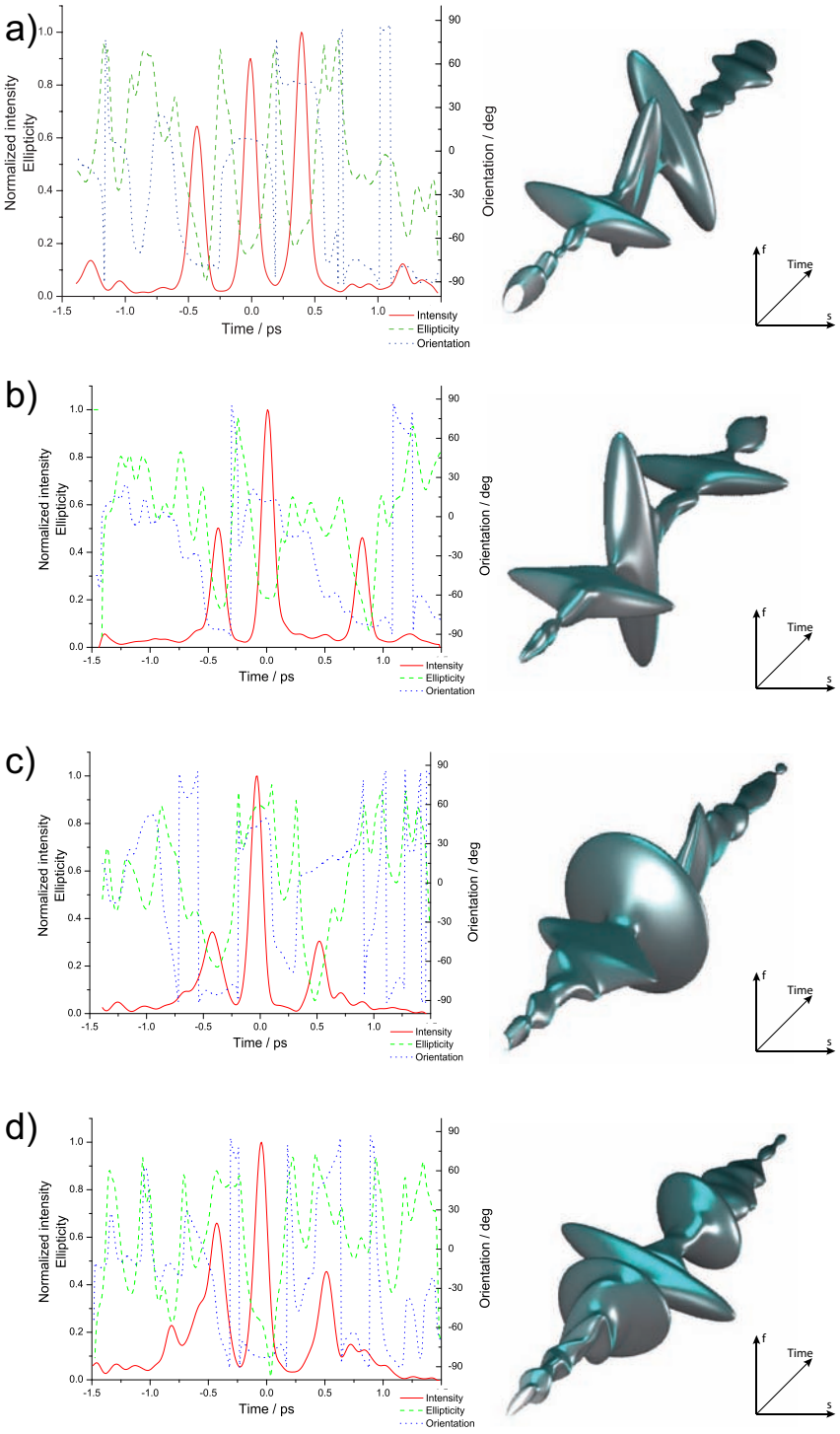


Figure 5.35: Triple pulse sequences after transmission through the hollow core photonic crystal fiber. These pulses are produced with the amplifier. This illustrates the control of the orientation in combination with the distance in time, chirp, energy, and ellipticity. The parameters of these pulses are given in the text.

### 5.7.4 Distortion of the fiber

In this section, the effects induced by distortion of the photonic crystal fiber will be investigated similarly as in the analyzation for the step-index fiber in section 5.5.9. The impact of the distortion on the pulse shape of the transmitted pulses is analyzed. This is discussed with respect to the construction and compensation of polarization shaped pulses in such a birefringent fiber. Mechanical stress is induced in the fiber by torsion and bending as well as by a knot which includes both.

#### Torsion of the hollow core photonic crystal fiber

The end of the where the shaped pulse exits the fiber is held in a rotatable mount. This allows for twisting the fiber. A linearly polarized pulse pulse, which is composed by the two prototype pulses with the phase compensation given in table 5.2, serves as a test. This pulse is very sensitive to changes in the dispersion of the fiber since the polarization state varies with small changes in differences of the spectral intensity, phase, chirps, and delay between f and s pulse. The pulse is detected after the fiber by the time-resolved ellipsometry procedure (cf. section 3.3.1). For a number of rotations of the fiber, the pulse is measured and its state of polarization determined. The ellipticity and the orientation of the pulse after transmission through the twisted fiber is presented in figure 5.36. Here, the end of the fiber was twisted counter-clockwise up to two full rotations ($-720°$).

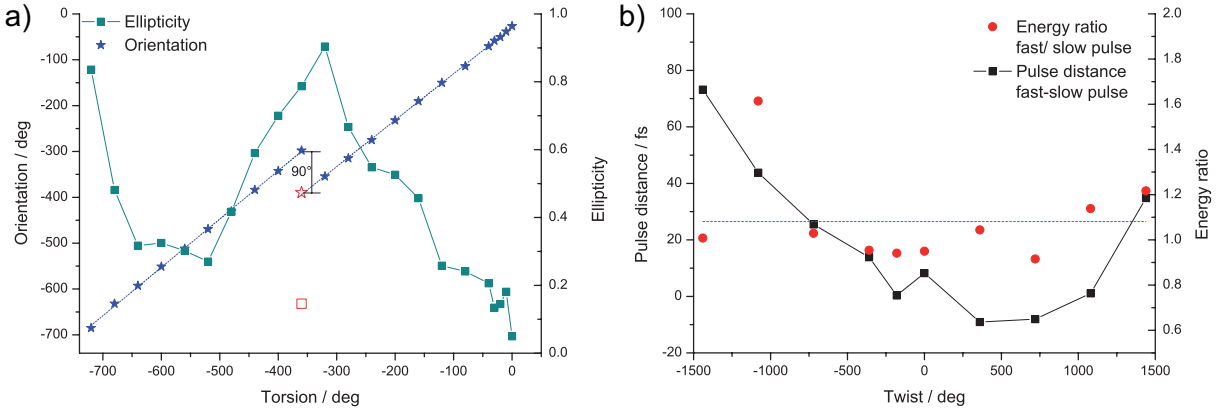


Figure 5.36: Effects on the pulse induced by twisting the hollow core photonic crystal fiber. In a), the state of polarization of the transmitted pulses is shown depending on the twist. In b), the prototype pulses – f and s pulse – are investigated. The time delay between these pulses and the ratio of the pulse intensity is analyzed.

The orientation of the transmitted pulse follows the rotation of one end of the fiber. This indicates that the optical axis of the fiber follows this rotation. In the time-dependent intensity trace no side pulses are detected. This proves that at the beginning of the fiber where the light enters the orientation of the principal axes of the fiber is not rotated. This behavior confirms the expectations for a birefringent fiber.

At a twist of $-360°$, the linear relation is interrupted by a step. The height of the step is determined to $90°$. This can be explained by an ellipticity change. When the ellipticity increases, crosses the state of circular light, and decreases again, the orientation of the

major axes of the electric field ellipse is rotated by 90°. This is proven by adding a phase shift of $\pi$ between the f and s pulse. A hollow red star indicates this data point. The orientation of electric field ellipse is flipped back by this phase shift and the straight line is continued. The pulse with the additional phase shift is nearly linearly polarized which is marked by the corresponding hollow red box. The twist position of $-360°$ where the phase shift reaches $\pi$ is purely random and is only connected to the length and the properties of the fiber.

The change of the birefringence can be observed in the curve for ellipticity. The ellipticity increases with larger twists. After approximately one rotation of the end of the fiber the pulse is circularly polarized. Then, the ellipticity decreases but does not reach the linear state of polarization before it increases again. From this observations can be concluded that by twisting the fiber a phase shift is induced. Further, there must be another torsion induced effect because the pulse in not getting linear for any twist. This is investigated by measuring the f and the s pulse independently. The amplitude ratio and the delay of the two pulses are depicted in figure 5.36b).

This graph reveals that the energy ratio between the f and the s pulse remains – within the error – constant. However, the delay between the two pulses changes by twisting the fiber. This change in the pulse delay results in a different state of polarization since the two pulses cannot interfere to the desired pulse shape.

The time shift can be observed in the cross-correlation traces for the f and s pulse, which is depicted in figure 5.37a). The same holds for distortions induced by bending the fiber. The time shift induced by a loop of 11 cm in diameter can be observed in figure 5.37b). After distortion of the fiber, new compensation parameters are required to recover complete interference and the ability to fully control the pulse.

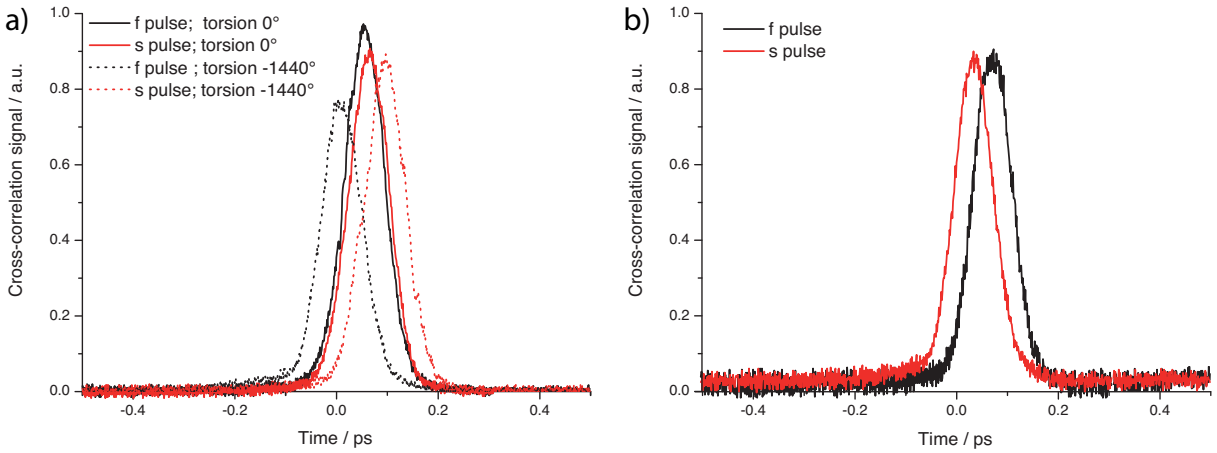


Figure 5.37: The effect of torsion and bending of the photonic crystal fiber on the f and s pulse is illustrated by two examples. The cross-correlation traces in direction of the fibers' principal axes are depicted. A torsion of 1440° results in a time delay of approximately 100 fs between f and s pulse. This is compared to the cross-correlation traces without twist: a). In b), the fiber is distorted by a loop of 11 cm. This results in a time shift of approximately 50 fs.

### A knot in the hollow core photonic crystal fiber

A knot combines the effect of twists and bends. The effect of a knot on the prototype pulses (f and s pulse) is portrayed in figure 5.38. The size of the knot can be estimated from the distance of the holes on the table which amounts to 25 mm (see 5.38a)). In this knot, the bending of the fiber is stronger than 11 cm in the example before. The cross-correlation trace of the f pulse and s pulse is depicted in figure 5.38b). A strong deviation from the undistorted prototype pulses is detected. The pulses are separated in time by 35 fs. The more important feature is the intensity distribution. The slow pulse is about 1.6 times stronger than the fast pulse. This imbalance in intensity and the time shift can be compensated to recover the optimal overlap in time and achieve optimal constructive interference. This is demonstrated for a triple pulse sequence which is generated after transmission of the knotted fiber. The time-dependent intensity and state of polarization is shown in figure 5.38c).

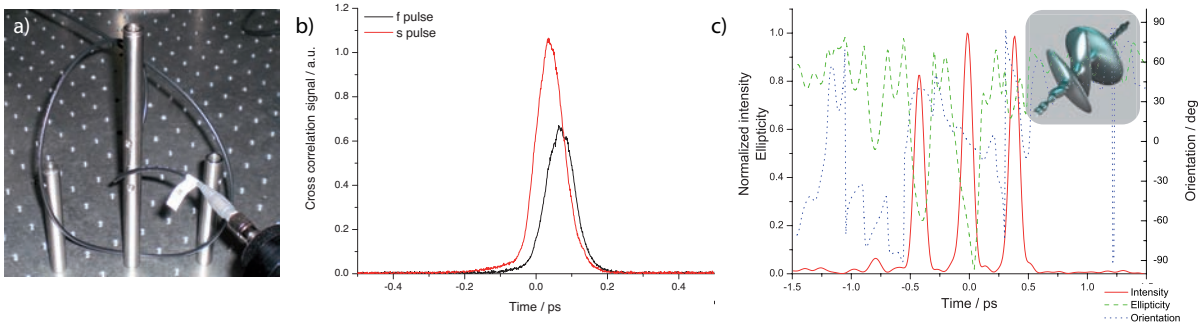


Figure 5.38: Distortion of the hollow core photonic crystal fiber by a knot. A photograph of the knot is shown in a). The knot induces changes to the compensation of the pulses. The change of the f and s pulse is observed in the cross-correlation trace: b). This shift can be adapted by a new compensation of the f and s pulse to recover the condition of optimal interferences. A triple pulse in c) serves as an example of a parametrically shaped pulse after transmission through the knotted fiber.

## 5.8 Beam profile

For the application of laser pulses, the beam profile plays an important role. Especially the size of the focus depends on the geometry and the smoothness of the beam profile. The quality of the beam profile is very poor after the pulse shaper. This is due to the reflections on the gratings and the pixelated masks of the liquid crystal modulator. Furthermore, the beam profile of shaped pulses is distorted by the effect of space-time coupling which is explained in section 3.2.4. A photograph of the beam profile of the amplified laser pulses after the pulse shaper is shown in figure 5.39a). It is very structured and asymmetric.

After transmission through the hollow core photonic crystal fiber the quality of the beam profile is improved enormously. This can be attributed to the single-mode properties of the fiber. The beam profile after transmission through the fiber is smooth and symmetric.

This is shown in figure 5.39b). It shows a Gaussian intensity distribution such as in a perfect $TEM_{00}$ mode. With this nearly perfect beam profile, the size of the focus can be reduced compared to the poor beam profile before. The reduced focal volume results in a larger field strength, which increases the yield in non-linear processes. Further, this leads to better spatial resolution in microscopy including two photon imaging.

The improvement of the beam profile also applies to other types of fibers, such as the single-mode step-index fiber which was investigated in section 5.5.

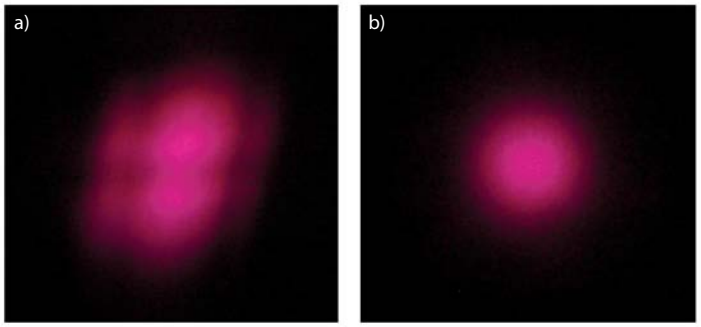


Figure 5.39: Photograph of the beam profile before a) and after b) the hollow core photonic crystal fiber.

## 5.9 Conclusion and outlook

In this chapter, the control of the light field of ultrafast laser pulses after propagation through optical fibers was demonstrated. The goal was to generate pulses arbitrarily shaped in phase, amplitude, and polarization after transmission through the fiber. In this work, two different types of fibers are investigated: a standard single-mode step-index fiber and a microstructured hollow core photonic crystal fiber. The light-guiding mechanism and the optical properties of the two fibers are entirely different. The step-index fiber is an example of a low birefringent fiber which has a large dispersion. In contrast to this, there is the photonic crystal fiber which has a very low dispersion because the light propagates in its hollow air-filled hole. But due to the asymmetry of the fiber's core it is strongly birefringent.

For the purpose of analytically controlled pulse sequences, the properties and the effects that are induced by the fibers are thoroughly investigated. The dispersion of the fiber results in temporally broadened pulses and difference in group delay. The birefringence of the fiber is important since it changes the state of polarization of the transmitted pulses. For each type of fiber, a different scheme was developed to create parametrically shaped pulse sequences. It was shown that in these sequences, which consist of a number of sub-pulses, each sub-pulse can be controlled individually and independently in its physically intuitive parameters. These parameters are energy, distance in time, phase, and chirps as well as the state of polarization, which is described by ellipticity, helicity, and orientation.

The functionality of this procedure is demonstrated on the systematic variation of single

pulse parameters exemplified on single pulses and double pulse sequences. Further, more complex multi-pulse sequences are presented.

For precise control, the energy of the transmitted pulses is limited by the occurrence of non-linear effects, such as self-phase modulation, which are determined by the core material. The scaling of the energy and the limits are investigated for both types of fibers with sub 80 fs pulses. In case of the step-index fiber, the maximal sub-pulse energy amounts to about 10 pJ for pulses with a duration of 67 fs. In the photonic crystal fiber, the suitable pulse energy is much larger because most of the light propagates in the air-filled hole. Here, shaped pulses with sub-pulse energies of 20 nJ can be obtained after propagation through the fiber.

Furthermore, the impact of twisting and bending the fiber on the pulse shape of the transmitted pulses is investigated. By adapting the pre-compensation, the shaped femtosecond laser pulses can be controlled after propagation through the distorted fibers.

The presented experiments are the first experiments in which arbitrarily and specifically shaped pulses are generated after propagation through optical fibers.

The development of these techniques provides the possibility to bring shaped femtosecond laser pulses to locations which are not accessible by an open beam. This could be used throughout the entire field of laser physics. In a laser lab, the shaped pulses can be transported safely to various places by optical fibers in a plug and play manner. This allows for a flexible use of shaped pulses on different experiments without changing optics, beam paths and re-alignment.

The methods which have been introduced can be extended to a broader range of applications and easier handling. For flexible application, it would be desirable to constantly get the same pulse after the fiber even if the fiber is moved or distorted. This could be realized by implementing a procedure which adapts the compensation parameters on the basis of a feedback signal. This could be achieved by detecting a fraction of the pulse which is reflected back through the fiber [154]. Another possibility is to employ sum-frequency generation after the fiber using micro optics, guiding light of the sum-frequencies back, e.g. in a second fiber, and detecting this light in order to compensate the pulse of the fundamental frequency.

The range of available frequencies after the fiber can be extended to multiples of the frequency range which is transmitted through the fiber. This can be achieved by using a non-linear crystal such as a BBO after the fiber. When two crystals are used with their optical axis oriented perpendicularly to each other, the control of the polarization is maintained [112]. This would allow for bringing pulses in the ultra-violet to any desired place, even if the fiber is not transparent for these frequencies.

An interesting application of the shaped pulses which propagate through the fiber is the investigation of processes which also occur within the fiber. The large field strength, the phase coherence, and the long interaction pathway in the core makes the fibers a miniature lab in which the non-linear processes such as the Raman effect or four-wave mixing can be studied [155]. The core can be filled with gasses or doped by molecules which could be investigated with shaped pulses. For this, the generation of solitons or even vector solitons in the fiber could be qualified [156, 157, 158]. Further, the generation

of super-continuum or high harmonics in the fiber could be improved or the intensity distribution could be changed [150, 159]. The highly confined light field at the end of the fiber can be employed in near field microscopy with nanometer spatial and femtosecond temporal resolution [160]. This approach is promising for surface modification beyond the diffraction limit [161].

Further, the use of optical fibers allows for employing ultrafast laser pulses in endoscopy. Especially biophysics and medicine would benefit from *in vivo* application of shaped femtosecond laser pulses. Two- or multi-photon microscopy allows for taking three-dimensional pictures of tissue [162]. Femtosecond spectroscopy would enable to specify the composition of substances in the human body. Another area of application is the photodynamic therapy and inactivation of viruses by pulsed lasers [12, 163].

# Chapter 6

# Coherent control via an optical fiber

In this chapter, the phase, amplitude, and polarization shaped pulses which are transmitted through an optical fiber are used for coherent control. The application on a molecular test system proves the functionality of the procedures which were developed and described in the previous chapter. In the experiments presented, the multi-photon ionization of the diatomic potassium molecule ($K_2$) is investigated. For this purpose, closed feedback loop optimizations are carried out in which parametrically shaped sequences are optimized. In a complementary experiment, the dynamics of the dimer is analyzed by shaper-assisted pump-probe spectroscopy. In both experiments, the parametrically phase, amplitude, and polarization shaped pulses are employed after transmission through the optical fiber.

First, the molecular beam apparatus is introduced in section 6.1. The experiments using the feedback loop optimization are presented in section 6.2. The pump-probe experiments are presented in section 6.3. The interpretation of the data including a discussion of the relevance of the polarization for efficient excitation is presented in section 6.4. This chapter closes with a conclusion in section 6.5.

## 6.1 Molecular beam apparatus

The potassium dimer is chosen as a test system because it is a very simple molecule which has already been investigated in a number of experiments and a number of theoretical calculations [2, 164, 165, 166, 167]. Further, the electronic transitions can be directly addressed by the frequency range provided by Ti:Sapphire lasers and the transmission of the hollow core fiber.

The potassium dimer is brought into the gas phase in a continuous supersonic molecular beam. This beam is produced by adiabatic co-expansion of potassium vapor and argon. A schematic of the molecular beam apparatus is depicted in figure 6.1.

A cartridge made of TZM (titanium-zirconium-molybdenum) contains the potassium which is filled under an inert gas atmosphere. By irradiative heating with wolfram filaments to about 600°C the potassium is evaporated. Together with argon at a pressure of about 2.5 bar it expands into the vacuum through a nozzle of 70 $\mu$m diameter. After passing a skimmer of 1 mm in diameter, the clusters enter the detection chamber. Here,

they interact with the shaped laser pulses which cross the beam perpendicularly. The ions which are created in the focus of the laser are extracted by ion optics and mass selected by a quadrupole mass filter (Balzers QMS-420). Then, the ions are detected by a secondary electron multiplier which signal is converted by an AD-converter and processed by the computer.

The vacuum of the differential pumped chambers is produced by a system of pumps. The pre-vacuum of about $10^{-2}$ to $10^{-3}$ mbar is provided by a rotary vane pump followed by a roots pump. The oven chamber is pumped by a diffusion oil pump (5000 l/s) which is combined with a cooled trap to prevent contamination of the chamber with oil. The pressure in this chamber is in the order of $10^{-4}$ mbar when the molecular beam is present. The detection chamber is pumped by a turbo molecular pump (2200 l/s) which keeps the pressure in the order of $10^{-5}$ mbar.

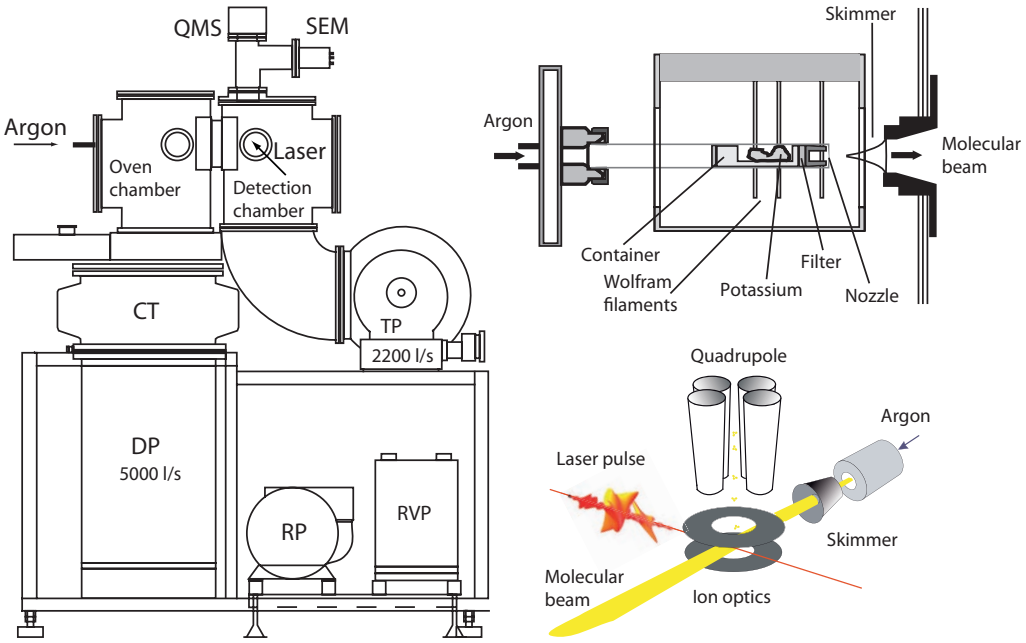


Figure 6.1: Molecular beam apparatus. The vacuum chamber consists of the oven chamber and the detection chamber separated by a skimmer. Theses chambers are differentially pumped. The oven chamber is pumped by an oil diffusion pump (DP). The detection chamber is pumped by a turbo molecular pump (TP). The pre-vacuum is created by a rotary van pump (RVP) and a roots pump (RP). In the upper right, a schematic of the oven cartridge, the heating with the wolfram filaments and the skimmer is shown. The molecules are ionized by the laser pulses and are extracted by ion optics which is depicted in the lower left. Then, the ions are mass selected by a quadrupole (QMS) and detected by a secondary electron multiplier (SEM).

The conditions for the molecular expansion are chosen in order to have mainly potassium dimers in the molecular beam. The potassium dimers have a rotational temperature below 10 K and a vibrational temperature below 50 K. Therefore, they occupy almost solely the lowest vibrational state ($v$=0) of the electronic ground state [164]. This means that the population is well-localized – energetically and spatially – which is an ideal starting point for coherent control experiments.

The detailed description of this particular molecular beam apparatus can be found in [164, 168, 169]. An overview of the principles of molecular beams can be found in [170].

## 6.2 Closed feedback loop optimization

The multi-photon ionization of potassium dimers is investigated in a closed feedback loop optimization. The ion rate of the $^{39,39}K_2$ isotopomer, which is the naturally most occurring (>86%), serves as a fitness. The laser pulses are guided by an optical fiber to the molecular beam. For this experiment, the hollow core photonic crystal fiber was used since it allows for the transmission of pulses with larger energy compared to the step-index fiber. The measurements were carried out using pulses from the oscillator as well as also stronger pulses from the amplifier. In the measurements which employed the oscillator for pulse generation, the signal-to-noise ratio was too low and the optimizations converged to many different solutions. In case of the amplified pulses, the signal-to-noise ratio was significantly larger and the reproducibility of the optimizations was better. Therefore, only these results are presented. The central wavelength of the amplified laser pulses is set to 805 nm with a spectral width of 22 nm as in section 5.6.4. For the generation of the shaped pulses, the identical pulse shaper and the same procedure as described in section 5.7 are used. After transmission through the fiber the beam size was increased with a telescope and then focused on the molecular beam in order to generate a smaller focus with higher intensity (cf. equation 3.1).

The ion signal is processed by the evolutionary algorithm described in section 2.7. The fitness of each generation is normalized by the fitness of a short pulse in order to compensate any long-term fluctuations of the molecular beam. For the optimization, the parametric sub-pulse encoding is employed which has shown to converge very fast (cf. section 4.6.2).

A triple pulse sequence was chosen because three photons were required for ionization of the potassium dimer. The energy is equally distributed to all sub-pulses. All sub-pulses are set to linear polarization either along the fast or the slow principal axis of the hollow core photonic crystal fiber. Often, a short pulse is very efficient for driving non-linear or multi-photon processes [171]. To avoid this trivial solution in which the algorithm creates one single strong pulse by shifting the sub-pulses in time the parameter space of each sub-pulse is restricted. The first and the last pulse can be shifted in a time window of $-1000$ fs to $-200$ fs and $+200$ fs to $+1000$ fs, respectively. The second pulse is fixed at zero time delay. The chirps of the sub-pulses are optimized in the limits of $\pm 3.0\times10^3$ fs$^2$ for the linear chirp, $\pm 3.0\times10^5$ fs$^3$ for the quadratic chirp, and $\pm 6.0\times10^6$ fs$^4$ for the third order chirp. The phase of each sub-pulse was optimized in the range from $-\pi$ to $+\pi$.

Different types of optimizations were carried out. The orientations of the sub-pulses in the sequences are indicated by a triple consisting of X and Y. The X corresponds to a pulse which is parallel aligned to the fast axis and Y to the slow axis of the hollow core fiber. For example, a series in which all three sub-pulses are oriented parallel is denoted as XXX or YYY. The sequences in which the second pulse is perpendicularly polarized to the outer ones are denoted as XYX or YXY. Optimizations are carried out several times for each permutation of possible sub-pulse combinations.

| Type | Average Fitness | Number of Optimizations |
|---|---|---|
| **XXX** | 1.46±0.17 | 11 |
| **YYY** | 1.69±0.12 | 6 |
| **XYX** | 1.90±0.10 | 15 |
| **YXY** | 1.81±0.12 | 8 |
| **XXY** | 1.82±0.17 | 4 |
| **YYX** | 2.03±0.28 | 12 |
| **XYY** | 1.69±0.17 | 7 |
| **YXX** | 1.87±0.09 | 3 |

Table 6.1: Fitness obtained by feedback loop optimization of parametrically shaped triple pulses. All sub-pulses are linearly polarized and oriented parallel or perpendicular. The orientation of the sub-pulses within the pulse sequence is indicated by a triple of X or Y. The table also lists the number of optimizations which have been carried out for the respective orientation.

### 6.2.1 Results of the optimization

Due to the reduced search space the algorithm converges after about 20-30 generations. The resulting pulse is characterized by the time-resolved ellipsometry scheme which is introduced in section 3.3.1. The fitness is determined by the ion signal obtained by the optimized pulse compared to the ion signal obtained by a short pulse of the same energy. The fitness values which are obtained for the respective optimizations are summarized in table 6.1. In all types of optimizations, the fitness of the optimized pulse is larger than one, which means that distributing the pulse energy to three sub-pulses with adequate chirp is better suited for multi-photon ionization of the potassium dimer than a short pulse with the same energy.

In case of the optimizations of a pulse sequence consisting of three parallel pulses (XXX and YYY), the obtained fitness is about 1.5 times better than the fitness of a short pulse of the same energy. In all other types of optimizations, the orientation of one pulse is perpendicular to the others. The fitness of these optimizations ranges from 1.7 to 2.1. This value is approximately 30% better than for a sequence of three parallel polarized pulses.

These values can be compared to the ones obtained by a single pulse. The intensity dependence of the excitation with a short linearly polarized pulse was measured and can be described by a power function ($\propto I^p$) in which the exponent was fitted to $p = 2.5 \pm 0.2$. Furthermore, an optimization of the chirp and phase of a single pulse was performed. The fitness of the optimized single pulse which is linearly polarized amounts to approximately 1.5. The shape of the time-dependent intensity shows the characteristic asymmetry of a quadratic chirp.

### 6.2.2 Optimized pulse shapes

In order to investigate the process of the multi-photon ionization, two representative types of optimized pulse sequences are selected. In one set of optimizations, the sub-pulses are all parallel oriented (XXX) and in the other set the second sub-pulse is perpendicularly oriented to the outer sub-pulses (XYX). These two sets are selected because within each set the optimal solutions are very similar. From this observation can be concluded that there are common features in the pulse sequences which are very important for the molecular excitation process.

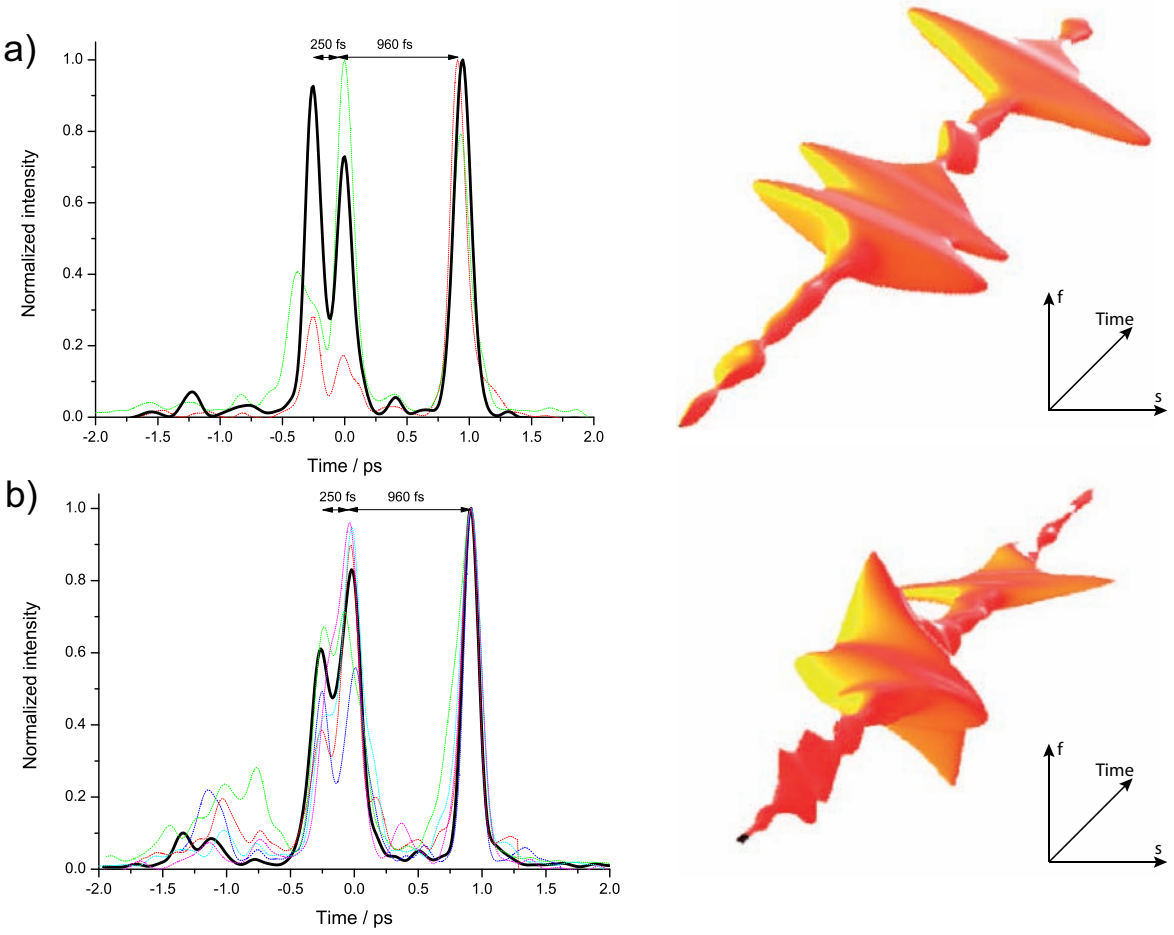


Figure 6.2: Time-dependent intensity of the pulses obtained by closed feedback loop optimization of the multi-photon ionization of the potassium dimer. For this purpose, a parametrically shaped sequence of three linearly polarized sub-pulses is optimized. The results of several optimizations is depicted. In a), all sub-pulses are oriented parallel (XXX). In b), the pulse in the middle is perpendicularly polarized to the two outer ones (XYX). In the right part of the figure, the three-dimensional representations of one optimized pulse is illustrated. The selected examples correspond to the respective black curve with the thicker line width.

The intensity evolution of the optimized pulses for the two different types of optimizations are depicted in figure 6.2. The similar and perseverative distances of the sub-pulses in the optimized pulse sequences are noticeable. The distance between the first and the second

pulse amounts to approximately 250 fs. The distance between the second and third pulse is optimized to 960 fs.

In spite of the high similarity between the cross-correlation traces of the two different types of optimizations, the fitness which is obtained differs. In case of the optimization in which all three sub-pulses are linearly polarized and oriented in one direction, the fitness amounts to $1.46 \pm 0.17$. In contrast, the fitness which is obtained by the XYX optimization is significantly larger ($1.90 \pm 0.10$). By changing the orientation of the second pulse, the fitness is increased additionally by approximately 30%. This effect can be understood by considering the orbital angular momentum of the participating electronic states. In the excitation pathway of the potassium dimer $\Sigma$ and $\Pi$ states are involved. This is illustrated in the excitation scheme in figure 6.4. The transition dipole moment of a $\Sigma \leftarrow \Sigma$ transition is oriented parallel to the internuclear axis of the molecule. On the other hand, the transition dipole moment of a $\Pi \leftarrow \Sigma$ transition is perpendicularly oriented to the internuclear axis of the molecule. These two transitions occur subsequently in the excitation of the potassium dimer. Therefore, the pulse sequence which consists of two perpendicular sub-pulses is better suited for this excitation pathway. In case of the pulse sequence of three parallel polarized sub-pulses, only the fraction of the field which is projected on the transition dipole moment acts and the overall efficiency for the two-photon excitation is reduced. This can be directly interpreted considering the scalar product of the dipole moment and the electric field ($-\mathbf{E}(t) \cdot \boldsymbol{\mu}$) which describes the interaction of a molecule with the electric field of the light (cf. section 2.5.2).

The ionization step which is performed by the third photon is not polarization sensitive since the angular momentum is carried by the emitted electron. Therefore, the relative orientation of this ionizing sub-pulse is not relevant.

## 6.3 Pump-probe spectroscopy

A popular tool for the investigation of molecular dynamics is the time-resolved pump-probe spectroscopy. In this standard technique of molecular physics, two spatially overlapping laser pulses are focussed on a sample and the signal of interest is recorded depending on the time delay between the two pulses.

Here, this procedure was carried out by shaper-assisted pump-probe spectroscopy. In order to generate the two pulses, the parametric pulse shaping technique, which has been introduced in chapter 4.2 is employed. The two pulses are created and the time delay between them was changed by the shaper as demonstrated in figure 5.28 in section 5.7.3. This makes the mechanical delay stage and the alignment of the spatial and temporal overlap, which are necessary in conventional pump-probe spectroscopy, obsolete. The experimental setup is identical to the one used in the feedback loop optimization. Again, these measurements were carried out with pulses which were transmitted through the hollow core fiber before they interact with the molecular beam.

Pump-probe spectra are recorded for two parallel pulses (XX) and for a pair of perpendicular pulses (XY). The time delay was scanned from $-2\ 000$ fs to $+2\ 000$ fs in steps of 8 fs while the ion signal was recorded. In order to compensate for the effect of fluctuations of the molecular beam, the average of several XX and XY type of pump-probe

traces is taken. The resulting transients are depicted in figure 6.3a). The transients show an oscillatory behavior for parallel and perpendicular pairs of pump-probe pulses. The signal peaks for coincidence of the parallel pump and probe pulses. This is an artifact of the parameterization of the pulse sequence. When the two pulses are not delayed to each other, the available pulse energy is nearly doubled.

In order to determine the oscillation frequency in the pump-probe scans, a fast Fourier transformation was performed on the delay-dependent ion signal. To exclude the effects which occur at zero delay, the signal is separately processed for positive and negative delays. The Fourier spectrum for both types of pump-probe scans (XX and XY) is depicted in figure 6.3b). The spectra of the XX and the XY pump-probe scans show frequency components which correspond to an oscillation period of 250 fs and 500 fs, respectively. In case of the pump-probe scan of two perpendicular pulses, an additional frequency component contributes which corresponds to an oscillation period of about 960 fs. The oscillation periods of 250 fs and 960 fs are also found in the sub-pulse delays of the optimized pulses.

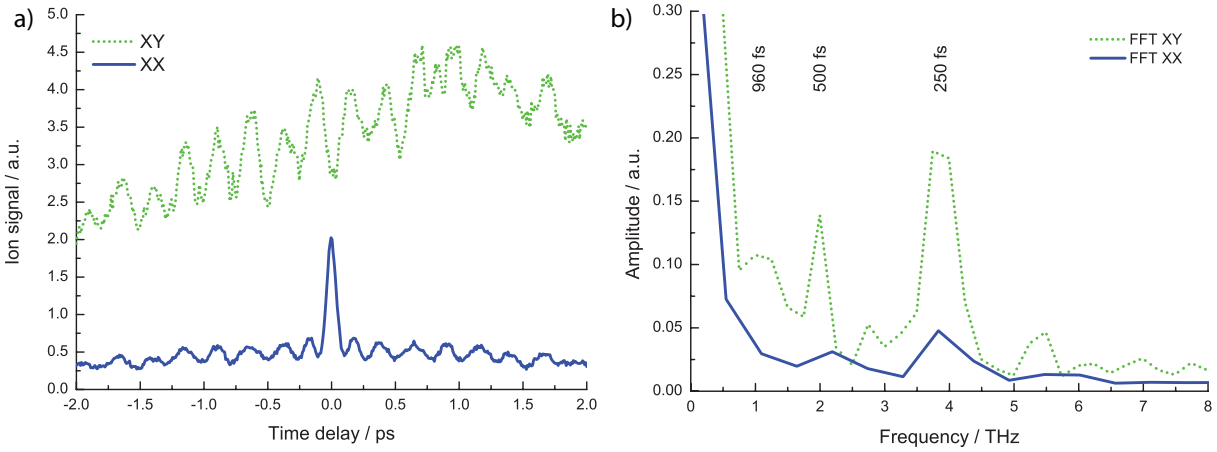


Figure 6.3: Investigation of the multi-photon ionization with shaper-assisted pump-probe spectroscopy using pulses which are transmitted through a hollow core photonic crystal fiber. In a), the transients obtained by parallel pump and probe pulses is compared to the case where pump and probe pulse are perpendicular. In b), the analysis of the oscillations in the transients by fast Fourier transformation is depicted.

## 6.4 Excitation dynamics

Pump-probe experiments are very well-suited to reveal information about the dynamics in the excitation process. The ionization of the potassium dimer is achieved in two excitation steps. Each is driven either by the pump or the probe pulse. Since the ionization process requires three photons two excitation pathways exist when neglecting the three-photon transition, which is very unlikely. The fraction in the ion signal which is produced by the three-photon transitions is not expected to contribute since the probability of these processes is significantly smaller.

Path A (1×pump, 2×probe) is indicated by the dashed yellow lines in the excitation

scheme depicted in figure 6.4. The first pulse creates a wavepacket in the $A^1\Sigma_u^+$ state. In this first excited state, the wavepacket oscillates with a period of 500 fs before it is transferred to the ionic state by a resonant two-photon transition. The transient Franck Condon point strongly depends on the wavelength of the exciting pulse. For the used wavelength, the resonance condition yields a transition point which is situated before the classical turning point of the wavepacket [167]. Therefore, the wavepacket crosses this transition point twice in one oscillation. The equidistant order of the modulation suggests a transition point which is situated temporally symmetric in between the classical turning points. This results in a doubled frequency in the modulation of the ion signal in the pump-probe trace. The distance of the first maxima to zero delay of the two pulses is approximately 120 fs to 170 fs. This is shorter than the oscillation period in the transient which supports the explanation with the central transition point.

Path B (2×pump, 1×probe) is indicated by the purple dotted arrows in figure 6.4. Starting from the ground state, a wavepacket is created in the second excited state $2^1\Pi_g$ by a two photon transition. The investigation in [167] reveals an oscillation period of roughly 750 fs in this state. However, due to the bandwidth of the pulses used in this experiment, which is almost three times broader, the population of higher vibrational states is favored due to larger Franck Condon factors. This results in a longer round trip time of 960 fs for the wavepacket. This wavepacket is then transferred to the ionic state which is more likely at the outer turning point. This is due to the Franck-Condon factors which depend on the internuclear distance [167].

With this information about the excited state dynamics, the pathway of the optimized pulse can be revealed. It is marked by the red arrows in the excitation scheme which is depicted in figure 6.4. The solid vertical lines indicate the one-photon transitions which are driven by each sub-pulse of the optimized pulse sequences. The first pulse creates a wavepacket in the $A^1\Sigma_u^+$ state. After 250 fs, this population is transferred to the $(2)^1\Pi_g$ state by the second pulse. The transition at the center is not allowed due to the temporal restrictions in the parameterization. Further, the wavepacket is shaped due to the chirp of the first pulse which might also shift the temporal position of the optimal transition point. In this $(2)^1\Pi_g$ state, the wavepacket cycles one full period before it is transfered to the ionic state. This explains the delay of 960 fs between the second and the third sub-pulse.

## 6.5 Conclusion and outlook

In this chapter, a new method for coherent control in remote places using optical fibers was introduced. Here, a hollow core photonic crystal fiber was employed to guide amplified ultrafast laser pulses to the desired object. The femtosecond laser pulses were shaped in phase, amplitude, and polarization after transmission through the fiber. The independent and unrestricted control allows for the implementation of a parametric pulse shaping approach in which the intuitive parameters of a pulse sequence are controlled. The capabilities of the pulse shaping techniques in combination with the fiber were demonstrated on the multi-photon ionization of the diatomic potassium molecules.

This process was investigated by shaper-assisted pump-probe spectroscopy and in a closed

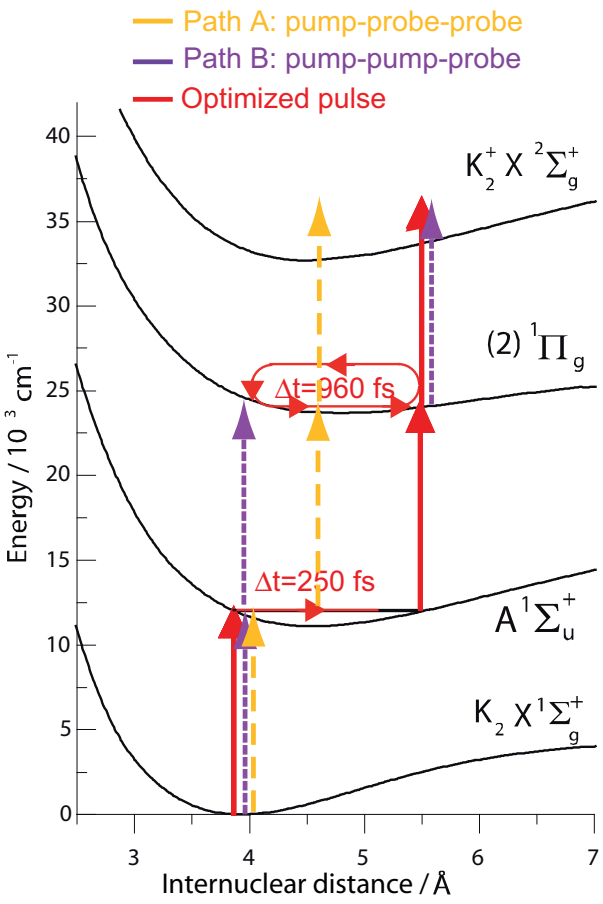


Figure 6.4: Potential energy curves for the potassium dimer. In this excitation scheme, different excitation pathways are marked. Vertical arrows indicate the single photon transition. The path A and B which occur in pump-probe excitation are represented by the yellow dashed and the purple dotted lines. The pathway excitation pathway of the optimized pulse is plotted with solid red lines. Potential curves are adapted from [172, 173].

feedback loop optimization. Both experiments are based on parametrically shaped pulse sequences and consistently revealed the vibrational dynamics in the electronic states which participate in the multi-photon ionization. It has been shown, that the parameterization in a pulse sequence is optimally suited for the investigation of excitation dynamics in simple molecules. The obtained pulse pattern is easier to interpret since it only consists of a few sub-pulses compared to free optimizations in which abstract parameters such as voltages of the modulator are optimized. In the presented example of the multi-photon ionization, each sub-pulse was directly associated with an excitation step.

Further, the relative orientation of the transition dipole moments was considered by including the polarization control. This increased the ion signal which highlights the relevance of polarization shaping.

In the future, it would be interesting to apply the parametrically shaped pulses to more complex systems to investigate their dynamics. These parametrically phase, amplitude, and polarization shaped pulses are not only usable for investigating but also for active control of the excitation. An interesting experiment has already been started in collaboration with R. Dörner. This experiment investigates the excitation pathway of an optimal pulse using the COLTRIMS technique [174, 175]. If successful, this would allow for tracking the reaction path and identifying the participating states.

# Chapter 7

# Ultrafast excitation dynamics in ultracold gases

In this chapter, the investigation of ultracold matter with femtosecond laser pulses is presented. Propelled by a number of theoretical proposals for pulsed photoassociation, which occurred in 2006, a cooperation with the group of M. Weidemüller was initiated. Merging the world of ultracold atoms with the world of shaped ultrafast laser pulses was promising to realize the photoassociation of ultracold atoms to molecules with femtosecond laser pulses. These experiments were the first of this kind. The series of experiments in this cooperation yielded a number of results, which were supported by theoretical calculations of C. P. Koch *et al.*. In this work, some of these results are presented which were not obvious in the beginning but helped in combination with the corresponding theoretical calculations to understand the interaction process of the ultracold atomic ensemble with the field of the laser pulse. Further, a closed feedback loop optimization on the multi-photon ionization of ultracold rubidium molecules is presented, which utilizes parametrically shaped femtosecond laser pulses.

This chapter is structured as follows: in section 7.1, a motivation for the interest in ultracold molecules is given. This is followed by a review of techniques to obtain cold and ultracold molecules including an introduction to the photoassociation process. In section 7.2, an overview of the experiments concerning pulsed photoassociation is given and set in relation to the results of the experiments presented here. The experimental setup is described in section 7.3. The magneto-optical trap and the setup for the time-resolved pump-probe measurements are explained. The methods used for the theoretical calculations are presented in section 7.4. The results of the pump-probe experiments and the corresponding quantum-dynamical calculations are presented in section 7.5 followed by an analysis of the interaction process. In section 7.6, the results obtained by closed feedback loop optimization of the multi-photon ionization of ultracold rubidium molecules are presented. The interpretation reveals the excitation pathway. Finally in section 7.7, a conclusion is given followed by an outlook.

## 7.1 Ultracold molecules

The invention of quantum mechanics revolutionized the entire field of physics and the related fields of science. With these developments the interest in cold matter increased since quantum effects become more apparent at low temperatures. In the course of the time, the temperature limit which could be experimentally reached was pushed towards the absolute zero point of 0 K. Nowadays, it is distinguished between the cold (1 mK-1 K) and the ultracold temperature regime (<1mK). At these low temperatures, the wave-particle duality of matter start to get relevant and the particles – atoms and molecules – can be described by their de Broglie wave. The de Broglie wavelength increases with decreasing temperatures. Further, less states are populated which allows for state selective excitation and investigation.

The invention of laser cooling and trapping was the key to create ultracold atomic samples [176, 177]. These inventions were awarded with the Nobel Prize in 1997 for S. Chu, C. Cohen-Tannoudji, and W. D. Philips. The temperature of this atomic ensemble was further decreased to quantum degeneracy. At this point, the atoms can be described by one common wavefunction. This new state of matter was already proposed by S. Bose and A. Einstein. Therefore, it is named Bose-Einstein condensate (BEC). The experimental realization of a BEC was also honored with the Nobel Prize in 2001 for E. A. Cornell, W. Ketterle, and C. E. Wieman [178, 179]. One of the first applications of the BEC was an intense coherent matter beam analog to the photon beam of the laser [180]. Many different applications followed and a new category of physics was established.

The impact of creating ultracold molecules is expected to be as large and profound as in the case of ultracold atoms. Due to their internal degrees of freedom molecules offer a richer level structure and are, therefore, more complex and thus more interesting.

These ultracold samples of molecules can be used for ultrahigh-precision spectroscopy to determine lifetimes, to analyze the time-dependency of fundamental constants, or to investigate the long-range dipole-dipole interaction. The cross sections in molecule-molecule or molecule-atoms collisions are different at ultracold temperatures. Their investigation provides information about the long-range interaction potentials, which are difficult to predict by theory. Further, ultracold molecules have properties which go beyond the molecular physics of today. They could be used to verify the standard model of particle physics. Here, the parity violation and the determination of the possible dipole moment of the electron are to be referenced. Due to the long coherence time ultracold molecules could be employed for quantum computing and quantum simulations.

Similar to the applications of an atomic BEC, which were not thought of 20 years before, the molecular condensate would have a large variety of new applications. A comprehensive overview about the science, technology, and the applications of cold and ultracold molecules was recently published in [181].

A direct transfer of the laser cooling scheme to molecules is not possible due to the complex structure of molecular energy levels. Yet, there are several theoretical considerations for a few molecules in which a closed cooling cycle might be implemented [182, 183, 184]. In a first experiment, momentum transfer on a molecule by optical cycling was demonstrated [185].

Different approaches have to be applied to obtain cold or ultracold molecular ensembles. These approaches can be divided into two different classes: the direct cooling and the indirect pathway in which atoms are assembled to molecules.

### 7.1.1 Direct cooling

The direct cooling procedures start with an ensemble of rather hot molecules which are subsequently cooled. A very versatile technique is sympathetic cooling, which can be applied to any molecule or atom for neutrals and ions. The molecules are loaded in a cryogenic cell which is additionally filled with a buffer gas. By collisions of the molecules with the buffer gas they thermalize and are cooled close to the temperature of the buffer gas. To produce a pure molecular beam separated from the buffer gas, magnetic or electric field guides can be positioned behind the output of the cell. The temperatures which can be reached by this method are about a few hundred mK for helium as a buffer gas [186, 187].

Other techniques use a molecular beam as a source for the molecules. These molecules are already rotationally and vibrationally cold (cf. section 6.1). The beams can be slowed down by different methods. A mechanical approach utilizes a rotating nozzle [188]. This allows for producing a slow molecular beam in the lab frame. In the collision of two perpendicular molecular beams cold molecules are produced [189]. This method is applicable to many molecular species but the production efficiency and the resulting temperatures are very limited.

Electric or magnetic fields are employed to produce and trap cold molecules. A molecular beam which consists of polar molecules in a selected quantum state can be slowed down to arbitrary low velocities, which correspond to very low temperatures, by employing the Stark effect. A Stark decelerator consists of a sequence of electrodes which can be switched with an alternating voltage. A molecule which resides in a low field seeking state and enters a region with a higher field looses kinetic energy. In a Stark decelerator the fields of the electrode sequences are switched when the molecule is still in the high field. Therefore, kinetic energy cannot be regained. By appropriately switching of the voltages a bunch of molecules is traveling against a potential well, looses energy at each stage, and is slowed down. The velocity distribution of the slow molecules is very narrow [190, 191, 192].

All these direct cooling methods are limited so far to the regime of cold molecules with temperatures above 1 mK. In order to obtain molecules that are ultracold, which is defined as the temperature range below 1 mK, different approaches are required.

### 7.1.2 Association of ultracold atoms

An entirely different approach is used for the generation of ultracold molecules. These methods start with an ultracold ensemble of atoms which is produced by using the well-established techniques of laser cooling and trapping. These ultracold atoms are then assembled to ultracold molecules by magnetic or optical fields.

### Feshbach resonances

One procedure utilizes a Feshbach resonance, which is a magnetically tunable scattering resonance. Due to the different magnetic moments of the colliding atom pair and the molecule their energies can be matched by tuning an external magnetic field. The state of the unbound colliding atom pair is coupled to the bound molecular state. After the formation of molecules the molecular potential is returned to the unperturbed initial state while the molecules remain bound [193]. The formation of ultracold molecules has been demonstrated for the first time in 2003 [194, 195]. These molecules are produced in the excited state. By subsequent spontaneous emission the molecules can relax to the ground state. In both states, the molecules are vibrationally highly excited. For stabilization of these molecules, a STIRAP process (cf. section 2.6) can be employed for the transfer to deeper bound states or even to the lowest rotational vibrational state in the ground state [196, 197, 198].

### Photoassociation

The other pathway is denoted as photoassociation, which utilizes photons for the molecule formation. The concept was introduced by H. R. Thorsheim *et al.* in 1987 and was successfully realized in the production of the sodium dimer in 1993 by P. D. Lett *et al.* [13, 199]. A schematic of this process is depicted in figure 7.1a). A narrow bandwidth continuous wave laser excites an ultracold atom pair in the electronic ground state. This laser is red detuned to the atomic resonance. At resonance, one vibrational level in the molecular excited state is populated. The transition can be interpreted as a vertical transition which occurs at long internuclear distances that are in the order of 100 $\mathring{A}$ [200]. This process benefits from the different r-dependencies of the potential curves of the ground state ($\propto r^{-6}$) and the first excited state ($\propto r^{-3}$).

The bound molecules in the excited state are vibrationally highly excited. These photoassociated molecules have a short lifetime and decay back to the ground state by spontaneous emission. Depending on the internuclear distance and the Franck-Condon factors the final state is again an atom pair or a loosely bound molecule. This has been demonstrated first for homo-nuclear molecules in a magneto-optical trap for cesium and rubidium [201, 202]. These techniques have been extended to create ultracold hetero-nuclear dimers [203, 204]. Similar to the Feshbach molecules these dimers have been transferred to more deeply bound molecular states [205, 206].

The trapping lasers in a magneto-optical trap can also photoassociate atoms, which results in a constant molecular production rate. This has been found for rubidium and lithium-cesium magneto-optical traps [207, 208].

## 7.2 Pulsed photoassociation

The idea to employ pulsed lasers for photoassociation dates back to 1994. In a theoretical proposal of M. Machholm *et al.*, a pump-probe scheme is suggested in order to utilize wavepacket dynamics in the excited state for bond formation [209]. The excitation by

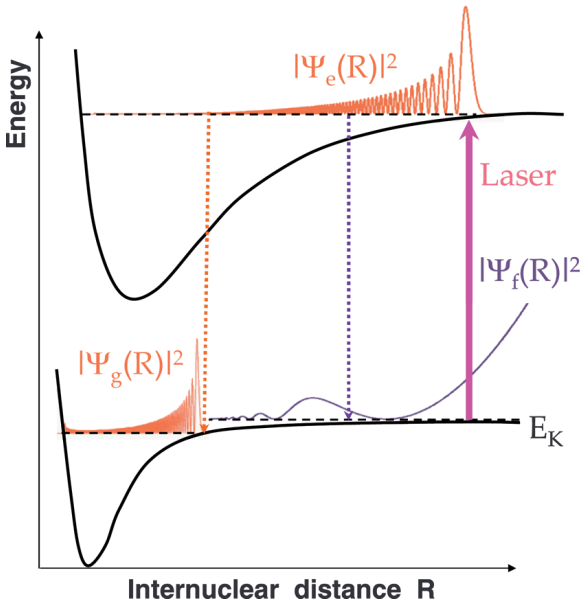


Figure 7.1: Production of ultracold molecules by photoassociation using a continuous wave laser with a narrow bandwidth. The laser transition is indicated by a vertical arrow. The excited state decays back to either a bound state (red dotted line) or a pair of free atoms (blue dotted line). The absolute square of the wavefunctions of the molecular ground and excited state are indicated by a red line. The curve which corresponds to a free pair of atoms is plotted in blue.

the laser pulses forms a wavepacket at long internuclear distances. This wavepacket propagates in the attractive molecular potential to smaller internuclear distances, which could be probed by a second laser pulse. An experiment that is very closely related to this proposal was carried out by F. Fatemi *et al.* in 2001 [210]. They used picosecond pulses for the pump-probe measurements and observed a dramatic flux enhancement on a nanosecond time scale due to the motion on the intermediate potentials. However, they could not observe wavepacket dynamics. A number of theoretical proposals followed which analyzed different prospects of pulsed photoassociation.

The advantage of laser pulses is their large spectral width, which allows for simultaneous excitation of several states and creation of a wavepacket. This wavepacket can be controlled by employing the techniques of pulse shaping and coherent control, which are introduced in section 2.6. These powerful tools have been proven successful in controlling the final state in an excitation process in many fields of physics and chemistry [211].

Shaped femtosecond laser pulses would allow for tailoring the field to the specific system for example by chirping. In a down-chirped pulse the laser is in resonance over a finite region of internuclear distances and follows the wavepacket on the way to smaller internuclear distances [14, 15, 16]. The parameters of the pulse can be chosen to fulfill the conditions for a $\pi$-pulse, which adiabatically transfers the population from the unbound ground state to a bound excited state. The corresponding experimental implementation of photoassociation with chirped nanosecond laser pulse was reported by M. J. Wright *et al.* in 1995, which was the first approach to coherently control the molecule formation [28].

By shaping the wavepacket it could be temporally focused to be well-localized at the inner turning point in the excited state. This would support the transfer from the long bound excited molecule to shorter internuclear distances and make the transition to deeply bound states in the ground state of the molecule by a dump pulse more efficient [15, 212, 213]. Further, pulsed lasers are suggested to stabilize the photoassociated molecules [17, 18]. Particularly, the publications of C. P. Koch motivated the experimental implementation of laser pulses for photoassociation.

### 7.2.1 Femtosecond photoassociation: what has been done so far?

The first femtosecond experiments were initiated in 2004 in collaboration with the group of M. Weidemüller with the long-term goal of creating ultracold rubidium molecules in the ground state using coherent control. A second experiment was set up at the same time in Oxford in the group of I. A. Walmsley. In these first experiments, the creation of molecules in the ground state by femtosecond laser pulses was not successful. Instead of increasing the molecular population in the ground state the existing molecules were destroyed. This process was investigated in order to get information about the process which counteracts the molecular formation. The power-dependence of the destruction of molecules was explained by a rate equation. Furthermore, we carried out a closed feedback loop experiment in which the phase and amplitude of the femtosecond laser pulse was optimized in order to destroy the existing molecules which are present in the trap due to photoassociation. The spectra of the resulting pulses exhibited some similarities which could be attributed to excitation to fragmenting channels [214]. Later, the Oxford group published the suppression of molecular formation by chirped femtosecond laser pulses [215].

In a second campaign, which started in 2006, the project of femtosecond photoassociation of ultracold molecules was resumed. This time, a more dedicated experimental setup was used. Implementing a dark SPOT increased the density of atoms in the magneto-optical trap. The creation of molecules in the first excited state was investigated by two-color femtosecond pump-probe spectroscopy. Employing a quadrupole mass filter allowed for the continuous measurement of the molecular ion signal. With this setup, which is described in detail in section 7.3, many pump-probe experiments were carried out. The excitation scheme is depicted in figure 7.2a). In these experiments, the atomic resonance was removed by amplitude shaping from the pump pulse with a sharp knife-edge in the Fourier plane of the pulse shaper. The intensity of the pump pulses is situated only red to the atomic resonance, which is under investigation, in order to address the bound levels in the excited state (cf. figure 7.2b)). Examples of the resulting molecular transients for pulses, which are red detuned, are depicted in figure 7.2c). The resulting transients showed an oscillatory behavior which is strongly dependent on the cut-off detuning respective to the atomic resonance. Parallel to that, similar dynamics are observed for the fluorescence of the trap which indicate delay-dependent losses from the ultracold atomic ensemble [216, 217]. This dependency of the molecular transients was thoroughly investigated with pulses which addressed the states corresponding to the $D_1$ and the $D_2$ resonance, respectively. All these measurements were performed for different intensities and various linear chirps of the pump pulse. Further, the dependency on the atomic density in the magneto-optical trap was investigated. Additionally, the population in the ground state was analyzed for different configurations of the hyperfine structure. This large set of data was supported by quantum dynamical calculations of the corresponding process. The main results are summarized in [218]. A detailed description of the experiments can be found in [216]. The corresponding theoretical considerations and the interpretation are explained in [219].

The group in Oxford also proceeded with a modified setup. The experimental setup which they used is very similar to ours. They also investigated the photoassociation

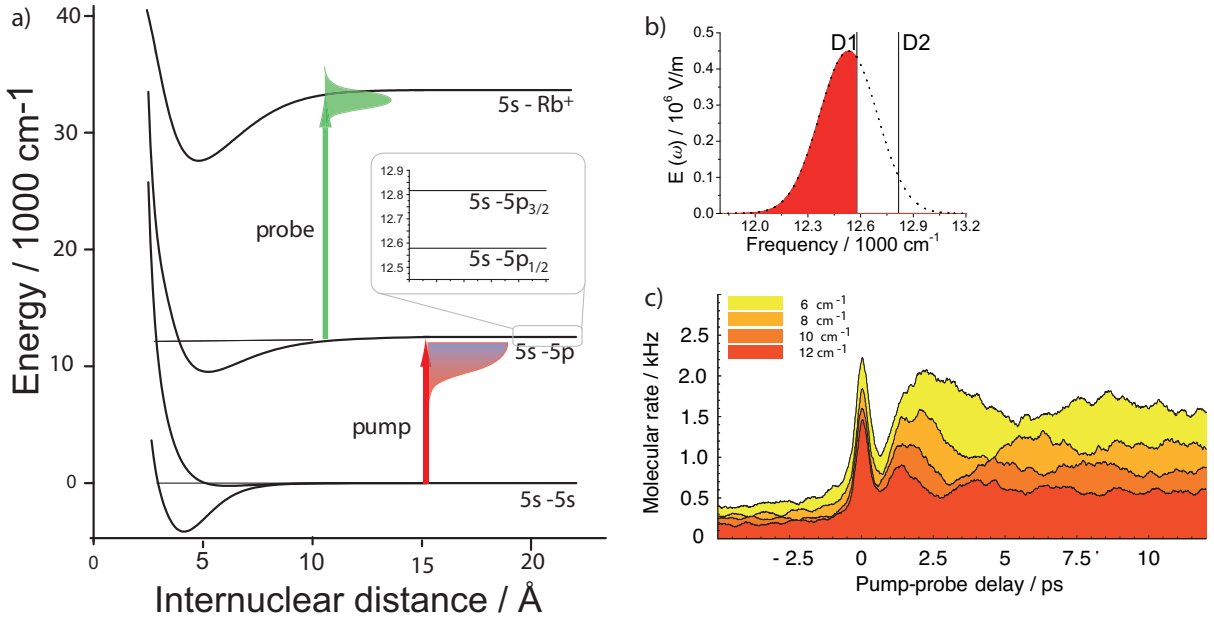


Figure 7.2: Investigation of the photoassociation with femtosecond laser pulses. In a), the pump-probe excitation scheme is shown. b) depicts the frequency-modulated pump pulse which is red detuned to the atomic $D_1$ resonance. In c), the resulting transients are displayed for different cut-off positions.

process by pump-probe spectroscopy with the emphasis on the dynamics on longer time scales [220, 221].

In this context, another example for femtosecond photoassociation should also be mentioned. The coherent bond formation by femtosecond laser pulses was also studied by pump-probe spectroscopy in hot gases. In a vapor cell at temperatures of about 160°C mercury forms van der Waals clusters. These loosely bound clusters are the starting point of this experiment. The nearly free Hg atoms are transferred to the bound excited state of the dimer by a femtosecond laser pulse. This state is probed by the depletion of laser induced fluorescence. However, wavepacket oscillation was not observed in this experiment [222, 223].

### 7.2.2 How does this work contribute to the understanding of femtosecond photoassociation?

The interpretation of the molecular transients was not obvious in the beginning. Wavepacket oscillations which were expected and hoped for seemed not to explain the underlying process. The oscillation period in the pump-probe experiment was one order of magnitude shorter than expected. Furthermore, the dependence of the oscillation period in the molecular pump-probe spectra on the cut-off detuning is not consistent with any physical potential. It was not understood for a long time how the pulse interacts with the ultracold atomic ensemble. Therefore, many experiments were performed to collect indications for a model of the excitation process.

A pump-probe measurement which utilized different spectral shapes of the pump pulse

contributed additional puzzle pieces. The transients resulting from pump pulses with a blue detuned spectrum were very similar to the transients of red detuned pulses. The pulses which are blue detuned only address unbound states in the excited state. With this data the approach of interpretation of bound molecule formation by populating vibrational levels in the excited state including the connected wavepacket propagation was finally destroyed. The questions remaining were: what is the underlying process and does the femtosecond laser photoassociate ultracold atoms to molecules?

These questions were answered with the help of quantum dynamical simulations which precisely described all measured data. Here, the experiments are presented which utilized blue detuned pulses and which were, in the beginning, counterintuitive regarding the naive picture of femtosecond photoassociation. This data is presented along with the corresponding theoretical calculations. Further, the transients for blue detuned pulses are compared to the one obtained with red detuned pulses. Moreover, different spectral shapes which enclose nearly the full bandwidth or only a narrow fraction of the femtosecond laser pulse were applied to test the theoretical model. Taken together, the analysis of this data provides a complete picture of the process.

## 7.3 Experimental setup

### 7.3.1 Magneto-optical trap

A magneto-optical trap provides the ensemble of ultracold rubidium atoms. The magneto-optical trap makes use of the laser cooling and the spatially dependent radiation pressure in an inhomogeneous magnetic field. Laser cooling of neutral atoms was suggested by T. Hänsch and A. Schawlow in 1975. This scheme utilizes the Doppler shift, which occurs when atoms move relative to the light source. When atoms move in direction of a laser which is red detuned respective to the atomic resonance, they get in resonance and absorb a photon. Due to the momentum of the photon – $\mathbf{p} = \hbar\mathbf{k}$ – an impulse is transferred. After the lifetime of the atom it relaxes back to its ground state by spontaneous emission of a photon. In many excitation-emission cycles the impulse of the spontaneously emitted photons is averaged to zero and a net impulse is transferred to the atom in direction of the laser and the kinetic energy of the atom is reduced. For cooling to occur, the lasers must illuminate the atom in all six spatial directions. This arrangement is denoted as optical molasses since the atoms feel a force contrary to their direction of movement similar to a particle in a viscous medium.

For spatial confinement of the atoms, a spatially varying magnetic quadrupole field is created in the intersection of the six laser beams. This configuration of lasers and the pair of coils in anti-Helmholtz configuration is denoted as magneto-optical trap (MOT) and is depicted in 7.3a). This magnetic field causes Zeeman splitting of the energetically degenerated hyperfine states. The splitting increases with the distance from the center of the trap. This brings an atom that moves outwards in resonance with the laser and increases the probability of excitation and momentum transfer. The direction transfer is determined by the polarization of the laser which is left-handed circular in one direction and right-handed circular in the other direction. The selection rules for the transition only

allow an impulse transfer in direction of the center of the trap. The excitation scheme is illustrated in figure 7.3b). Real atoms have more than a single state in which they can relax by spontaneous emission that can be seen in the term diagram of $^{85}$Rb depicted in figure 7.3c). The cooling laser does not address these states and the atoms are lost. In order to close the optical cycle and return these atoms to the trap a second repump laser is required.

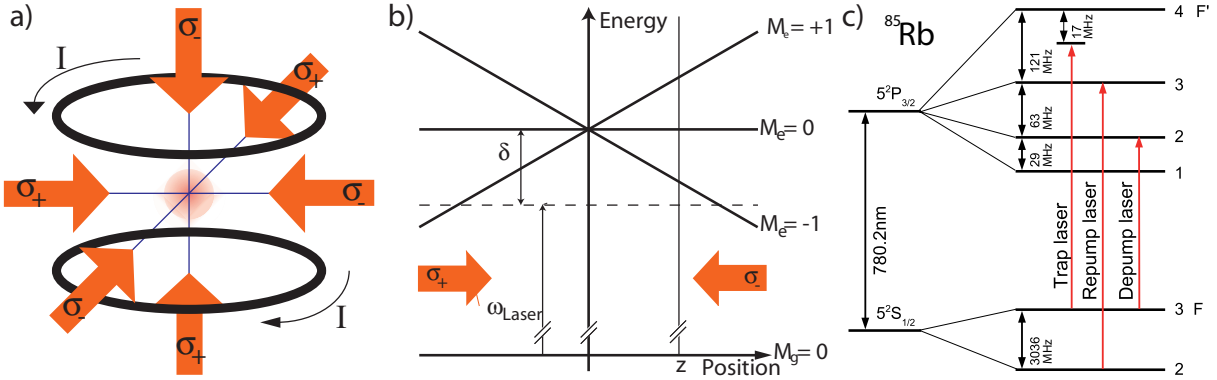


Figure 7.3: Principle of a magneto-optical trap. In a), the arrangement of the lasers and the magnetic field is depicted. The Zeeman splitting and optical pumping by circularly polarized light results in a direction-dependent radiation pressure: b). The term scheme of $^{85}Rb_2$ is displayed in c). The transitions which are addressed by the lasers are indicated by vertical red arrows.

### Dark SPOT

The density of the magneto optical trap can be increased by one order of magnitude when it is operated in dark SPOT configuration [224]. This acronym stands for dark spontaneous optical force trap. In a standard magneto-optical trap the density is limited by scattering and reabsorbtion of trap light. This results in an outwards-directed force and counteracts the compression force of the trap. This can be prevented when the atoms are stored in the lower F=2 hyperfine ground state, which is far detuned from the trapping laser. This state can be reached via off-resonant excitation of the F'=3 state or additional excitation with a depump laser and subsequent spontaneous emission. The repump laser in standard MOT configuration returns this population back to the cooling cycle. When the intensity of the repump beam in the center of the trap is removed, the atoms remain in the lower F=2 hyperfine state, which is denoted as dark state. Therefore, atoms are not excited in the center of the trap and the radiation pressure in the center of the trap is minimized. The distribution of the population of the two hyperfine ground states is described by the bright state fraction $p$.

$$p = \frac{N_{F=3}}{N_{F=3} + N_{F=2}} \tag{7.1}$$

The bright state fraction can be tuned by intensity variation of a fill-in beam of repump light and an additional depump laser. The bright state fraction is connected to the density

of the trap. For the standard MOT configuration, p is equal to one. The density increases as p is reduced. The maximal density is found at p=0.1. For smaller p, the density decreases again [225]. In this work, the measurements are carried out in dark SPOT with p=0.1 and normal MOT configuration with p=1.0. This corresponds to densities of $10^{11}$ atoms/cm$^3$ and $10^{10}$ atoms/cm$^3$, respectively.

**The portable MOT**

The magneto-optical trap which was used in these experiments was constructed by W. Salzmann. The specification of the trap and a detailed description can be found in his dissertation [226]. A special feature of this trap is the high mobility, which simplified the transport from Freiburg to the laboratory in Berlin and allowed for the experiments combining the femtosecond laser system and the ultracold atoms.

The laser system of the trap consists of two home-built extended cavity grating diode lasers. They were actively frequency stabilized to the respective transition within a few MHz by Doppler free frequency modulation spectroscopy. The trapping laser is red detuned by several line width to the $F' = 4 \leftarrow F = 3$ transition using an acousto-optical modulator. The repump laser drives the $F' = 3 \leftarrow F = 2$ transition and is detuned by 30 MHz. The laser beams are guided by polarization maintaining single-mode optical fibers to the vacuum chamber. For the dark SPOT configuration, the core of the repump beam is blocked by a disc of 3 mm in diameter that is imaged into the trap by a telescope.

The laser beams are crossed in the vacuum chamber where the magnetic field is placed, which is generated by two coils in anti Helmholtz configuration. The vacuum is sustained by a titanium sublimation pump and an ion-getter pump at a pressure of about $10^{-10}$ mbar. The MOT is loaded with rubidium captured from the background gas which is enriched by electrically controllable dispensers. The trapped atoms in the magneto-optical trap have a temperature of about 100 $\mu$K.

The interaction with the laser pulses can be monitored by recording the fluorescence and the detection of the produced ions. The fluorescence of the trap is a measure for the atomic density. It is collected with a lens and detected by a photodiode. The atomic and molecular ions produced in the trap are extracted by an electric field of 40 Vcm$^{-1}$ created by a push and pull electrode, then mass filtered by a radio frequency quadrupole, and detected by a channeltron with single ion detection efficiency.

Further, the ion detection can be used in a time of flight modus. This option is valuable when the ground state molecules are detected by resonantly enhanced two-photon ionization (REMPI) with a Nd:YAG pumped dye laser operated at 602 nm with 10 mJ pulse energy and a repetition rate of 10-20 Hz.

### 7.3.2 Setup for two-color pump-probe spectroscopy

For time-resolved measurements, the pulses from the regenerative amplifier are used at a repetition rate of 100 KHz. The central wavelength is set to 795 nm for the experiments at the atomic $D_1$ resonance addressing the states of the electronically excited $5s + 5p_{1/2}$ state. In the measurements concerning the $5s + 5p_{3/2}$ states corresponding to the atomic

$D_2$ resonance, the central wavelength is set to 785 nm. The spectral width amounts in both cases to 25 nm FWHM. The pulse energy of about 4 $\mu$J is divided by a beam splitter.

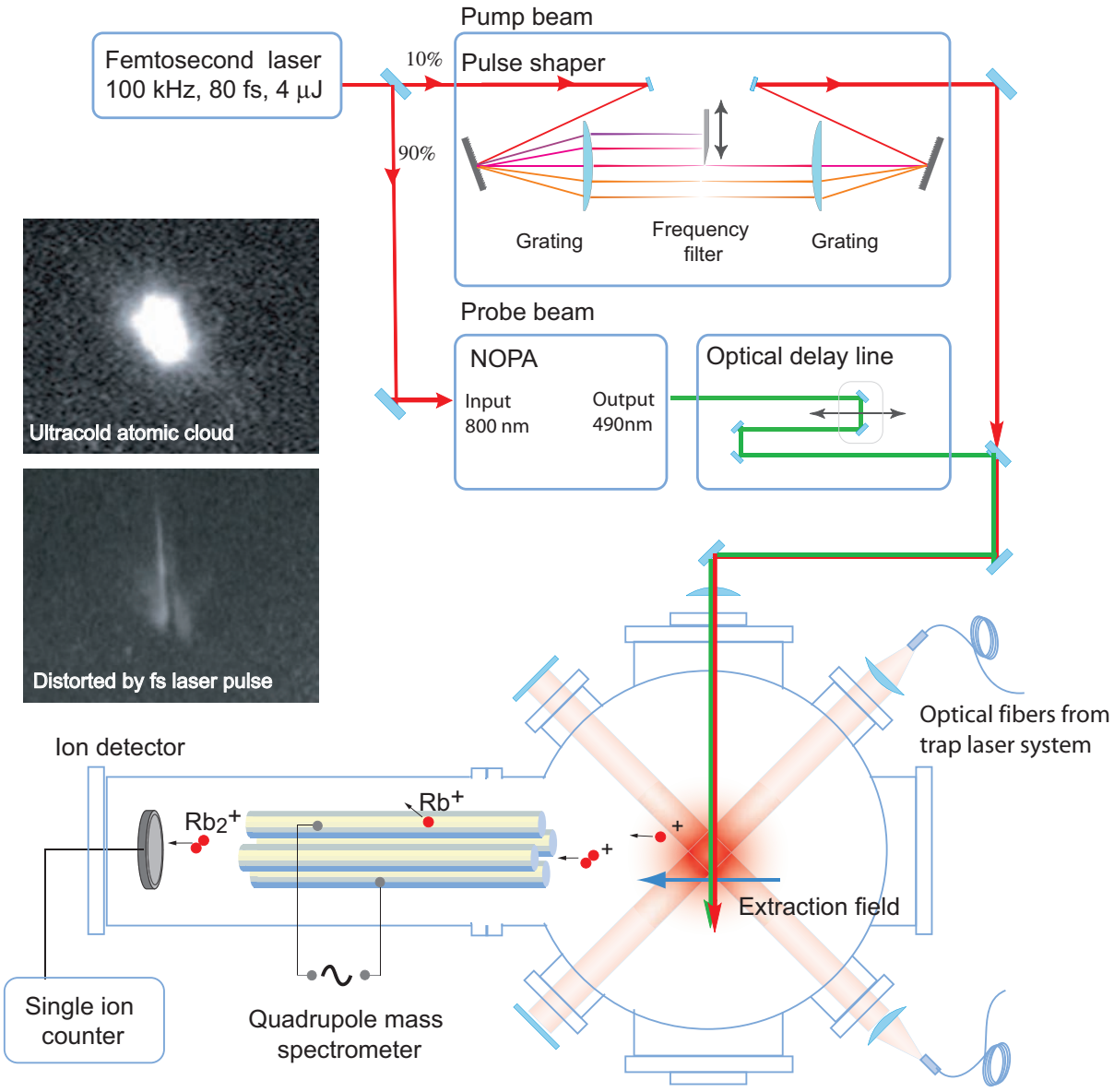


Figure 7.4: Experimental setup for femtosecond two-color pump-probe spectroscopy on ultracold rubidium. The laser system and the magneto-optical trap are schematically depicted. The two insets on the left are images of the fluorescence emitted by the ultracold atomic cloud. The upper one shows fluorescence of the atoms in standard MOT configuration without femtosecond laser. In the lower picture, the trap is disturbed by an ultrashort pulse which is not frequency filtered and includes the atomic resonances in its frequency spectrum.

90% of the energy are used to pump a NOPA (cf. section 3.1.2) in order to produce green probe pulses with a central wavelength of about 490 nm and 25 nm FWHM spectral width. These pulses have a pulse energy of about 0.2 $\mu$J and a pulse length of about 425 fs. The remaining part of the laser (10%) serves as a pump pulse. This pulse is modulated in the Fourier plane of a 4-f line. The gratings have 2000 lines/mm and the cylindrical lenses

have a focal length of 250 mm. In the presented experiments, the pulses are amplitude-modulated by applying different frequency filters. Physical blocks are chosen for two reasons. First, the resolution which can be obtained by positioning with a high precision stage is better than the resolution of the liquid crystal modulator. Second, at maximal attenuation with the pulse shaper about 2% of the light is still transmitted, which is not sufficient to suppress the excitation of atoms. The transition of atoms is orders of magnitude stronger than for molecules and resonant light easily distorts the atomic cloud by multi-photon ionization and radiation pressure. For the high-pass filter, a razor blade in the Fourier plane blocks the frequencies below the cut off position including the atomic resonance. The band-pass in which a narrow band is transmitted is created by a slit formed by two razor blades. The width and the position of the transmitted frequency band is both set by a precision stage. A needle of 1.6 mm in diameter acts as a notch filter and removes a band of approximately 35 wavenumbers. The cut-off position of the frequency filters is specified respective to the atomic resonance under investigation. In case of the needle, the reference point is taken to be the lower frequency edge. It is precisely determined by measuring of the difference in the fluorescence with and without the pump pulse present in the trap.

In the investigation of states corresponding to the atomic $D_1$ resonance, the frequencies above 12794 $cm^{-1}$ including the atomic $D_2$ resonance were removed by a fixed additional blocker in the Fourier plane of the 4-f line. The spectra of the particular pump pulses are depicted in the respective section.

The pump and probe pulse are collinearly overlapped using a dielectric mirror. They are focused in the trap by a lens of 300 mm focal length. The peak intensity of the pulses is determined to $6.1\times10^{10}$ W/cm$^2$ for the pump and $1.4\times10^{9}$ W/cm$^2$ for the probe. The time delay between pump and probe pulse is variable and typically scanned between $-5$ ps and $+10$ ps.

## 7.4 Numerical methods

In order to gain deeper insight into the excitation process, the interaction of the shaped laser pulse with a pair of ultracold colliding atoms is theoretically studied. For this purpose, the time-dependent Schrödinger equation is numerically solved. These calculations were carried out in cooperation with C. P. Koch and R. Ağanoğlu. They included the potentials which correspond to the ground and excited state in their algorithm and implemented the spectral filter for the pump pulse.

For the simulations two electronic states were taken into account. The ground state with diatomic potential $V_g$ and the excited state with $V_e$. These states are coupled by the time-dependent laser field $E(t)$ in the dipole and rotating wave approximations. The corresponding Hamiltonian reads

$$\hat{\mathbf{H}} = \begin{pmatrix} \hat{\mathbf{T}} + V_g(\hat{\mathbf{R}}) & \hat{\mu}E(t) \\ -\hat{\mu}E(t)^* & \hat{\mathbf{T}} + V_e(\hat{\mathbf{R}}) - \Delta \end{pmatrix}. \tag{7.2}$$

Here, $\Delta$ is the detuning of the pump pulse's central frequency relative to the dissociation limit of the particular excited state. $\hat{\mathbf{T}}$ is the kinetic energy operator, $\hat{\mathbf{R}}$ the internuclear

distance, and $\hat{\mu}$ the transition dipole moment of the diatomic molecule. The electric field of the pulse in time $E(t)$ is obtained by Fourier transformation of the frequency modulated spectrum as described in reference [219]. To represent the wavefunctions and operators, a Fourier grid method with adaptive step size [227] is employed. The time evolution is achieved using the Chebyshev propagator [228]. This method has already been successfully applied to model the transients obtained for femtosecond laser pulses shaped with different low-pass filters near the 5s+5p$_{1/2}$ ($D_1$) and 5s+5p$_{3/2}$ ($D_2$) asymptote including linear chirps [219, 229]. It was shown that the effect is only due to electronic dynamics. The propagation of a well-localized wavepacket could not be observed due to the very long round trip time and a very rapid dephasing in these high-lying states. The exact shape of the respective electronic state would only change the overall excitation rate due to the differing Franck-Condon factors. Therefore, the calculations are carried out exemplarily for two electronic states only. The interaction process starts with a continuum scattering state of the $a^3\Sigma_u^+$ potential with a collision energy corresponding to 100 $\mu$K, which is the temperature in the magneto-optical trap. The electronically excited molecular state is taken to be the $1_g$ potential for the states near the $D_1$ atomic resonance, and $0_g^-$ for the 5s+5p$_{3/2}$ asymptote ($D_2$).

The effect of the ionizing probe pulse is modelled by convoluting the transient by a normalized Gaussian of 425 fs FWHM. The measured data is fitted to the quantum dynamical simulations only by a single linear scaling factor.

## 7.5 Results of pump-probe experiments

In this section, the data resulting from the pump-probe experiments is discussed. The measured data is presented along with the corresponding quantum dynamical calculations. The excitation scheme is already displayed in figure 7.2. A shaped pump pulse creates molecular population in the 5s+5p states. This population is transferred by a second pulse with variable time delay to an ionic state. The ions created only by the probe pulse arise from molecules produced by trap light and give a constant background signal, which is indicated by a dashed line in all graphs.

Here, the transients of pump pulses with different spectral modulations are discussed. Each type of modulation is presented in the respective subsection in the frequency and time domain.

### 7.5.1 Blue detuned pump pulses near the atomic $D_1$ and $D_2$ resonance

Firstly, the transients produced by pump pulses which are amplitude shaped using a high-pass filter are presented. In these part, the frequencies below the cut-off position, including the atomic resonance, are removed yielding a pulse with its frequencies blue detuned to the atomic resonance. The cut-off position of the filter is given relative to the particular atomic resonance. The states belonging to the 5s+5p$_{1/2}$ ($D_1$) and the 5s+5p$_{3/2}$ ($D_2$) asymptote are investigated with separate pump pulses. In the case of the

$5s+5p_{1/2}$ asymptote, the frequencies of the $D_2$ resonance and above from the spectrum are additionally removed. This allows for suppressing effects originating from the $5s+5p_{3/2}$ asymptote and to avoid distortion of the MOT.

The spectrum of two exemplary pump pulses for the investigation of the states associated with the $5s+5p_{1/2}$ or $5s+5p_{3/2}$ asymptote are depicted in figure 7.5a) and c). The time-evolution of the pulses is depicted in figure 7.5b) and d). Compared to an uncut pulse the pulses are longer. In the case of the pulse investigating the states near the $5s+5p_{1/2}$ asymptote ($D_1$), where the spectral intensity is modulated with two sharp cuts (figure 7.5c)), the temporal profile of the pulse features an oscillatory envelope (figure 7.5d)).

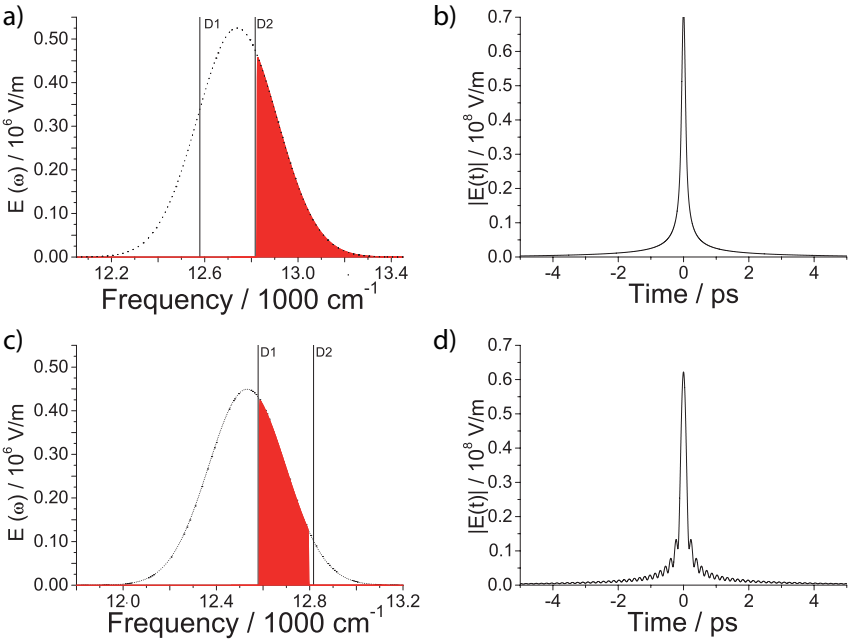


Figure 7.5: Pump pulses which are blue detuned to the atomic $D_1$ and $D_2$ resonance, respectively. Both pulses are frequency modulated with a sharp frequency filter. In a), the spectrum of the pulse which addresses the states of the $5s+5p_{3/2}$ asymptote is shown. In b), the temporal evolution of the amplitude shaped pulse is depicted. In c) and d), the corresponding pulse which addresses the states of the $5s+5p_{1/2}$ asymptote is pictured in the time and frequency domain. The curves are calculated and correspond to the transients presented in figure 7.6.

The measured and calculated transients for different cut-off positions are depicted in figure 7.6. These transients obtained for a pulse close to the atomic $D_1$ resonance (figure 7.6a)) are very similar to the ones obtained by the pulse close to the atomic $D_2$ resonance (figure 7.6c)). The transients can be divided in three characteristic parts. For negative time delays, when the probe pulse precedes the shaped pump pulse a constant ion count rate is obtained. At zero delay, the signal exhibits a peak. After this peak, at positive time delays, the signal increases and shows modulations which decrease in amplitude. The frequency of the oscillation is increasing with a larger detuning of the cut-off position from the atomic resonance. The experimental data is in both cases very well-reproduced by the quantum dynamical calculations. Only at negative delays the simulation deviates from the measured data. In the experiment, molecular ions are detected, whereas in the

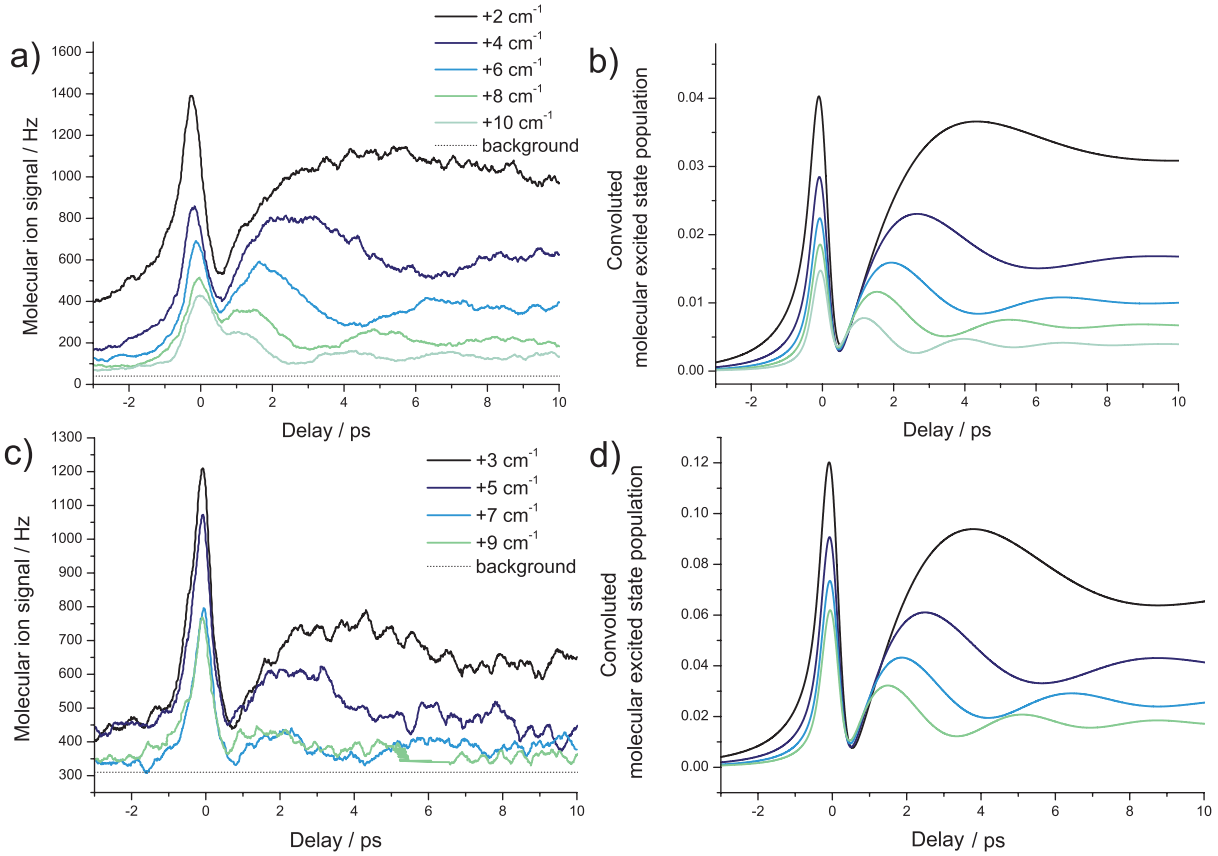


Figure 7.6: Transients obtained by blue detuned pump pulses. The position of the cut-off frequency is varied. In a), the transients are shown which result for pulses that are situated at the $5s+5p_{3/2}$ asymptote. The corresponding quantum dynamical calculations are depicted in b). In c) and d), the experimental and the theoretical data for a blue detuned pulse at the $5s+5p_{1/2}$ asymptote are presented.

simulations no molecular population can be observed. This detail is elaborated in the interpretation of the process in section 7.5.7.

The measurements near the $5s+5p_{1/2}$ ($D_1$) and $5s+5p_{3/2}$ ($D_2$) resonance slightly differ regarding their absolute ion signal. It is higher for the $D_2$ resonance, which is mainly due to the larger transition dipole moment and differences in the spectral intensity distribution. The difference in the spectral intensity distribution could be caused by a deviation in pulse energy, central wavelength, spectral width, or the second cut which is required to remove the atomic resonance that is not under investigation.

### 7.5.2 Blue versus red detuned pulses

The transients which are obtained by blue detuned pulses are very similar to the transients which are obtained by red detuned pulses. This qualitative similarity can be observed when comparing figure 7.2c) and figure 7.7.

In this section, the transients obtained by pulses having the spectral intensity blue or red detuned respective to the atomic resonance are quantitatively compared. For this purpose, the differences have to be separated from differences which occur due to a variation of pulse parameters such as central wavelength or intensity. The main parameters which affect the transients are the position of the spectral cut-off and the power of the pump pulse. Because of experimental fluctuations and variations in the spectral intensity distribution between the pulses which have their spectral components situated either on the blue or the red side of the atomic resonance it is difficult to resolve the differences experimentally.

For an accurate and detailed comparison of the transients obtained by this different types of shaped pulses, the theoretically calculated simulations are employed. In these simulations, the pulse parameters are chosen to have a symmetrical distribution of the spectral intensity. The spectral intensity distribution of the pulse on the blue side of the atomic resonance is the mirror image of the pulse which has its spectral intensity on the red side of the resonance. This is illustrated in the spectrum depicted in the inset of figure 7.7. The position of the cut-off frequency is negative for the pulses with frequencies below the resonance and positive for the ones with frequencies above. In both cases, the atomic resonance is not enclosed in the spectrum. The states corresponding to the $5s+5p_{3/2}$ ($D_2$) asymptote were not taken into account in order to analyze only the interaction with the states corresponding to the $5s+5p_{1/2}$ ($D_1$) asymptote.

The theoretically obtained transients for a cut-off detuning of $\pm 2$ cm$^{-1}$ and $\pm 6$ cm$^{-1}$ are presented in figure 7.7. The overall transients for pulses that have the frequency components on the blue side (cut-off position of $+2$ and $+6$ cm$^{-1}$) of the atomic resonance are similar to the ones obtained with pulses where the frequencies are situated on the red side of the atomic resonance (cut-off position of $-2$ cm$^{-1}$ and $-6$ cm$^{-1}$). Upon closer inspection it can be observed that the population in the bound levels of the excited state is larger for the pulse with its spectral intensity red to the atomic resonance. The difference in molecular population is also plotted in figure 7.7. It decreases with larger cut-off position. The variation of the difference over time is similar (dashed lines) to the transients itself, but shifted by a quarter period of the oscillation.

The difference in the transients is reflected by the distribution of the population in the

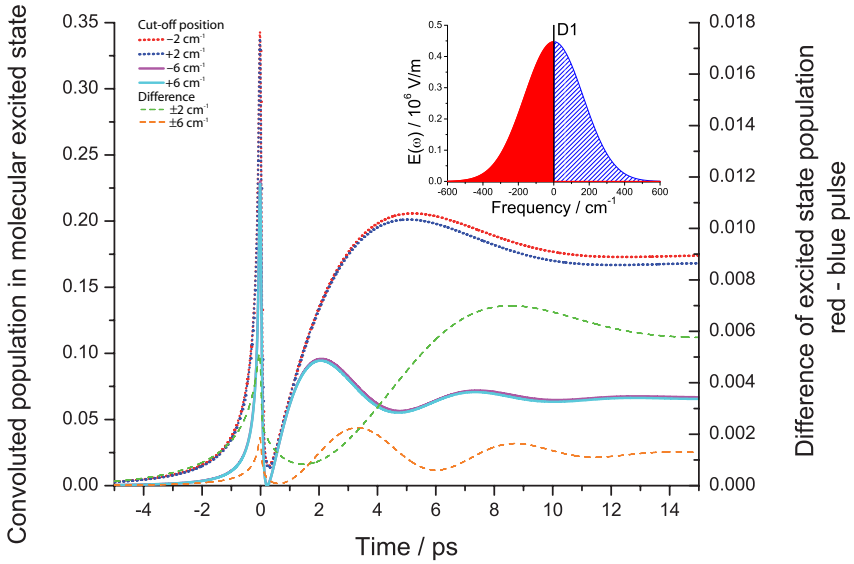


Figure 7.7: Comparison of the calculated transient molecular population in the excited state for pulses which are red (red and magenta line) and blue (blue and cyan line) detuned from the atomic $D_1$ resonance. The spectrum of the pump pulse is either situated on the red side of the atomic resonance or on the blue side, which can be seen in the inset that depicts the spectrum of the red and blue detuned pump pulse. The transients are plotted for detunings of $\pm 2$ (dotted lines) and $\pm$ 6 cm$^{-1}$ (solid lines). Moreover, the difference in population produced by each transient pair is also depicted in dashed green ($\pm 2$ cm$^{-1}$) and dashed orange ($\pm 6$ cm$^{-1}$) on a separate scale.

vibrational states. Figure 7.8 compares the vibrational distributions in the excited state for pulses with their spectral intensity on the blue or red side of the atomic resonance. Since the differences in the transients obtained for the cut-off position of $\pm 2$ cm$^{-1}$ respective to the atomic resonance are most clearly exposed, they serve as an example. For both pump pulses, the major fraction of the population in the molecular excited state accumulates in the vibrational levels from $v$=250 to 271, which is very close to the atomic resonance. The binding energy of theses states amounts to less than 0.015 cm$^{-1}$. These states cannot be resonantly addressed by one of the frequency modulated pulses. Therefore, this population must be created due to the high peak intensity of the pump pulse. Non-linear effects like power broadening, Stark shift, and Rabi cycling become relevant and can transfer population non-resonantly to these levels.

The difference in population is mainly localized in the vibrational states $v$=200 to 246. This fraction of the excited state population is more deeply bound than the major part of the molecular population. These vibrational states cannot be populated resonantly by the pulse which has spectral components on the red side of the resonance (see figure 7.8). The pulse with its frequency components blue detuned to the resonance has no overlap with any bound molecular state. This portion of molecules which is additionally produced by the red detuned pulse amounts to only three percent of the total population. The population difference in these states can be explained by their binding energy. The binding energy of the vibrational state $v$=220, where the difference in molecular population has its maximum, is $-0.7487$ cm$^{-1}$. For this state, the effective detuning consists of the actual detuning and the binding energy. In case of the pulse with the frequency components

blue detuned to the resonance the detuning increases. For the pulse with its frequency components red detuned to the resonance it decreases. The molecular rate is decreasing with larger detunings for both types of spectra (cf. figure 7.5). The shift is relatively larger for small detunings. Therefore, the difference is getting larger when the cut position is closer to the atomic resonance. For higher vibrational levels ($v$>250), the binding energy is smaller than 0.015 cm $^{-1}$ and the shift has almost no effect. For vibrational levels below $v$=200 the Franck-Condon factors get too small for efficient population. However, for the major part of photoassociated molecules it does not matter if the spectral intensity is situated above or below the atomic resonances.

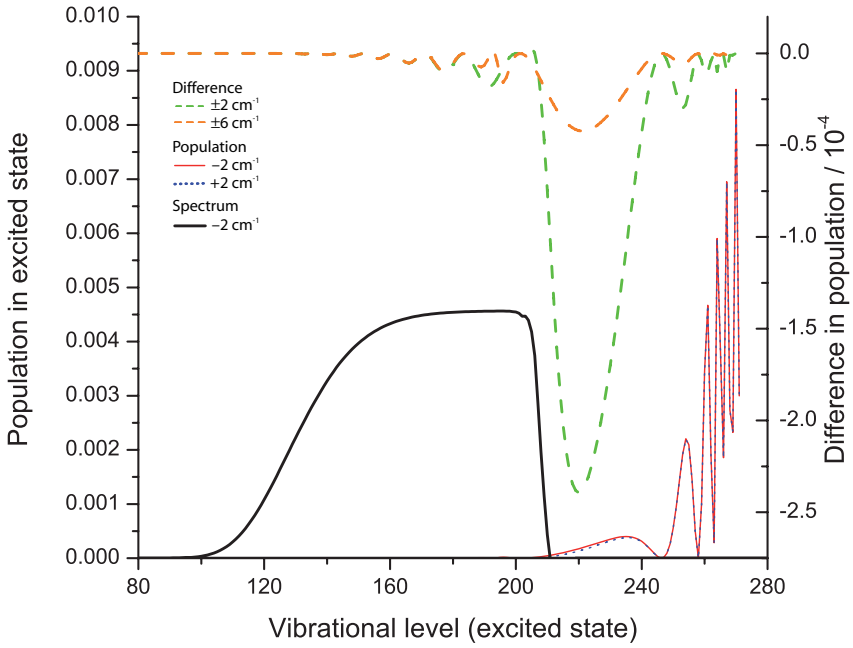


Figure 7.8: The vibrational distribution of the excited state molecules after the interaction with the frequency modulated pump pulse. The cut-off position in case of the high-pass filter is +2 cm$^{-1}$ yielding the blue frequency components (blue dotted line). For the low-pass filter it is set to −2 cm$^{-1}$ (red line). The difference in the population between high-pass and low-pass filtered pulses is shown for a cut-off position of ±2 and ±6 cm$^{-1}$ (green dashed line and orange dashed line). The spectrum of the red detuned pulse (−2 cm$^{-1}$) is provided to put the scale of the vibrational level in relation with the frequency domain (black line).

### 7.5.3 Combining the red and blue detuned pulses

In the previous section, the transients of pulses which are red or blue detuned to the atomic resonance were compared. The resulting transients are very similar and only exhibit a tiny difference, which could be observed by considering the theoretical calculations. The process which is driven by the laser pulses can be assumed to be the same for red and blue detuned pulses. Because of this, it seems to be logical to use both frequency components of the pulse, situated on the blue and red side of the atomic resonance, simultaneously. Such a pulse covers nearly twice the frequency components, which should lead to an increase in controllability. This combination of blue and red frequencies results in a nearly Gaussian

spectral distribution with a dip at the atomic resonance. This dip is again necessary to avoid perturbation of the trap. It is experimentally created by a needle in the Fourier plane of the pulse shaper which removes a frequency band of 35 wavenumbers. A spectrum of this type of pump pulse and the corresponding time evolution is shown in figure 7.9. The spectral intensity of the pulse is distributed around the $D_1$ and investigates the states of the $5s+5p_{1/2}$ asymptote. Since the experiments and simulations have shown that the transients do not depend on the characteristics of the states belonging to the $5s+5p_{1/2}$ ($D_1$) or $5s+5p_{3/2}$ ($D_2$) asymptote, the presentation of the data is restricted to the experiments at the atomic $D_1$ resonance.

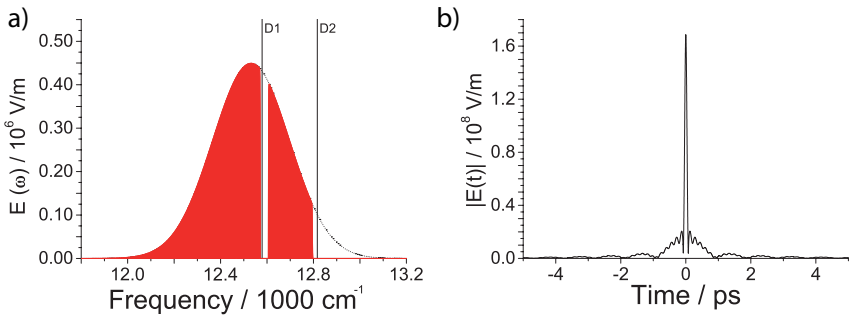


Figure 7.9: Pump pulse which is amplitude shaped by a notch filter. The frequency filter removes a band from $-8$ cm$^{-1}$ to $+27$ cm$^{-1}$. The spectrum is depicted in a). The corresponding time evolution of the pulse is shown in b).

The transients of five different filter positions along with quantum dynamical simulations are depicted in figure 7.10. The first three graphs of figure 7.10a), b), and c) show transients resulting from pump pulses where the $D_1$ resonance is blocked by the needle. In the three other graphs (figure 7.10d) – f)) the transients result from a pulse where the atomic resonance is enclosed in the spectrum. In figure 7.10d) and e), the frequency filter is situated below the atomic $D_1$ resonance whereas in f) it blocks a frequency band above.

The population in the excited state depends on the position of the blocked frequency band. When the frequency components from $-20$ cm$^{-1}$ to $+15$ cm$^{-1}$ are blocked (figure 7.10a)), almost no molecular population remains in the excited state after the pulse is over. Going to the filter position of $-12$ cm$^{-1}$ to $+23$ cm$^{-1}$ (figure 7.10b)) the number of created molecules rises, and when the needle blocks the frequencies from $-8$ cm$^{-1}$ to $+27$ cm$^{-1}$ (figure 7.10c)) the population is even larger. The closer the atomic resonance is set to the edge of the frequency filter the larger the signal is at positive time delay. Further, the oscillations in the signal at positive time delays become more visible.

Transients where the resonance is enclosed in the spectrum of the pump pulse are shown in figure 7.10d), e) and f). For the band filter blocking the frequencies from $-40$ cm$^{-1}$ to $-5$ cm$^{-1}$ (figure 7.10d)), the atomic $D_1$ resonance is enclosed in the spectrum. The molecular signal increases steeply and remains on a relatively high level where an oscillation can be observed. In figure 7.10e), the frequency filter is also situated on the red side of the atomic resonance removing a band of $-38$ cm$^{-1}$ to $-3$ cm$^{-1}$, which is closer to the atomic resonance compared to figure 7.10d). In the example which is depicted in figure 7.10f), the frequency filter is situated on the blue side of the atomic resonance blocking a band from $+2$ cm$^{-1}$ to $+37$ cm$^{-1}$. The molecular ion signal peaks at zero time delay and drops down to half of the maximal value. The beginning of an oscillation with

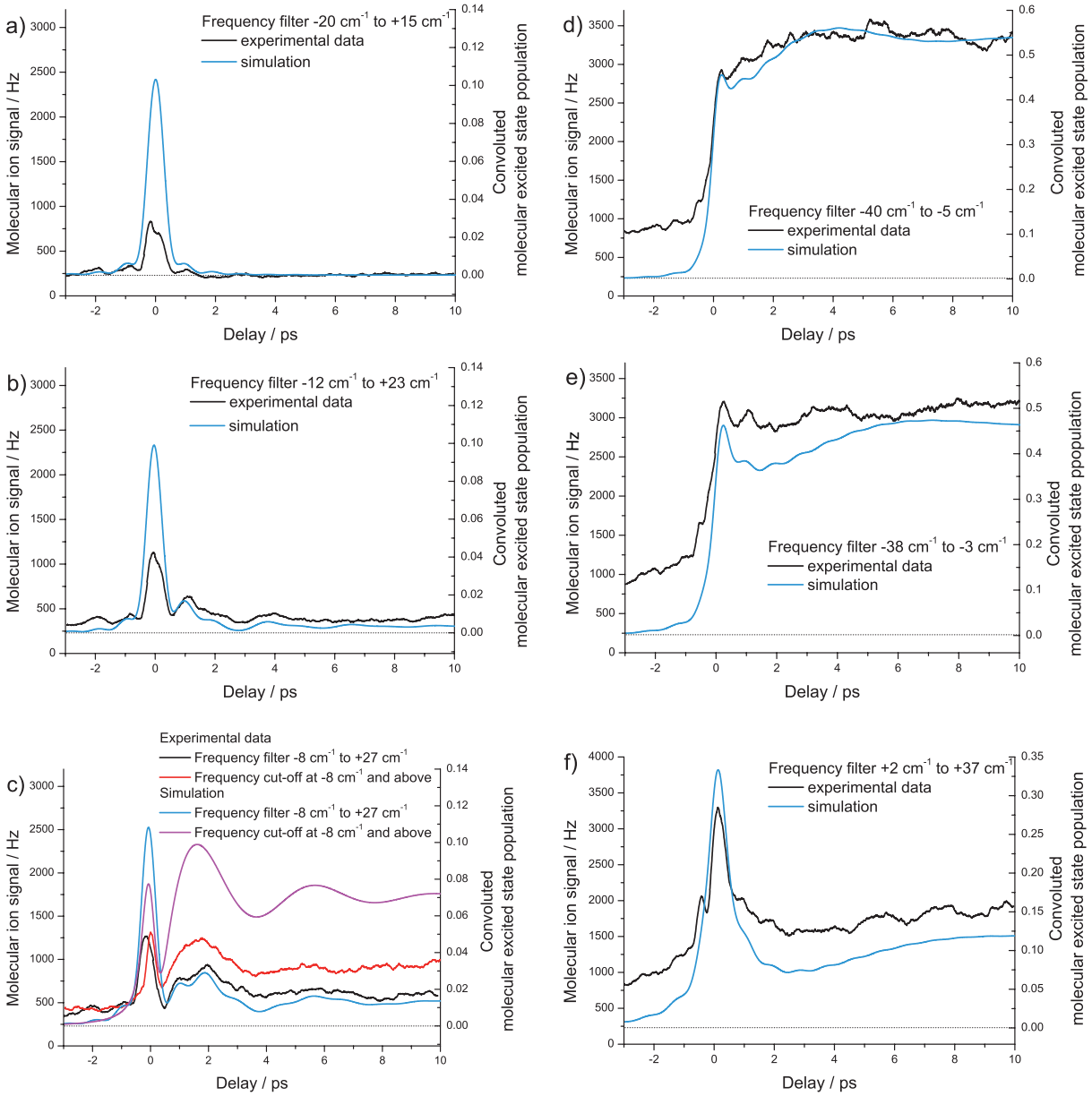


Figure 7.10: Measured and calculated transients obtained with the pulse which is amplitude modulated by the notch filter. In a), b), and c), the atomic $D_1$ resonance is removed by the frequency filter. In d), e), and f), the atomic resonance is enclosed in the spectrum of the pump-pulse. In c), the transients are compared to the ones produced by a low-pass filter which has an identical cut-off position.

a period longer than the time window of the graph can be constituted. In all cases, the transients can be reproduced by theory including the fast and the slow oscillations.

The scaling between theory and experimental data has to be changed compared to the non-resonant case. In the resonant case (figure 7.10d), e) and f)), photon pressure and atomic multi-photon ionization has an impact on the ultracold ensemble. The density is reduced and the initial state distribution of the atoms is changed. This is not taken into account in the simulations. The real number of molecules which can be created by a pulse depends on the number of atoms present in the focus of the pump pulse and the distribution of the spectral intensity. There is a trade-off between having frequencies very close to the resonance in the pump pulse and perturbation of the trapped ultracold atomic ensemble.

The transients obtained by all these pump pulses are similar to the ones in which the frequencies above or below the atomic resonance are blocked. One additional feature is observed: the ion signal at positive delay is additionally modulated by a second higher frequency. This frequency can be attributed to the second cut-off in the spectrum. The slow oscillation is due to the frequency cut-off close to the resonance, e.g. at $-8$ cm$^{-1}$ in figure 7.10c). The transient of a pulse with the same cut-off position ($-8$ cm$^{-1}$) having its spectral components on the red side of the resonance is also depicted (turquoise line). This transient has the same long oscillation period due to the same frequency cut-off. The faster second oscillation is expected to arise from the second cut-off in the spectrum obtained by a pulse which is frequency modulated by the notch filter (at $+27$ cm$^{-1}$). Since this cut-off is further detuned from the resonance, this oscillation is faster. A detailed quantitative analysis of the oscillations in the transients is presented in section 7.5.5.

### 7.5.4 Comparison of transients produced by low-pass and notch filter

The transients resulting from pulses which consist of red and blue frequency components and pulses which provide only the red frequency components differ in the ion signal. The peak at zero time delay is higher in case of the band filter, which can be attributed to the higher peak power of the electric field. The ion signal at positive delays produced by the pulses containing both frequency components, red and blue to the resonance, is smaller although these pulses provide a higher spectral intensity. This difference can be explained by destructive interference of the red and blue frequencies, which is sensitive to the relative phase of these components [230]. To confirm this interference effect the transients are investigated by applying a step function to the spectral phase. The position of the phase step was set to the atomic $D_1$ resonance. The calculations for different heights of the step for the band filter blocking the frequencies from $-8$ cm$^{-1}$ to $+27$ cm$^{-1}$ are depicted in figure 7.11. The transient signal increases with the step height and becomes maximal for a step height of $\pi$. Furthermore, the phase of the faster oscillation is shifted by this phase step modulation. The good agreement of the experimental results with the simulation without phase step shows that the spectral phase of the experimentally used pulses is indeed flat.

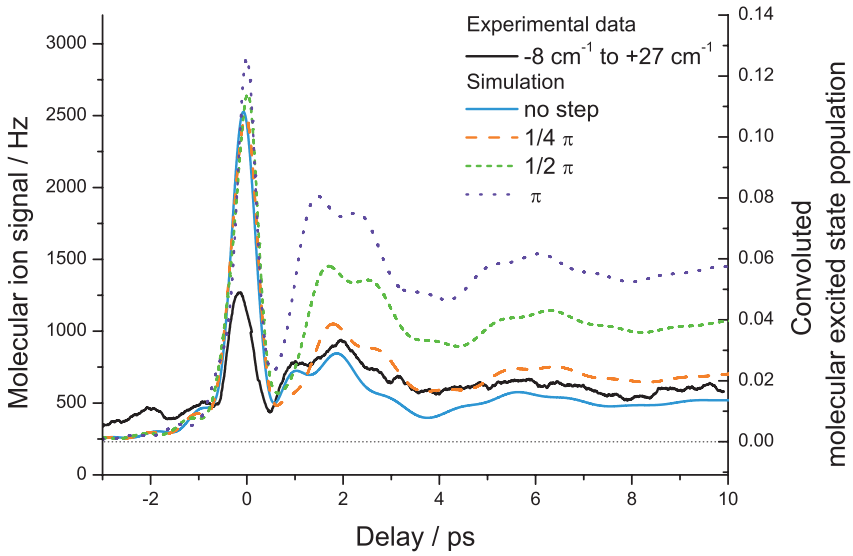


Figure 7.11: This figure illustrates the effect of a spectral phase step located at the atomic $D_1$ resonance. The frequency filter is kept constant removing a band from $-8$ cm$^{-1}$ to $+27$ cm$^{-1}$ as in the example in figure 7.10c). The calculated transients with different step heights are compared to the experimental data.

### 7.5.5 Frequency analysis

The transients exhibit an oscillatory behavior after the interaction with the major part of the pump pulse, which corresponds to times greater than zero. If more than one cut is applied to the pulse spectrum, additional modulations are observed in the oscillation of the excited state population. The frequencies of these oscillations are analyzed in detail in this section.

This analysis is carried out for the transients at the atomic $D_1$ resonance. The transients obtained with a blue detuned pulse of the type depicted in figure 7.5c) serve as an example for two cuts in the spectrum. The transients obtained by the pulse which is modulated by a notch filter provide the basis for an analysis of three cuts in the spectral domain, which is shown in figure 7.9a). In order to extract the frequency and amplitude of the additional modulations, a spectral analysis is performed on the calculated transients. For this purpose, the transient population is not convoluted to maintain a higher contrast and visibility of the modulation. The filter diagonalization method [231, 232] is particularly suited since it is able to extract spectral information from very few oscillation periods. In this procedure, the signal is decomposed into a sum of decaying exponentials, $C(t) = \sum_k d_k e^{-i\omega_k t - \Gamma_k t}$. Using this method, the frequencies $\omega_k$, decay rates $\Gamma_k$, and complex amplitudes $d_k$ are extracted from the signal. Two periods of the data sets which are in between the arrows shown in figure 7.12a), d), and g) are used. The analyzed data is presented in three parts: the unconvoluted transient population in the excited state is accompanied by the associated frequency spectrum including the weights of the dominating frequency components and the corresponding lifetimes ($|\Gamma_k|^{-1}$).

The first example which is depicted in figures 7.12a) to c) shows the case of two cut-off positions in the spectrum. One cut-off position is kept constant removing frequencies which are further than $+216$ cm$^{-1}$ detuned from the atomic $D_1$ resonance in order to

remove the atomic $D_2$ resonance. The other cut-off position is situated close to the atomic $D_1$ at $+5$ cm$^{-1}$ (black line) and $+9$ cm$^{-1}$ (blue dashed line), respectively. The absolute spectral weights $|d_k|$ of the dominating frequencies $\omega_k$ are shown in figure 7.16b). The zero frequency component of the spectrum gives a constant offset to the oscillations. The cut-off positions close to the atomic resonance at $\omega = 9$ cm$^{-1}$ (black line) and $\omega = 5$ cm$^{-1}$ (blue dashed line) as well as the cut far from the atomic resonance is revealed. Further, the difference of the two cut-off positions $\omega = 207$ cm$^{-1}$ (black line), $\omega = 211$ cm$^{-1}$ (blue dashed line) occur. Besides these components, unexpected frequencies such as $\omega = 6.5$ cm$^{-1}$ , $\omega = 211.7$ cm$^{-1}$ (black lines) or $\omega = 6.2$ cm$^{-1}$ , $\omega = 217.3$ cm$^{-1}$ (blue dashed lines) are also observed.

In order to interpret these additional lines, the lifetimes of the corresponding frequencies are examined and shown in figure 7.12c). The frequencies corresponding to a cut-off position or to the difference of cut-off positions have significantly larger lifetimes than the other frequencies in the spectrum (note the logarithmic scale). The frequencies with short lifetimes are most effective at time $t = 0$ where the pulse is still strong. This indicates that the unexpected lines are caused by the interaction between the molecules and the strong field during the main peak of the pulse at time zero. To understand the intensity dependence of the unexpected lines, the same spectral analysis is performed for two different intensities: the intensity which was used for the calculations above (I, black line) and a tenth of this intensity (I/10, red dashed line). For this analysis, the cut-off positions are set to $+216$ cm$^{-1}$ and $+9$ cm$^{-1}$, as in the example before. The results are shown in figures 7.12d) to f).

An analogous analysis is performed for three cut-off positions, which corresponds to a spectral intensity distribution shown in figure 7.9a). The first cut-off is situated at $+216$ cm$^{-1}$, the second is set to $-8$ cm$^{-1}$ and the third cut-off is set to $+27$ cm$^{-1}$ with respect to the $D_1$ resonance. The unconvoluted transient population, the spectrum, and the lifetimes are presented in figure 7.12g) to i).

For higher intensity, a splitting of the frequencies around the cut-off positions as well as around the difference of the cut-off positions is observed. Moreover, unexpected lines with large spectral weight are observed, cf. figures 7.12e) and 7.12h). For a lower intensity, these unexpected lines disappear. At full intensity the frequency components at the cut-off positions and the difference of the cut-off positions show a large, symmetric splitting. The strong intensity dependency of the components with short lifetimes indicates that they are caused by the strong interaction near the pulse maximum.

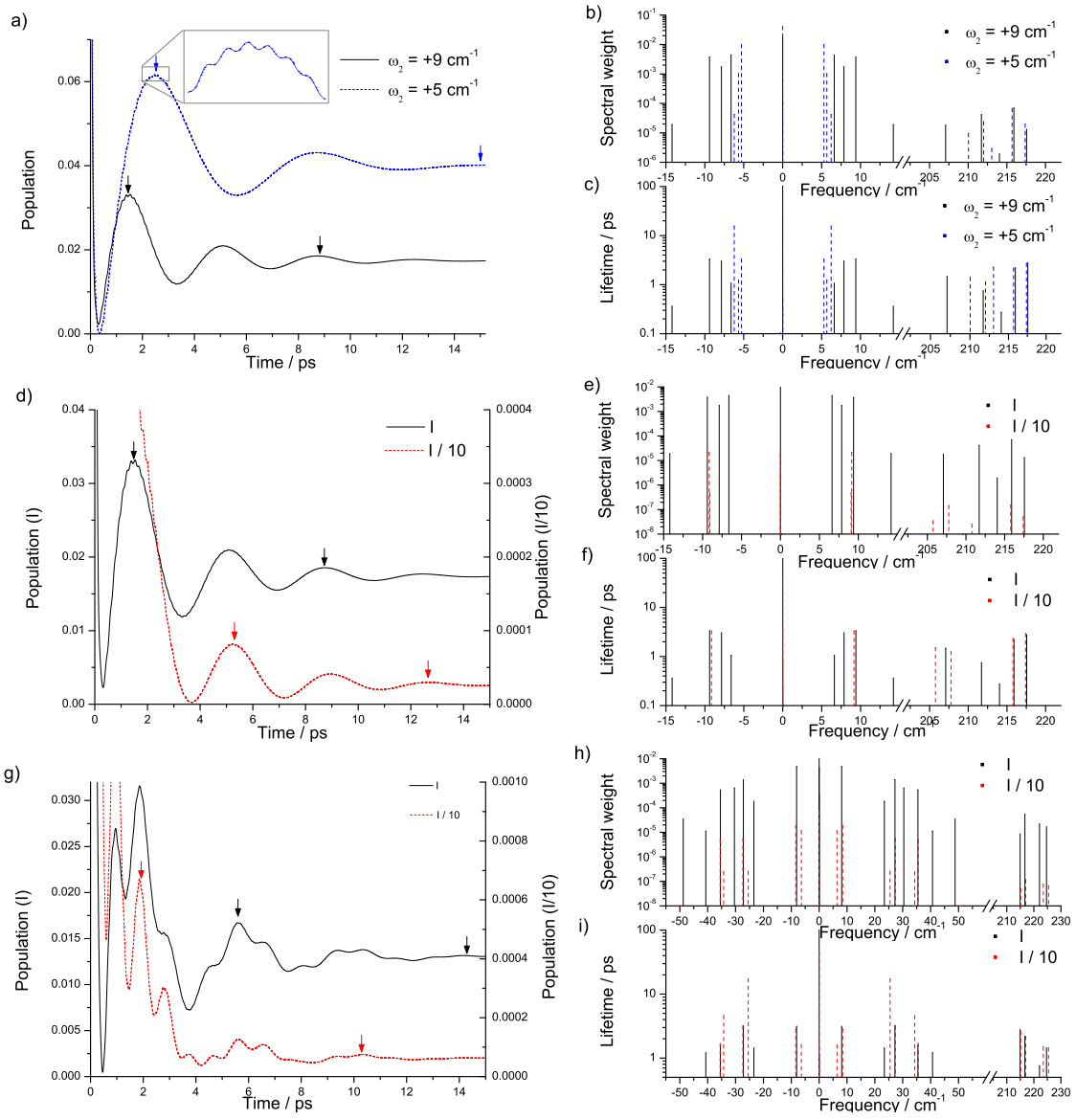


Figure 7.12: Analysis of the oscillation of the transient population. The pulses at the atomic $D_1$ resonance with two and three cut-offs in the spectrum (cf. figure 7.5c) and 7.9a)) serve as an example. The frequency spectrum of the oscillation including the respective spectral weights and the lifetimes are presented. This analysis is performed for two different intensities: I and I/10.

### 7.5.6 Investigations with a pulse of narrow bandwidth

The measurements in the previous sections revealed that the frequencies close to the atomic resonance are responsible for the creation of molecular population in the excited state. In this process, the frequency below and above the atomic resonance are nearly equal. Here, a narrow frequency band is used to analyze the frequency dependence of the process. For this purpose, a narrow slit in the Fourier plane of the 4-f line transmits only a frequency band of 13 wavenumbers spectral width. This particular spectral width results from a trade-off between spectral resolution and a reasonable amount of ion signal. This narrow frequency band forms a picosecond pulse of about 3 ps duration. Due to the sharp spectral cuts the envelope features an oscillatory envelope. The spectrum and time evolution of such a pulse can be seen in figure 7.13. By changing the position of the slit the transmitted wavelengths are shifted and the creation of molecular population can be measured frequency-resolved. Another reason for this experiment is the theoretical proposal for utilizing picosecond pulses for photoassociation.

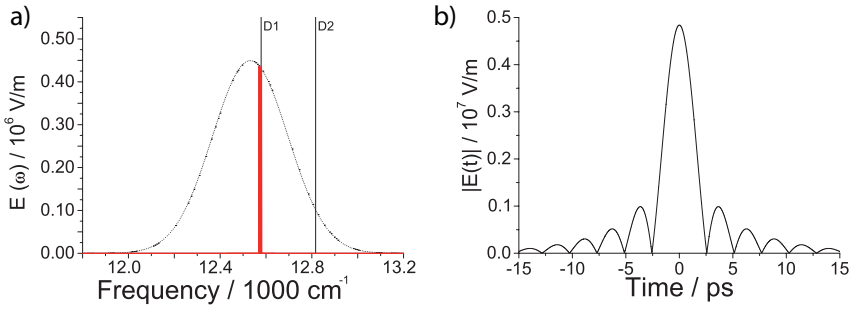


Figure 7.13: A pulse with a narrow band width is produced by a slit placed in the Fourier plane of the 4-f line which only transmits a frequency band of 13 $cm^{-1}$ width. The spectrum is shown in a). This narrow bandwidth corresponds to a pulse duration of about 3 ps (FWHM), which can be observed in the time evolution of the pulse depicted in b).

The frequency band is scanned through the spectrum in steps of about 0.5 $cm^{-1}$. At each position, approximately $10^7$ pump probe sequences are measured and averaged to create a data point. These spectra are measured for three different time delays. For negative delay at $-20$ ps, at coincidence of pump and probe pulse, and for positive delay at $+20$ ps where the oscillation is fully declined. The data is presented in figure 7.14a).

In case of positive and negative time delays, the molecular ion rate exhibits a broad peak with a plateau like shape. For both delays, the width of the interval in which the molecular ion rate is increased corresponds to the width of the frequency band which forms the pulse. This means that the width of the transition band or its structure cannot be resolved. The signal level of the data taken at positive time delays is larger than for negative delays. The ratio between negative and positive time delays is approximately 0.3.

In case of coincidence of the pump and probe pulse, the curve of the molecular ion rate has a completely different shape. The data forms a double maximum having a dip in between centered at the atomic resonance. The maxima are located at $-4$ $cm^{-1}$ and $+7$ $cm^{-1}$. At this point the obtained molecular ion rate of 1600 Hz is equal to the maximal rate

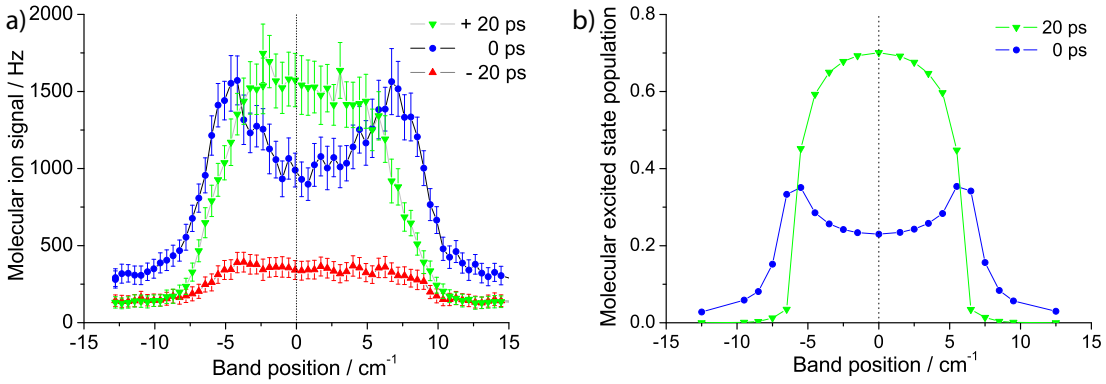


Figure 7.14: Investigation of the molecular ion rate with a pulse of narrow bandwidth at different time delays. In a), the experimental data is presented. The corresponding results obtained by quantum dynamical calculations is displayed in b).

obtained at positive delays. The width of the interval in which the ion rate is increased is larger than in the case of the positive delay.

For a more precise understanding of the effect which leads to the difference in the shape of the curves, quantum dynamical calculations were carried out. For negative delays no data can be calculated since the interaction has not taken place yet. The simulation for zero and positive time delays are depicted in figure 7.14b) and agree quite well with the data measured. The double peak and the increased width in the signal are clearly visible in the simulation. The positions of the maxima are symmetrically located at $-5.5$ cm$^{-1}$ and $+5.5$ cm$^{-1}$. The maximal population for positive delays is by a factor of two larger than at zero delay. The lower experimental values in the experiment can be explained by the distortion of the trap by multi-photon ionization and photon pressure. This effects the signal at positive delay more than for zero delay because in coincidence of the two pulses the population is directly transferred to an ionic state and the impact of the distortion is smaller. The shift of the measured data by $+1$ cm$^{-1}$ is not reproduced by the calculations and has to be attributed to the inaccuracy of the position/frequency determination.

The time-dependent population is calculated for different spectral positions of the transmission band. The corresponding transients are presented in figure 7.15. The transients are similar to the ones presented in the previous sections. The positions where the static measurement is carried out are indicated by vertical dotted lines. The measurement at zero delay strongly depends on the population rise. For long time delays, when the interaction with the pump pulse is long gone, the measurement only depends on the number of produced molecules in the excited state.

For off-resonant band positions, the population in the excited state population rises earlier than in case of frequency bands which enclose the atomic resonance. When the atomic resonance is not included in the spectrum of the pump pulse, the transient population in the excited state is maximal at zero delay. After the interaction with the non-resonant pump pulse the molecular population in the excited state declines strongly. In the case of off-resonant excitation with the pump pulse, the molecular population is only transiently transferred to the excited state during the interaction with the pump pulse. This transient

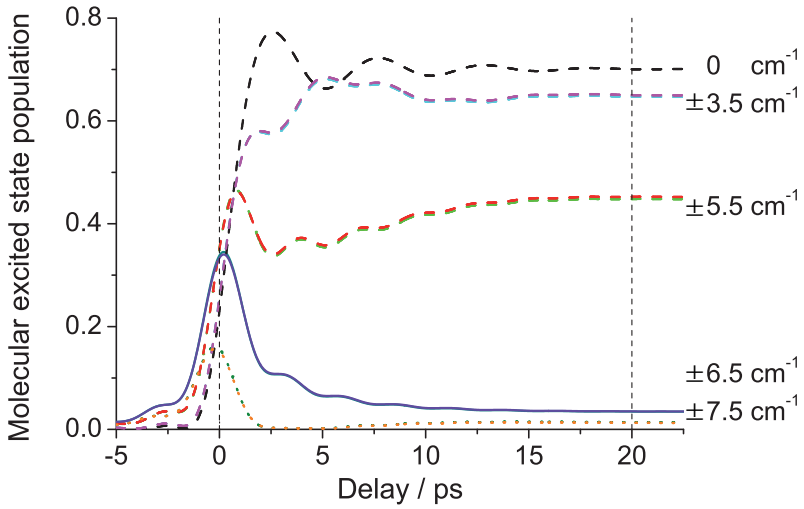


Figure 7.15: The calculated transient for different positions of the narrow frequency band. The molecular population at 0 ps and +20 ps time delay forms the frequency-resolved molecular ion rate, which is presented in figure 7.14b). The positions of the frequency bands center is determined relative to the atomic resonance.

contribution causes the increased peak width in case of coincidence of pump and probe pulse.

In case of the symmetric band position in which the atomic resonance is included the rise is maximal delayed. The population finally produced for this resonant frequency band exceeds that population obtained by other band positions. The symmetry of the frequency band respective to the atomic resonance determines the starting point of the rise of the molecular population. This effect produces the double peak structure in the molecular excited state population for coincidence of pump and probe pulse. In this experiment, the transient behavior is different compared to the transients before. This is due to the extremely reduced peak intensity of the pump pulse.

The dependency of the molecular signal at the presence of the pump pulse on the symmetry of the frequency band distribution respective to the atomic resonance indicates the appearance of interferences. If frequencies blue and red to the atomic resonance are simultaneously present in the pulse, they interfere destructively. This effect suppresses the production of molecules in the excited state and, therefore, the rise in the molecular population is delayed. The effect of destructive interference is maximal when blue and red frequency components are equally present in the pulse. This is exactly the case for the symmetric frequency band position and explains the dip in the frequency-resolved spectrum of the molecular production at zero delay. The effect of interferences between frequencies which are situated on the blue and the red side of the atomic resonance have been discussed for the excitation of atoms in a gas cell by N. Dudovic *et al.* [230].

### 7.5.7 The interaction process

The interaction process of the shaped pump pulses with the ultracold atomic ensemble is summarized in this section. A more detailed analysis can be found in [219]. The solution of the time-dependent Schrödinger equation, which precisely describes the experimentally measured data, allows for a detailed investigation of the interaction process. In order to understand the underlying process, it is discussed exemplarily for a blue detuned pulse at the atomic $D_2$ resonance. This example is the simplest because the spectrum exhibits only one cut-off position. However, the dynamic of the transients is entirely revealed and the explanation can easily be transferred to the other pump pulse shapes.

The spectrum of the pulse and the corresponding representation in the time domain is depicted in figure 7.5a). Due to the sharp cuts in the spectrum the pulse deviates strongly from the initially transform-limited short pulse. The amplitude shaped pulse features long tails which stretch out several picoseconds before and after the pulses maximum. For a single cut-off position at $+8$ cm$^{-1}$ blue detuned from the atomic $D_2$ resonance, the instantaneous frequency is represented by a green line in figure 7.16a). Around time zero where the maximum of the pulse is present the instantaneous frequency of the pulse sweeps over the frequency spectrum of the pulse. Within the tails of the pulse the electric field oscillates with the frequency matching the cut-off position of the frequency filter. When two or more cuts are applied, a beating pattern is observed.

The analysis of the vibrational state distribution, which is depicted in figure 7.8, provides information about the population transfer by the pump pulse. It reveals that the major fraction of the molecular population is situated in weakly bound molecular states which cannot be directly addressed by the frequencies provided by the pump pulse spectrum. The population transfer to the bound molecular states is achieved by off-resonant excitation. This non-linear process can be only driven by the strong field in the maximum of the pulse. A molecular dipole is induced by the high peak intensities. The frequency of the induced dipole is determined by the vibrational state distribution in the excited state. Therefore, it is after interaction with the peak of the pulse very close to the atomic transition frequency. In figure 7.16a), the frequency of the dipole is compared to the instantaneous frequency of the pulse and the atomic resonance.

The oscillations in the excited state population are induced by coherent transients [233]. This process has already been observed in the fluorescence of atoms when exciting with short pulses [234]. The transient is determined by the induced dipole of the weakly bound molecule and the electric field of the pulse in the tails. Especially the instantaneous frequency of the dipole and the driving electric field as well as the relative phase determine the transient dynamics. The dipole and the field oscillate with different frequencies which results in a beating of the transient molecular population. The beating frequency is given as the difference of the two frequencies, which matches the cut-off detuning. This could be proven for many cut-off positions and is confirmed by the frequency analysis by filter diagonalization presented in section 7.5.5. When the relative phase between the electric field and the dipole goes through $2\pi$, one oscillation in the transient population is observed (cf. figure 7.16b) and c)). For odd multiples of $\pi$ the dipole and the field oscillate diametrically. This results in a minimum in the transient population.

As the pulse passes by, the intensity of the electric field decreases and the interaction with

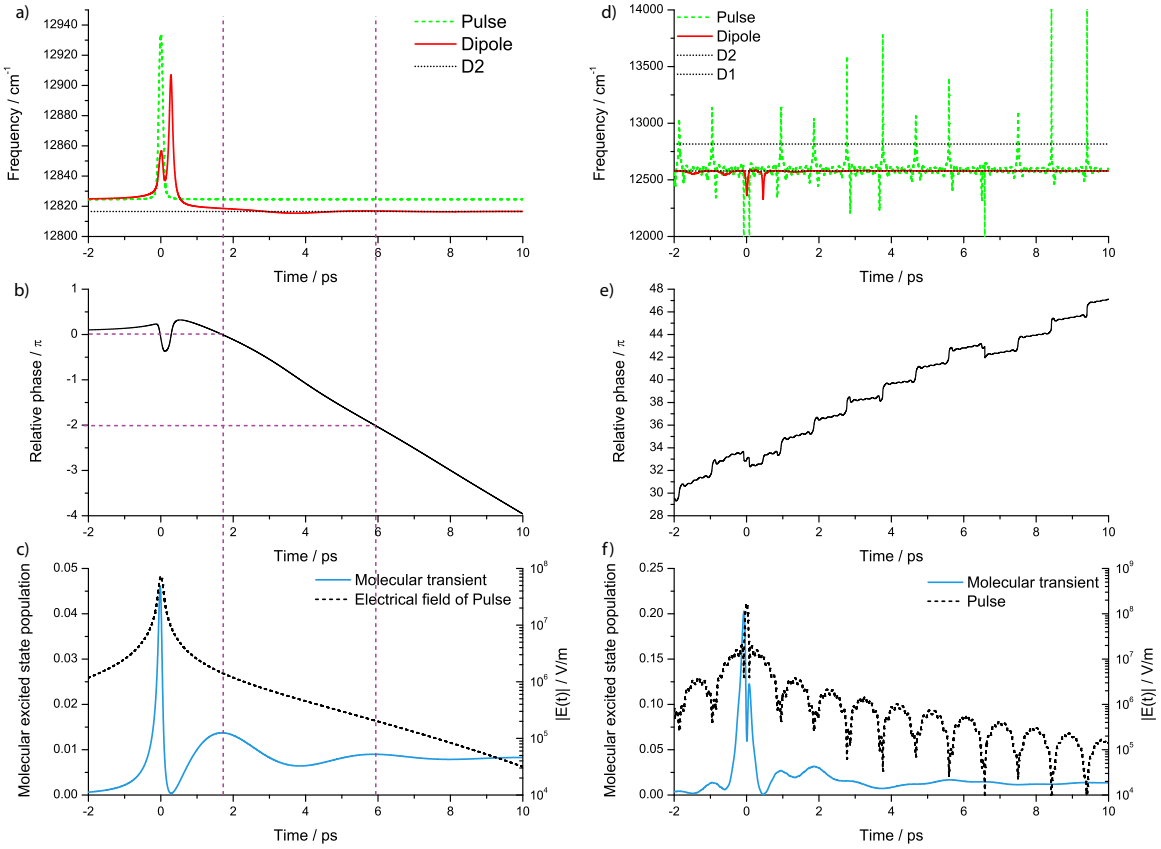


Figure 7.16: Theoretical analysis of the ultrafast dipole dynamics. In a), b), and c), the dynamics is illustrated for a pulse which is blue detuned to the atomic $D_2$ resonance with a cut-off position of $+8$ cm$^{-1}$. The spectral and temporal shape of this particular pulse is depicted in figure 7.5a) and b). The instantaneous frequency of the pulse is depicted in a) along with the frequency of the dipole and the atomic $D_2$ resonance. The relative phase between the two frequencies is depicted in b). The resulting transient population and a logarithmic curve of the electric field is displayed in c). The same analysis is performed for a pulse which is modulated by a notch filter removing the frequencies from $-8$ cm$^{-1}$ to $+27$ cm$^{-1}$. The spectral and temporal shape of this pulse are depicted in figure 7.9. The corresponding curves are shown in d), e), and f).

the dipole declines. Therefore, the amplitude of the transient oscillation decreases.

The calculations are also performed for a pulse in which a small band of spectral amplitude is removed by a notch filter. These calculations correspond to the measurements in which the pump pulse is situated at the atomic $D_1$ resonance. This pulse is amplitude modulated by removing a frequency band from $-8$ cm$^{-1}$ to $+27$ cm$^{-1}$ and a far detuned cut-off position at $+216$ cm$^{-1}$. The corresponding spectrum and time profile of the pulse is depicted in figure 7.9. In case of this three cut-off positions, the instantaneous frequency of the pulse is very complicated which can be seen in figure 7.16d). Therefore, the frequency of the dipole and its dynamics are more complex and not understandable at a first glance. The relative phase, presented in figure 7.16e) is very structured. The resulting transient and the field are depicted in figure 7.16f).

The transients are purely due to electronic transitions. Therefore, the shape of the molecular potential is almost irrelevant.

### 7.5.8 Photoassociation

The quantum dynamical calculations revealed the process of non-perturbative interaction. In this process, a free atom pair is transferred to a bound molecular state. The excitation populates non-resonantly the high lying vibrational levels. Further, indications of the photoassociation can be extracted from the experimental data. Here, the indications are qualitatively summarized and the complete and detailed analysis is performed in [216].

The explanation of photoassociation induced by the femtosecond laser pulses is supported by measurements for different hyperfine configurations of the magneto-optical trap. The photoassociation by trap lasers strongly depends on the hyperfine configuration of the atoms. The contribution of the photoassociation by trap laser is investigated for different bright state fractions p. The molecules produced by trap light can either reside in the ground state or in the excited state. The creation of excited state molecules by trap light is investigated by probing the molecular ion signal with the NOPA pulse only. The ground state molecules which are produced by photoassociation with trap light and subsequent spontaneous emission are detected by two photon REMPI with a nanosecond dye laser. The molecular production rate shows for both detection methods a maximum for bright state fractions of p=0.5 and 0.6, respectively. The asymptotic molecular ion signal which is measured for long time delays where the oscillation is already declined shows a different dependency of the bright state fraction. The maximum is obtained for p=0.1. This value corresponds to the configuration with the highest density that is equal to the highest pair density, which is the relevant parameter for photoassociation. This experimental data excludes the explanation approach that molecules which are produced in the trap are responsible for the transients behavior.

Finally, a single feature of the transients is discussed which is not reproduced by the quantum dynamical calculations. At negative delay, the molecular ion signal is always larger than the rate obtained with the probe pulse only. This feature is due to the repetitive character of the experiment. After the interaction with the pump pulse, molecules have been created in the excited state. After a lifetime of about 12 ns, these molecules decay back to the ground state by spontaneous emission. In the experiment, this population can

be transferred to an ionic state by the next pair of probe and pump pulse which follows after 10 $\mu$s. By this order of probe and pump pulse which corresponds to negative time delays the excitation pathway utilizes the states corresponding to the 5s+5d and 5s+6s asymptote. The analysis of different sets of pump probe traces (cut-off detunings and intensity dependency for $D_1$ and $D_2$) revealed a constant ratio of the signal recorded at negative time delays to the one recorded at large positive time delays. This correlation indicates the production of ground state molecules by femtosecond laser pulses.

## 7.6 Multi-photon ionization of ultracold $Rb_2$

So far, only the excitation process in ultracold rubidium to the first electronically excited state was investigated. In this section, the excitation to higher lying states and the ionization of the rubidium dimer is studied. For this purpose, two complementary experiments were performed. Their analysis revealed the excitation pathway including the participating electronically excited states. In the first experiment, optimal control techniques are employed for the investigation of the multi-photon ionization by closed feedback loop optimization. In the supplementary experiment, the frequency components which are relevant for the process were investigated with a notch filter in the pump spectrum similar to the experiments in section 7.5.3.

### 7.6.1 Experimental setup

In these experiments, the complete ionization process is driven by pulses which have a central wavelength of 780 nm. The repetition rate of the regenerative amplifier was changed to 250 kHz in order to have a better signal to noise ratio. The slightly reduced pulse energy of 3.5 $\mu$J is no disadvantage since the complete pulse energy is used for the resonant multi-photon ionization. The pulses enter the pulse shaper which is identical to the experiment before. The only difference is that a double liquid crystal modulator is placed in the Fourier plane to allow for independent phase and amplitude shaping (cf. section 3.2.2). The use of the gratings with 2000 groves per mm and the modulator with 640 pixesl (SLM-640, CRi) provides a high frequency resolution of 0.14 nm/pixel (2.3 $cm^{-1}$/pixel). Alternatively, a needle with a diameter of 1.5 mm which is placed in the Fourier plane allows for removing a frequency band of 35 $cm^{-1}$ width from the pulse spectrum. The frequencies which are removed can be precisely selected by changing the position with a micrometer stage. Since only a small fraction of the spectrum is removed from the pulse, it is nearly transform-limited with high peak intensity. In order to avoid distortion of the trap by high peak intensities, which is especially the case for resonant pulses, the laser power is reduced to about 88 mW before the trap.

For the feedback loop optimization the trap was operated in dark SPOT configuration. The measurements with pulses which are amplitude modulated by the notch filter were carried out in both dark SPOT and standard MOT configuration.

In the magneto-optical trap the molecules are continuously formed by either three body collisions or photoassociation through the trap lasers [202, 207]. These molecules which are present in the trap are investigated in the following.

### 7.6.2 Optimization in a closed feedback loop

The setup for the optimization of the ion yield in a closed feedback loop is depicted in figure 7.17. The goal of the optimization is the maximization of the molecular ion rate. This rate depends on two processes – production and ionization of molecules – which both have to be considered in the optimization. The molecular formation rate in the magneto-optical trap depends on the atomic density [207]. The density is reduced by the

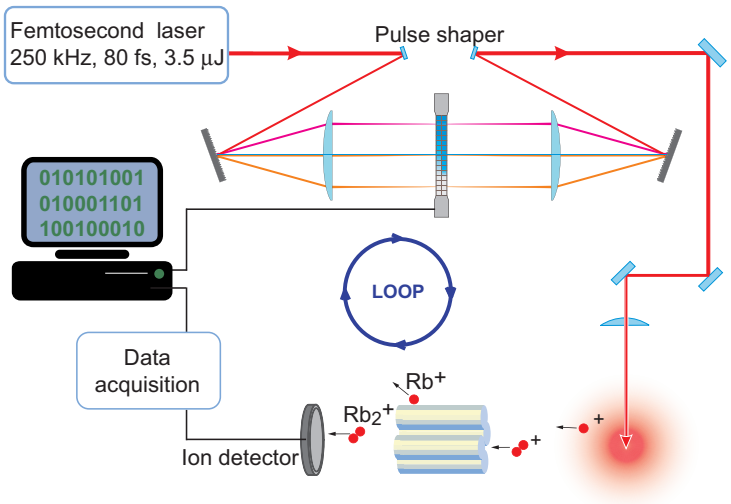


Figure 7.17: Schematic of the setup used for closed feedback loop optimization of the multi-photon ionization of $Rb_2$. The laser pulses are shaped in phase and amplitude by a double liquid crystal array modulator placed in the Fourier plane of a 4-f line. These pulses interact with the molecules which are present in the trap. The molecular ion signal which is obtained by the channeltron after a quadrupole mass filter is processed using a computer. On the basis of the ion signal an evolutionary algorithm controls the liquid crystal modulator. This closes the loop and the ion signal can be iteratively maximized.

femtosecond laser pulses due to atomic ionization and light scattering forces. Therefore, the formation and ionization of molecules must be balanced with the atomic depletion.

To find this optimal pulse a parametric algorithm is employed. This particular algorithm optimizes four Gaussian peaks in the spectral amplitude of the laser pulse whereas the phase pattern is freely optimized [119]. The parameters of each Gaussian peak are the position that can be shifted within the limits of ±15 nm around the central wavelength, the spectral width, which can be varied from 0 to 0.55 nm (0 to 9 $cm^{-1}$), and the amplitude with a transmission range from zero to one. By overlapping peaks or setting the width or transmission to zero the algorithm can reduce the number of spectral peaks. Spectral frequency bands with a larger width can be produced by setting two or more peaks side by side. The spectrum of the resulting pulse is less complex and easier to interpret than the one obtained by free optimization of the amplitudes. It reveals only the most important frequencies which are relevant for the excitations. Therefore, this algorithm is very well-suited to find the relevant transitions in the excitation to the ionic state.

The other advantage of the parametric algorithm is the smaller search space, which leads to a reduction of the duration of the optimization. In this experiment, this is a very important factor. Because of the low molecular ion rate and the noise in the detection a long averaging time of 16 seconds per individual is required resulting in eight minutes per generation. The parameterization kept the duration of the total optimization in a feasible limit.

The molecular ion yield acts as the feedback signal for the algorithm and has to be maximized in order to find the transitions which are optimal for the ionization. Starting from random initial conditions it increases and converges after about ten generations, as de-

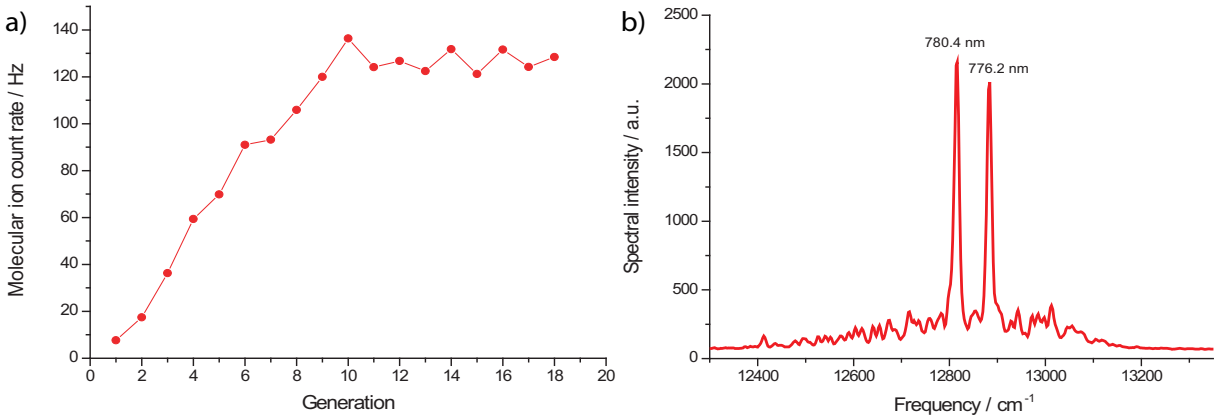


Figure 7.18: Results of the parametric feedback loop optimization. In a), the learning curve is depicted. In b), the spectrum of the finally optimized pulse is displayed. It exhibits two frequency bands at 12 815 and 12 883 $cm^{-1}$ (780.4 and 776.2 nm).

picted in figure 7.18a). The $Rb_2^+$ count rate obtained with the optimized pulse is enhanced by a factor of about 17 compared to an unshaped short pulse of the same power (22 mW). The spectrum of the obtained optimal pulse is shown in figure 7.18b). It exhibits two frequency bands at 12 815 and 12 883 $cm^{-1}$ (780.4 and 776.2 nm). The spectral width of these two frequency bands amounts to 0.34 $cm^{-1}$ and 0.31 $cm^{-1}$, respectively. The four Gaussian peaks are reduced to these two frequency bands by the algorithm. Thus, other frequencies seem to be irrelevant or even obstructive for the ionization process.

In principle, the width and the shape of the spectral bands obtained by the optimization would reveal information about the vibrational distribution of the ultracold molecules formed in the magneto-optical trap, if the spectral resolution was high enough.

This experiment was repeated using pulses produced by the oscillator, which have a lower pulse energy (nJ compared to $\mu$J) but a higher repetition rate, so that the mean power is comparable. With these pulses the obtained ion count rate using the optimized spectrum is also enhanced compared to no shaping, but the molecular count rate is seven times smaller than in the high intensity case. This is consistent with a multi-photon ionization, which is a non-linear effect, where high peak intensities are more efficient.

### 7.6.3 Analysis by frequency filtering

In a second supplementary experiment, the molecular ion rate is measured depending on the position of a blocked frequency band of 35 wavenumbers. In order to investigate the frequencies which emerged in the optimization, the frequencies beneath (12 599 $cm^{-1}$) including the atomic $D_1$ resonance are removed from the spectrum. In this part of the experiment, the pulse consists of nearly the full spectrum. Therefore, the laser power is reduced to 10% to avoid disturbances of the trap. In addition to the molecular ion rate, the fluorescence of the trap is recorded. The position of the needle is scanned in steps of 0.5 nm through the frequency range of interest. To form a data point, at each position of the frequency filter the value for the molecular ion rate and the fluorescence of the atomic cloud is obtained by averaging over more than $10^7$ pulses. The results of

the measurements are presented in figure 7.19.

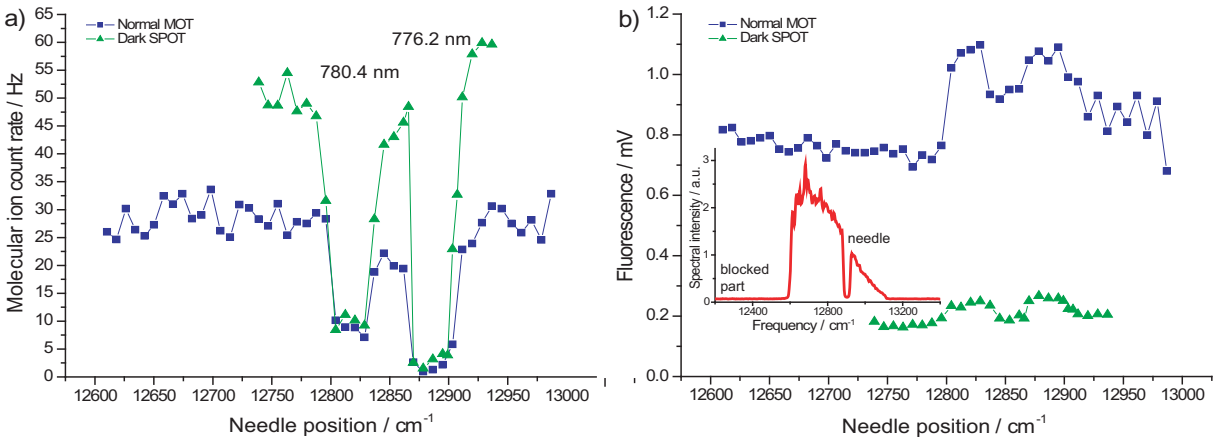


Figure 7.19: In a), the ion signal depending on the position of narrow frequency filter is displayed. In b), the corresponding fluorescence of the ultracold atomic cloud is depicted. The inset illustrates the spectral amplitude distribution which is obtained by frequency filtering by placing a needle in the Fourier plane of the 4-f line. In this example, the needle blocks a band of frequencies located at 12 903 $cm^{-1}$ (775.0 nm). The frequencies below 12 903 $cm^{-1}$ are remove ion order to avoid excitation to the atomic $D_1$ resonance.

This measurement is performed for normal MOT and dark SPOT configuration. The resulting curves are qualitatively similar for both trap configurations. The graph shows a constant signal apart from two frequency bands. When the needle removes a band around the frequencies 12 815 $cm^{-1}$ (780.4 nm) and 12 883 $cm^{-1}$ (776.2 nm), the molecular ion signal drops. The frequency band around 12 883 $cm^{-1}$ seems to have a greater effect on the total molecular ion yield, as the signal plunges practically to zero when it is removed from the spectrum, compared to the finite rate of approximately 10 Hz, when the frequency band around 12 815 $cm^{-1}$ is blocked. This applies to both, normal and dark SPOT configuration.

The fluorescence shows the opposite behavior. When one of the bands is removed by the needle, the fluorescence increases by approximately 30–40%. The only difference between the results obtained with dark SPOT and normal MOT is the fluorescence being four times higher for the latter. The fluorescence is a measure for the steady-state number of excited atoms in the trap. Likely trap-loss mechanisms include: resonant excitation of atomic rubidium by the two frequencies followed by ionization, and loss of atoms due to photon pressure. This demonstrates that both frequency bands contribute to a reduction of the of trapped atoms.

### 7.6.4 Analysis of the excitation pathway

Both experiments – the feedback loop optimization and the frequency filter scan – revealed the relevance of two frequency bands in the multi-photon ionization of ultracold rubidium dimers. These frequency bands which are enclosed in the spectrum of the pulses are situated at 12 815 $cm^{-1}$ (780.4 nm) and 12 883 $cm^{-1}$ (776.2 nm). The excitation process to the first ionic state requires at least three photons. In this pathway, only these two

frequency bands contribute efficiently. The observed frequency bands can be associated with the corresponding transitions in the potential energy scheme, which is depicted in figure 7.20. The molecules which are present in the trap reside in the ground state and are vibrationally highly excited. This means the population is concentrated within a few wavenumbers below the dissociation limit [202]. By excitation with the frequency band which is situated at around 12 815 $cm^{-1}$ (780.4 nm) the long-range bound molecules are transferred to the electronic states which correspond to the $5s5p_{3/2}$ asymptote. The states associated to the $5s5p_{1/2}$ asymptote do not or only negligibly contribute to the process since the frequencies which correspond to the transition do not appear in the optimized spectrum.

In the next excitation step, the frequencies of the other band, which is situated at 12 883 $cm^{-1}$ (776.2 nm), transfer the population to the potential energy curves which are associated with the potentials of the 5s5d asymptote. The energy difference between the $5s5p_{3/2}$ asymptote and the 5s5d asymptote matches exactly the frequencies in the band situated at 12 883 $cm^{-1}$ (776.2 nm). The fine structure splitting of the states corresponding to the $5s5d_{3/2}$ and $5s5d_{5/2}$ amounts to 2.96 $cm^{-1}$ (0.18 nm), which cannot be resolved in this experiment. This excitation pathway agrees with the results of another experiment which utilized a combination of ultrafast laser pulses and narrow band lasers [235].

Besides the confirmation of the two spectral bands the scan of the frequency filter implies further information about the excitation process. The molecular ion signal is reduced to about 10 Hz when the frequencies situated at 12 815 $cm^{-1}$ (780.4 nm) are removed from the spectrum. On the other hand, the molecular ion signal is zero when the frequency band situated at around 12 883 $cm^{-1}$ (776.2 nm) is removed from the spectrum of the pulse. This reveals the importance of the two frequency bands. Further, these results suggest that the frequencies situated at 12 883 $cm^{-1}$ (776.2 nm) are the bottleneck in the excitation process.

The existence of molecular ions, even when the frequency band situated at about 12 815 $cm^{-1}$ (780.4 nm) is removed from the spectrum, can be explained by the production mechanism of the molecules which are present in the trap. As an intermediate product of the photoassociation which is induced by the trap lasers a fraction of the photoassociated molecules is electronically excited in the states associated to the $5s5p_{3/2}$ asymptote. These molecules can be directly excited to the states corresponding to the 5s5d asymptotes and can be ionized subsequently by the frequency band situated at around 12 883 $cm^{-1}$ (776.2 nm).

The energy potential curves which are associated to the 5p5p asymptote are situated below the states associated to the 5s5d asymptote and could – in principle – be reached by the excitation with the laser pulse. To keep the excitation scheme simple the states corresponding to the 5p5p asymptote are not plotted in figure 7.20. This excitation would start in the 5s5s states, evolve via the 5s5p to the 5p5p states and from there to the ionic state driven by two photons of 12 815 $cm^{-1}$ (780.4 nm). The states corresponding to the 5p5p asymptote are not involved in the excitation process, since the ion yield vanishes when the frequencies of the band situated at 12 883 $cm^{-1}$ (776.2 nm) are removed from the spectrum.

Excluding these states which are associated with the 5p5p asymptote provides informa-

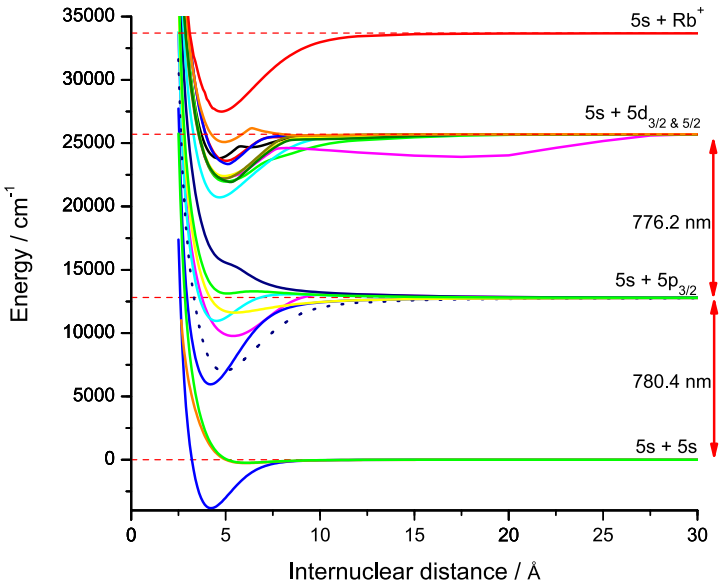


Figure 7.20: Excitation scheme for multi-photon ionization of ultracold rubidium dimers. The participating potential energy curves are taken from [236]. They are represented in Hund's case (a) notation. The molecules are present in the $^1\Sigma_g$, $^3\Sigma_g$, and $^3\Sigma_u$ ground state in the vibrational energy levels just below the 5s5s asymptote. These molecules are transfered by a frequency band situated at 12 815 cm$^{-1}$ (780.4 nm) to the energy potentials $^3\Sigma_u^+$, $^1\Sigma_g^+$, $^1\Sigma_u^+$, $^1\Pi_g$, $^1\Pi_u$, $^3\Pi_g$, and $^1\Pi_u$, which corresponds to the 5s5p$_{3/2}$ asymptote. The next excitation step utilizes the other frequency band which is situated at 12 883 cm$^{-1}$ (776.2 nm) and leads to the 5s5d asymptotes and the corresponding states: $^1\Pi_g$, $^1\Delta_g$, $^3\Sigma_g^+$, $^3\Pi_g$, $^3\Delta_g$, $^1\Sigma_u^+$, $^1\Pi_u$, $^1\Delta_u$, $^3\Pi_u$, and $^3\Delta_u$. In the last excitation step, the molecules are transfered to the $^2\Sigma_g$ ionic ground state by either one of the frequency bands. The red vertical arrows indicate the transitions which are addressed by the two frequency bands that are revealed by feedback loop optimization and frequency filter scan.

tion about the internuclear distance of the molecules. For long internuclear distances, the selection rules for the optical transitions are mostly dominated by the atomic selection rules of the far separated atoms. Regarding these atomic selection rules, the transition from the 5p5p states to the ionic 5s+Rb$^+$ state cannot be achieved by a single photon. Starting from the 5p5p state, the ionization would require two or three photons. However, this multi-photon processes are very unlikely due to the absence of resonances and are therefore not considered. In case of short internuclear distances, the selection rules are purely molecular and would allow the direct ionization from the 5p5p states by a single photon. Thus, the states which are associated with the 5s5d asymptote would not necessarily be preferred to the ones of the 5p5p asymptote. This indicates that the molecular ions are very long bound, such as the molecules which are produced by the photoassociation induced by the trap lasers. This means that in the excitation process no transfer to shorter internuclear distances occurs due to wavepacket dynamics.

The ionization step can be achieved by using either the frequencies of 12 883 cm$^{-1}$ (776.2 nm) or 12 815 cm$^{-1}$ (780.4 nm) and leads to the $^2\Sigma_g$ ground state of the ion. Other excited ionic states cannot be addressed with single photon transition by the provided frequencies of the optimized pulse. Due to the presence of repulsive potential energy

curves and the considerable excess energy a high degree of fragmentation may occur in the ionic state.

Photoassociation may also occur during the ionization process. This is indicated by comparison with measurements of the molecular counting rate obtained with a dye laser [216, 229]. In this detection scheme, the number of ground state molecules is detected directly by a REMPI process. For comparable MOT configurations, the number of molecules detected in a dark SPOT is significantly smaller than in a brighter normal MOT. In the needle scans, the average number of molecules in a dark SPOT is approximately twice as high as in normal MOT configuration (cf. figure 7.19a)), when both frequency bands are enclosed in the pulse. Thus, in the more dense dark SPOT the femtosecond laser pulse seems to increase the number of molecules. When the band around 12 815 $cm^{-1}$ (780.4 nm) is blocked, molecules cannot be photoassociated by the femtosecond laser pulse. Further, ground state molecules formed by the trap lasers and subsequent spontaneous emission cannot be transferred to the states corresponding to the 5s5p asymptote. This can be observed in the molecular ion signal. The photoassociation process occurs proba-

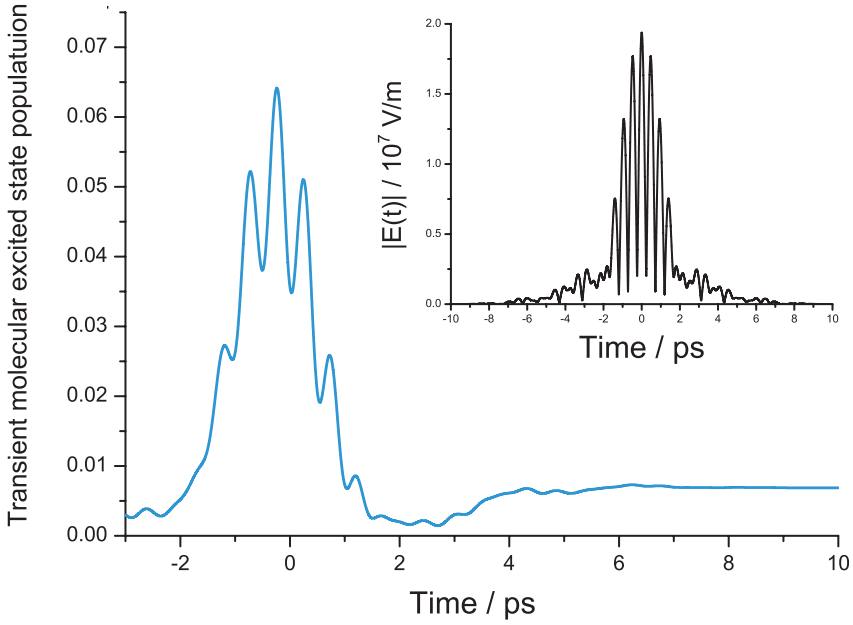


Figure 7.21: Calculation of the transient molecular population in the excited states which correspond to the $5s5p_{3/2}$ asymptote for the optimal pulse obtained by feedback loop experiment. The inset depicts the time evolution of the pulse.

bly in the transition from the 5s5s to the 5s5p states. This first excitation step is modeled with the quantum dynamical calculations introduced in section 7.4. In this calculations a purely atomic ensemble is assumed as a starting point. The transient molecular population in the first excited state which is produced by the optimized pulse is depicted in figure 7.21. This transient has a similar shape such as the transients presented before. The optimized pulse is about 3 ps long and its envelope exhibits a very strong oscillatory behavior because it consists of two narrow frequency bands which interfere. This fast oscillation envelope of the pulse is reflected in the oscillation of the transient. However, the transient molecular population in the first excited state supports the indication that molecules which are produced by the femtosecond laser pulse also contribute to the molec-

ular ion signal. After the interaction with the pulse some molecules remain in the excited state. These portion will spontaneously decay to the ground state.

## 7.7 Conclusion and outlook

In this chapter, some of the first experiments have been presented which investigate the interaction of ultracold atoms and molecules with femtosecond laser pulses. The main objective of these experiments was the photoassociation of an ultracold colliding atom pair to a bound molecule. This process was investigated using time-resolved two-color pump-probe spectroscopy. The pump pulse was amplitude shaped in order to remove the atomic resonances which distort the ultracold atomic ensemble. The focus of this work was the application of spectrally modulated pulses that not only address the bound states of the molecular excited state, which is the intuitive approach for bond formation. Using blue detuned laser pulses which only address repulsive potentials have proven to cause the same molecular transients as the red detuned transients which address the bound states. In addition, the interaction process was studied theoretically by the solutions of the time-dependent Schrödinger equation which agrees very well with the measured data. This exact solution allows for a precise comparison of the transients produced by the red and blue detuned pulses. The analysis revealed that there are small differences in the transients for pulses in which the frequencies are situated above or below the atomic resonance. Further, the transients produced by pulses that contain both – red and blue – frequency components respective to the atomic resonance were considered. In this case, the amplitude of the transient population is determined by the interference of these frequencies. The frequency of the oscillation in the transients is analyzed in detail by using the filter diagonalization method. The frequencies of the oscillation in the molecular population in the excited state are directly connected to the cut-off positions of the respective frequency filters. The spectral components which are relevant for this process are situated close to the atomic resonance. This was investigated by spectroscopy using a pulse with a tunable narrow frequency band. All these experiments and the corresponding theoretical calculations contributed to create a detailed and complete picture of the interaction process. The interaction of the femtosecond laser pulse with the ultracold atomic ensemble is dominated by a strong field effect. The high peak intensity of the pump pulse creates molecular population in the excited state and forms a molecular dipole. This dipole interacts with the declining electric field. This results in modulation of the molecular population.

In a second experiment, the multi-photon ionization was optimized in a closed feedback loop optimization with a parametrical amplitude encoding. The optimized pulse exhibits two frequency bands which are responsible for the multi-photon ionization process. A second complementary experiment confirmed this result. By analyzing these results, the ionization pathway was extracted and the molecule was determined to be long bound. Further, the contribution of pulsed photoassociation was discussed.

These first experiments demonstrated the formation and control of ultracold molecules with femtosecond laser pulses. However, the intended creation of wavepackets by shaped femtosecond laser pulses was not accomplished. In the future, the experimental approach could be modified, which is discussed in the following. For the creation of wavepackets

in the excited state, the applications of picosecond laser pulses are a more promising approach. These pulses address only a band of vibrational levels below but close to the atomic resonance. Moreover, the duration of these pulses would better fit the time scale of the vibrational dynamics at large internuclear distances. Appropriate methods for the shaping of picosecond pulses still need to be developed.

A major challenge in pulsed photoassociation is the issue that the transitions to bound molecular states are very close to the atomic resonance. The strong atomic transition is a competing process since it leads to depletion of the trap. This could be avoided by the selection of a two-photon transition for photoassociation in which the atomic transition could be suppressed by adequate phase shaping. Employing interferences would allow for the application of coherent control schemes, which could utilize the full bandwidth of femtosecond laser pulses [117, 237].

Photoassociation is very sensitive to the pair density in the ultracold atomic ensemble. By employing an additional external field, the pair density could be increased at intermediate and short distances. This Feshbach-optimized photoassociation scheme is suggested in [238]. Another approach would start from a Bose-Einstein condensate, which provides an ensemble of degenerated atoms with a large density.

Femtosecond laser pulses could also be employed for the stabilization of ultracold molecules and transfer to the vibrational ground state. Recently, femtosecond laser pulses were used to redistribute the population in the vibrational states [239, 240]. This method relies on optical pumping and spontaneous emission. The coherence of the laser pulses was not exploited so far but would possibly increase the efficiency. The experimental implementation of pulse shapes which are predicted by theory in order to coherently transfer the vibrationally excited molecule to deeper bound states in the electronic ground state [17, 18] still has to be tested.

The control of molecular formation with shaped femtosecond laser pulses could also be extended to different molecular species or heteronuclear molecules. Experiments which start with van der Waals clusters (e.g. mercury), which could also be doped with a reactant, could be a starting point for creation of molecules with stronger bonds. In the future, photoassociation could be extended to larger molecular systems. For this purpose, helium droplets which contain the reactants – atoms or molecular fragments – could be a promising environment.

# Bibliography


[1] T. H. Maiman: *Stimulated Optical Radiation in Ruby*. Nature **187**, 493-494 (1960).

[2] T. Brixner, G. Krampert, T. Pfeifer, R. Selle, G. Gerber, M. Wollenhaupt, O. Graefe, C. Horn, D. Liese, and T. Baumert: *Quantum Control by Ultrafast Polarization Shaping*. Phys. Rev. Lett. **92**, 208301 (2004).

[3] N. Dudovich, D. Oron, and Y. Silberberg: *Quantum Control of the Angular Momentum Distribution in Multiphoton Absorption Processes*. Phys. Rev. Lett. **92**, 103003 (2004).

[4] M. Aeschlimann, M. Bauer, D. Bayer, T. Brixner, F.J.G. de Abajo, W. Pfeiffer, M. Rohmer, C. Spindler, and F. Steeb: *Adaptive subwavelength control of nano-optical fields*. Nature **446**, 301-304 (2007).

[5] D. V. Voronine, D. Abramavicius, and S. Mukamel: *Manipulating multidimensional electronic spectra of excitons by polarization pulse shaping*. J. Chem. Phys. **126**, 044508 (2007).

[6] M. Ivanov, P. B. Corkum, T. Zuo, and A. Bandrauk: *Routes to Control of Intense-Field Atomic Polarizability*. Phys. Rev. Lett. **74**, 2933-2936 (1995).

[7] G. Sansone, E. Benedetti, J. P. Caumes, S. Stagira, C. Vozzi, M. Nisoli, L. Poletto, P. Villoresi, V. Strelkov, I. Sola, L. B. Elouga, A. Zaïr, E. Mével, and E. Constant: *Shaping of attosecond pulses by phase-stabilized polarization gating*. Phys. Rev. A **80**, 063837 (2009).

[8] M. Shapiro and P. Brumer: *Controlled photon induced symmetry breaking: Chiral molecular products from achiral precursors*. J. Chem. Phys. **95**, 8658-8661 (1991).

[9] L. González, D. Kröner, and I. R. Solá: *Separation of enantiomers by ultraviolet laser pulses in $H_2POSH$: $\pi$ pulses versus adiabatic transitions*. J. Chem. Phys. **115**, 2519-2529 (2001).

[10] I. Barth and J. Manz: *Electric ring currents in atomic orbitals and magnetic fields induced by short intense circularly polarized $\pi$ laser pulses*. Phys. Rev. A **75**, 012510 (2007).

[11] S.-P. Tai, M.-C. Chan, T.-H. Tsai, S.-H. Guol, L.-J. Chen, and C.-K. Sun: *Two-photon fluorescence microscope with a hollow-core photonic crystal fiber*. Opt. Express **12**, 6122-6128 (2004).

[12] M. Sawa, K. Awazu, T. Takahashi, H. Sakaguchi, H. Horiike, M. Ohji, and Y. Tano:

*Application of femtosecond ultrashort pulse laser to photodynamic therapy mediated by indocyanine green*. Br. J. Ophthalmol. **88**, 826-831 (2004).

[13] P. D. Lett, K. Helmerson, W. D. Phillips, L. P. Ratliff, S. L. Rolston, and M. E. Wagshul: *Spectroscopy of $Na_2$ by photoassociation of laser-cooled Na*. Phys. Rev. Lett. **71**, 2200-2203 (1993).

[14] J. Vala, O. Dulieu, F. Masnou-Seeuws, P. Pillet, and R. Kosloff: *Coherent control of cold-molecule formation through photoassociation using a chirped-pulsed-laser field*. Phys. Rev. A **63**, 013412 (2000).

[15] E. Luc-Koenig, R. Kosloff, F. Masnou-Seeuws, and M. Vatasescu: *Photoassociation of cold atoms with chirped laser pulses: Time-dependent calculations and analysis of the adiabatic transfer within a two-state model*. Phys. Rev. A **70**, 033414 (2004).

[16] C. P. Koch, R. Kosloff, E. Luc-Koenig, F. Masnou-Seeuws, and A. Crubellier: *Photoassociation with chirped laser pulses: calculation of the absolute number of molecules per pulse*. J. Phys. B.: At. Mol. Opt. Phys. **39**, 1017 (2006).

[17] C. P. Koch, J. P. Palao, R. Kosloff, and F. Masnou-Seeuws: *Stabilization of Ultracold Molecules Using Optimal Control Theory*. Phys. Rev. A **70**, 013402 (2004).

[18] B. Schäfer-Bung, R. Mitric, and V. Bonačić-Koutecký: *Photostabilization of the ultracold $Rb_2$ molecule by optimal control*. J. Phys. B.: At. Mol. Opt. Phys. **39**, S1043 (2006).

[19] J. D. Jackson: *Classical Electrodynamics*. Hamilton Printing Company (1993).

[20] M. Plewicki: *Phase, amplitude, and polarization pulse shaping in order to influence molecular processes*. Ph. D. thesis, Freie Universität Berlin, (2006).

[21] H. Hurwitz and R. C. Jones: *A New Calculus for the Treatment of Optical Systems I. Description and Discussion of the Calculus*. J. Opt. Soc. Am. **31**, 488-493 (1941).

[22] E. Collet: *Polarized Light*. Marcel Dekker, Inc (1993).

[23] H. Hurwitz and R. C. Jones: *A New Calculus for the Treatment of Optical Systems II. Proof of Three General Equivalence Theorems*. J. Opt. Soc. Am. **31**, 493-499 (1941).

[24] H. Hurwitz and R. C. Jones: *A New Calculus for the Treatment of Optical Systems III. The Sohncke Theory of Optical Activity*. J. Opt. Soc. Am. **31**, 500-503 (1941).

[25] A.M. Weiner, D.E. Leaird, J.S. Patel, and J.R. Wullert: *Programmable shaping of femtosecond optical pulses by use of 128-element liquid crystal phase modulators*. IEEE J. Quant. Elec. **28**, 908 - 920 (1992).

[26] Data sheet: *Spatial Light Modulator (SLM) System*, CRi.

[27] J. Diels and W. Rudolph: *Ultrashort Laser Pulse Phenomena: Fundamentals, Techniques, and Applications on a Femtosecond Time Scale*. Academic Press (1996).

[28] M. J. Wright, S. D. Gensemer, J. Vala, R. Kosloff, and P. L. Gould: *Control of Ultracold Collisions with Frequency-Chirped Light*. Phys. Rev. Lett **95**, 063001 (2005).

[29] A. Bartelt: *Steuerung der Wellenpaketdynamik in kleinen Alkaliclustern mit optimierten Femtosekundenpulsen*. Ph. D. thesis, Freie Universität Berlin, (2002).

[30] F. Schwabl: *Quantenmechanik*. Springer-Verlag, Berlin-Heidelberg (1993).

[31] D. J. Tannor: *Introduction to quantum mechanics: A time-dependent perspective*. Univ. Science Books (2006).

[32] I. Grenthe: *Nobel Lectures, Chemistry 1996-2000*. World Scientific Publishing Co. (2003).

[33] T. Brixner and G. Gerber: *Laser-optimierte Femtochemie*. Physikalische Blätter **57**, 33-39 (2001).

[34] P. Brumer and M. Shapiro: *Control of unimolecular reactions using coherent light*. Chem. Phys. Lett. **126**, 541-546 (1986).

[35] Ce Chen, Yi-Yian Yin, and D. S. Elliott: *Interference between optical transitions*. Phys. Rev. Lett. **64**, 507-510 (1990).

[36] L. Zhu, V.ria Kleiman, X. Li, S. P. Lu, K. Trentelman, and R. J. Gordon: *Coherent Laser Control of the Product Distribution Obtained in the Photoexcitation of HI*. Science **270**, 77-80 (1995).

[37] D. J. Tannor, R. Kosloff, and S. A. Rice: *Coherent pulse sequence induced control of selectivity of reactions: Exact quantum mechanical calculations*. J. Chem. Phys. **85**, 5805-5820 (1986).

[38] E.D. Potter, J.L. Herek, S. Pedersen, Q. Liu, and A.H. Zewail: *Femtosecond laser control of a chemical reaction*. Nature, (1992).

[39] K. Bergmann, H. Theuer, and B. W. Shore: *Coherent population transfer among quantum states of atoms and molecules*. Rev. Mod. Phys. **70**, 1003-1025 (1998).

[40] N. V. Vitanov, T. Halfmann, B. W. Shore, and K. Bergmann: *Laser-induced population transfer by adiabatic passage techniques*. Ann. Rev. Phys. Chem. **52**, 763-809 (2001).

[41] W. S. Warren, H. Rabitz, and M. Dahleh: *Coherent Control of Quantum Dynamics: The Dream Is Alive*. Science **259**, 1581-1589 (1993).

[42] A. P. Peirce, M. A. Dahleh, and H. Rabitz: *Optimal control of quantum-mechanical systems: Existence, numerical approximation, and applications*. Phys. Rev. A **37**, 4950-4964 (1988).

[43] R. S. Judson and H. Rabitz: *Teaching lasers to control molecules*. Phys. Rev. Lett. **68**, 1500 (1992).

[44] C.J. Bardeen, V.V. Yakovlev, K.R. Wilson, S.D. Carpenter, P.M. Weber, and W.S. Warren: *Feedback quantum control of molecular electronic population transfer*. Chem. Phys. Lett. **280**, 151-158 (1997).

[45] T. Suzuki, S. Minemoto, T. Kanai, and H. Sakai: *Optimal Control of Multiphoton Ionization Processes in Aligned $I_2$ Molecules with Time-Dependent Polarization Pulses*. Phys. Rev. Lett. **92**, 133005 (2004).

[46] G. Vogt, G. Krampert, P. Niklaus, P. Nuernberger, and G. Gerber: *Optimal Control of Photoisomerization*. Phys. Rev. Lett. **94**, 068305 (2005).

[47] R. J. Levis, G. M. Menkir, and H. Rabitz: *Selective Bond Dissociation and Rearrangement with Optimally Tailored, Strong-Field Laser Pulses*. Science **292**, 709-713 (2001).

[48] A. Lindinger, C. Lupulescu, M. Plewicki, F. Vetter, A. Merli, S. M. Weber, and L. Wöste: *Isotope Selective Ionization by Optimal Control Using Shaped Femtosecond Laser Pulses*. Phys. Rev. Lett. **93**, 033001 (2004).

[49] Roth M., L. Guyon, J. Roslund, V. Boutou, F. Courvoisier, J.-P. Wolf, and H. Rabitz: *Quantum Control of Tightly Competitive Product Channels*. Phys. Rev. Lett. **102**, 253001 (2009).

[50] J. Kunde, B. Baumann, S. Arlt, F. Morier-Genoud, U. Siegner, and U. Keller: *Adaptive feedback control of ultrafast semiconductor nonlinearities*. Appl. Phys. Lett. **77**, 924-926 (2000).

[51] I. Otake, S. S. Kano, and A. Wada: *Pulse shaping effect on two-photon excitation efficiency of alpha-perylene crystals and perylene in chloroform solution*. J. Chem. Phys. **124**, 014501 (2006).

[52] J. L. Herek, W. Wohlleben, R. J. Cogdell, D. Zeidler, and M. Motzkus: *Quantum control of energy flow in light harvesting*. Nature **417**, 533-535 (2002).

[53] J. P. Ogilvie, D. Débarre, X. Solinas, J.-L. Martin, E. Beaurepaire, and M. Joffre: *Use of coherent control for selective two-photon fluorescence microscopy in live organisms*. Opt. Express **14**, 759-766 (2006).

[54] T. Feurer, Joshua C. Vaughan, and Keith A. Nelson: *Spatiotemporal Coherent Control of Lattice Vibrational Waves*. Science **299**, 374-377 (2003).

[55] R. Bartels, S. Backus, E. Zeek, L. Misoguti, G. Vdovin, I. P. Christov, M. M. Murnane, and H. C. Kapteyn: *Shaped-pulse optimization of coherent emission of high-harmonic soft X-rays*. Nature **406**, 164-166 (2000).

[56] T. Pfeifer, D. Walter, C. Winterfeldt, C. Spielmann, and G. Gerber: *Controlling the spectral shape of coherent soft x-rays*. Appl. Phys. B **80**, 277-280 (2005).

[57] T. Feurer: *Feedback-Controlled Optimization of Soft-X-Ray Radiation from Femtosecond Laser-Produced Plasmas*. Appl. Phys. B **68**, 55 (1999).

[58] S. Kirkpatrick, Jr. Gelatt, C. D., and M. P. Vecchi: *Optimization by Simulated Annealing*. Science **220**, 671-680 (1983).

[59] D.-E. Goldberg: *Genetic Algorithms in Search, Optimization and Machine Learning*. Addison-Wesley Professional (1989).

[60] H. P. Schwefel: *Numerical Optimization for Computer Models*. John Wiley (1981).

[61] G. J. Tóth, A. Lorincz, and H. Rabitz: *The effect of control field and measurement imprecision on laboratory feedback control of quantum systems*. J. Chem. Phys. **101**, 3715-3722 (1994).

[62] A. R. Wallace to C. R. Darwin: *Letter 5140*. Darwin Correspondence Project, (1866).

[63] J.H. Holland: *Adaption in Natural and Artificial Systems*. University of Michigan Press, (1975).

[64] S. M. Weber: *New concepts for optimal control experiments using femtosecond pulse shaping*. Ph. D. thesis, Freie Universität Berlin, (2007).

[65] I. Rechenberg: *Evolutionsstrategie: Optimierung technischer Systeme nach Prinzipien der biologischen Evolution*. Frommann-Holzboog-Verlag, Stuttgart, 1973 (1973).

[66] C. Rulliere: *Femtosecond Laser Pulses*. Springer (2004).

[67] Data sheet: *The Coherent Mira Seed Laser*, Coherent.

[68] Data sheet: *Verdi V5*, Coherent.

[69] Data sheet: *RegA Model 9050 Laser*, Coherent.

[70] Data sheet: *Millennia X*, Spectra Physics.

[71] T. Wilhelm, J. Piel, and E. Riedle: *Sub-20-fs pulses tunable across the visible from a blue-pumped single-pass noncollinear parametric converter*. Opt. Lett. **22**, 1494 (1997).

[72] J. Piel, E. Riedle, L. Gundlach, R. Ernstorfer, and R. Eichberger: *Sub-20 fs visible pulses with 750 nJ energy from a 100 kHz noncollinear optical parametric amplifier*. Opt. Lett. **31**, 1289-1291 (2006).

[73] J.H. Marburger: *Self-focusing: Theory*. Prog. Quant. Electr. **4**, 35-110 (1975).

[74] P. Chernev and V. Petrov: *Self-focusing of light pulses in the presence of normal group-velocity dispersion*. Opt. Lett. **17**, 172-174 (1992).

[75] F. Shimizu: *Frequency Broadening in Liquids by a Short Light Pulse*. Phys. Rev. Lett. **19**, 1097-1100 (1967).

[76] R. R. Alfano and S. L. Shapiro: *Observation of Self-Phase Modulation and Small-Scale Filaments in Crystals and Glasses*. Phys. Rev. Lett. **24**, 592-594 (1970).

[77] A. Brodeur and S. L. Chin: *Ultrafast white-light continuum generation and self-focusing in transparent condensed media*. J. Opt. Soc. Am. B **16**, 637-650 (1999).

[78] O. E. Martinez: *3000 Times Grating Compressor with Positive Group Velocity Dispersion: Application to Fiber Compensation in 1.3-1.6 μm Region*. IEEE J. Quant. Elec. **23**, 59 (1987).

[79] A. Monmayrant and B. Chatel: *New phase and amplitude high resolution pulse shaper*. Rev. Sci. Instrum. **75**, 2668-2671 (2004).

[80] A. M. Weiner, J. P. Heritage, and E. M. Kirschner: *High-resolution femtosecond pulse shaping*. J. Opt. Soc. Am. B **5**, 1563-1572 (1988).

[81] A. M. Weiner and J. P. Heritage: *Shaping optical pulses by amplitude and phase masking*. Patent, US4655547 (1987).

[82] C. W. Hillegas, J. X. Tull, D. Goswami, D. Strickland, and W. S. Warren: *Femtosecond laser pulse shaping by use of microsecond radio-frequency pulses*. Opt. Lett. **19**, 737-739 (1994).

[83] M. Roth, M. Mehendale, A. Bartelt, and H. Rabitz: *Acousto-optical shaping of ultraviolet femtosecond pulses*. Appl. Phys. B **80**, 441-444 (2005).

[84] N. Krebs, R. A. Probst, and E. Riedle: *Sub-20 fs pulses shaped directly in the UV by an acousto-optic programmable dispersive filter*. Opt. Express **18**, 6164-6171 (2010).

[85] M. Hacker, G. Stobrawa, R. Sauerbrey, T. Buckup, M. Motzkus, M. Wildenhain, and A. Gehner: *Micromirror SLM for femtosecond pulse shaping in the ultraviolet*. Appl. Phys. B **76**, 711-714 (2003).

[86] A. Rondi, J. Extermann, L. Bonacina, S. M. Weber, and J.-P. Wolf: *Characterization of a MEMS-based pulse-shaping device in the deep ultraviolet*. Appl. Phys. B **96**, 757-761 (2009).

[87] A. M. Weiner, D. E. Leaird, J. S. Patel, and J. R. Wullert: *Programmable femtosecond pulse shaping by use of a multielement liquid-crystal phase modulator*. Opt. Lett. **15**, 326-328 (1990).

[88] M. Plewicki, S. M. Weber, F. Weise, and A. Lindinger: *Independent control over the amplitude, phase, and polarization of femtosecond pulses*. Appl. Phys. B **86**, 259-263 (2007).

[89] B J. Sussman, R. Lausten, and A. Stolow: *Focusing of light following a 4-f pulse shaper: Considerations for quantum control*. Phys. Rev. A **77**, 043416 (2008).

[90] F. Frei, A. Galler, and T. Feurer: *Space-time coupling in femtosecond pulse shaping and its effects on coherent control*. J. Chem. Phys. **130**, 034302 (2009).

[91] S. M. Weber: *Application of Evolution Strategies on Arbitrary Pulse Form Generation, White Light Generation and Isotope Ratio Optimization of $K_2$*. Diploma thesis, FU Berlin (2003).

[92] J. Vaughan, T. Feurer, K. Stone, and K. Nelson: *Analysis of replica pulses in femtosecond pulse shaping with pixelated devices*. Opt. Express **14**, 1314-1328 (2006).

[93] K. D. Kammmeyer: *Nachrichtenübertragung*. Teubner (2004).

[94] M. M. Wefers and K. A. Nelson: *Generation of high-fidelity programmable ultrafast optical waveforms*. Opt. Lett **20**, 1047-1049 (1995).

[95] T. Brixner and G. Gerber: *Femtosecond polarization pulse shaping*. Opt. Lett. **26**, 557-559 (2001).

[96] L. Polachek, D. Oron, and Y. Silberberg: *Full control of the spectral polarization of ultrashort pulses*. Opt. Lett. **31**, 631-633 (2006).

[97] M. Plewicki, F. Weise, S. M. Weber, and A. Lindinger: *Phase, amplitude, and polarization shaping with a pulse shaper in a Mach-Zehnder interferometer*. Appl. Opt. **45**, 8356 (2006).

[98] M. Wollenhaupt, M. Krug, J. Köhler, T. Bayer, C. Sarpe-Tudoran, and T. Baumert: *Photoelectron angular distributions from strong-field coherent electronic excitation*. Appl. Phys. B **95**, 245-259 (2009).

[99] S.C. Barden, J. A. Arns, W. S. Colburn, and J.B. Williams: *Volume-Phase Holographic Gratings and the Efficiency of Three Simple Volume-Phase Holographic Gratings*. Publications of the Astronomical Society of the Pacific **112**, 809-820 (2000).

[100] M. Akbulut, R. Nelson, A. M. Weiner, P. Cronin, and P. J. Miller: *Broadband polarization correction with programmable liquid-crystal modulator arrays*. Opt. Lett. **29**, 1129-1131 (2004).

[101] H. Miao, A. M. Weiner, L. Mirkin, and P. J. Miller: *Broadband all-order polarization mode dispersion compensation via wavelength-by-wavelength Jones matrix correction*. Opt. Lett. **32**, 2360-2362 (2007).

[102] H. Miao, A. M. Weiner, L. Mirkin, and P. J. Miller: *All-Order Polarization-Mode Dispersion (PMD) Compensation via Virtually Imaged Phased Array (VIPA)-Based Pulse Shaper*. IEEE PTL **20**, 545-547 (2008).

[103] F. Weise, S. M. Weber, M. Plewicki, and A. Lindinger: *Application of phase, amplitude, and polarization shaped pulses for optimal control on molecules*. Chem. Phys. **332**, 313-317 (2007).

[104] S. M. Weber, M. Plewicki, F. Weise, and A. Lindinger: *Parametric polarization pulse shaping demonstrated for optimal control of NaK*. J. Chem. Phys. **128**, 174306 (2008).

[105] Y. Esumi, M. D. Kabir, and F. Kannari: *Spatiotemporal vector pulse shaping of femtosecond laser pulses with a multi-pass two-dimensional spatial light modulator*. Opt. Express **17**, 19153-19159 (2009).

[106] S. M. Weber, F. Weise, M. Plewicki, and A. Lindinger: *Interferometric generation of parametrically shaped polarization pulses*. Appl. Opt. **46**, 5987-5990 (2007).

[107] F. Weise: *Entwicklung der Pulsformung in Phase, Amplitude und Polarisation sowie kohärente Kontrolle in der MOT*. Diploma thesis, FU Berlin (2006).

[108] M. Sato, T. Suzuki, and K. Misawa: *Interferometric polarization pulse shaper stabilized by an external laser diode for arbitrary vector field shaping*. Rev. Sci. Instrum. **80**, 123107 (2009).

[109] M. Ninck, A. Galler, T. Feurer, and T. Brixner: *Programmable common-path vector field synthesizer for femtosecond pulses*. Opt. Lett **32**, 3379 (2007).

[110] O. Masihzadeh, P. Schlup, and R. A. Bartels: *Complete polarization state control of ultrafast laser pulses with a single linear spatial light modulator*. Opt. Express **15**, 18025-18032 (2007).

[111] C. T. Middleton, D. B. Strasfeld, and M. T. Zanni: *Polarization shaping in the mid-IR and polarization-based balanced heterodyne detection with application to 2D IR spectroscopy*. Opt. Express **17**, 14526-14533 (2009).

[112] P. Nuernberger, R. Selle, F. Langhojer, F. Dimler, S. Fechner, G. Gerber, and T. Brixner: *Polarization-shaped femtosecond laser pulses in the ultraviolet*. J. Opt. A: Pure and Applied Optics **11**, 085202 (2009).

[113] D. Zeidler, S. Frey, K.-L. Kompa, and M. Motzkus: *Evolutionary algorithms and their application to optimal control studies*. Phys. Rev. A **64**, 023420 (2001).

[114] M. Comstock, V. Lozovoy, I. Pastirk, and M. Dantus: *Multiphoton intrapulse interference 6; binary phase shaping*. Opt. Express **12**, 1061-1066 (2004).

[115] L. Xu, N. Nakagawa, R. Morita, H. Shigekawa, and M. Yamashita: *Programmable chirp compensation for 6-fs pulse generation with a prism-pair-formed pulse shaper*. IEEE J. Quant. Elec. **36**, 893-899 (2000).

[116] S. H. Lee, A. L. Cavalieri, D. M. Fritz, M. Myaing, and D. A. Reis: *Adaptive dispersion compensation for remote fiber delivery of near-infrared femtosecond pulses*. Opt. Lett. **29**, 2602-2604 (2004).

[117] D. Meshulach and Y. Silberberg: *Coherent quantum control of two-photon transitions by a femtosecond laser pulse*. Nature **396**, 239-242 (1998).

[118] H. Ibrahim, M. Héjjas, and N. Schwentner: *Tracing, Amplifying, and Steering Chromophore-Bath Coherences by Ultrashort Pulse Trains*. Phys. Rev. Lett. **102**, 088301 (2009).

[119] S. M. Weber, A. Lindinger, F. Vetter, M. Plewicki, A. Merli, and L. Wöste: *Application of parametric time and frequency domain shaping*. Eur. Phys. J. D **33**, 39-42 (2005).

[120] F. Weise, S. Birkner, A. Merli, S. M. Weber, F. Sauer, L. Wöste, A. Lindinger, W. Salzmann, T. Mullins, J. Eng, M. Albert, R. Wester, and M. Weidemüller: *Optimal control of multiphoton ionization of $Rb_2$ molecules in a magneto-optical trap*. Phys. Rev. A **76**, 063404 (2007).

[121] T. Hornung, R. Meier, and M. Motzkus: *Optimal control of molecular states in a learning loop with a parameterization in frequency and time domain*. Chem. Phys. Lett. **326**, 445-453 (2000).

[122] F. Dimler, S. Fechner, A. Rodenberg, T. Brixner, and D. J. Tannor: *Accurate and efficient implementation of the von Neumann representation for laser pulses with discrete and finite spectra*. New J. Phys. **11**, 105052 (2009).

[123] T. Brixner: *Poincaré representation of polarization-shaped femtosecond laser pulses*. Appl. Phys. B **76**, 531-540 (2003).

[124] B. E. Schmidt: *White Light Filamentation: Tailoring & Application for Charge Reversal of $Ag_3^-$*. Ph. D. thesis, Freie Universität Berlin, (2008).

[125] W. J. Walecki, D. Fittinghoff, A. L. Smirl, and R. Trebino: *Characterization of the polarization state of weak ultrashort coherent signals by dual-channelspectral interferometry*. Opt. Lett. **22**, 81-83 (1997).

[126] P. Brumer, E. Frishman, and M. Shapiro: *Principles of electric-dipole-allowed optical control of molecular chirality*. Phys. Rev. A **65**, 015401 (2001).

[127] D. Oron, Y. Silberberg, N. Dudovich, and D. M. Villeneuve: *Efficient polarization gating of high-order harmonic generation by polarization-shaped ultrashort pulses*. Phys. Rev. A **72**, 063816 (2006).

[128] T. Brixner, F. J. García de Abajo, J. Schneider, and W. Pfeiffer: *Nanoscopic Ultrafast Space - Time-Resolved Spectroscopy*. Phys. Rev. Lett. **95**, 093901 (2005).

[129] K. Hosaka, H. Shimada, H. Chiba, H. Katsuki, Y. Teranishi, Y. Ohtsuki, and K. Ohmori: *Ultrafast Fourier Transform with a Femtosecond-Laser-Driven Molecule*. Phys. Rev. Lett. **104**, 180501 (2010).

[130] I. Barth, J. Manz, Y. Shigeta, and K. Yagi: *Unidirectional Electronic Ring Current Driven by a Few Cycle Circularly Polarized Laser Pulse: Quantum Model Simulations for Mg-Porphyrin*. J. Am. Chem. Soc. **128**, 7043-7049 (2006).

[131] J.-D. Colladon: *La Fontaine Colladon*. La Nature, 325 (1884).

[132] J. Hecht: *City of Light: The story of Fiber Optics*. Oxford University Press (1999).

[133] S. W. Clark, F. Ö. Ilday, and F. W. Wise: *Fiber delivery of femtosecond pulses from a Ti:sapphire laser*. Opt. Lett. **26**, 1320-1322 (2001).

[134] P. Russell: *Photonic Crystal Fibers*. Science **299**, 358-362 (2003).

[135] W. Göbel, A. Nimmerjahn, and F. Helmchen: *Distortion-free delivery of nanojoule femtosecond pulses from a Ti:sapphire laser through a hollow-core photonic crystal fiber*. Opt. Lett. **29**, 1285-1287 (2004).

[136] A. I. Talukder, K. Totsuka, and M. Tomita: *Propagation of arbitrarily shaped femtosecond laser pulses through a photonic crystal fiber*. Appl. Phys. Lett. **89**, 054103 (2006).

[137] G. P. Agrawal: *Nonlinear Fiber optics*. Academic Press (2001).

[138] T. A. Birks, J. C. Knight, and P. S. J. Russell: *Endlessly single-mode photonic crystal fiber*. Opt. Lett. **22**, 961-963 (1997).

[139] R. F. Cregan, B. J. Mangan, J. C. Knight, T. A. Birks, P. S. J. Russell, P. J. Roberts, and D. C. Allan: *Single-Mode Photonic Band Gap Guidance of Light in Air*. Science **285**, 1537-1539 (1999).

[140] F. Benabid, J. Knight, and P. Russell: *Particle levitation and guidance in hollow-core photonic crystal fiber*. Opt. Express **10**, 1195-1203 (2002).

[141] P. S. J. Russell: *Photonic-Crystal Fibers*. Journal of Lightwave Technology **24**, 4729 (2006).

[142] Data sheet: *Hollow Core Photonic Bandgap Fiber HC-800-01*, Blaze Photonics.

[143] A. M. Vengsarkar and W. A. Reed: *Dispersion-compensating single-mode fibers: efficient designs for first- and second-order compensation*. Opt. Lett. **18**, 924-926 (1993).

[144] K. O. Hill, F. Bilodeau, B. Malo, T. Kitagawa, S. Thériault, D. C. Johnson, J. Albert, and K. Takiguchi: *Chirped in-fiber Bragg gratings for compensation of optical-fiber dispersion*. Opt. Lett. **19**, 1314-1316 (1994).

[145] B. R. Washburn, J. A. Buck, and S. E. Ralph: *Transform-limited spectral compression due to self-phase modulation in fibers*. Opt. Lett. **25**, 445-447 (2000).

[146] M. T. Myaing., J. Urayama, A. Braun, and T. Norris: *Nonlinear propagation of negatively chirped pulses: Maximizing the peak intensity at the output of a fiber probe.* Opt. Express **7**, 210-214 (2000).

[147] C.-C. Chang, H. P. Sardesai, and A. M. Weiner: *Dispersion-free fiber transmission for femtosecond pulses by use of a dispersion-compensating fiber and a programmable pulse shaper.* Opt. Lett. **23**, 283-285 (1998).

[148] C.-L. Chen: *Foundations for Guided-Wave Optics.* John Wiley & Sons, Inc (2007).

[149] I. P. Kaminow and T. L. Koch: *Optical Fiber Communications.* Academic Press (2002).

[150] J. M. Dudley, G. Genty, and S. Coen: *Supercontinuum generation in photonic crystal fiber.* Rev. Mod. Phys. **78**, 1135-1184 (2006).

[151] M. Oberthaler and R. A. Höpfel: *Special narrowing of ultrashort laser pulses by self-phase modulation in optical fibers.* Appl. Phys. Lett. **63**, 1017-1019 (1993).

[152] B. Schmidt, M. Hacker, G. Stobrawa, and T. Feurer: *LAB2-A virtual femtosecond laser lab.* http://www.lab2.de.

[153] B. Schmidt, M. Hacker, G. Stobrawa, and T. Feurer: *LAB2 - User Manual.* http://www.lab2.de/filez/manual.pdf.

[154] G. Achazi, F. Weise, M. Pawłowska, A. Patas, and A. Lindinger: *Characterising pulses after propagation throught an optical fiber by detection of a fraction of back-reflected light.* in preparation.

[155] S. O. Konorov, E. E. Serebryannikov, A. B. Fedotov, R. B. Miles, and A. M. Zheltikov: *Phase-matched waveguide four-wave mixing scaled to higher peak powers with large-core-area hollow photonic-crystal fibers.* Phys. Rev. E **71**, 057603 (2005).

[156] F. Luan, J. Knight, P. Russell, S. Campbell, D. Xiao, D. Reid, B. Mangan, D. Williams, and P. Roberts: *Femtosecond soliton pulse delivery at 800nm wavelength in hollow-core photonic bandgap fibers.* Opt. Express **12**, 835-840 (2004).

[157] F. Gèrôme, P. Dupriez, J. Clowes, J. C. Knight, and W. J. Wadsworth: *High power tunable femtosecond soliton sourceusing hollow-core photonic bandgap fiber, andits use for frequency doubling.* Opt. Express **16**, 2381-2386 (2008).

[158] D. Rand, I. Glesk, C.-S. Brès, D. A. Nolan, X. Chen, J. Koh, J. W. Fleischer, K. Steiglitz, and P. R. Prucnal: *Observation of Temporal Vector Soliton Propagation and Collision in Birefringent Fiber.* Phys. Rev. Lett. **98**, 053902 (2007).

[159] A. Paul, R. A. Bartels, R. Tobey, H. Green, S. Weiman, I. P. Christov, M. M. Murnane, H. C. Kapteyn, and S. Backus: *Quasi-phase-matched generation of coherent extreme-ultraviolet light.* Nature **421**, 51-54 (2002).

[160] B. A. Nechay, U. Siegner, M. Achermann, H. Bielefeldt, and U. Keller: *Femtosecond pump-probe near-field optical microscopy.* Rev. Sci. Instrum. **70**, 2758-2764 (1999).

[161] S. Nolte, B. N. Chichkov, H. Welling, Y. Shani, K. Lieberman, and H. Terkel: *Nanostructuring with spatially localized femtosecond laser pulses.* Opt. Lett. **24**, 914-916 (1999).

[162] K. König: *Multiphoton microscopy in life sciences*. Journal of Microscopy **200**, 83-104 (2000).

[163] K. T. Tsen, S.-W. D. Tsen, C.-L. Chang, C.-F. Hung, T.-C. Wu, and J. G. Kiang: *Inactivation of viruses with a very low power visible femtosecond laser*. J. Phys. B.: At. Mol. Opt. Phys. **19**, 322102 (2007).

[164] S. Rutz: *Femtosekundenspektroskopie zur Wellenpaketdynamik in Alkalidimeren und -trimeren*. Ph. D. thesis, Freie Universität Berlin, (1996).

[165] S. Rutz, R. de Vivie-Riedle, and E. Schreiber: *Femtosecond wave-packet propagation in spin-orbit-coupled electronic states of* $^{39,39}K_2$ *and* $^{39,41}K_2$. Phys. Rev. A **54**, 306-313 (1996).

[166] R. de Vivie-Riedle, K. Kobe, J. Manz, W. Meyer, B. Reischl, S. Rutz, E. Schreiber, and L. Wöste: *Femtosecond Study of Multiphoton Ionization Processes in* $K_2$*: from Pump-Probe to Control*. J. Phys. Chem. **100**, 7789-7796 (1996).

[167] C. Nicole, M. A. Bouchène, C. Meier, S. Magnier, E. Schreiber, and B. Girard: *Competition of different ionization pathways in* $K_2$ *studied by ultrafast pump–probe spectroscopy: A comparison between theory and experiment*. J. Chem. Phys. **111**, 7857-7864 (1999).

[168] H. Kühling: *Ultrakurzzeit-Spektroskopie an kleinen Alkaliclustern*. Ph. D. thesis, Freie Universität Berlin, (1993).

[169] F. Sauer: *Wellenpaketdynamik in Alkali-Dimeren Untersuchung und Steuerung durch kohärente Anregung mit fs-Pulsen*. Ph. D. thesis, Freie Universität Berlin, (2007).

[170] H. Pauly: *Atom, Molecule and Cluster Beams I*. Springer-Verlag, Berlin-Heidelberg (2000).

[171] V. V. Lozovoy, X. Zhu, T. C. Gunaratne, D. A. Harris, J. C. Shane, and M. Dantus: *Control of Molecular Fragmentation Using Shaped Femtosecond Pulses*. J. Phys. Chem. **12**, 3789-3812 (2008).

[172] R. de Vivie-Riedle, B. Reischl, S. Rutz, and E. Schreiber: *Femtosecond Study of Multiphoton Ionization Processes in* $K_2$ *at Moderate Laser Intensities*. J. Phys. Chem. **99**, 16829-16834 (1995).

[173] G. Jong, L. Li, T. J. Whang, W. C. Stwalley, J. A. Coxon, M. Li, and A. M. Lyyra: *CW all-optical triple-resonance spectroscopy of* $K_2$*: Deperturbation analysis of the* $A^1\Sigma_u^+$ *(*$v \leq 12$*) and* $b^3\Pi_u$ *(*$13 \leq v \leq 24$*) states*. J. Mol. Spec. **155**, 115-135 (1992).

[174] J. Ullrich and H. Schmidt-Böcking: *Time-of-flight spectrometer for the determination of microradian projectile scattering angles in atomic collisions*. Phys. Lett. A **125**, 193-196 (1987).

[175] M. Meckel, D. Comtois, D. Zeidler, A. Staudte, D. Pavicic, H. C. Bandulet, H. Pepin, J. C. Kieffer, R. Dörner, D. M. Villeneuve, and P. B. Corkum: *Laser-Induced Electron Tunneling and Diffraction*. Science **320**, 1478-1482 (2008).

[176] E. L. Raab, M. Prentiss, Alex Cable, Steven Chu, and D. E. Pritchard: *Trapping of Neutral Sodium Atoms with Radiation Pressure*. Phys. Rev. Lett. **59**, 2631-2634 (1987).

[177] W. D. Phillips: *Laser cooling and trapping of neutral atoms*. Rev. Mod. Phys. **70**, 721-741 (1998).

[178] K. B. Davis, M. O. Mewes, M. R. Andrews, N. J. van Druten, D. S. Durfee, D. M. Kurn, and W. Ketterle: *Bose-Einstein Condensation in a Gas of Sodium Atoms*. Phys. Rev. Lett. **75**, 3969-3973 (1995).

[179] M. H. Anderson, J. R. Ensher, M. R. Matthews, C. E. Wieman, and E. A. Cornell: *Observation of Bose-Einstein Condensation in a Dilute Atomic Vapor*. Science **269**, 198-201 (1995).

[180] M.-O. Mewes, M. R. Andrews, D. M. Kurn, D. S. Durfee, C. G. Townsend, and W. Ketterle: *Output Coupler for Bose-Einstein Condensed Atoms*. Phys. Rev. Lett. **78**, 582-585 (1997).

[181] L. D. Carr, D. DeMille, R. V. Krems, and J. Ye: *Cold and ultracold molecules: science, technology and applications*. New J. Phys. **11**, 055049 (2009).

[182] J. T. Bahns, W. C. Stwalley, and P. L. Gould: *Laser cooling of molecules: A sequential scheme for rotation, translation, and vibration*. J. Chem. Phys. **104**, 9689-9697 (1996).

[183] M.D. Di Rosa: *Laser-cooling molecules*. Eur. Phys. J. D **31**, 395-402 (2004).

[184] B. L. Lev, A. Vukics, E. R. Hudson, B. C. Sawyer, P. Domokos, H. Ritsch, and J. Ye: *Prospects for the cavity-assisted laser cooling of molecules*. Phys. Rev. A **77**, 023402 (2008).

[185] E. S. Shuman, J. F. Barry, D. R. Glenn, and D. DeMille: *Radiative Force from Optical Cycling on a Diatomic Molecule*. Phys. Rev. Lett. **103**, 223001 (2009).

[186] J. M. Doyle, B. Friedrich, J. Kim, and D. Patterson: *Buffer-gas loading of atoms and molecules into a magnetic trap*. Phys. Rev. A **52**, R2515-R2518 (1995).

[187] J. D. Weinstein, R. de Carvalho, T. Guillet, B. Friedrich, and J. M. Doyle: *Magnetic trapping of calcium monohydride molecules at millikelvin temperatures*. Nature **395**, 148-150 (1998).

[188] M. Gupta and D. Herschbach: *A Mechanical Means to Produce Intense Beams of Slow Molecules*. J. Phys. Chem. A **103**, 10670-10673 (1999).

[189] M. S. Elioff, J. J. Valentini, and D. W. Chandler: *Subkelvin Cooling NO Molecules via "Billiard-like" Collisions with Argon*. Science **302**, 1940-1943 (2003).

[190] H. L. Bethlem, G. Berden, and G. Meijer: *Decelerating Neutral Dipolar Molecules*. Phys. Rev. Lett. **83**, 1558 (1999).

[191] H. L. Bethlem and G. Meijer: *Production and application of translationally cold molecules*. Int. Rev. Phys. Chem. **22**, 73-128 (2003).

[192] S. A. Meek, H. Conrad, and Gerard M.: *Trapping Molecules on a Chip*. Science **324**, 1699-1702 (2009).

[193] T. Köhler, K. Góral, and P. S. Julienne: *Production of cold molecules via magnetically tunable Feshbach resonances*. Rev. Mod. Phys. **78**, 1311 (2006).

[194] J. Herbig, T. Kraemer, M. Mark, T. Weber, C. Chin, H.-C. Nägerl, and R. Grimm: *Preparation of a Pure Molecular Quantum Gas*. Science **301**, 1510-1513 (2003).

[195] M. Greiner, C. A. Regal, and D. S. Jin: *Emergence of a molecular Bose-Einstein condensate from a Fermi gas*. Nature **426**, 537-540 (2003).

[196] K. Winkler, F. Lang, G. Thalhammer, P. v. d. Straten, R. Grimm, and J. Hecker Denschlag: *Coherent Optical Transfer of Feshbach Molecules to a Lower Vibrational State*. Phys. Rev. Lett. **98**, 043201 (2007).

[197] K.-K. Ni, S. Ospelkaus, M. H. G. de Miranda, A. Pe'er, B. Neyenhuis, J. J. Zirbel, S. Kotochigova, P. S. Julienne, D. S. Jin, and J. Ye: *A High Phase-Space-Density Gas of Polar Molecules*. Science **322**, 231-235 (2008).

[198] J. G. Danzl, M. J. Mark, E. Haller, M. Gustavsson, R. Hart, J. Aldegunde, J. M. Hutson, and H.-C. Nägerl: *An ultracold high-density sample of rovibronic ground-state molecules in an optical lattice*. Nature Physics **6**, 265-270 (2010).

[199] H. R. Thorsheim, J. Weiner, and P. S. Julienne: *Laser-induced photoassociation of ultracold sodium atoms*. Phys. Rev. Lett. **58**, 2420-2423 (1987).

[200] M. Kemmann, I. Mistrik, S. Nussmann, H. Helm, C. J. Williams, and P. S. Julienne: *Near-threshold photoassociation of* $^{87}Rb_2$. Phys. Rev. A **69**, 022715 (2004).

[201] A. Fioretti, D. Comparat, A. Crubellier, O. Dulieu, F. Masnou-Seeuws, and P. Pillet: *Formation of Cold* $Cs_2$ *Molecules through Photoassociation*. Phys. Rev. Lett. **80**, 4402-4405 (1998).

[202] C. Gabbanini, A. Fioretti, A. Lucchesini, S. Gozzini, and M. Mazzoni: *Cold Rubidium Molecules Formed in a Magneto-Optical Trap*. Phys. Rev. Lett. **84**, 2814-2817 (2000).

[203] A. J. Kerman, J. M. Sage, S. Sainis, Th. Bergeman, and D. DeMille: *Production and State-Selective Detection of Ultracold RbCs Molecules*. Phys. Rev. Lett. **92**, 153001 (2004).

[204] C. Haimberger, J. Kleinert, M. Bhattacharya, and N. P. Bigelow: *Formation and detection of ultracold ground-state polar molecules*. Phys. Rev. A **70**, 021402 (2004).

[205] J. M. Sage, S. Sainis, T. Bergeman, and D. DeMille: *Optical Production of Ultracold Polar Molecules*. Phys. Rev. Lett. **94**, 203001 (2005).

[206] J. Qian, L. Zhou, K. Zhang, and W. Zhang: *Efficient production of polar molecular Bose-Einstein condensates via an all-optical R-type atom-molecule adiabatic passage*. New J. Phys. **12**, 033002 (2010).

[207] A. R. L. Caires, V. A. Nascimento, D. C. J. Rezende, V. S. Bagnato, and L. G. Marcassa: *Atomic density and light intensity dependences of the* $Rb_2$ *molecule formation rate constant in a magneto-optical trap*. Phys. Rev. A **71**, 043403 (2005).

[208] S. D. Kraft, P. Staanum, J. Lange, L. Vogel, R. Wester, and M. Weidemüller: *Formation of ultracold LiCs molecules*. J. Phys. B.: At. Mol. Opt. Phys. **39**, 993 (2006).

[209] M. Machholm, A. Giusti-Suzor, and F. H. Mies: *Photoassociation of atoms in ultracold collisions probed by wave-packet dynamics*. Phys. Rev. A **50**, 5025-5036 (1994).

[210] F. Fatemi, K. M. Jones, H. Wang, I. A. Walmsley, and P. D. Lett: *Dynamics of photoinduced collisions of cold atoms probed with picosecond laser pulses*. Phys. Rev. A **64**, 033421 (2001).

[211] C. Brif, R. C., and H. Rabitz: *Control of quantum phenomena: Past, present, and future*. http://arxiv.org/abs/0912.5121v1, (2009).

[212] C. P. Koch, R. Kosloff, and F. Masnou-Seeuws: *Short-pulse photoassociation in rubidium below the $D_1$ line*. Phys. Rev. A **73**, 043409 (2006).

[213] C. P. Koch, E. Luc-Koenig, and F. Masnou-Seeuws: *Making ultracold molecules in a two-color pump-dump photoassociation scheme using chirped pulses*. Phys. Rev. A **73**, 033408 (2006).

[214] W. Salzmann, U. Poschinger, R. Wester, M. Weidemüller, A. Merli, S. M. Weber, F. Sauer, M. Plewicki, F. Weise, A. M. Esparza, L. Wöste, and A. Lindinger: *Coherent control with shaped femtosecond laser pulses applied to ultracold molecules*. Phys. Rev. A **73**, 023414 (2006).

[215] B. L. Brown, A. J. Dicks, and I. A. Walmsley: *Coherent Control of Ultracold Molecule Dynamics in a Magneto-Optical Trap by Use of Chirped Femtosecond Laser Pulses*. Phys. Rev. Lett. **96**, 173002 (2006).

[216] T. Mullins, W. Salzmann, S. Götz, M. Albert, J. Eng, R. Wester, M. Weidemüller, F. Weise, A. Merli, S. M. Weber, F. Sauer, L. Wöste, and A. Lindinger: *Photoassociation and coherent transient dynamics in the interaction of ultracold rubidium atoms with shaped femtosecond pulses. I. Experiment*. Phys. Rev. A **80**, 063416 (2009).

[217] M. Albert, T. Mullins, S. Götz, W. Salzmann, R. Wester, and M. Weidemülller: *The interaction of a spectrally cut laser-pulse with a two-level atom*. J. Mod. Opt. **55**, 3359-3368 (2008).

[218] W. Salzmann, T. Mullins, J. Eng, M. Albert, R. Wester, M. Weidemüller, A. Merli, S. M. Weber, F. Sauer, M. Plewicki, F. Weise, L. Wöste, and A. Lindinger: *Coherent Transients in the Femtosecond Photoassociation of Ultracold Molecules*. Phys. Rev. Lett. **100**, 233003 (2008).

[219] A. Merli, F. Eimer, F. Weise, A. Lindinger, W. Salzmann, T. Mullins, S. Götz, R. Wester, M. Weidemüller, R. Ağanoğlu, and C. P. Koch: *Photoassociation and coherent transient dynamics in the interaction of ultracold rubidium atoms with shaped femtosecond pulses. II. Theory*. Phys. Rev. A **80**, 063417 (2009).

[220] David J. McCabe, Duncan G. England, Hugo E. L. Martay, Melissa E. Friedman, Jovana Petrovic, Emiliya Dimova, Béatrice Chatel, and Ian A. Walmsley: *Pump-probe study of the formation of rubidium molecules by ultrafast photoassociation of ultracold atoms*. Phys. Rev. A **80**, 033404 (2009).

[221] H. E. L. Martay, D. J. McCabe, D. G. England, M. E. Friedman, J. Petrovic, and I. A. Walmsley: *Demonstrating coherent control in $^{85}Rb_2$ using ultrafast laser pulses: A theoretical outline of two experiments*. Phys. Rev. A **80**, 033403 (2009).

[222] U. Marvet and M. Dantus: *Femtosecond photoassociation spectroscopy: coherent bond formation*. Chem. Phys. Lett. **245**, 393-399 (1995).

[223] P. Backhaus, B. Schmidt, and M. Dantus: *Control of photoassociation yield: a quantum-dynamical study of the mercury system to explore the role of pulse duration from nanoseconds to femtoseconds*. Chem. Phys. Lett. **306**, 18-24 (1999).

[224] W. Ketterle, K. B. Davis, M. A. Joffe, A. Martin, and D. E. Pritchard: *High densities of cold atoms in a dark spontaneous-force optical trap*. Phys. Rev. Lett. **70**, 2253 (1993).

[225] C. G. Townsend, N. H. Edwards, K. P. Zetie, C. J. Cooper, J. Rink, and C. J. Foot: *High-density trapping of cesium atoms in a dark magneto-optical trap*. Phys. Rev. A **53**, 1702-1714 (1996).

[226] W. Salzmann: *Photoassociation and coherent control of ultracold molecules by femtosecond pulses*. Ph. D. thesis, Albert-Ludwigs-Universität Freiburg, (2007).

[227] V. Kokoouline, O. Dulieu, R. Kosloff, and F. Masnou-Seeuws: *Mapped Fourier methods for long-range molecules: Application to perturbations in the $Rb_2(0_u^+)$ photoassociation spectrum*. J. Chem. Phys. **110**, 9865-9876 (1999).

[228] R. Kosloff: *Time-dependent quantum-mechanical methods for molecular dynamics*. J. Phys. Chem. **92**, 2087-2100 (1988).

[229] A. Merli: *Steuerung photoinduzierter Prozesse an kalten und ultrakalten Alkalidimeren mittels geformter Femtosekunden-Laserpuls*. Ph. D. thesis, Freie Universität Berlin, (2008).

[230] N. Dudovich, D. Oron, and Y. Silberberg: *Coherent transient enhancement of optically induced resonant transitions*. Phys. Rev. Lett. **88**, 123004-123004 (2002).

[231] D. Neuhauser: *Bound state eigenfunctions from wave packets: Time - energy resolution*. J. Chem. Phys. **93**, 2611-2616 (1990).

[232] V. A. Mandelshtam and H. S. Taylor: *Harmonic inversion of time signals and its applications*. J. Chem. Phys. **107**, 6756-6769 (1997).

[233] M. Shapiro and P. Brumer: *Principles of quantum control*. Wiley Interscience, New York (2003).

[234] A. Monmayrant, B. Chatel, and B. Girard: *Quantum State Measurement Using Coherent Transients*. Phys. Rev. Lett. **96**, 103002 (2006).

[235] G. Veshapidze, M. L. Trachy, H. U. Jang, C. W. Fehrenbach, and B. D. DePaola: *Pathway for two-color photoassociative ionization with ultrafast optical pulses in a Rb magneto-optical trap*. Phys. Rev. A **76**, 051401 (2007).

[236] S. J. Park, S. W. Suh, Y. Sup Lee, and G.-H. Jeungy: *Theoretical Study of the Electronic States of the $Rb_2$ Molecule*. J. Mol. Spec. **207**, 129-135 (2001).

[237] C. P. Koch, M. Ndong, and R. Kosloff: *Two-photon coherent control of femtosecond photoassociation*. Faraday Discuss., (2009).

[238] P. Pellegrini, M. Gacesa, and R. Côté: *Giant Formation Rates of Ultracold Molecules via Feshbach-Optimized Photoassociation*. Phys. Rev. Lett. **101**, 053201 (2008).

[239] M. Viteau, A. Chotia, M. Allegrini, N. Bouloufa, O. Dulieu, D. Comparat, and P. Pillet: *Optical Pumping and Vibrational Cooling of Molecules*. Science **321**, 232 (2008).

[240] M. Viteau, A. Chotia, M. Allegrini, N. Bouloufa, O. Dulieu, D. Comparat, and P. Pillet: *Efficient formation of deeply bound ultracold molecules probed by broadband detection*. Phys. Rev. A **79**, 021402 (2009).

# List of publications


1. W. Salzmann, U. Poschinger, R. Wester, M. Weidemüller, A. Merli, S. M. Weber, F. Sauer, M. Plewicki, F. Weise, A. M. Esparza, L. Wöste, and A. Lindinger: *Coherent control with shaped femtosecond laser pulses applied to ultracold molecules.* Phys. Rev. A **73**, 023414 (2006).

2. M. Plewicki, F. Weise, S. M. Weber, and A. Lindinger: *Phase, amplitude, and polarization shaping with a pulse shaper in a Mach-Zehnder interferometer.* Appl. Opt. **45**, 8356 (2006).

3. F. Weise, S. M. Weber, M. Plewicki, and A. Lindinger: *Application of phase, amplitude, and polarization shaped pulses for optimal control on molecules.* Chem. Phys. **332**, 313-317 (2007).

4. F. Weise, S. Birkner, A. Merli, S. M. Weber, F. Sauer, L. Wöste, A. Lindinger, W. Salzmann, T. Mullins, J. Eng, M. Albert, R. Wester, and M. Weidemüller: *Optimal control of multiphoton ionization of $Rb_2$ molecules in a magneto-optical trap.* Phys. Rev. A **76**, 063404 (2007).

5. M. Plewicki, S. M. Weber, F. Weise, and A. Lindinger: *Independent control over the amplitude, phase, and polarization of femtosecond pulses.* Appl. Phys. B **86**, 259-263 (2007).

6. Stefan M. Weber, Fabian Weise, Mateusz Plewicki, and Albrecht Lindinger: *Interferometric generation of parametrically shaped polarization pulses.* Appl. Opt. **46**, 5987-5990 (2007).

7. W. Salzmann, T. Mullins, J. Eng, M. Albert, R. Wester, M. Weidemüller, A. Merli, S. M. Weber, F. Sauer, M. Plewicki, F. Weise, L. Wöste, and A. Lindinger: *Coherent Transients in the Femtosecond Photoassociation of Ultracold Molecules.* Phys. Rev. Lett. **100**, 233003 (2008).

8. A. Lindinger, S. M. Weber, F. Weise, and M. Plewicki: *Phase, amplitude, and polarization shaping by interferometric pulse generation.* in: Atomic Cluster Collisions, Structure and Dynamics from the Nuclear to the Biological Scale, 283-293 (2008).

9. Stefan M. Weber, Mateusz Plewicki, Fabian Weise, and Albrecht Lindinger: *Parametric polarization pulse shaping demonstrated for optimal control of NaK.* J. Chem. Phys. **128**, 174306 (2008).

10. Terry Mullins, Wenzel Salzmann, Simone Götz, Magnus Albert, Judith Eng, Roland Wester, Matthias Weidemüller, Fabian Weise, Andrea Merli, Stefan M. Weber,

Franziska Sauer, Ludger Wöste, and Albrecht Lindinger: *Photoassociation and coherent transient dynamics in the interaction of ultracold rubidium atoms with shaped femtosecond pulses. I. Experiment.* Phys. Rev. A **80**, 063416 (2009).

11. Andrea Merli, Frauke Eimer, Fabian Weise, Albrecht Lindinger, Wenzel Salzmann, Terry Mullins, Simone Götz, Roland Wester, Matthias Weidemüller, Ruzin Ağanoğlu, and Christiane P. Koch: *Photoassociation and coherent transient dynamics in the interaction of ultracold rubidium atoms with shaped femtosecond pulses. II. Theory.* Phys. Rev. A **80**, 063417 (2009).

12. F. Eimer, F. Weise, A. Merli, S. Birkner, F. Sauer, L. Wöste, A. Lindinger, R. Ağanoğlu, C. P. Koch, W. Salzmann, T. Mullins, S. Götz, R. Wester, and M. Weidemüller: *Spectrally resolved coherent transient signal for ultracold rubidium molecules.* Eur. Phys. J. D **54**, 711-714 (2009).

13. Fabian Weise, Andrea Merli, Frauke Eimer, Sascha Birkner, Franziska Sauer, Ludger Wöste, Albrecht Lindinger, Wenzel Salzmann, Terence G Mullins, Roland Wester, Matthias Weidemüller, Ruzin Ağanoğlu, and Christiane P Koch: *Characteristic oscillations in the coherent transients of ultracold rubidium molecules using red and blue detuned pulses for photoassociation.* J. Phys. B.: At. Mol. Opt. Phys. **42**, 215307 (2009).

14. Fabian Weise and Albrecht Lindinger: *Full control over the electric field using four liquid crystal arrays.* Opt. Lett. **34**, 1258-1260 (2009).

15. A. Lindinger, S. M. Weber, M. Plewicki, and F. Weise: *Simultaneous phase, amplitude, and polarization control of femtosecond laser pulses.* in: AIP Conference Proceedings for ICCMSE 2009, Symposium 22, Rhodos, Greece, in press.

16. Fabian Weise and Albrecht Lindinger: *Full parametric pulse shaping in phase, amplitude, and polarization using an effective four-array modulator.* Appl. Phys. B in press, (2010).

17. Fabian Weise, Georg Achazi, and Albrecht Lindinger: *Parametrically polarization-shaped pulses using a hollow-core optical fiber for coherent control.* submitted to Phys. Rev. Lett.

18. Georg Achazi, Fabian Weise, Monika Pawlowska, Alexander Patas, and Albrecht Lindinger: *Characterising pulses after propagation throught an optical fiber by detection of a fraction of back-reflected light.* in preparation.

19. Fabian Weise, Georg Achazi, Monika Pawłowska, and Albrecht Lindinger: *Full control of polarization shaped femosecond laser pulses via a hollow core photonic crystal fiber.* in preparation.

20. Fabian Weise, Monika Pawłowska, Georg Achazi, and Albrecht Lindinger: *Paramtrically phase, amplitude, and polarization shaped femtosecond laser pulses guided via a step-index fiber.* in preparation.

# Patents

1. Albrecht Lindinger, Stefan M. Weber, Mateusz Plewicki, and Fabian Weise
   *Vorrichtung und Verfahren zur Herstellung und Detektion in Amplitude, Phase und Polarization geformter Laserpulse.*
   DE 10 2006 029 035 B4 (2006).
2. Albrecht Lindinger, Fabian Weise, and Georg Achazi
   *Method and system for generating laser pulses.*
   patent pending.

# Curriculum vitae

Der Lebenslauf ist in der Online-Version aus Gründen des Datenschutzes nicht enthalten

# Danksagung

Ganz herzlich möchte ich mich bei Prof. Dr. Ludger Wöste bedanken, der mir die Möglichkeit gegeben hat, in seiner Arbeitsgruppe zu promovieren. Die Aktivitäten seiner Gruppe waren immer sehr bereichernd. Insbesondere möchte ich die Erlebnisse und Erfahrungen in Paris nicht missen.
Dr. Albrecht Lindinger möchte ich für seinen Pragmatismus und sein Engagement im Patentierungsverfahren sowie für die Unterstützung danken, die er mir bei der Realisierung der Experimente zur Polarisationspulsformung entgegengebracht hat.
Mit Dr. Stefan M. Weber und Dr. Mateusz Plewicki hat das Abenteuer der Femtosekunden-Polarisationsformung begonnen und ohne sie würde diese Arbeit wahrscheinlich anders aussehen.
Zur Verbindung von ultrakurzen Laserpulsen und ultrakalten Gasen trugen Viele bei: Mit Dr. Franziska Sauer, Dr. Andrea Merli, Sascha Birkner und Frauke Eimer vergingen die langen Messnächte wie im Fluge. Die Experimente wären ohne das Team um Prof. Dr. Matthias Weidemüller aus Freiburg nicht möglich gewesen. Mein besonderer Dank gilt Dr. Roland Wester, Dr. Wenzel Salzmann und Terry Mullins die immer zur Stelle waren, wenn die MOT mal wieder heiß zu laufen drohte.
Dr. Christiane Koch möchte ich für ihre wissenschaftlichen Ratschläge sowie für die theoretischen Simulationen danken, die das Verständnis der Modulationen in unserem Ionensignal erst ermöglichten. Ruzin Ağanoğlu danke ich für ihre große Geduld beim Anpassen des Programms auf meine ständig neuen Wünsche.
Als es darum ging, geformte ultrakurze Laserpulse durch optische Fasern zu transportieren waren Monika Pawłowska und Georg Achazi eine große Hilfe. Ihnen danke ich für ihre Ausdauer beim Rotieren der Waveplates und der Aufnahme unendlich vieler Kreuzkorrelationen.
Dr. Torsten Siebert und Marcel Krenz gaben mir viele Einblicke in die Geheimnisse der Lasertechnik und halfen mir oft mit der notwendigen Optik aus.
Das Team um Detlef Müller aus der Feinwerktechnik erledigte oft scheinbar unmögliche Konstruktionen und Reparaturen sehr schnell und half dabei, die Experimente am Laufen zu halten.
Ich danke der gesamten Arbeitsgruppe Wöste für ihre Hilfsbereitschaft und die tolle Atmosphäre in der Gruppe. Die Reisen nach Polen und Rumänien waren Höhepunkte meiner Promotionszeit.
Dem Sonderforschungsbereich 450 danke ich für die Finanzierung meiner Promotion und die vielen spannenden Dienstagnachmittage.
Meiner Familie danke ich von ganzem Herzen für ihre immerwährende Unterstützung.
Ein ganz besonders großer Dank gilt meiner Freundin Lena für ihre unerschöpfliche Geduld und Liebe.